FAU Studien aus dem Maschinenbau 417

Benjamin Lengenfelder

Remote photoacoustic sensing using speckle-analysis for biomedical imaging

FAU University Press

Benjamin Lengenfelder

Remote photoacoustic sensing using speckle-analysis for biomedical imaging

FAU Studien aus dem Maschinenbau

Band 417

Benjamin Lengenfelder

Remote photoacoustic sensing using speckle-analysis for biomedical imaging

Dissertation aus dem Lehrstuhl für Photonische Technologien (LPT) Prof. Dr.-Ing. Michael Schmidt

Erlangen
FAU University Press
2023

Bibliografische Information der Deutschen Nationalbibliothek:
Die Deutsche Nationalbibliothek verzeichnet diese Publikation in der Deutschen Nationalbibliografie; detaillierte bibliografische Daten sind im Internet über http://dnb.d-nb.de abrufbar.

Bitte zitieren als
Lengenfelder, Benjamin. 2023. *Remote photoacoustic sensing using speckle-analysis for biomedical imaging.* FAU Studien aus dem Maschinenbau Band 417. Erlangen: FAU University Press. DOI: 10.25593/978-3-96147-618-3.

Der vollständige Inhalt des Buchs ist als PDF über den OPUS-Server der Friedrich-Alexander-Universität Erlangen-Nürnberg abrufbar:
https://opus4.kobv.de/opus4-fau/home

Verlag und Auslieferung:
FAU University Press, Universitätsstraße 4, 91054 Erlangen

Druck: docupoint GmbH

ISBN: 978-3-96147-617-6 (Druckausgabe)
eISBN: 978-3-96147-618-3 (Online-Ausgabe)
ISSN: 2625-9974
DOI: 10.25593/978-3-96147-618-3

Remote photoacoustic sensing using speckle-analysis for biomedical imaging

Der Technischen Fakultät
der Friedrich-Alexander-Universität
Erlangen-Nürnberg

zur
Erlangung des Doktorgrades Dr.-Ing.

vorgelegt von

Benjamin Lengenfelder, M.Sc.

aus Neumarkt i.d.OPf

Als Dissertation genehmigt
von der Technischen Fakultät
der Friedrich-Alexander-Universität Erlangen-Nürnberg

Tag der mündlichen Prüfung:	20.10.2022

Gutachter:	Prof. Dr.-Ing. Michael Schmidt Prof. Dr. rer. nat. Alexander Jesacher, Medizinische Universität Innsbruck, Österreich Prof. Dr. Zeev Zalevsky, Bar-Ilan University, Israel

Preface

This dissertation was written during my work as a research assistant at the Institute of Photonic Technologies (LPT). The work was initiated by a research project, which showed that the topic is suitable for a dissertation.

My special thanks go to my doctoral supervisor Professor Michael Schmidt for making my graduation possible, for the competent supervision and the freedom granted for my scientific activities. Furthermore, I would like to thank Professor Zeev Zalevsky for the lively exchange of ideas, many suggestions on the topic and for a research stay at his institute. In addition, I am grateful for the continuous medical advice from Professor Maximilian Waldner.

I would also like to thank my colleagues at the LPT for the pleasant working atmosphere. Special thanks go to Martin Hohmann, who has had a significant influence on my career, first as a supervisor of my Bachelor and Master thesis and later as a colleague. Furthermore, thanks to Dr.-Ing. Florian Klämpfl, who introduced me to the scientific working style and many relevant scientific questions, especially at the beginning of my time at the LPT. I would also like to thank Jennifer Webersdorfer, my friends Martin Schmaußer, Florian Hundsdorfer and Christian Freihart for proof-reading this dissertation.

Thanks go to my family, who has supported me throughout my life. My greatest thanks go to my life partner Carina, who with her advice and unconditional emotional support enabled me to overcome difficult periods during my work. Furthermore, she gave me all the necessary freedom to finish my dissertation.

Erlangen, 2021

Contents

List of Symbols and Abbreviations

Abbreviation	*Description*
APS	Avalanche-photodiode sensor
AR-PAM	Acoustic Resolution Photoacoustic Microscopy
AOM	Acousto-optic modulator
BS	Beam splitter
CT	Computed Tomography
CW	Continuous wave
DA	Detection aperture
DNA	Deoxyribonucleic acid
FPC	Fabry-Pérot Cavity
GUI	Graphical user interface
Hb	Haemoglobin
HbO_2	Oxy-haemoglobin
HbR	Deoxy-haemoglobin
HSMIU	High-speed microscopic imaging unit
LIU	Laser induced ultrasound
MbR	Reduced myoglobin
MbO_2	Oxy-myoglobin
MCS	Monte Carlo Simulation
MEMS	Microelectromechanical systems
MIP	Maximum intensity projection
$MIP_x/MIP_y/MIP_z$	Maximum intensity projection in x/y/z-direction
MPE	Maximum permissible exposure
MPM	Multi-Photon Microscopy
MRI	Magnetic Resonance Imaging
MRT	Magnetic Resonance Tomography
Nd:YAG	Neodymium-doped yttrium aluminum garnet
NEP	Noise equivalent pressure
OCT	Optical Coherence Tomography

Abbreviation	*Description*
OR-PAM	Optical Resolution Photoacoustic Microscopy
PA	Photoacoustic(s)
PACT	Photoacoustic Computed Tomography
PAE	Photoacoustic Endoscopy
PAI	Photoacoustic Imaging
PAM	Photoacoustic Microscopy
PD	Photodetector
PD_1, PD_2, PD_3, PD_4	Measurement Photodiodes
PVCP	Polyvinylchloride plastisol
PVDF	Polyvinylidene Fluoride
PSD	Position-sensitive detector
PZT	Lead Zirconate Titanate
RNA	Ribonucleic acid
ROI	Region of interest
Ti:Sapphire	Titanium:Sapphire Laser
US	Ultrasound
UST	Ultrasound transducer

Symbol	***Unit***	***Description***
A,B	-	Fourier Transformation of successive image frames
$A_{speckle}$	a.u.	Single speckle area
a,b	-	Successive image frames
B_d	Hz	Detector bandwidth
B_s	Hz	Source bandwidth
C	-	Speckle pattern contrast
C_p	$JK^{-1}kg^{-1}$	Specific heat capacity
C_{sing}	-	Single speckle contrast
C_{sp}	a.u.	Speckle centre of mass
Circ	-	Single speckle circularity
c	ms^{-1}	Speed of sound
c_{pe}	ms^{-1}	Speed of sound in piezoelectric material
d_1	m	Distance absorber surface - detection surface (reflection-mode)
d_2	m	Distance absorber surface - detection surface (transmission-mode)
d_3	m	increased acoustic transit distance
d_{px}	m	Pixel size
D	$dbm^{-1}Hz^{-1}$	Constant for acoustic attenuation description
D_a	m	Absorber diameter
D_{ex}	m	Photoacoustic excitation area length
D_{ill}	m	Illumination diameter
D_t	m^2s^{-1}	Thermal diffusivity
E	-	Constant for acoustic attenuation description
E_p	J	Pulse energy
F	Jm^{-2}	Local fluence
F_o	Jm^{-2}	Superficial energy exposure
f	Hz	Frequency
f_o	Hz	Detector central frequency

Symbol	*Unit*	*Description*
f_{os}	Hz	Source central frequency
f_f	m	Focal length
g	-	Anisotropy factor
H	Jm^{-3}	Local energy deposition density
h_{px}	pixel	Vertical sensor resolution
$I_{a,sp}$	a.u.	Mean intensity of speckle pattern
I_{back}	a.u.	Single speckle background intensity
$I_{speckle}$	a.u.	Single speckle intensity
k	m	Acoustic penetration coordinate / absorber depth
L	m	Piezoelectric element thickness
L_D	m	Side length for detector area
l_{depo}	m	Depolarization length
$l_{depo,M}$	m	Mie depolarization length
$l_{depo,R}$	m	Rayleigh depolarization length
L_t	m	Thermal diffusion length
l_s	m	Speckle size
M	-	Magnification
n_r	-	Index of refraction
p	Pa	Pressure
p_o	Pa	Initial photoacoustic pressure amplitude
R	m	Acoustic source/absorber - detector distance
R_M	-	Mie-scattering ratio
R_R	-	Rayleigh-scattering ratio
r	m	Absorber radius
$\vec{r}_d$	(m,m,m)	Detector element position
$r_{shell,t}$	m	Radius of spherical shell
$\vec{r}_v$	(m,m,m)	Volume element position
S_d	Pa	Sensitivity
$S_{d,nm}$	nm	Deformation detection sensitivity

Symbol	***Unit***	***Description***
$S_{d,\alpha}$	°	Minimal detectable tilt / tilt detection sensitivity
t	s	Time
t_p	s	Pulse duration
t_s	s	Stress relaxation time
t_{sp}	a.u.	Speckle vector length
t_t	s	Acoustic propagation time
U	-	Heaviside function
$V_{shell,t}$	m^3	Volume of spherical shell
$W_{shell,t}$	Jm^{-3}	Deposited energy of spherical shell
w_{px}	pixel	Horizontal sensor resolution
X_a	m	rectangular absorber width
X_o,Y_o,Z_o	m	Object dimensions
$X_{max/real}$	-	maximal/realistic ratio for detection time increase
x, y, z	a.u.	Speckle coordinates
x_d, y_d, z_d	m	Detector element coordinates
x_{so}	a.u.	Horizontal movement of subjective speckle pattern
$x_{so,real}$	a.u.	Real horizontal movement of subjective speckle pattern
x_{sp}, y_{sp}	a.u.	Speckle centre of mass
$x_{sp,max}$, $y_{sp,max}$	a.u.	Maximal detectable speckle centre of mass
$x_{sp,real}$	a.u.	Real speckle shift in horizontal direction
x_v, y_v, z_v	m	Volume element /object coordinates
y_{so}	a.u.	Vertical movement of subjective speckle pattern
Z	m	Speckle pattern distance to surface
Z_{ac}	$kgm^{-2}s^{-1}$	Acoustic impedance

Symbol	*Unit*	*Description*
α	°	Tilt
α_{ac}	°	Absorber surface opening angle
$\alpha_{max,x}$, $\alpha_{max,y}$	°	Maximal detectable tilt
α_x, α_y	°	Tilt in horizontal/vertical direction
β	K^{-1}	Volume expansion coefficient
Γ	-	Grueneisen coefficient
Δd	m	Detector element spacing
δ_o	a.u.	Objective speckle pattern movement
δ_s	a.u.	Subjective speckle pattern movement
$\delta_{s,min}$	a.u.	Minimal detectable subjective speckle pattern movement
$\delta_{s,tot}$	a.u.	Total movement of subjective speckle pattern
$\Delta\alpha$	°	Surface tilt change
$\Delta\alpha_x$, $\Delta\alpha_y$	°	Surface tilt change in horizontal/vertical direction
Δ_{so}	a.u.	Shift extraction error
ϵ	m	Axial surface deformation
ϵ_x, ϵ_y	m	From $\alpha_{x/y}$ reconstructed axial surface deformation
ϵ_{max}	m	Maximal axial surface deformation
$\epsilon_{max,measure}$	m	Maximal axial surface deformation for interferometric measurement
$\epsilon_{max,simulation}$	m	Maximal axial surface deformation from simulation
η, τ	-	Spatial image frequency coordinates
κ	$mkg^{-1}s^{-2}$	Compressibility
κ_p	-	Electromechanical coupling coefficient
λ	m	(Optical) wavelength
λ_a	m	Acoustic wavelength
λ_{lat}	m	Lateral acoustic surface wavelength
μ	m^{-1}	Optical attenuation coefficient

Symbol	***Unit***	***Description***
μ_{eff}	m^{-1}	Effective optical attenuaton coefficent
μ_a	m^{-1}	Optical absorption coefficient
μ_s	m^{-1}	Optical scattering coefficient
μ_s'	m^{-1}	Reduced scattering coefficient
ρ	kgm^{-3}	Material density
σ	m^{-1} / dbm^{-1}	Acoustic attenuation coefficent
σ_a	m^{-1}	Acoustic absorption coefficent
σ_{gauss}	-	Standard deviation of Gaussian filter
σ_{nf}	-	Noise level
σ_{pen}	m	Optical penetration depth
σ_{prec}	m	Algorithmic speckle shift extraction precision
σ_s	m^{-1}	Acoustic scattering coefficient
σ_{sp}	a.u.	Standard deviation of speckle pattern
σ_s	m^{-1}	Acoustic scattering coefficient
ϕ	°	Angle of incidence/deflection
Ψ	m^2s^{-1}	Velocity potential

1 Introduction

William Osler, who is considered to be the father of modern medicine, described medicine as "a science of uncertainty and an art of probability"[1] in the last century turn. This famous saying describes the high uncertainty and risks of mistakes for diagnostic and therapeutic decisions in medicine for former times and may still be transferred to our days.

However, during the last century technical progress in the field of medical imaging helped to reduce this uncertainty significantly and is a key factor for precise diagnosis and therapy monitoring in modern medicine [2]. The modalities for structural medical imaging can be separated in two groups considering the imaging penetration depths: X-ray Computed Tomography (CT) and Magnet Resonance Tomography (MRT) allow entire body imaging, whereas Ultrasound (US) and optical methods provide imaging of sub-surface regions with a specific penetration depth [3].

CT measures the attenuated X-ray radiation which has passed through the human body [4]. These measurements are performed in different angles along the body which allows tomographic data reconstruction [5]. The image contrast which is based on radiation attenuation is especially high for bone structures, nevertheless, it is lower for soft tissue [6]. In addition, the generated radiation is harmful to the human body since it is ionizing. Magnetic Resonance Imaging (MRI), in contrast, makes use of strong magnetic fields and spatial localized excitation by radio frequency pulses to acquire tomographic information and is thus harmless to the human body [7]. The selective excitation of hydrogen atoms which are predominantly found in water and fat, results in a good imaging contrast for soft tissue [8]. In general, the CT is the means of choice in emergency situations which require fast, full-body information especially for bone fractures [9]. The MRT may be preferred, for less time critical cases which require detailed soft tissue imaging. In general, the imaging resolution of full-body CT and MRI is limited to the millimetre scale and does thus only provide macroscale imaging without any cellular information [4]. In addition, the procedure for both modalities is quite expensive, time-consuming, requires a separate room and radiation or magnetic shielding, respectively [10]. These mentioned downsides lead to the widespread use of the non-invasive US technique and optical methods for soft tissue imaging which even offer resolution levels at the micrometre scale, therefore allowing cell structure imaging.

US systems excite the body using acoustic waves and detect their reflection from the inside of the body using simple transducers and allow thus fast,

cheap and harmless soft tissue imaging [11]. Furthermore, imaging depths of several centimetres may be achieved due to the low acoustic attenuation in soft tissue which is sufficiently high for most medical indications needing soft tissue information [10]. However, the acoustic reflection strength from the tissue and thus the imaging contrast is based on the mechanical properties of the tissue and consequently limited for soft tissue [7]. In contrast to this limitation, the strong differences in the optical properties of soft tissue enable an high imaging contrast for optical methods. The common optical methods Optical Coherence Tomography (OCT), Microscopy or Multi-Photon Microscopy (MPM) detect a reflection or fluorescence signal after optical excitation. These optical modalities are non-invasive, and allow very precise sensing with resolutions down to 1 µm which can not be achieved with any other modality [12]. The penetration depth, however, is limited to about two millimetres due to the high optical attenuation in soft tissue [13].

Photoacoustic Imaging (PAI) overcomes the limitations of low penetration depth for optical imaging, low contrast for US by combining the two mentioned methods and opens new possibilities for the current state of the art for medical imaging [14]. Therefore, PAI is at the moment an emerging modality [15]. For Photoacoustics (PA), a laser pulse is used for acoustic signal excitation inside the tissue. The detection of the excited acoustic signal by sound transducers leads to unavoidable tissue contact which makes the technique unsuitable for special medical applications like wound imaging, endoscopy of difficult accessible regions or laser surgery feedback [16]. A remote and stable detection modality would thus be beneficial and could help to widespread the usage of PAI. That is why, this thesis investigates a new, remote sensing technique for its usage for photoacoustic detection.

2 State of the art

In the beginning of this chapter the basics of PA are described by introducing the different modalities, explaining the signal generation and image formation process. The emphasis is on the acoustic detection in the last section, since this thesis investigates a new sensing technology for its usability for photoacoustic detection.

2.1 Basics of photoacoustics

2.1.1 Modalities

PAI can be grouped in three modalities: Photoacoustic Microscopy (PAM), Photoacoustic Computed Tomography (PACT) and Photoacoustic Endoscopy (PAE) [17]. For all three setups, the acoustic signal excitation is performed with a short laser pulse and the detection is done with transducers. Figure 1 gives an overview on these modalities, their similarities and differences, respectively.

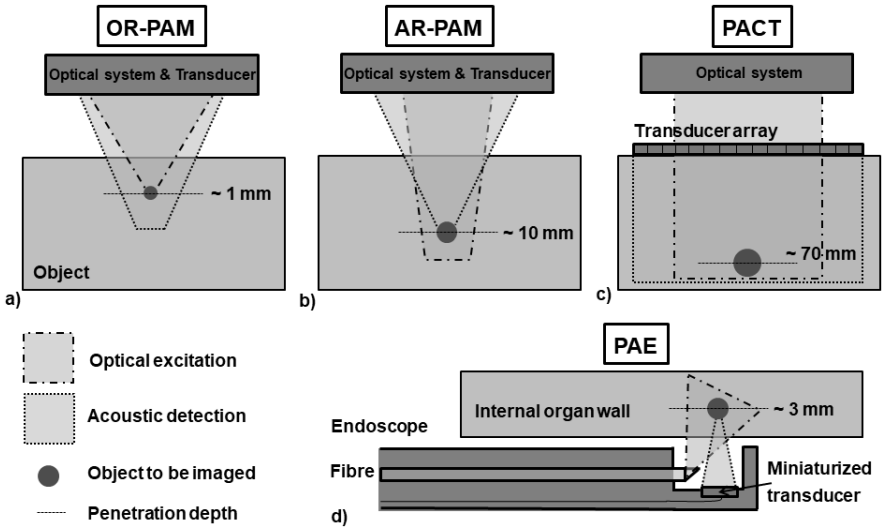

Figure 1: Overview on PAI modalities: Optical Resolution Photoacoustic Microscopy (OR-PAM, a), Acoustic Resolution Photoacoustic Microscopy (AR-PAM, b), Photoacoustic Computed Tomography (PACT, c) and Photoacoustic Endoscopy (PAE, d).

For PAM, the optical excitation and acoustic detection are spatially co-focused at the region of interest and a single point measurement is performed. This localization results on the one side in very high imaging resolutions, but low penetration depths on the other side compared to PACT [17]. Depending

on the kind of relevant focus, PAM can be grouped in Optical Resolution Photoacoustic Microscopy (OR-PAM) and Acoustic Resolution Photoacoustic Microscopy (AR-PAM). For OR-PAM, the optical excitation focus is smaller than the acoustic detection focus. This allows a very high lateral imaging resolution in the range of 1 µm, however, the penetration depth is limited to about 1 mm due to the optical attenuation of the object [18]. In AR-PAM, the acoustic focusing is tight compared to optical focusing. Consequently, the acoustic focus lies inside the loosely focused optical focus. This approach provides lower lateral imaging resolutions, but higher penetration depths compared to OR-PAM. Penetration depths up to 1 cm can be achieved [19]. The lateral resolution can be up to 50 µm [20].

In PACT, the complete region of interest is optically excited by an expanded beam and the generated acoustic signal is detected by a transducer array. This imaging approach results in higher penetration depths compared to PAM since multiple-scattered photons, which have broken the diffusion limit, generate an detectable acoustic signal [20]. However, the spatial resolution is limited, since there is no tight acoustic or optic focusing, respectively. Imaging penetration depths up to 7 cm can be achieved [20]. The lateral resolution can reach 100 µm [21].

PAE represents the latest embodiment of PAI which is used to image tissue from the inside of the body. This approach allows the efficient optical excitation and ultrasonic detection of interior organs like the oesophagus or colon which cannot be achieved by PAM, nor PACT [22]. There are several design possibilities for the acoustic excitation and detection. In general, a fibre is used to deliver the excitation pulse to the endoscopic tip and thus to the region of interest through an opening window. Afterwards a miniaturized transducer detects the acoustic signal. In general, the restricted space limits the freedom for fibre and transducer placement, therefore PAE systems offer mainly only side-view capabilities [23]. Qu et al. for example achieved this side-view using a MEMS-scanner [24]. In contrast to this approach, Xi et al. implemented a side-looking prism [25].

2.1.2 Signal generation

Figure 2 illustrates the signal generation steps and parameters for PAI in soft tissue which are universally valid for the three modalities. The tissue under investigation is excited by a short laser pulse with the pulse energy E_p, which leads to the superficial exposure F_o. A slight part of the excitation photons are reflected at the surface and the majority enters the tissue where the tissue photon interaction can be described by the fundamental processes of absorption and scattering.

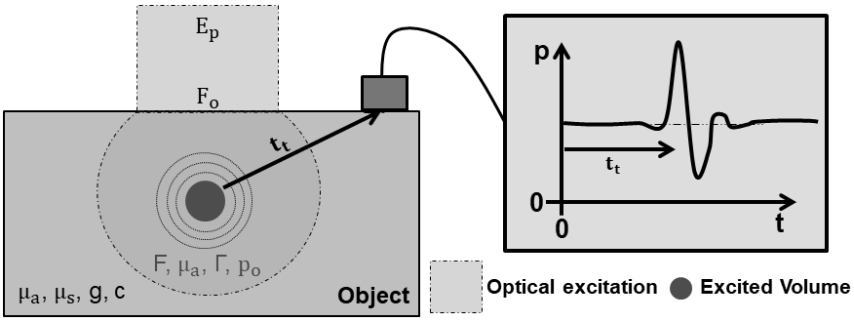

Figure 2: Signal generation for PAI

Absorption is described by the absorption coefficient μ_a which represents the probability for absorption of a photon over its propagation path. The absorption of a photon generates an excited molecule state which relaxes by radiative processes like fluorescence or by heat generation. Tissue contains a huge variety of different absorbers: For example water, melanin, haemoglobin (Hb), proteins or lipid. The tissue composition defines thus the absorption properties. Figure 3 shows the absorption coefficients for the most relevant absorbers in tissue and for skin.

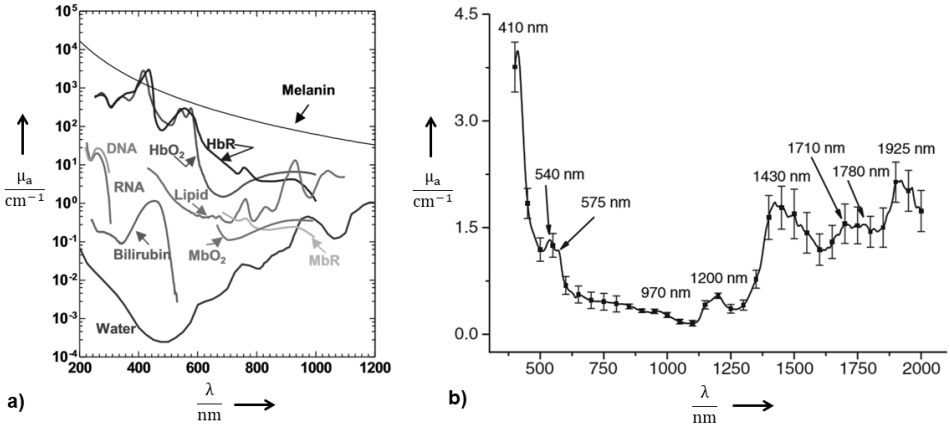

Figure 3: a) Absorption spectra of major endogenous contrast agents in biological tissue at normal concentrations for the wavelength range from 200 nm to 1200 nm: oxy-haemoglobin (HbO_2), deoxy-haemoglobin (HbR), DNA (deoxyribonucleic acid), RNA (ribonucleic acid), reduced myoglobin (MbR), oxy-myoglobin (MbO_2) [26]. b) The absorption coefficient for skin tissue is plotted [27].

There are two different kinds of scattering: elastic and non-elastic scattering. For non-elastic scattering like Raman- and Brillouin-scattering, an energy transfer between photon and scattering molecule takes place. For elastic

scattering, no energy transfer between photon and scattering center takes place and the scattered photon changes its initial propagation direction after the scattering event. In particular, these elastic scattering processes describe the light distribution in tissue and the scattering coefficient μ_s represents the probability of a scattering event for a photon over its propagation path. The anisotropy factor g defines the elastic scattering characteristics, meaning the propagation direction distribution of the scattered photon for several scattering events. It can take values from -1 to 1. A value of g=−1 describes purely backward scattering, g=0 isotropic scattering and g=1 purely forward scattering. The cause of scattering is the interaction of photons with tissue structures like muscle fibers, cells, mitochondria or cell membranes. The size of the interacting structure defines the elastic scattering characteristics. For scatterers which are bigger or the same size as the wavelength, Mie-scattering takes place. For structures which are much smaller than the wavelength, Rayleigh-scattering occurs. Mie-scattering is asymmetric (g≈1) and only weakly dependent on the wavelength λ. Rayleigh-scattering is isotropic (g=0) and its probability of occurrence is inversely proportional to λ^4. Since tissue contains a variety of scattering structures, both kinds of elastic scattering occur and forward scattering dominates (g≈0.75-0.95). Often the influence of the scattering characteristics is taken into account by the reduced scattering coefficient $\mu_s'=\mu_s(1\text{-}g)$. The inverse of this factor describes the penetration depth in which photons completely loose their direction information. Figure 4 shows μ_s', the proportion of Rayleigh- and Mie-scattering and the light penetration depth σ_{pen} of skin tissue for λ=400 nm-2000 nm. This depth is determined by the inverse of the effective attenuation coefficient

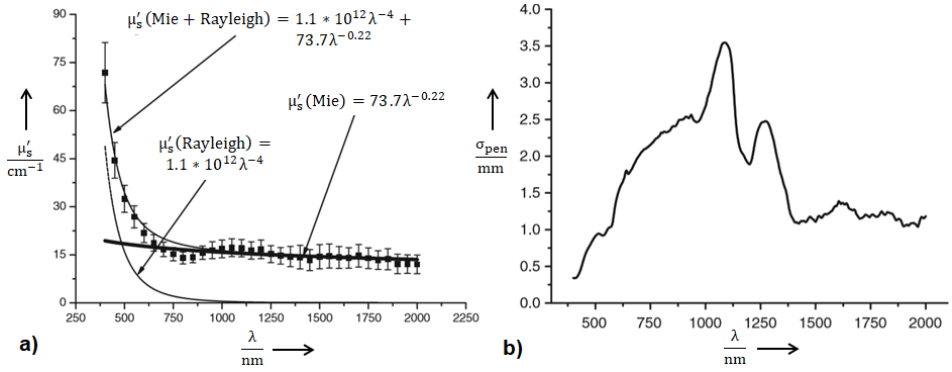

Figure 4: a) The reduced scattering coefficient μ_s', the proportion of Rayleigh- and Mie-scattering are shown [27]. b) The light penetration depth for skin tissue is shown [27].

($\mu_{eff} = \sqrt{3\mu_a(\mu_a + \mu_s')}$) and is described by eq. (1) [28]:

$$\sigma_{pen} = \frac{1}{\sqrt{3\mu_a(\mu_a + \mu_s')}}. \quad (1)$$

The penetration depth σ_{pen} describes the depth which is reached by a proportion of $\frac{1}{e}$ of all photons. The depth decay for the intensity is defined by eq. (2) whereas k describes the penetration depth inside the attenuating tissue.

$$I(k) = I_0 e^{-\mu_{eff} k} \quad (2)$$

Since light scattering and absorption attenuate as well as spread the light inside the tissue volume, these parameters determine thus the local fluence F inside the tissue volume. As previously mentioned, the absorption of a photon generates an excited molecule state which relaxes by radiative or non-radiative processes. For PA, the non-radiative processes are relevant which generate heat [29]. This heat causes volume expansion and therefore a pressure signal with the amplitude p_0 is generated. In PA, temperature rises in the order of 10 mK occur which lead to initial pressure amplitudes normally smaller than 10 kPA [30]. This process is summarized in eq. (3) [29].

$$p_0 = \Gamma \mu_a F(\mu_a, \mu_s, g) = \Gamma H(\mu_a, \mu_s, g) \quad (3)$$

The Grüneisen coefficient $\Gamma = \frac{\beta c^2}{C_p}$ describes the conversion efficiency from heat to pressure for the specific tissue and is defined by the ratio of the volume expansion coefficient β, the speed of sound c and the specific heat capacity C_p [29]. H is the local energy deposition density for the tissue. The generated acoustic wave spreads inside the tissue volume and reaches the acoustic transducer for detection of the pressure p. Therefore, the transit time t_t is defined by the spatial distance between the pressure origin and the transducer location at the surface.

For efficient and localized pressure generation, the thermal and stress confinement need to be fulfilled for the excitation pulse duration t_p. The thermal confinement requires that the thermal diffusion length $L_t = 2\sqrt{D_t t_p}$, which is defined by t_p and the thermal diffusivity D_t, is smaller than the spatial imaging resolution σ_x [31]. This allows maximal energy densities for the excited volume since thermal diffusion is not significant during the excitation [32]. The stress confinement describes the condition that t_p is smaller than the stress propagation time ($t_s = \frac{\sigma_x}{c}$), which is defined by c and σ_x [31]. For high imaging resolutions in the μm range, thermal diffusion occurs at μs to

ms time scales and t_s is in the order of several hundred ns. Consequently, both conditions can be met using ns laser pulses. Solid State lasers can easily achieve these pulse durations and furthermore they are capable of generating high pulse energies of several mJ for strong acoustic signal generation. Thus, Q-switched Nd:YAG and Ti:Sapphire lasers represent the most widely used laser sources for PA [20].

The magnitude of E_p for PA, however, is limited by the maximum permissible exposure (MPE) for soft tissue which therefore defines the maximum for F_0. The MPE for soft tissue is dependent on the excitation wavelength, duration and on the laser repetition rate of the used light sources. It is defined by the American National Standards Institute (ANSI) [31]. Since the effect of laser light on tissue is wavelength dependent, a correction factor C_A is defined for three wavelength bands [33]:

- C_A=1 for 400 to 700 nm
- C_A=$10^{2(\lambda-0.7)}$ for 700 to 1050 nm
- C_A=5 for 1050 to 1400 nm

The MPE for a single pulse is then determined by C_A and t_p [33]:

- MPE=$2C_A 10^{-2}\frac{J}{cm^2}$ for $t_p \in [10^{-9}\text{s},\ 10^{-7}\text{s}]$
- MPE=$1.1C_A t_p^{0.25}\frac{J}{cm^2}$ for $t_p \in [10^{-7}\text{s},\ 10\,\text{s}]$
- MPE=$0.2C_A\frac{W}{cm^2}$ for $t_p \in [10\,\text{s},\ 3\times 10^4\text{s}]$

For a single pulse excitation with t_p=10 ns at 1064 nm, the MPE is for example 100 $\frac{mJ}{cm^2}$. For repetitive pulsed lasers there are two rules of which the more restrictive one applies [34]:

- Single pulse rule: Calculate the MPE accordingly to a single pulse by using t_p
- Complete exposure rule: Calculate the MPE by using the complete exposure time for t_p and divide by the number of single pulses

In case the tissue is irradiated by different lasers, the MPE is partitioned and the following formula can for example apply for two different laser sources: $\frac{F_1}{MPE_1}+\frac{F_2}{MPE_2}<1$. The indices 1 and 2 describe in this case the two different laser sources used for tissue irradiation.

As it can be seen in eq. (3), the fluence, μ_a and Γ determine the signal strength in PAI. Since the mechanical and thermodynamic properties do not vary significantly for soft tissues, μ_a is the dominating contrast mechanism for PA [35]. Soft tissue is composed of several absorbing chromophores (water, melanin, haemoglobin, lipid, proteins) [36]. Melanin and haemoglobin are

the dominating absorbers inside the optical window, which ranges from wavelengths λ=600 nm to λ=1300 nm and allows high optical penetration depths [37]. Inside this window, their absorption contrast is at least one order of magnitude higher than for the other chromophores (water, lipid, protein) for λ<900 nm (see fig. 3) [38]. Melanin is only found in superficial skin layers or the retina and does thus not play an essential role for PAI [29]. In contrast, haemoglobin is a major constituent of blood and offers high absorption inside the optical window. Due to this fact, PAI is highly suitable for visualizing vasculature with high contrast or measuring blood oxygenation. Lao et al. therefore demonstrated the capability of photoacoustic imaging of the developing vasculature during early tumor growth [39]. Stein et al. imaged the blood-oxygenation within the mouse brain by PA [40].

2.1.3 Sound propagation

After the excited thermoelastic expansion, the acoustic impulse spreads through the tissue in form of longitudinal compression waves and finally reaches the detector [41]. Since the pressure spreads uniformly in all directions away from the absorbing location, p_o gets attenuated by the factor $\frac{r}{R}$, whereas r is the absorbing radius and R the distance between transducer and the absorber [30]. The speed for the mentioned propagation is material specific and is defined in eq. (4) by the material density ρ and compressibility κ [41]:

$$c = \sqrt{\frac{1}{\rho\kappa}} \tag{4}$$

This means, that the speed of sound increases for more rigid materials. However, inside the soft tissue group, it does not differ a lot: c ranges from 1490 $\frac{m}{s}$ to 1610 $\frac{m}{s}$ [42]. The acoustic impedance Z_{ac}=cρ and speed of sound determine the acoustic reflection and refraction at structures larger than the acoustic wavelength λ_a, similar to the index of refraction n_r in optics. The reflection factor for the reflected acoustic pressure amplitude at an macroscopic interface with different Z_{ac} at normal incidence is described by: $\frac{Z_{2,ac}-Z_{1,ac}}{Z_{2,ac}+Z_{1,ac}}$ [43]. If an acoustic wave hits a boundary with an angle ϕ it gets refracted and the propagation direction changes according to eq. (5) [44].

$$\frac{sin(\phi_1)}{sin(\phi_2)} = \frac{c_1}{c_2} \tag{5}$$

The indices 1 and 2 stand for the two tissue types which define the boundary. Although, it needs to be emphasized that c and Z do not differ significantly

inside the soft tissue group [42]. This means that losses due to reflection or changes of propagation direction due to refraction at tissue boundaries, respectively, do not influence PA sensing. Nevertheless, acoustic scattering (σ_s) and absorption (σ_a) are sources of attenuation and define thus the acoustic attenuation factor σ=σ_a+σ_s [43]. Scattering occurs if an ultrasound wave hits a tissue inhomogeneity which is smaller or similar to λ_a. A scattering effect results in a change of the ultrasound propagation direction without loss of energy. The scattering probability of ultrasound is dependent on the ratio between its wavelength and the size of the inhomogeneity. For scatterers smaller than λ_a, the scattering intensity is proportional to f^4, whereas it is proportional to f^2 for scatters with a size in the wavelength range [45]. However, since soft tissue is considered to be mechanically homogeneous, scattering contributes less than 10 % to the total attenuation and therefore, absorption is the dominating attenuation factor [46]. The major reasons for absorption are the tissue viscoelasticity, leading to frictional forces which oppose the particle movement, heat conduction and chemical relaxation processes [47]. These effects are strongly frequency dependent which results in the description of the attenuation with the two constants D and E: σ=Df^E. Furthermore, it is important to note that σ can be given in two units: $\frac{db}{cm}$ an cm^{-1}. The acoustic attenuation coefficient $\sigma_{db/cm}$ and its conversion between the two units is defined by eq. (6) whereas k describes the penetration depth inside the attenuating material:

$$\sigma_{db/cm} = \frac{1}{k} 20log \frac{p(k)}{p(k=0)} = 8.686 * \sigma_{1/cm} \tag{6}$$

In the framework of this thesis the abbreviation σ is used for both units. Table 1 gives an overview on acoustic properties for tissue which are relevant for PAI. Regarding the acoustic attenuation, it has to be noted, that σ is about 2-3 orders of magnitude lower than the effective optical attenuation for light in soft tissue [41]. For the acoustic attenuation a factor of $\frac{0.7}{cm}$ at 3 MHz can be assumed, which is small compared to an estimated optical attenuation of $\frac{50}{cm}$ at an excitation in the visible range. This fact enables the high imaging depths for PA compared to purely optical imaging methods.

Table 1: Acoustic properties for tissues relevant for PAI. The data is collected from the following literature: Azhari et al. [48], Moran et al. [49], Nassiri et al. [50].

	$\rho\ [\frac{g}{cm^3}]$	c $[\frac{m}{s}]$	$Z_{ac}\ [\frac{kg}{sm^2} \times 10^6]$	$\sigma = Df^E\ [\frac{db}{cmMHz}]$ D $[\frac{db}{cmMHz}]$ | E
blood	1.055	1575	1.66	0.15 | 1.21
fat	0.95	1450	1.38	0.6 | 1
brain	1.03	1550	1.60	0.8 | 1.35
muscle	1.065	1575	1.68	2.9 | 1
skin	1.15	1730	1.99	0.44 | 1.55

2.1.4 Image formation

For each measurement of PAM and PAE, the temporal acoustic signal is acquired after optical excitation. This single measurement represents a 1D information with either optically or acoustically limited resolution [24]. Therefore, in order to provide 3D information, scanning is required for both setups. In AR-PAM, the sensing spot is laterally moved by mechanical raster scanning of the complete system with a step motor or a voice-coil scanner [18]. For OR-PAM, optical scanning of the excitation beam by galvanometers or microelectromechanical systems (MEMS) mirrors provide a scanning alternative [18]. In PAE, the imaging direction can be rotated with a rotating mirror in order to offer 2D information [23]. Linear movement of the complete endoscopic system further allows 3D imaging. In addition, there is the possibility to laterally scan the optical excitation beam inside a small field of view with MEMS-mirrors [24]. The imaging speeds for PAM and PAE are thus limited to the scanning speed and furthermore to the laser pulse repetition rate due to the repeated excitation process.

An expanded laser beam excites the complete region of interest of the tissue for PACT. Due to the light diffusion, a large tissue volume can be excited at once, in contrast to PAM and PAE [29]. The generated acoustic signal inside this volume is afterwards spatially and temporally resolved detected at the tissue surface. For this detection, a scanned single transducer or a transducer array (which consists of several single transducer elements) can be used. The detected signal for each sensing position can therefore be considered as an integral of all initial acoustic signals lying inside its detection aperture. This fact allows the reconstruction of the initial pressure sources inside the excited volume by using back-reconstruction techniques. The most common

reconstruction technique for PACT is the simple back-projection in time domain. The basic principle of this reconstruction algorithm is illustrated in fig. 5.

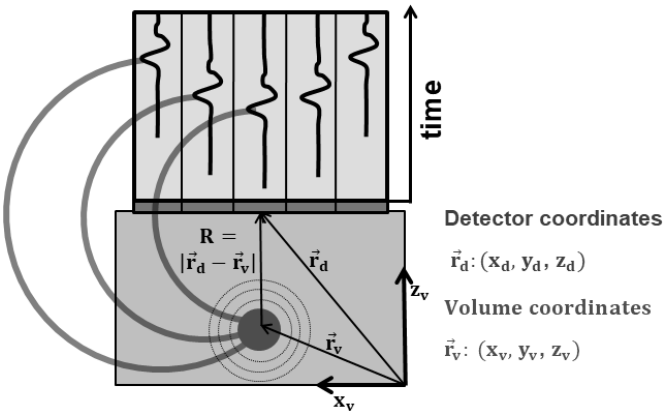

Figure 5: Schematic of simple back-projection for PACT. The detected pressure signals are back-projected on the tissue volume. Figure after [29].

First, for each volume element, the acoustic propagation time t_t is calculated using the spatial detector distance R=$|\vec{r_d}\text{-}\vec{r_v}|$: $t_t = \frac{|\vec{r_d}-\vec{r_v}|}{c} = \frac{\sqrt{(x_d-x_v)^2+(y_d-y_v)^2+(z_d-z_v)^2}}{c}$. The variables (x_d, y_d, z_d), (x_v, y_v, z_v) represent the detector and volume element coordinates in a global coordinate system. For each volume element, it is possible to sum up the matching pressure amplitude from each transducer element in order to reconstruct the initial photoacoustic pressure distribution $(p_0(x_v, y_v, z_v))$, according to eq. (7) [34].

$$p_0(x_v, y_v, z_v) = \int_{-\infty}^{\infty}\int_{-\infty}^{\infty} p(x_d, y_d, t_t = \frac{|\vec{r_d} - \vec{r_v}|}{c})dx_d dy_d \qquad (7)$$

2.2 Photoacoustic detection

2.2.1 Detector characteristics

The most important parameters to characterize a detection system for PA are the following: central frequency f_0, bandwidth B_d and sensitivity S_d. The central frequency and bandwidth are in the unit of MHz and describe the frequency response for an acoustic detector. They are critical for the desired imaging resolution and range of detectable structures [51]. The sensitivity is specified in Pa and determines the noise equivalent pressure (NEP) which is synonymic with the minimal detectable pressure of an acoustic detector. In

order to evaluate the importance of the mentioned parameters, it is essential to understand the photoacoustic signal characteristics.

As illustrated in fig. 2, the detected photoacoustic signal has a characteristic bipolar shape [52]. The positive peak has its origin in the initial volume expansion due to the heating which leads to compression at the transducer. After the tissue heating, cooling takes place, which requires shrinkage. This initial shrinkage results in a decompression at the transducer and thus explains the negative signal part. This characteristic signal shape can be seen in fig. 6 which shows exemplary photoacoustic time (t) domain signals and their frequency (f) spectra for three different absorber radii r and detector distances R according to an analytical solution from Wang et al. which assumes delta pulse heating and homogeneous spherical absorbers [53].

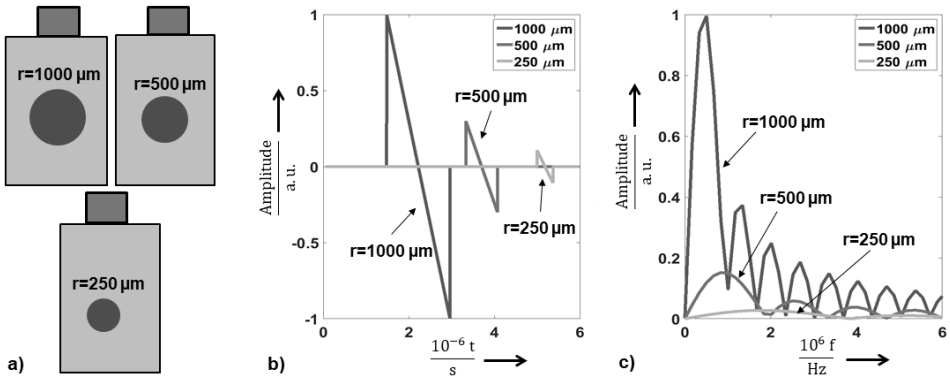

Figure 6: Photoacoustic signal for three different spherical absorber radii (a) in time domain (b) and frequency domain (c). The absorber-detector separation R is 3, 5, 7 mm for decreasing radius and c=1350 $\frac{m}{s}$ for the excited volume. Figure after [41].

Furthermore, it is obvious that the temporal duration for a photoacoustic pulse is inversely proportional to the absorbing object size and the pressure amplitude is proportional to it [52]. Also, it can be seen that in general a photoacoustic signal contains a broad spectrum of frequencies in the kHz and MHz range. The central frequency f_{0s} and bandwidth B_s of a photoacoustic source are determined by its frequency spectrum. The maximal amplitude of the frequency spectrum defines f_{0s} and follows $f_{0s}=\frac{0.8c}{2r}$ [41]. The full width at half maximum of the first lobe in the frequency spectrum is approximately 600 kHz for r=1000 µm determines B_s. Figure 6 shows that B_s significantly increases for smaller structures. The change of f_{0s} and B_s for different absorber sizes implies that tissue, which contains a huge variety of anatomical structures, emits a very broadband acoustic frequency spectrum [41]. For example, tissue structures from 1 mm down to 50 µm size emit photoacoustic

frequencies with f_{0s} from 1 MHz to 22 MHz. This fact combined with the condition that the upper detection limit needs to be approximately four times f_{0s} for accurate signal detection [54], require for the detection hardware a high f_0 and bandwidth (B_d of several MHz) in order to sense tissue features with high-resolution. Besides, it needs to be noted that the selection of the detection frequencies determines the achievable imaging depth in PA. The acoustic attenuation is frequency dependent and high frequencies are more attenuated [20]. This means that high-resolution imaging is limited to only shallow depths. For great depths, the high frequency content of the photoacoustic spectrum is damped and only the sensing of the lower acoustic frequencies is possible which does not allow high-resolution imaging.

In order to give an estimation for the required detector sensitivity, the photoacoustic pressure amplitude needs to be assessed. According to eq. (3), the initial generated amplitude inside tissue can be calculated to 12 kPa using the following parameters, which are realistic for tissue: F=10 $\frac{mJ}{cm^2}$, μ_a=$\frac{10}{cm}$, Γ=0.12 [55]. The optical properties are selected according to Cheong et al. [56]. Since a high local fluence F, which is close to the MPE for single pulse excitation, is selected for this value, it represents the pressure amplitude for an absorbing dimension which is near the surface. For deeper absorbing tissue structures, the fluence drops quickly as a result of the optical attenuation. Due to this effect, the initial pressure amplitude in PA can be estimated to lie in the range of 12 kPa to 100 Pa, whereas 100 Pa represents the amplitude for deeper structures. As already mentioned, the initial pressure signal propagates in all directions and its amplitude is thus reduced with the factor $\frac{r}{R}$ [30]. By assuming a superficial absorber with r=50 µm, R=0.5 mm and a deeper absorber with r=500 µm, R=30 mm, the pressures reaching the detector can be estimated to range from 1200 Pa to 1 Pa. However, for this estimation, the acoustic attenuation is neglected. Taking into account a constant and realistic value of σ=3$\frac{db}{cm}$ [57], this available pressure range for detection even drops down to 1100 Pa to 0.1 Pa. The upper limit of this interval for the available pressures corresponds to superficial absorbers and the lower limit is associated with pressures originating from deeper tissue that are reduced more due to the acoustic attenuation and spherical propagation. Regarding the photoacoustic detection hardware, this means that a sensitivity in the Pa or sub-Pa range is required to acquire signals from deep tissue structures. Furthermore, a high dynamic range is desired for simultaneous collection of pressures from superficial and deep structures.

2.2.2 Piezoelectric detection

The detection of the photoacoustic signal by acoustic transducers using piezoelectric materials is taken over from ultrasound imaging and is declared to be current state of the art [41]. Piezoelectric material has the property to produce a voltage difference when being deformed due to an internal reorientation of electrical dipoles [58]. In general, this voltage signal is proportional to the mechanical deformation and thus, temporal pressure variations can be acquired. The decisive parameter in order to evaluate the photoacoustic detection capability of a piezeoelectric material is the electromechanical coupling coefficient κ_p which describes the efficiency of the conversion from mechanical to electrical energy [41]. There are three major material groups that are suitable for photoacoustic sensing: ceramics, polymers and piezo-composites [59]. PZT (Lead Zirconate Titanate) is the most common piezoelectric ceramic since it offers a good electromechanical conversion (κ_p=0.55) [60]. However, its usage for PAI requires strong impedance matching since its acoustic impedance differs widely from tissue [43]. Without impedance matching, there would be a huge loss at the piezoelement due to acoustic reflection. As a result of this problem, piezoelectric polymers are also considered. For this group, PVDF (Polyvinylidene Fluoride) is the most widespread as it provides more flexibility, a similar impedance to soft tissue and consequently a reduced need for impedance matching [43]. Nevertheless, its coupling efficiency is lower than for PZT (κ_p=0.11) [60]. This trade-off between coupling efficiency and efficient impedance matching resulted in the development of composite materials which combine the desirable characteristics of PZT and PVDF [61]. Their mechanical tissue compliance and electromechanical coupling efficiency can be controlled by adjusting the ceramic-to-matrix ratio, which makes them suitable for the specific application [59]. Yet, it also needs to be noted that the fabrication costs for composites are higher than for piezoelectric ceramics or polymers [60].

2.2.2.1 Transducer

Figure 7 illustrates the basic design of a single element transducer. Since the matching layer which is in contact to the tissue is impedance matched, it reduces acoustic reflections at the tissue-piezoelectric material interface and maximizes therefore the energy transfer [58]. The most important part of the transducer is the piezoelectric element with the thickness L which generates an electric signal when vibrating [41]. It is coupled to the connector via electrodes. This element can be considered as a mechanical resonator which is excited by the ultrasound signal. Therefore, L defines its resonance

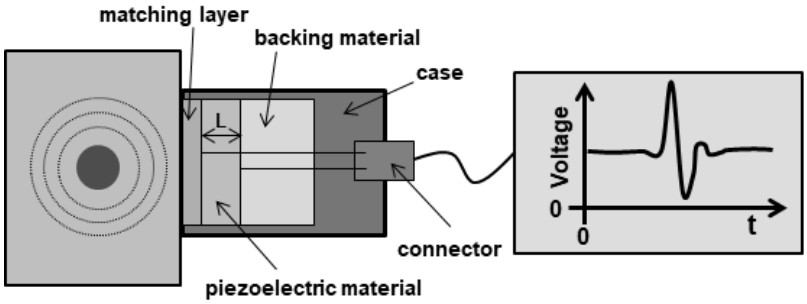

Figure 7: The basic scheme of an ultrasound transducer. Figure after [62].

frequency and thus the central frequency, with c_{pe} being the speed of sound for the piezoelectric material (eq. (8)) [44].

$$f_0 = \frac{c_{pe}}{2L} \tag{8}$$

In order to increase the bandwidth for the mentioned resonator, a backing material is placed behind the piezo element which dampens the acoustic oscillation. Nevertheless, there is a trade off between transducer sensitivity and bandwidth. If the damping layer is perfectly impedance matched to the piezo element, acoustic back-reflections can be neglected, leading to a reduced energy transfer into the sensitive element and therefore maximal damping of the acoustic oscillation [41]. Consequently, the bandwidth increases at cost of reduced sensitivity. In the case that the interface piezo element-backing material is not impedance matched, the back-reflections need to be considered which results in an increased sensitivity and lower bandwidth. Another option to increase the sensitivity for a piezo transducer is the usage of bigger piezo elements which is however not desired for plenty of applications.

In order to make the transducer applicable for PAM, the acoustic detection area can be focused by using acoustic lenses or curved transducer shapes [60]. Furthermore several transducers can be arranged in an array which is convenient for PACT systems since they require time parallel detection.

In general, piezo transducers which are especially designed for broadband PA detection, achieve high sensitivities: For a detection of acoustic frequencies in the range of 10 MHz to 50 MHz with an element size of 30 mm², S_d can be estimated to lie between 1.5 Pa and 3.5 Pa [63]. Arrays have a smaller active area per detector element and thus lower sensitivity. An optimized ultrasonic line array can have a sensitivity of 110 Pa for a single element [64].

Even so, the mechanical resonance behaviour of piezoelectric transducers results in a non-uniform detection bandwidth and there is always a compromise between detection sensitivity and bandwidth. Furthermore, the need for tissue contact makes them not suitable for special medical applications, for instance imaging during surgeries or imaging of wound regions, respectively. In addition, these transducers are bulky, hard to miniaturize, opaque and their sensitivity is dependent on the piezoelectric element size. These facts make the design of PAE systems challenging, especially for forward-view systems. The mentioned problems have lead to the investigation of optical detection modalities for PA which are described in the following chapter.

2.2.3 Optical detection

Optical techniques offer high-bandwidth photoacoustic detection, are easy to miniaturize and represent therefore an attractive alternative to the contact transducer. The optical detection techniques can be grouped in two classes: Cavity-based optical detection and remote optical detection. In the case of cavity-based detection a resonant structure is used which reacts to the acoustic field and is read out by a laser beam. Purely remote optical detection means non-contact, cavity-free photoacoustic detection.

2.2.3.1 Cavity-based optical detection

Fabry-Pérot cavity Beard et al. established the principle of photoacoustic sensing using a Fabry-Pérot cavity [65]. Figure 8 illustrates the sensing principle. A thin polymer film which is transparent for the excitation light, is in contact to the investigated sample and acts as a resonant Fabry-Pérot cavity for the probe light. If the acoustic signal interacts with this cavity, its thickness and thus resonant properties are changed which leads to a change in the detected reflection signal. A sensing bandwidth of 39 MHz, and S_d of 0.3 kPA could be achieved with a 22 µm thick polymer cavity which allowed high-resolution imaging of superficial vessels at a resolution of 20 µm [66]. By placing a thin cavity at each fiber end of a fiber bundle, a forward-looking endoscopic probe with optical detection was also realized [67].

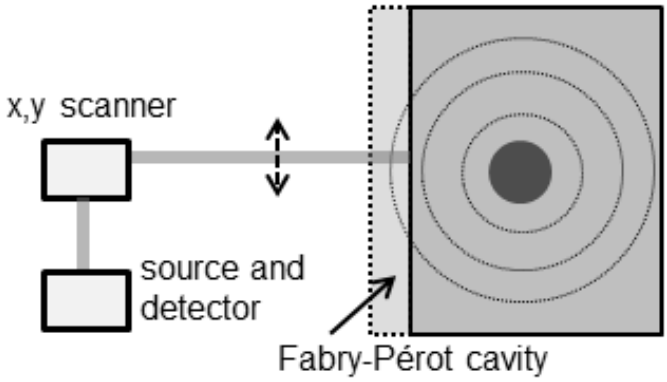

Figure 8: Measurement principle of optical photoacoustic sensig using a Fabry-Pérot cavity.

Micro-ring resonator Figure 9 illustrates the principle of optical photoacoustic detection using a micro-ring resonator (MRR). For this approach, the probe light is coupled to a thin waveguide which interacts with the MRR. The acoustic signal interaction changes the resonance properties of the microring, therefore the interaction with the waveguide and the transmitted light intensity changes which can be detected. Li et al. achieved a sensing bandwidth of 140 MHz and S_d of 6.8 Pa with a polymer MRR with a diameter of 60 µm [68]. Since this sensing system is transparent for the excitation light, miniaturization is facilitated and an endoscopic probe was also realized [69].

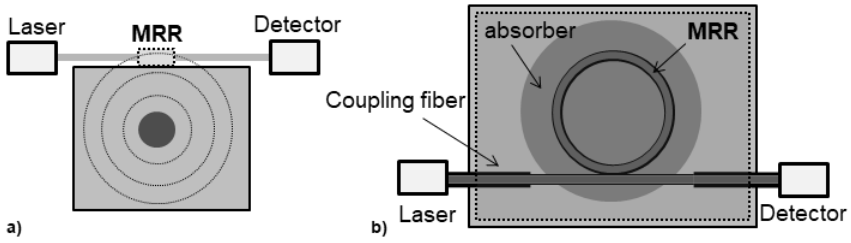

Figure 9: Side-view (a) and top-view (b) of a micro-ring resonator (MRR) system for photoacoustic detection.

Limitations Cavity-based optical detection for PA allows high bandwidth sensing. Furthermore the systems are transparent for the excitation light which facilitates system design and its miniaturization for endoscopy. However, the need for the cavity still restricts the design freedom for endoscopic probes and leads to sample contact which makes these approaches unsuitable for applications like wound imaging or laser surgery.

2.2.3.2 Purely remote optical detection

The purely remote optical photoacoustic sensing techniques are grouped in deflectometry, interferometry and simple reflection-sensing. Most of these techniques are sensitive to surface displacements, which are induced due to the acoustic signal, rather than pressure. Therefore, the sensitivity for these optical techniques $S_{d,nm}$ is described in the unit nm.

Deflectometry It is possible to detect a photoacoustic signal and reconstruct images by measuring the deflection of a probe beam which is parallel to the surface under investigation. This probe beam passes shortly above the region of interest and is deflected when the part of the air transmitted ultrasound hits it. The reason for this deflection which is monitored with a position-sensitive detector (PSD) is the change of the index of refraction in air due to the transmitted acoustic signal. The basic setup can be seen in fig. 10.

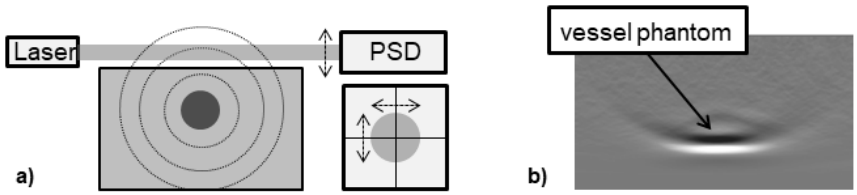

Figure 10: Exemplary representation of laser deflectometry for photoacoustic detection (a). Successful reconstruction of a 5.60 mm diameter vessel phantom (b). PSD=Position-sensitive detector. (Figure after [70])

The bandwidth for this PA detection modality is proportional to the speed of sound in air (330 $\frac{m}{s}$ [5]) and inversely proportional to the probe beam diameter. Johnson et al. achieved a bandwidth of 0.85 MHz and sensitivity of 0.2 nm with a probe beam diameter of 800 µm and were able to reconstruct a 5.6 mm diameter vessel phantom with a detector 5.8 cm above the surface [70]. The detection bandwidth could still be increased by focusing the probe beam. However, the bandwidth and thus the imaging resolution would then decrease for off-focus regions as a result of beam divergence.

Interferometry Several interferometric techniques have been tested for remote photoacoustic detection: Michelson [71–73], Mach-Zehnder [74, 75], Fabry-Pérot [76] and Doppler [77, 78]. Figure 11 gives a simplified overview on the established setups.

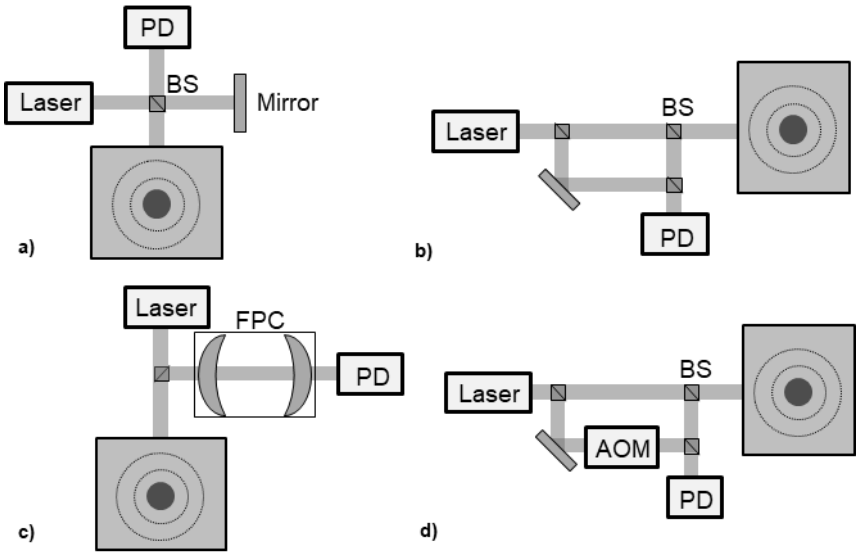

Figure 11: Interferometric setups for remote photoacoustic detection: Michelson (a), Mach-Zehnder (b), Fabry-Pérot (c) and Doppler (d). Abbreviations: AOM= Acousto-optic modulator, BS=Beam splitter, FPC= Fabry-Pérot Cavity, PD=Photo detector. Figure after [79].

In a Michelson Interferometer, the laser beam is divided into a reference and probe beam which illuminates the sample under investigation. The photoacoustic surface deformation results in a change of the path length for the probe beam. This change leads to a modulation of the interference signal of reference and probe beam and can thus be detected. Speirs et al. achieved a $S_{d,nm}$ of 0.5 nm and bandwidth of 20 MHz [71]. By moving the sample, they were able to measure the acoustic signal on several surface positions which enabled the reconstruction of a 500 µm diameter silicone tube filled with ink. However, it needs to be mentioned, that a thin mirror was placed on the sample surface to ensure a high probe beam reflection.

The Mach-Zehnder interferometer is also capable of detecting photoacoustically induced phase differences of the probe beam which is directed onto the object. Hochreiner et al. achieved a sensitivity of approximately 6 pm at a bandwidth of 20 MHz. Reconstruction of a ink filled silicone loop with inner diameter of 300 µm and outer diameter of 600 µm was achieved by mechanical raster scanning. By replacing the photo detector with a camera,

Horstmann et al. were able to reconstruct photoacoustic tomographic information without raster scanning [75]. Nevertheless, their displacement sensing sensitivity was limited to 1 nm at 10 MHz bandwidth.

The Fabry-Pérot and Doppler Interferometer sense changes in frequency for the reflected probe beam. These changes are induced by the Doppler shift due to the moving surface. Fabry-Pérot Interferometers use a resonant cavity (Fabry-Pérot Cavity, FPC) to read out these frequency modulations in the form of light intensity modulations [79]. By mechanical scanning, Rousseau et al. were able to image blood vessel phantoms at a diameter of 500 µm inside chicken breast with a sensitivity of 0.8 pm at 3 MHz bandwidth [76].

In contrast to Fabry-Pérot, the Doppler Interferometer makes use of frequency modulation by combining the reflected probe beam with the reference beam. The Doppler frequency shift and therefore the sample vibration speed is measured by analyzing the resulting interference pattern. The modulation of the reference beam by an AOM (acousto-optic modulator) is required for the determination of the sample movement direction. The reference beam is modulated by a specific frequency and a static sample surface results in an interference pattern with this specific modulation frequency. However, the modulation frequency of the interference pattern increases when the sample moves towards the measuring system and decreases when the sample moves away. Carp et al. achieved a sensitivity of 0.3 nm with a 500 MHz bandwidth. Mirror and sample movement allows image reconstruction for ink filled tubes at a diameter of 160 µm. Most of these interferometric detection approaches have already been realized in a fiber-based setup [80]. This fact demonstrates the potential of interferometry for easy miniaturization and therefore implementation in PAE.

Reflection-sensing Hajireza et al. presented a non-interferometric detection approach which is sensitive to refractive index modulations inside the excited medium which are a result of the thermoelastic expansion directly after short pulse excitation [81]. A low-coherence probe beam is focused inside the medium under investigation and its reflection is sensed during photoacoustic excitation. The thermoelastic expansion modulates the index of refraction which alters the probe beam reflection. Similar to PAM, one can distinguish between two setups which are illustrated in fig. 12: high resolution and deep penetrating [16]. For the high-resolution approach, the lateral resolution is determined by the tight focus of the excitation beam. This enables high-resolution imaging up to 2.7 µm at costs of a low penetration depth which is limited to about 1 mm by the optical attenuation of the excitation beam [81]. In contrast to this high-resolution mode, the excitation beam is loosely focused for the deep penetrating mode. The probe beam is deeply

focused to measure the reflection from the inside of the object. For this mode, penetration depths are up to 2.5 mm at a lateral resolution of 9 µm [16]. By galvanometric scanning, successful reconstruction of mouse ear vessel structures were demonstrated with both imaging modes.

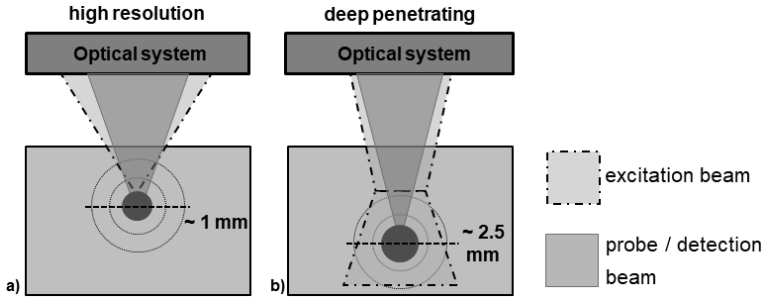

Figure 12: Basic scheme for reflection-sensing. For the high-resolution mode, the excitation beam is tightly focused (a), whereas it is loosely focused for the deep penetrating mode. Figure after [16].

Limitations The mentioned purely remote, optical detection techniques offer a lot of advantages compared to the contact piezo transducer: no need for impedance matching, ease of miniaturization, high and uniform bandwidth. However there are also downsides which limit their applicability. For beam deflectometry, the used image reconstruction techniques do not consider the interaction of the probe beam with the acoustic signal from multiple acoustic sources. For the shown experiments only a single absorber was used. This downside makes the technique so far not suitable for PACT [51]. Furthermore, the need to guide the laser beam over the investigated area makes the implementation of this technique for special imaging applications or PAE systems, respectively, impossible. Interferometric systems are very sensitive and have already proven the potential of endoscopic application, but they are expensive, complicated and very sensitive to noise from temperature drifts or vibrations [51]. In addition, these systems often require surface preparation to ensure a stable reflection signal from diffuse reflecting surfaces. The non-interferometric reflection-sensing technique does not suffer from these problems since it acquires reflections from the object inside. However, the penetration depth is low as a result of the optical focusing process. In contrast to the other techniques it does not provide temporal signal acquisition which makes the technique not applicable for PACT. Furthermore, complicated optical sectioning is required for depth information acquisition which distorts imaging resolution [16].

2.2.3.3 Comparison of optical detection approaches

Table 2 summarizes the optical modalities for photoacoustic signal detection according to the relevant features for special medical applications like wound imaging, endoscopic imaging or laser surgery: contact, costs, robustness, usability for PACT/PAE, sensitivity S_d and bandwidth B_d. As already mentioned, the Fabry-Pérot and micro-ring modality require a cavity which is in direct tissue contact. In contrast to this, deflectometry, interferometry and the reflection-sensing approach are purely remote. Regarding the costs, it can be summarized that interferometric approaches are expensive due to the components and complicated read-out systems. Also the contact-based techniques Fabry-Pérot and micro-ring can be evaluated as expensive due to the need of an additional cavity and special read out systems. The reflection-sensing approach is considered to require medium costs due to the lack of an additional cavity and interferometric read-out. Deflectometry offers the cheapest approach since only a CW-laser and a PSD is needed for sensing. Since interferometric approaches are sensitive to temperature drifts, they can be classified with low robustness against noise signals. The other techniques except reflection-sensing offer medium robustness against noise signals. The reflection-sensing approach offers high robustness since it detects the acoustic signal directly at its origin. Of the mentioned detection techniques, only Fabry-Pérot and interferometry have already proven their potential for tomographic imaging. In the case of micro-ring sensing, it is difficult to produce an array which might have prevented tomographic imaging. For deflectometry, it is difficult to cover a larger area and for reflection-sensing the signal is directly detected at its origin and therefore spatial scanning is required for image formation, which is inconvenient for PACT. All modalities, except deflectometry, can be miniaturized and are thus usable for PAE. Regarding

Table 2: Comparison of the photoacoustic optical detection techniques. (+++: high, ++: medium, +: low)

	Contact	**Costs**	**Robustness**	**PACT/PAE**	S_d/B_d
Fabry-Pérot	yes	+++	++	yes/yes	++/++
Micro-ring	yes	+++	++	no/yes	+++/+++
Deflectom.	no	+	++	no/no	+/+
Interferom.	no	+++	+	yes/yes	+++/+++
Refl.-sens.	no	++	+++	no/yes	++/++

the sensitivity and bandwidth, all techniques are convenient for precise photoacoustic sensing and imaging, except deflectometry. For this approach, the signal is detected in air above tissue and thus strongly attenuated before detection which does not allow high detection sensitivities.

By analyzing table 2, it gets obvious that there is at the moment no purely remote, low-cost, non-interferometric photoaocustic detection modality that offers high sensitivity, bandwidth and which is suitable for PACT and PAE. The remote speckle-analysis is an easy, robust, non-interferometric sensing technique which is sensitive to temporal surface tilts and thus capable to sense surface vibrations [82]. Moreover, its potential for tissue applications has already been demonstrated by sensing low-frequency biosignals in the Hz-range. Beiderman et al. estimated the blood-pressure using speckle-analysis [83]. Golberg et al. even validated these remote blood pressure measurement in a large clinical study [84]. Bishitz et al. classified pigmented lesions by speckle-analysis on skin tissue [85]. Therefore, this thesis investigates the remote speckle-analysis for its applicability for photoacoustic detection, endoscopic usage and image reconstruction. The theory for the speckle-analysis vibration detection is explained in the following section.

2.3 Speckle-analysis

2.3.1 Speckle properties

Speckles are generated through self-interference of reflected laser light from a rough surface [86]. The reflected light can be described as secondary spherical waves with a random phase due to the surface roughness. These waves interfere and create a spotted intensity pattern at the plane of observation. A bright spot of this pattern is defined as a speckle. A speckle pattern spreads into all three dimensions starting from the surface. By capturing the pattern on a screen or camera chip, it is possible to look at a cross-section through the three dimensional distribution. This cross-section is called an objective speckle pattern, if no optics are used for acquisition and a subjective speckle pattern if optics are used for imaging. Figure 13 illustrates the laser illumination, random reflection at a rough surface and an exemplary speckle pattern which is observed at a screen with the distance Z to the surface.

The speckle size l_s is dependent on the size of the illuminated area D_{ill}, the observation distance Z and the wavelength λ: $l_s = \frac{\lambda Z}{D_{ill}}$ [87]. Furthermore the speckle pattern can be described by its contrast C in eq. (9).

$$C = \frac{\sigma_{sp}}{I_{a,sp}} \tag{9}$$

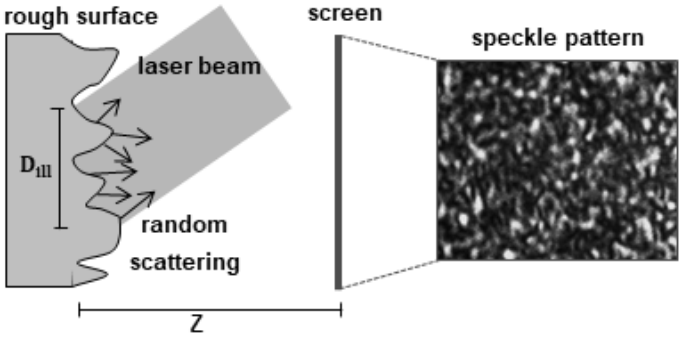

Figure 13: Generation and observation of a speckle pattern on a screen.

The variable σ_{sp} stands for the standard deviation of the spatial intensity variations in the speckle pattern and $I_{a,sp}$ is the average intensity of the speckle pattern [88]. The speckle contrast reaches its maximum value of one for ideal speckle generating conditions [34]:

- Linearly polarized, highly coherent laser illumination
- Surface roughness is higher than the illumination wavelength
- A high number of scattering centres at the surface which maintains linear polarization

In practice, these conditions are not completely fulfilled which results in a contrast of smaller than one.

2.3.2 Theory

The speckle-sensing technique is based on the time-resolved detection of the position and amplitudes of a speckle pattern which consists of multiple speckles. It is possible to extract the tilt change of a laser illuminated surface by tracking the speckle pattern movement [82]. Figure 14 shows on the left side a tilting object surface and the right side illustrates the speckle-sensing technique. If the observation plane distance Z for the generated objective speckle pattern fulfils the far field approximation ($Z > \frac{D_{ill}^2}{4\lambda}$, [82]), the objective speckle pattern movement (δ_o) is only dependent on the surface tilt change $\Delta\alpha$ and Z. By imaging the objective speckle pattern using a camera with the magnification M a subjective speckle pattern is created on the camera sensor whose lateral movement δ_s is also linearly proportional to $\Delta\alpha$. Equation (10) explains the relation between the speckle movements (δ_o, δ_s), M and Z.

$$\delta_s = \delta_o \times M = tan(\Delta\alpha) \times Z \times M \tag{10}$$

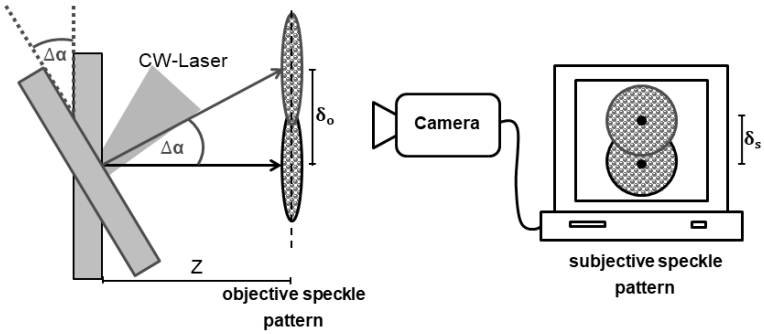

Figure 14: Speckle-sensing for remote PA signal detection.

The acquisition of the multiple speckles pattern allows the reconstruction of the subjective speckle shift in horizontal image direction x_{s0} and in vertical image direction y_{s0} between two successive frames (a,b) using eq. (11) [89].

$$\frac{A(\eta,\tau)B^*(\eta,\tau)}{|A(\eta,\tau)B^*(\eta,\tau)|} = e^{j2\pi(\eta x_{s0}+\tau y_{s0})} \tag{11}$$

A and B are the Fourier Transformations of the two images under investigation. The variables η and τ are the spatial image frequencies. By inverse Fourier Transformation and interpolation, it is possible to reconstruct x_{s0} and y_{s0}, which represent the surface tilt change in horizontal and vertical direction between the acquisition times of the two image frames a,b at 0.05 pixel accuracy [90]. This allows the calculation of the total subjective speckle pattern shift $\delta_{s,tot}$ between the two images a, b according to eq. (12).

$$\delta_{s,tot} = \sqrt{x_{s0}^2 + y_{s0}^2} \tag{12}$$

3 Goals

As concluded in the state of the art section, the speckle-sensing technique is a robust sensing technique for biosignal detection on tissue. Furthermore, it would add significant benefit to the field of photoacoustic imaging since it is easy, contact-free and non-interferometric. Therefore, this thesis investigates the applicability of the technique for photoacoustic detection in the MHz-range, endoscopic usage and image reconstruction. From this, the master hypothesis which is examined in the framework of this thesis can be derived: Speckle-sensing is a robust sensing technique which is suitable for PACT and PAE. In order to investigate this master hypothesis, eight sub-hypotheses in three fields (multiple speckle-analysis, single speckle-analysis, general) are defined. These master hypothesis, working fields and sub-hypotheses are illustrated in fig. 15 which represents a flowchart of this work. Based on the knowledge that speckle-analysis is already used for the detection of low-frequency vibrations on tissue, the three working fields and their hypotheses are addressed in order to evaluate the main hypothesis. H1, H2 and H3 cover the suitability of remote photoacoustic detection by multiple speckle-analysis. In order to investigate H1, a simulative model is introduced and verified by a comparison to interferometric experiments. With this model it is possible to evaluate the feasibility of photoacoustic detection using multiple speckle-analysis with a commercial high-speed camera. Based on these investigations, H2 and H3 are experimentally investigated using a commercial high-speed camera, imaging fiber-bundle, phantoms and ex-vivo samples. In order to replace the high-speed camera with a cheaper and faster sensing device, the applicability of PA detection by single speckle tracking with a low-resolution, diode-based sensor is investigated in H4 using phantoms and skin tissue. In H5 the possibility of automated single speckle tracking using image processing and its transferability to endoscopy is addressed. Phantom and ex-vivo skin measurements are shown. H6, H7 and H8 cover general investigations regarding the analysis techniques, speckle properties and imaging capability. In H6 the multiple speckle- and single speckle-analysis are compared to each other by evaluating the sensing properties such as sensitivity, sensing range, linearity and sensing depth. The wavelength influence on relevant speckle properties is examined in H7 with laser diodes and ex-vivo pig skin tissue. H8 covers the possibility to reconstruct a photoacoustic image using speckle-analysis by testing a reconstruction algorithm with the established model and an experimental test.

In chapter 4, the relevant materials and methods for the investigation of these hypotheses are described. Chapter 5 shows and discusses the obtained results

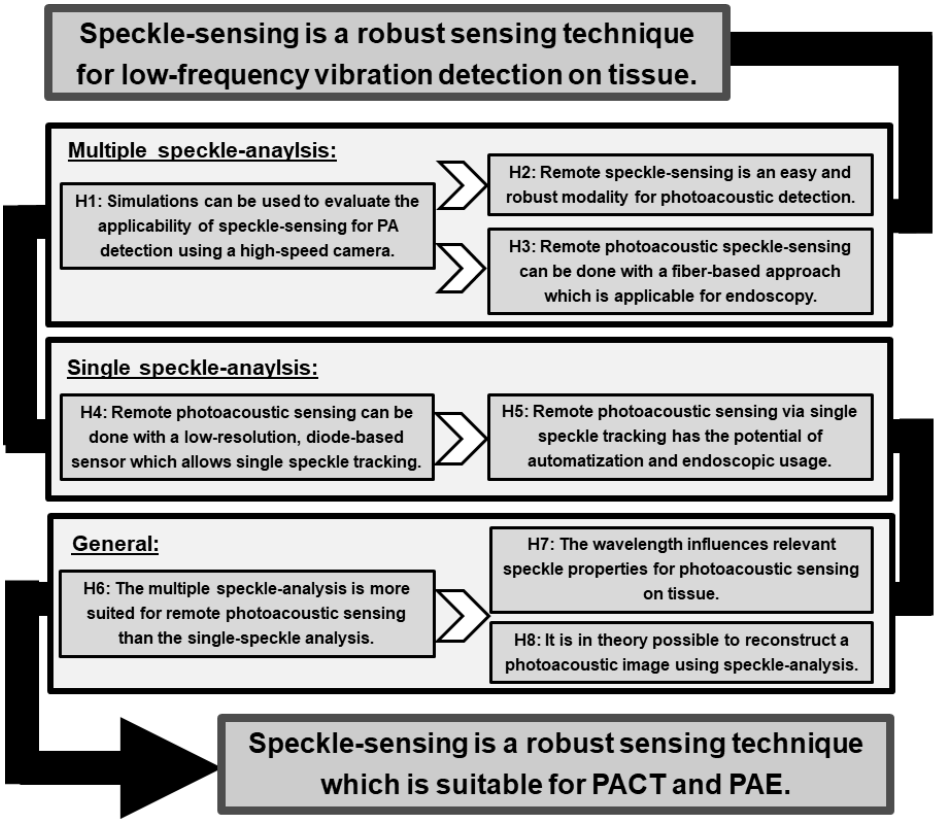

Figure 15: The flowchart which represents the way from the current state of the art towards the master hypothesis of this work. In order to evaluate this master hypothesis, three working fields and their hypotheses need to be treated.

for this thesis. Chapter 6 provides a short summary of this dissertation. In addition, a conclusion and an overview on the future challenges is given in the end in chapter 7.

4 Materials and Methods

This chapter describes the relevant materials and methods for evaluating the hypotheses described in the previous chapter. Therefore, after the description of the sample materials, it essentially follows the described flowchart in its structure.

4.1 Sample materials

For this thesis, artificial phantoms and ex-vivo samples are manufactured for the photoacoustic measurements. Both samples consist of two parts: absorber and scattering matrix. Figure 16 illustrates the sample constituents and geometry for the artificial phantoms and ex-vivo samples.

Polyvinylchloride plastisol (PVCP, Standard Lure flex (medium), Lure Factors, Great Britain) is used as artificial phantom material since it offers long term stability and similar mechanical properties to soft tissue [55]. The detailed material preparation process for the phantom material can be found in the appendix. In order to adjust the optical properties of the sample parts, additives are added during the plastisol manufacturing process. A black plastic colour changes μ_a and $Ti0_2$-particles (Titanium(IV)-oxide, Sigma Aldrich, Germany) adjust the reduced scattering coefficient μ_s'. A colour-concentration of 7 Vol.-% and a TiO_2 concentration of 4 $\frac{mg}{ml(PVCP)}$ is used for the absorbing and scattering phantom parts, respectively. The absorption coefficient for the absorbing phantom part is 106 $\frac{1}{cm}$ and the reduced scattering coefficient for the scattering part is 21 $\frac{1}{cm}$ which was measured by spectrophotometric measurements [S1]. The scattering coefficient for the absorbing part and the absorbing coefficient for the scattering part can be neglected. The PVCP phantoms are produced in a three-step process. First, the bottom layer is manufactured and second, the absorbing part is produced. Third, the absorber is put on the bottom layer and the phantom cast is filled until the final phantom height is reached.

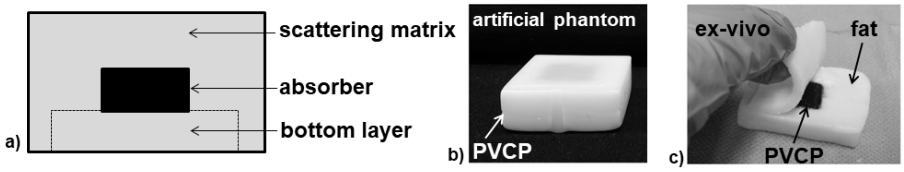

Figure 16: Sample constituents (a) and materials for the artificial phantoms (b) and ex-vivo samples (c) used in this thesis

The ex-vivo samples consist of a PVCP-absorber placed inside porcine fat which is illustrated in fig. 16. A hole is cut out of the fat tissue, the absorber is placed inside this hole which is closed by an additional fat layer. A thin coating of ultrasound gel on the absorber ensures good acoustic coupling. The speed of sound in the phantom material is measured using an ultrasound thickness measurement device (Mini Test 430, Elektro Physik, Germany) connected to a piezoelectric sensor head with a resonance frequency at 2 MHz. The material density is measured by volume displacement of ethanol. The speed of sound for the PVCP in this thesis is measured to lie between 1330 $\frac{m}{s}$ and 1340 $\frac{m}{s}$ and the density between 1040 $\frac{kg}{m^3}$ and 1200 $\frac{kg}{m^3}$. These values result in a impedance range from $1.38{\times}10^6 \frac{kg}{m^2 s}$ to $1.60{\times}10^6 \frac{kg}{m^2 s}$ for the PVCP material which is in good agreement with the values for soft tissue: The impedance of fat tissue is $1.4{\times}10^6 \frac{kg}{m^2 s}$ and for muscle $1.62{\times}10^6 \frac{kg}{m^2 s}$ [91]. The speed of sound for the used fat falls in the range from 1448 $\frac{m}{s}$ to 1450 $\frac{m}{s}$. In order to increase the optical back reflection for the experiments, the samples are coated with a white marker at the detection location. This layer can be considered as acoustical transparent for the measurements in the framework of this thesis due to its low thickness.

4.2 Simulative feasibility investigation

Figure 17 illustrates on top the incorporation of the hypothesis H1 into the flowchart of this work described in the previous chapter. The scheme pre-

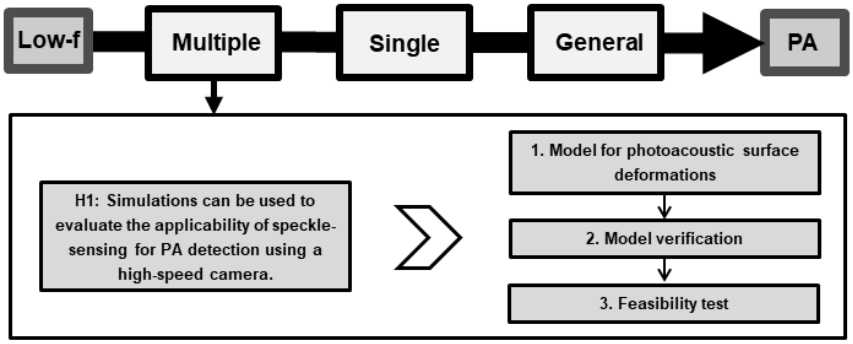

Figure 17: H1 and its subdivision are illustrated.

sented here is simplified, with 'Low-f' representing the starting point of the work: speckle-sensing is a robust sensing technique for detecting low-frequency vibrations on tissue. The abbreviation PA stands for photoacoustic and represents here the main hypothesis of the work: 'Speckle-sensing is a ro-

bust sensing technique suitable for PACT and PAE.' Between the starting point and the goal of the work, the three work fields addressed for the evaluation of the main hypothesis are shown: 'Multiple' for 'multiple speckle-analysis', 'Single' for 'single speckle-analysis' and 'General'. In addition, the necessary steps for the investigation of H1 are listed. This representation is used in the same way for all hypotheses and their corresponding results in this work. For the investigation of H1 (Simulations can be used to evaluate the applicability of speckle-sensing for PA detection using a high-speed camera), the model for the resulting photoacoustic surface deformations is introduced and its theory is explained first. This model has already been published by the author in [P1]. Second, the verification procedure of this model is elucidated. The maximal surface deformation and temporal deformation shape from simulations are compared to experimental results from a different research group. Finally, the simulative model for the feasibility test of photoacoustic detection using remote speckle-analysis with a commercial high-speed camera is introduced.

4.2.1 Model for photoacoustic surface deformations

An existing model by Jacques et al., which calculates the photoacoustic pressure, is extended with the calculation of the axial surface deformation. This model from Jacques et al. couples a Monte Carlo Simulation (MCS) of light transport to a stress wave simulation in order to compute the temporal photoacoustic pressure at the object surface [92]. Figure 18 illustrates the model geometry used for this thesis. The object consists, similar to the samples

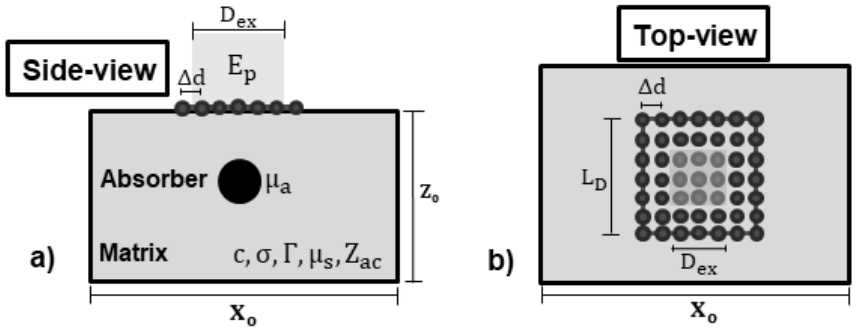

Figure 18: Side-view (a) and top-view (b) of the model geometry and its parameters.

for this thesis, of two constituents: absorber and scattering matrix. The MCS uses the object dimensions (X_o, Y_o, Z_o), optical properties (μ_a, μ_s) and excitation properties (E_p, excitation size D_{ex}) as input parameters and computes the spatial energy density H(x_v, y_v, z_v). By considering the acoustic properties (c, σ, Γ), the temporal pressure p at the rectangular detector area

(side length L_D) which consists of several detector elements with uniform spacing Δd is determined afterwards. This pressure computation is based on the computation and derivation of the velocity potential Ψ [93]. The velocity potential for a detector element is determined by temporally integrating the deposited energy in the object. For each time point t after the photoacoustic excitation, a spherical shell of deposited energy (W_{shell}) with the volume $V_{shell,t}$ and the radius $r_{shell,t}$=ct centered on the detector element will launch a stress wave that arrives at the detector element position at time t [92]. This allows the computation of $\Psi(t)$ for each detector element by summing up the deposited energy for each time point and by considering the acoustic attenuation (eq. (13)). The parameter dr stands for the radius step size which is defined by the voxel element size. It is then possible to compute the generated photoacoustic pressure for each single detector element according to eq. (14) [94].

$$\Psi(t) = -\frac{\beta}{4\pi\rho C_p}\frac{1}{dt}\int_{r_{shell,t}-dr/2}^{r_{shell,t}+dr/2}\left(\frac{W_{shell,t}}{r_{shell,t}}V_{shell,t}e^{-\sigma r_{shell,t}}\right)dr \tag{13}$$

$$p(t) = -\rho\frac{d\Psi(t)}{dt} \tag{14}$$

For the simulations within the framework of this thesis a calibration for each object geometry is performed using Γ. A homogeneous energy deposition H and negligible acoustic attenuation is assumed which results in a constant pressure of ΓH (see eq. (3)). With this calibration, a single object specific pre-factor can be determined using Γ which replaces the pre-factors from eq. (13) and eq. (14), respectively $\left(-\frac{\beta}{4\pi\rho C_p}, -\rho\right)$.

This model is extended with the calculation of the axial surface deformation ϵ. Assuming a plane acoustic wavefront, the axial surface displacement for each detector element can be determined according to eq. (15) [75].

$$\epsilon(t) = \frac{2}{Z_{ac}}\int_0^t p(t)dt \tag{15}$$

Finally, the lateral mechanical coupling of the detector elements is considered by spatial Gaussian filtering of the axial deformation values of the detector field.

4.2.2 Model verification

The model is verified by two comparisons to a research group which measured the photoacoustic surface deformations with a Mach-Zehnder interferometer approach. First, the simulated maximal axial displacement ϵ_{max} is evaluated and second, the simulated temporal deformation shape for the detector field is compared.

4.2.2.1 Maximal surface deformation

Twelve experiments from Horstmann et al. are simulated with the previously described model and ϵ_{max} is compared to the interferometric measurements [34]. Figure 19 shows their experimental geometry and the necessary object dimensions. The photoacoustic simulations are performed in reflection-mode, which means that excitation and detection take place at the same sample side.

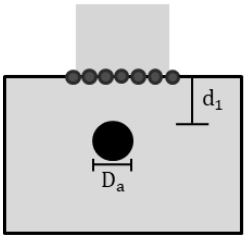

No.	μ_a [$\frac{1}{cm}$]	D_a [mm]	d_1 [mm]	No.	μ_a [$\frac{1}{cm}$]	D_a [mm]	d_1 [mm]
1	5	1	0.83	**7**	15	2	0.81
2	5	2	1.05	**8**	15	2	1.76
3	5	2	1.74	**9**	15	2	2.94
4	10	1	0.86	**10**	20	2	0.96
5	10	2	0.86	**11**	20	2	1.99
6	10	1	1.84	**12**	20	2	2.82

Figure 19: The experimental geometry from Horstmann et al. and the object dimensions are shown [34].

For the twelve experiments, silicone phantoms with spherical absorbers are used and their μ_a, depth d_1 and diameter D_a is varied. According to Horstmann et al., the simulative parameters are the following [34]: D_{ex}=4 mm, E_p=3.2 mJ, $\mu_{s,Matrix}$=25 $\frac{1}{cm}$, $\mu_{a,Matrix}$=0.25 $\frac{1}{cm}$, c=970 $\frac{m}{s}$, Γ=0.6, σ=12.2 $\frac{db}{cm}$, L_d=1 cm, Δd=0.05 cm, Z_{ac}=0.94×10^6 $\frac{kg}{m^2 s}$. The acoustic attenuation factor σ and impedance Z_{ac} are approximated for silicone doped with metallic powders according to Yamashita et al. [95].

The mentioned vales for the parameters $\mu_{s,Matrix}$, $\mu_{a,Matrix}$, c, Γ, σ, L_d, Δd and Z_{ac} hold for all simulations for H1. Furthermore, the following accounts for all H1 simulations. Roughly five million photons are used for the simulation which is considered to be sufficient for the simple phantom structure. Two dimensional filtering of the displacement values of the detector field

is performed with a 3 × 3 Gaussian filter and the Fresnel reflection at the excitation surface is approximated with the constant factor 0.05.

4.2.2.2 Temporal surface deformation

For the temporal verification of the simulative model, two comparisons to the interferometric measurements from Horstmann et al. are carried out. First, the temporal deformation of the phantom surface centre is considered. For the phantoms No. 2/5/7/8, the temporal deformations of the nine central detector points are averaged and the resulting mean is compared to the corresponding data from the interferometric measurements. Second, the temporal deformation shape of the complete detector field for a further silicone phantom geometry is compared to the corresponding interferometric measurements. The simulative parameters according to Horstmann et al. are the following [34]: D_{ex}=4 mm, E_p=3.2 mJ, d_1=0.64 mm, D_a=1 mm, $\mu_{a,Absorber}$=15 $\frac{1}{cm}$.

4.2.3 Simulative feasibility test

A first feasibility test for the remote photoacoustic detection using speckle-sensing with a high-speed camera is performed. The spherical absorber with a diameter of 3 mm is placed at d_1=3 mm inside the silicone scattering matrix. The simulative parameters are the following: E_p=19.6 mJ, D_{ex}=5 mm (Gaussian beam profile), $\mu_{a,Absorber}$=20 $\frac{1}{cm}$. The pulse energy is selected according to the MPE for soft tissue at 1064 nm (100 $\frac{mJ}{cm^2}$). Since the speckle-sensing technique detects surface tilt changes, the calculation of the temporal surface tilt is required. The surface tilts in horizontal and vertical direction (α_x, α_y) can be computed by taking the spatial gradients of the deformation field (ϵ) in horizontal and vertical direction, respectively. The tilt changes ($\Delta\alpha_x, \Delta\alpha_y$) are analysed for its detection potential by the speckle-analysis using a commercial high-speed camera system with a frame rate of 820 kHz and a pixel size d_{px} of 28 µm.

4.3 Remote photoacoustic sensing using a high-speed camera

After the simulative test of H1, this section describes the materials and methods for the experimental feasibility studies of remote photoacoustic sensing using a high-speed camera which are represented by H2 and H3. These two hypotheses are treated in a single section since they evaluate multiple-speckle analysis using the same imaging unit. The described procedures have already

been published by the author. The free-space speckle-sensing approach related to H2 can be found in [P2]. The endoscopic approach for the investigation of H3 is described in [P3]. Figure 20 illustrates the procedure of the investigations. First, the high-speed imaging unit and the data analysis which are used in the context of H2 and H3 are introduced. Second, in order to be able to investigate the hypotheses H2 the free-space speckle-sensing setup and the used samples are described. Third, the fiber-based speckle-sensing setup and the used samples are elucidated which are needed for the examination of H3. Finally, the verification procedure for the experiments in the framework of H2 and H3 is explained.

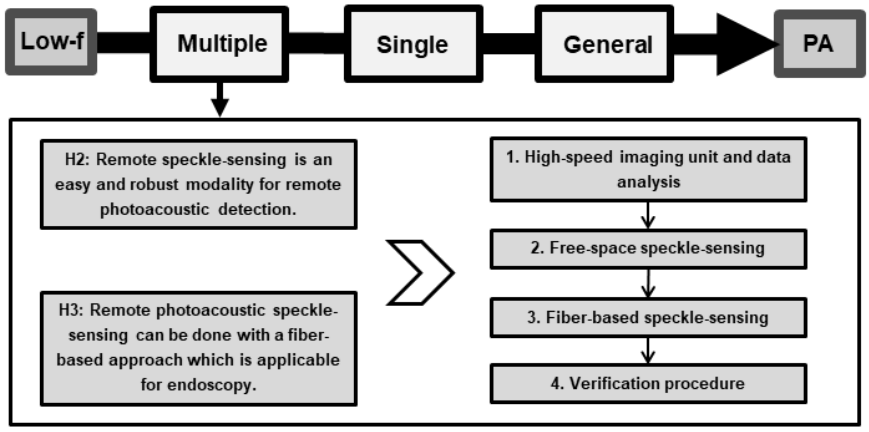

Figure 20: H2, H3 and its subdivision are illustrated.

4.3.1 High-speed imaging unit and data analysis

Figure 21 illustrates the established high-speed microscopic imaging unit (HSMIU) for speckle pattern imaging. This system consists of a high-speed video camera (Phantom v1210, d_{px}=28 µm, Vision Research, USA) and its imaging unit is composed of an infinity corrected microscope objective (Mitutoyo Plan Apochromat Objective, M=10, numerical aperture NA=0.28, working distance 34 mm), a bandpass for the speckle wavelength of 532 nm, a mechanical aperture (diameter adjustable from 0.8 mm to 12 mm) and a biconcave lens (f=200 mm). The aperture diameter can be adapted for each measurement in order to achieve a high speckle contrast. The resolution of the optical system is measured about 2.76 µm by a microscope test target (1951 USAF test target, fig. 21). The photoacoustic measurements for this thesis are done by single-pulse excitation with a short laser pulse (Q-Smart 450, Quantel laser, Les Ulis (France)) and the laser parameters are the follow-

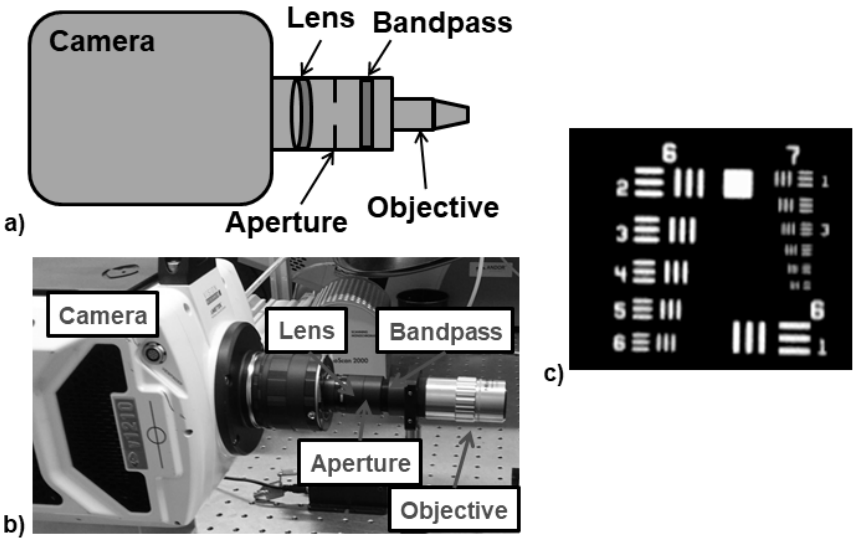

Figure 21: A sketch (a) and picture (b) of the high-speed imaging system is shown which consists of an microscope objective, bandpass-filter, aperture, lens and a high-speed camera. The resolution of the imaging system was measured at 2.76 µm (Group 7, Element 4) using a USAF 1951 Test Target (c).

ing: λ=1064 nm, t_p=5 ns , beam diameter 7 mm. The laser pulse triggers the acquisition start of a speckle pattern video with a sampling rate of 823500 frames per second and a resolution of 128×16 pixels by the imaging unit. This sampling rate is too low for precise photoacoustic sensing. However, it is high enough for the proof of concept demonstration in this work. The sampling rate leads to a time window of 1.2 µs between the frames. The captured speckle pattern video is analyzed with Matlab R2015b (The MathWorks, Inc., Narick, MA, USA). By using eq. (11) and eq. (12), $\delta_{s,tot}$ between subsequent video frames is computed. This signal represents the temporal vibration profile of the surface under investigation. The time points of this vibration profile represent the time difference between the trigger input of the HSMIU and the end of an exposure interval of the HSMIU. These time points are delayed with respect to the real temporal vibrations due to a delay between the laser pulse itself and the electronic trigger of the HSMIU and due to the long time interval between two image frames of 1.2 µs. The time shift of the trigger and the excitation laser pulse is approximately 0.4 µs for the used short laser pulse system in this work. The time stamps of the high-speed camera measurement represent the end of a sensor exposure interval. These time stamps are in average delayed by half of the time between two exposure ends (0.6 µs) related to the onset of the surface vibration since the surface vibration might start in between two measurement times. The described temporal

scheme is illustrated in fig. 22. In order to compensate for these effects, the two described delays are summed up and a value of 1 µs is subtracted from the initial time points.

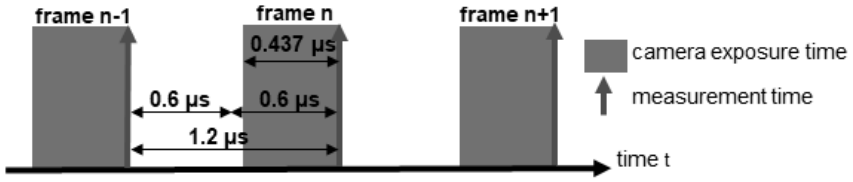

Figure 22: The time points given by the HSMIU represent the end of an exposure interval which lasts 0.437 µs. A detected surface vibration occurs in average 0.6 µs before a time stamp.

4.3.2 Free-space speckle-sensing

Figure 23 illustrates the sample geometries for the free-space speckle-sensing experiments.

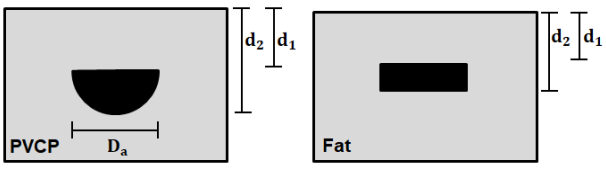

Sample	d_1 [mm]	d_2 [mm]
F1	2.9	12.9
F2	4.5	16.1
F3	6.3	16.5
Ex-vivo	3.4	7.0

Figure 23: The geometries for the PVCP samples and the ex-vivo sample for the free-space speckle-sensing are illustrated.

Three cylindrical PVCP-phantoms (F1, F2, F3) with a diameter of 46 mm are manufactured with D_a=17 mm. The distances d_1 and d_2 which represent the distance between absorbing core surface and detection surface for the experiments are varied. The cuboid ex-vivo sample has a side length of 35 mm. The speed of sound was measured to 1330 $\frac{m}{s}$ for the PVCP and assumed at 1450 $\frac{m}{s}$ for the fat tissue which was obtained from a local supermarket [48]. It needs to be mentioned that the used absorber sizes are not found in tissue for photoacoustic applications. However, the big absorbers are selected in order to ensure a high photoacoustic surface deformation and tilt for a proof of concept of detecting a photoacoustic signal using the speckle-analysis.

The samples are excited photoacoustically by the short laser pulse which targets the phantom centre. Photoacoustic measurements are done in transmission-mode and reflection-mode. The geometry and the optical setups (transmission/reflection) for the free-space speckle-sensing experiments are displayed in fig. 24. For proof of concept, E_p=40 mJ is selected for

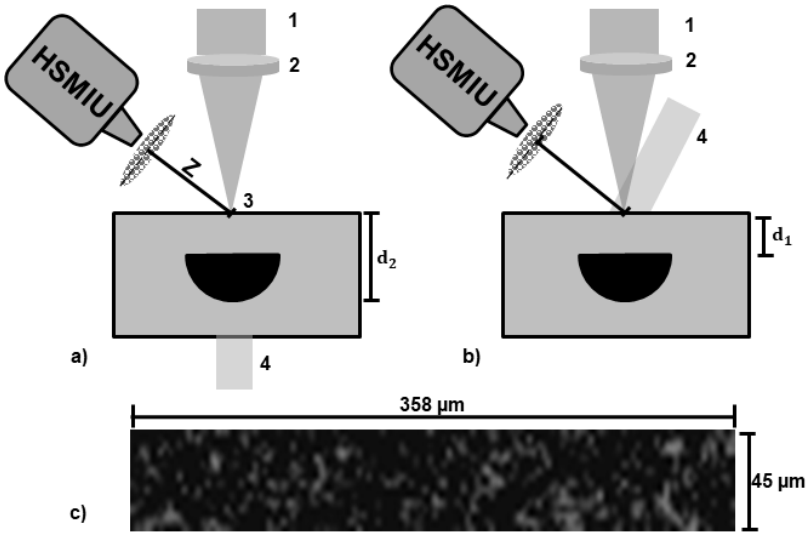

Figure 24: a) Optical setup for remote photoacoustic sensing in transmission-mode using speckle-analysis. The speckle pattern is generated by a CW-laser beam (1) which is focused on the phantom surface (3) using a lens (2). The sample is excited with a short laser pulse aiming at the phantom centre (4) which triggers the high-speed camera.
b) Optical setup for remote photoacoustic sensing in reflection-mode. Excitation and sensing take place on the same object side.
c) Example of a speckle image captured with the imaging setup (128 × 16 pixels). The scales are added using the available resolution, pixel size and the optical magnification $M = 10$.

the phantom experiments in reflection-mode, leading to an energy exposure of 104 $\frac{mJ}{cm^2}$. For the transmission-mode measurements, E_p=50 mJ is chosen which results in an exposure of 130 $\frac{mJ}{cm^2}$. Both exposures are higher than the MPE for single pulse photoacoustic excitation on soft tissue at 1064 nm (100 $\frac{mJ}{cm^2}$ [96]). The high excitation energy generates a high photoacoustic signal amplitude which can clearly be detected at the phantom surface and helps to understand the physical principles of the new detection approach for proof of concept. A CW-laser (532 nm, 100 mW) illuminates the detection side of the sample surface for speckle generation and the HSMIU, which is triggered by the single short laser pulse, captures the speckle pattern at the distance Z=5 cm. The illuminated diameter on the sample surface is approximately 300 µm. This results in a high exposure which is above the maximum allowed value for soft tissue. However, this exposure is selected in order to create a bright speckle pattern which can be detected by the optical imaging system for the demonstrated proof of concept experiments.

For each phantom, the photoacoustic measurements are repeated at least 17 times and for the ex-vivo sample at least 5 times in order to ensure statistical relevance. The reduced amount of measurements for the ex-vivo sample excludes the influence of tissue deformation or drying during the experiment.

4.3.3 Fiber-based speckle-sensing

Figure 25 illustrates the sample geometries for the fiber-based speckle-sensing experiments which demonstrate the applicability for endoscopy.

Sample	d_1 [mm]	d_2 [mm]
E1	1.7	5.7
E2	3.0	7.0
E3	4.5	8.5
Ex-vivo	1.8	10.0

Figure 25: The geometries for the PVCP samples and the ex-vivo sample for the fiber-based speckle-sensing experiments are illustrated

Three rectangular PVCP-phantoms with a side length of 30 mm are manufactured using a scattering matrix and an absorbing core. The rectangular absorbing part has a side length of 15 mm and a height of 4 mm. The ex-vivo sample consists of an absorber placed inside porcine fat which is obtained from a local supermarket. The speed of sound for the PVCP phantoms is measured at 1334 $\frac{m}{s}$ and for the fat tissue at 1448 $\frac{m}{s}$ using the ultrasound thickness measurement device. The distances d_1 and d_2 for the measurement in reflection- and transmission-mode are varied for the samples as shown in fig. 25. Similar to the samples for the free-space measurements, it needs to be mentioned that the used absorbers are not found in real tissue for endoscopic applications. However, the big absorbers are selected in order to ensure a high photoacoustic surface deformation and tilt for a proof of concept of detecting a photoacoustic signal using fiber-based speckle-sensing.

Figure 26 illustrates the fiber-based high-speed optical imaging system used for the photoacoustic measurements. An imaging fiber bundle (M=2.5, 30000 fibers, imaging resolution 1 µm, working distance 30 µm, field of view diameter 240 µm) captures the generated speckle pattern and transfers the speckle pattern image to the proximal bundle end where it is imaged by the HSMIU. The resolution of the optical system is measured about 2.76 µm by a microscope test target (1951 USAF test target, fig. 26). This fiber-based imaging system is used to measure the samples in transmission-mode and reflection-mode using speckle-analysis. The initial excitation beam diameter of 7 mm is expanded using a bi-concave lens (f=50 mm) which results in D_{ex}=12 mm

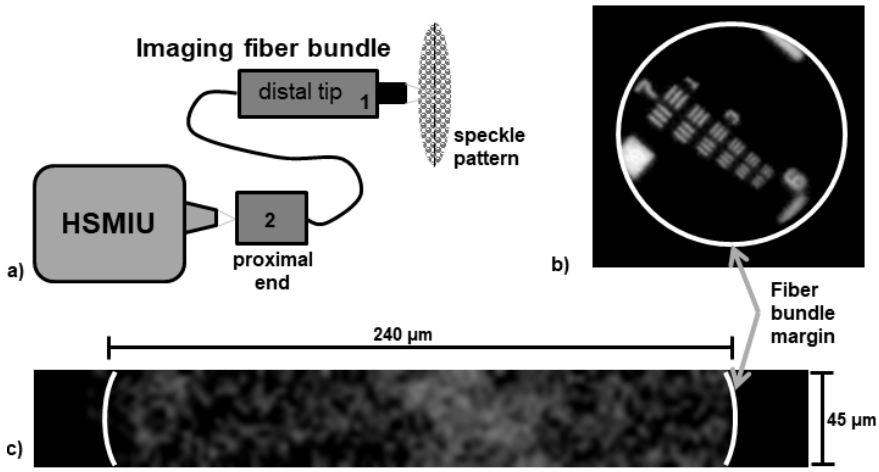

Figure 26: a) The endoscopic, high-speed imaging system is shown. The speckle pattern is imaged at the distal bundle end (1) and the image is transferred to the proximal end (2) where the HSMIU captures it.
b) The magnification of the complete imaging system (fiber bundle and HSMIU) is measured at 25 using a USAF 1951 Test Target.
c) Example of a speckle pattern captured with the setup (128×16 pixel which enable the sampling of the speckle pattern at a field of view of 45×240 μm). The width is restricted by the fiber bundle diameter (240 µm), whereas the height (45 µm) is defined by the available pixel amount ($\frac{16\,pixel \times 28\mu m}{M=10}$=45 µm.)

and F_0=93 $\frac{mJ}{cm^2}$ with E_p=105 mJ. This exposure is lower than the MPE for photoacoustic excitation on soft tissue for short laser pulses at 1064 nm (100 $\frac{mJ}{cm^2}$), when the exposure due to the CW-laser is neglected. A CW-laser (532 nm, 100 mW) illuminates the detection side of the sample surface for speckle generation. The illuminated diameter on the sample surface is approximately 300 µm which results in a high exposure above the maximum allowed value for soft tissue. However, this exposure is selected in order to create a bright speckle pattern which can be detected at the imaging distance Z=7 mm by the high-speed optical imaging system.

For the phantom measurement, at least 13 single measurements per phantom are carried out and analyzed in order to ensure statistical relevance. For the ex-vivo measurements, 10 measurements per sample were done. The reduced amount of measurements for the ex-vivo sample excludes the influence of tissue deformation or drying during the experiment.

4.3.4 Verification procedure

For verification of the reflection- and transmission-mode measurements, t_t for the corresponding acoustic travel distance to the detection surface is calculated using d_1 or d_2 and c of the sample material. Furthermore, a broadband contact ultrasound transducer (V111-RM, Olympus Corporation, Japan) with a resonance frequency of 10 MHz is used for the remote photoacoustic measurements in transmission-mode. Contact transducers are the state of the art for photoacoustic signal detection and this modality is considered as precise compared to the remote speckle-sensing approach.

4.4 Remote photoacoustic sensing using a low-resolution sensor

Since the frame rate of the high-speed camera described in the previous section is too low for precise photoacoustic sensing, H4 treats the usability of a faster, low-resolution, diode-based sensing system. This section describes the materials and methods for the investigation of the hypothesis H4. Figure 27 illustrates the necessary steps. First, the diode-based sensing system is described which replaces the HSMIU and allows single-speckle tracking. Second, the experimental setup for the remote photoacoustic measurements is shown. Finally, the data analysis and verification procedure is introduced. The described procedures have already been published in [P4].

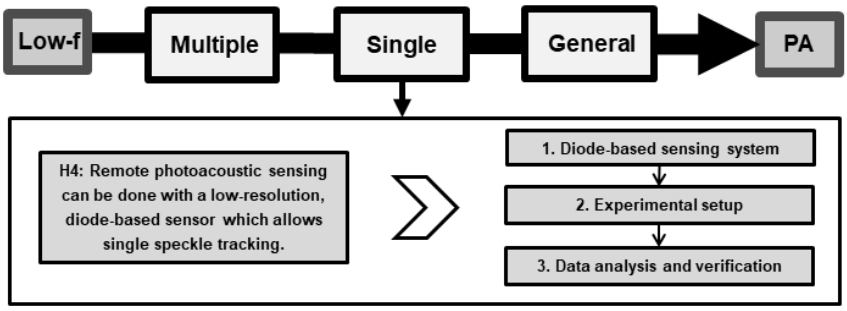

Figure 27: H4 and its subdivision are illustrated.

4.4.1 Diode-based sensing system

Figure 28 shows the established diode-based imaging system. A microscope

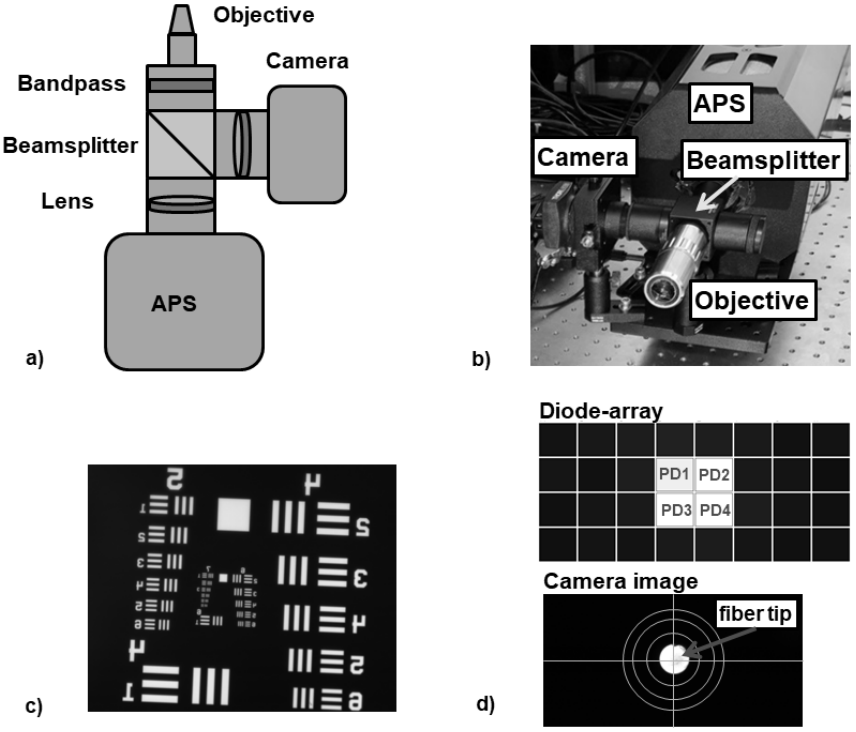

Figure 28: a) The structure of the avalanche-photodiode-sensor (APS) system is shown. b) Picture of the sensing system. c) The magnification of the sensing system is calculated at 5 using an USAF 1951 Test Target. d) The camera position of the sensing system is calibrated using a multi-mode fiber. The diode signals and the camera image are shown when an illuminated fiber is placed in their centre.

objective (10x) together with a beamsplitter and a lens (f=100mm) is used for image magnification on a reference camera (DCC1545M, Thorlabs, USA) and the avalanche-photodiode sensor (APS). A bandpass filter for the speckle wavelength is placed after the objective in order to block the photoacoustic excitation and room light. The magnification of the system is calculated at 5 with a microscope test target (M=5). The camera is used as a reference for image calibration and alignment. The calibration is done with a multi-mode fiber (AFS105/125Y, Thorlabs, USA) to which a halogen light source (HL-2000, Mikropack, Germany) is coupled. The fiber tip is then imaged on the camera and APS (fig. 28(d)) and the co-alignment of the camera image and the APS can be verified. The APS (APDcam, Fusion Instruments, Hungary) consists of a 4×8 avalanche-diode array (d_{px}=1.6 mm) and therefore offers 32 pixels.

Of these 32 pixels, only the four central pixels (PD1, PD2, PD3, PD4) are used for tracking of a single speckle in order to maximize the acquisition rate.

4.4.2 Experimental setup

Figure 29 illustrates the experimental setup for the remote photoacoustic measurements.

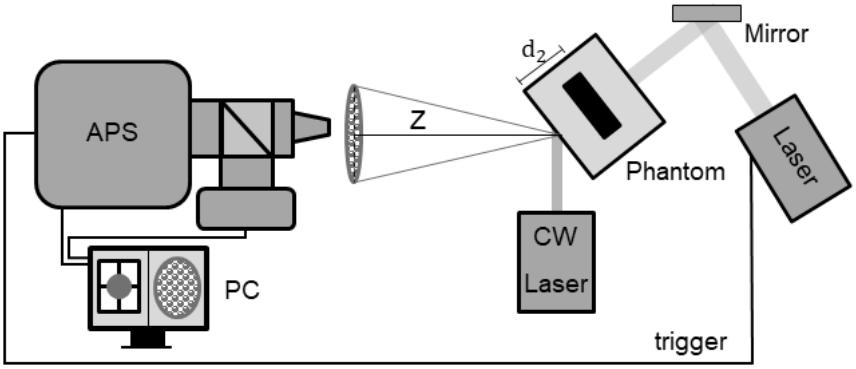

Figure 29: Experimental setup (transmission-mode) for the remote photoacoustic measurements using the APS.

Three different PVCP phantoms (Ph1, Ph2, Ph3) with increasing distances between absorber surface and detection surface (d_2) are measured in transmission-mode. Two PVCP phantoms are measured in reflection-mode (Ph4, Ph5). One skin tissue sample is measured in transmission-mode. For this sample, the absorber is located directly at the bottom surface in order to ensure high signal amplitude for proof of concept. The skin tissue is obtained from bisected pig heads which were obtained from the local slaughterhouse (Unifleisch GmbH & Co KG, Erlangen, Germany). Therefore, approval of ethics committee is not necessary. The tissue sample is prepared manually using a scalpel. A PVCP-absorber is placed at the sample bottom by cutting out a hole of the tissue. The speed of sound for the prepared skin sample is measured at 1300 $\frac{m}{s}$ and for the PVCP phantoms at 1330 $\frac{m}{s}$ with an ultrasound thickness measurement device (Mini Test 430, Elektro Physik, Germany). Figure 30 sketches the phantom position in regard to the excitation and illumination laser and shows the corresponding detection distances of all samples. The speckles are generated by CW illumination (532 nm, 80 mW, $D_{ill} = 0.75$ mm) of the sample surface and imaged at Z=20 cm. First, a convenient speckle is found by manually moving the APS using mechanical stages and visually tracking the camera image. A speckle is considered as convenient for the measurement if it is in the centre of the camera and therefore in the

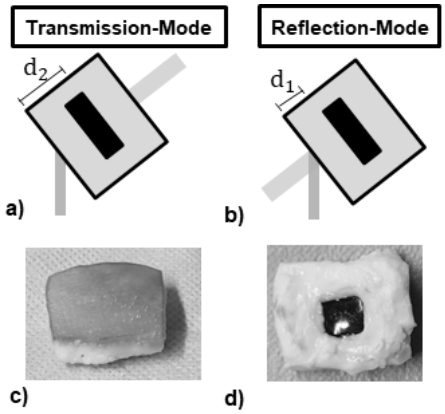

e)

Sample	d_1 [mm]	d_2 [mm]
Ph1	-	4
Ph2	-	5
Ph3	-	6
Ph4	3	-
Ph5	4	-
skin sample	-	10

Figure 30: The two experimental setups are sketched (a,b) and pictures of the skin tissue sample are shown (c,d). For the skin sample, the absorber is located directly at the bottom surface (d). The corresponding detection distances are summarized in the table (e).

centre of the APS (see fig. 31). Furthermore, the speckle size needs to be in the range of the pixel size of the APS (1.6 mm). This is ensured by comparing the tracked speckle size to the inner circle (diameter 1.4 mm) of the illustrated target which can be displayed by the camera software. For the photoacoustic

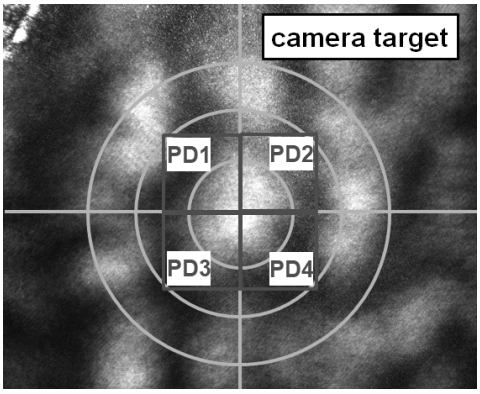

Figure 31: The camera image of an exemplary speckle, which is centered inside the four measurement diodes (PD1, PD2, PD3, PD4) and used for photoacoustic measurement, is shown. The speckle is placed in the center of the reference camera and thus in the center of APS by manually moving the complete imaging system.

measurements, the phantoms are excited with a short laser pulse (Q-Smart 450, Quantel laser, Les Ulis (France)) and the laser parameters are the following: λ=1064 nm, t_p=5 ns, beam diameter 7 mm, E_p=90 mJ. The laser pulse triggers the acquisition start of the APS with a sampling rate of 8×10^6Hz.

For each sample, 15 measurements are analysed in order to ensure statistical relevance.

4.4.3 Data analysis and verification

Figure 32 shows a speckle which is initially in the centre of the four measurement diodes PD1, PD2, PD3 and PD4 and moves to a different position. By using the temporal diode signals, it is possible to compute the temporal centre of mass of the speckle $C_{sp}(x_{sp}, y_{sp})$ and its total vector length t_{sp} by using eqs. (16) to (18) [97]. Since the speckle moves if the surface tilts, this centre of mass is related to the photoacoustic signal and it is possible to reconstruct the absorber depths d_1 and d_2.

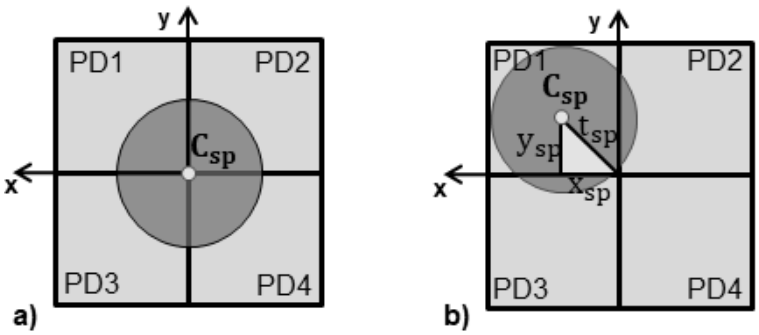

Figure 32: A perfect round speckle which is initially in the centre of the APS is shown (a). The diode signals (PD1, PD2, PD3, PD4) can be used to compute its centre of mass $C_{sp}(x_{sp}, y_{sp})$ and its total vector length t_{sp} in order to detect speckle movements (b).

$$x_{sp} = \frac{(PD1 + PD3) - (PD2 + PD4)}{(PD1 + PD2 + PD3 + PD4)} \tag{16}$$

$$y_{sp} = \frac{(PD1 + PD2) - (PD3 + PD4)}{(PD1 + PD2 + PD3 + PD4)} \tag{17}$$

$$t_{sp} = \sqrt{x_{sp}^2 + y_{sp}^2} \tag{18}$$

In order to proof the usability of the APS for remote photoacoustic detection, the coordinates of the speckle temporal centre of mass are computed and verified to t_t for the acoustic signal which is calculated using d_1/d_2 and c.

4.5 Automated single speckle tracking for remote photoacoustic sensing

For the previously described measurements, the positioning of the imaging unit is performed manually. This is time-consuming and not convenient considering an imaging application. Therefore, This section describes the materials and methods used for the investigation of the hypothesis H5 which treats automatization for single speckle-sensing. Figure 33 illustrates the necessary steps. First, the experimental setup is described and second, the automatization software and procedure is explained. The crucial part for automatization is the identification of a convenient speckle for sensing.

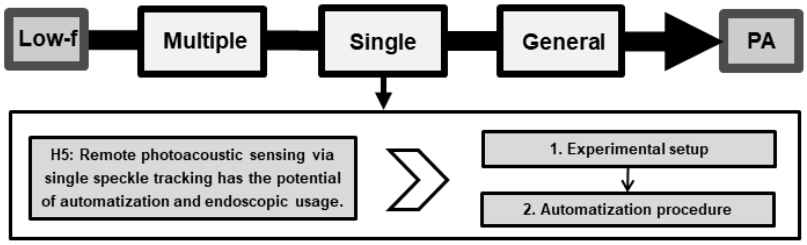

Figure 33: H5 and its subdivision are illustrated.

4.5.1 Experimental setup

The setup for the for the automatized measurements is similar to the setup described for single speckle-sensing in the previous section and is displayed in fig. 34 [S2]. However, the speckle pattern is acquired by the imaging fiber bundle used for endoscopic sensing. The proximal end of this imaging fiber bundle can be moved in lateral direction by electrical stages and the transferred speckle pattern is imaged by the APS. In contrast to the APS system previously described, a 20x magnification objective (WC95248318, Mitutoyo, Japan, 20x) is used. Furthermore, the imaging lens in the diode array arm is changed to f=200 mm. Together with the magnification of the imaging fiber bundle (M=2 5), these changes result in a higher magnification of 50 for the diode array arm and 25 for the camera arm which is verified by imaging an USAF Test Target. These higher magnifications allow speckle-sensing at a near imaging distance which is desired for endoscopic usage. The speckles are generated by focused CW illumination (532nm, 80mW, D_{ill}=50 µm) of the sample surface and imaged by the fiber bundle and APS system at Z=2 mm. A convenient speckle is found automatically by analyzing the camera image and moving the proximal fiber bundle end in lateral directions with the electrical stages. This automatization procedure is described in detail in the following

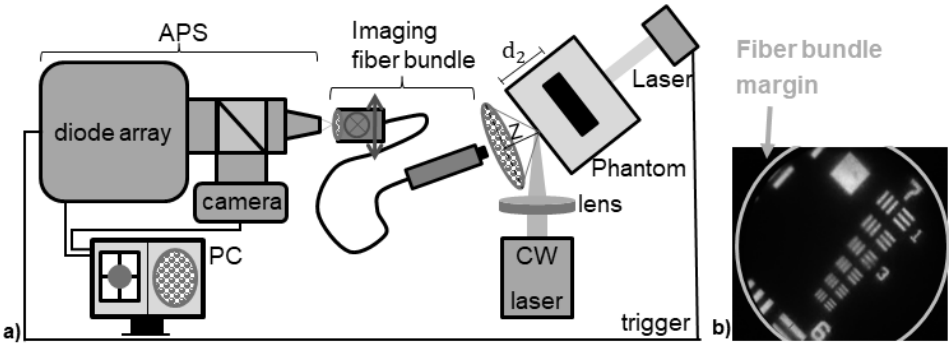

Figure 34: a) The experimental setup for automatized single speckle-sensing is shown. The speckle pattern is imaged by an endoscopic fiber bundle and sensed by the APS system. The proximal fiber bundle end can be moved in lateral positions by electrical stages which is indicated by the arrows. b) The magnification of the imaging system is experimentally verified at 25 for the camera arm and at 50 for the diode array arm with an USAF microscopic test target.

section. For the photoacoustic measurements, the phantoms are excited with a short laser pulse (Q-Smart 450, Quantel laser, Les Ulis (France)) and the laser parameters are the following: λ=1064 nm, t_p=5 ns, beam diameter 7 mm, E_p=110 mJ. The laser pulse triggers the acquisition start of the APS with a sampling rate of 8×10^6 Hz. Two PVCP phantoms (PhA1, PhA2) are measured in transmission-mode. The speed of sound for these samples is measured at 1349 $\frac{m}{s}$ with an ultrasound thickness measurement device (Mini Test 430, Elektro Physik, Germany). Figure 35 sketches the phantom position in regard to the excitation and illumination laser and shows the corresponding detection distances of all samples. For each phantom 10 measurements are analysed in order to ensure statistical relevance and the mean detection times by automated single speckle-analysis and their standard deviations are compared to the theoretical detection time t_t.

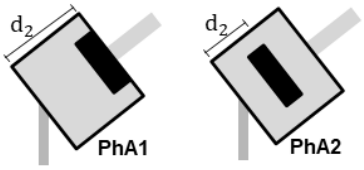

Sample	d_2 [mm]	t_t [µs]
PhA1	7.5	5.56
PhA2	5	3.71

Figure 35: The two PVCP phantoms used for automatized single speckle-sensing are sketched and the corresponding detection distances d_2 and theoretical times t_t are summarized in the table.

4.5.2 Automation procedure

In order to automatize the single speckle measurements with the imaging fiber bundle a graphical user interface (GUI) is developed using MATLAB [S2]. This GUI analyzes the speckle pattern which is imaged by the camera, finds the most suitable speckle for analysis and controls the stage movements in order to position the fiber bundle end correctly. Figure 36 illustrates the image processing steps therefore. Before these steps, the exposure time is adjusted

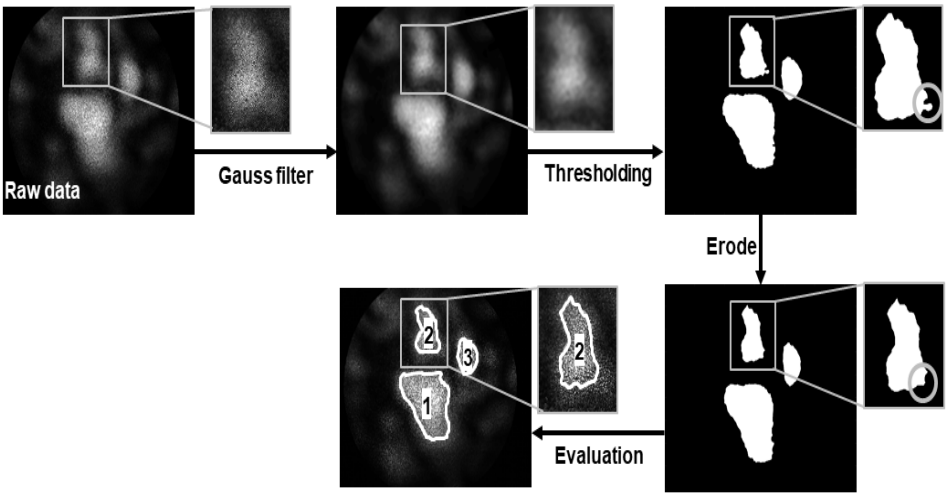

Figure 36: The image processing steps for speckle selection are illustrated. First the periodic fiber core structure is removed by Gaussian filtering. Second, thresholding is performed. Third, the speckles are eroded and finally, the speckles are evaluated. The selected speckle is marked green (3), suitable speckles are marked yellow (2) and non-suitable speckles are marked red (1).

automatically for avoiding camera overexposure. This automatic and flexible exposure time allows to set the mean image intensity of the 8-bit image (maximal pixel value of 255) to 30 which avoids pixel overexposure according to our observations. First, a Gaussian filter is used for smoothing the periodic pattern caused by the imaging fibers. Second, thresholding is performed to separate the speckles from the background. Here, a threshold value of 2.5 times the mean image intensity is chosen. Third, the MATLAB function 'imerode' is applied in order to erode the speckle circumference slightly and in order to remove very small speckles of only some pixels. The remaining speckles are now potential candidates for photoacoustic sensing and need to be evaluated according to their usability for single speckle-sensing. The three relevant evaluation criteria are summarized in table 3. The speckle needs to have a convenient area $A_{speckle}$ which is suitable for speckle-sensing with the diode pixels. Furthermore, the speckle needs to be clearly distinguishable from its

Table 3: The criteria for speckle evaluation are summarized.

Criterion	Calculation	Value
Speckle area $A_{speckle}$	Counting the pixels of the speckle after the image pre-processing steps	12500<$A_{speckle}$<50000
Single speckle contrast C_{sing}	$C_{sing} = \frac{I_{speckle}}{I_{back}}$	C_{sing}>2.5
Circularity Circ	$Circ = \frac{4\pi A_{speckle}}{scope}$	Circ>0.5

background. This requirement is considered by calculating the single speckle contrast C_{sing}=$\frac{I_{speckle}}{I_{back}}$ which is defined by the ratio between the total speckle intensity $I_{speckle}$ and the total background intensity I_{back}. The background for a single speckle is defined by the pixels not being assigned to the speckle, but falling into the virtual sensing area of the four measurement diodes centered at the speckle centre of mass. A single speckle and its background is illustrated in fig. 37 [S2]. Since an optimal speckle for single speckle-analysis

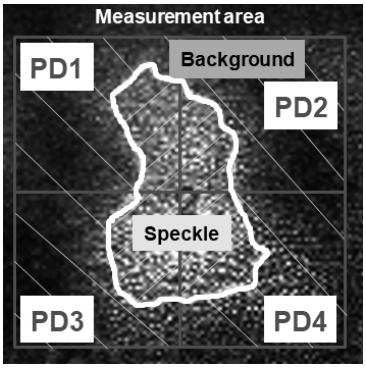

Figure 37: A speckle and its background are shown. The background is defined by the total intensity of the non-speckle pixel falling into the measurement area of the four sensing diodes.

would be circular, the speckle circularity is evaluated ($Circ$=$\frac{4\pi A_{single}}{scope}$). This can be done by dividing A_{single} by the scope of the single speckle. A single speckle is considered suitable for sensing if 12500<$A_{speckle}$<50000, C_{sing}>2.5 and Circ>0.5. If several speckles are suitable, the speckle with the highest contrast is selected for sensing. Non suitable speckles are marked red, suitable speckles yellow and the most suitable speckle is marked green. After this evaluation, the proximal fiber bundle end is moved laterally by the electrical

stages in order to position the selected single speckle in the center of the four measurement diodes and the photoacoustic measurement is started.

4.6 Evaluation of remote speckle-analysis for photoacoustic detection

For H2, H3 multiple speckle-analysis and for H4, H5 single speckle-sensing is used for photoacoustic detection. This section describes the evaluation of both sensing techniques and therefore the materials and methods for the investigation of H6. Figure 38 illustrates the necessary steps. First, the

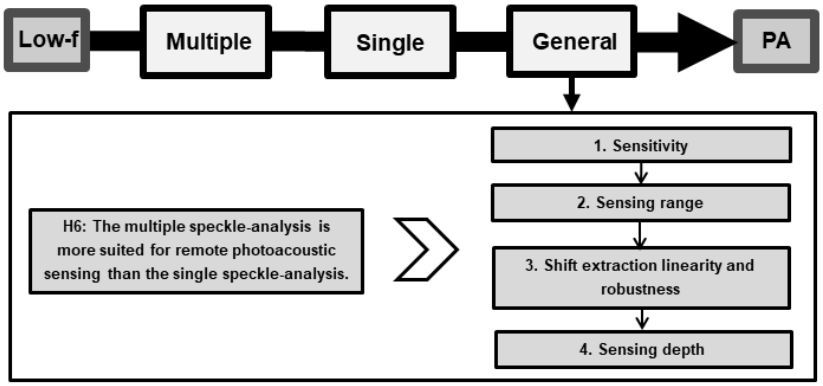

Figure 38: H6 and its subdivision are illustrated.

sensitivity of the established systems in this dissertation is evaluated by analyzing noise measurements. Second, their sensing ranges are discussed. Third, the shift extraction linearity and robustness is tested with simulations. Finally, the sensing depth is discussed. Therefore, the optical and acoustical properties of the used phantom material in this work are compared to realistic tissue properties. In addition, the sensing depth of the established sensing systems in this thesis is computed for a realistic tissue model.

4.6.1 Sensitivity

In order to evaluate the sensitivity of the developed systems it needs to be noted that two imaging systems were developed in the course of this thesis: The high-speed camera system described in section 4.3 and the diode-based sensing system described in section 4.4. The high-speed camera system measures surface tilt changes since it compares each video frame with the previous frame (eq. (11)) by analyzing multiple speckles. The diode sensing system, however, directly analyzes the center of gravity of a single speckle (see eqs. (16) and (17)) and measures thus the surface tilt. For the assessment

of the sensitivity of these two techniques the simplification that the surface tilt is equal to the surface tilt change is made. This case corresponds to the measurement of the surface tilt in regard to an untilted surface.

The sensitivity in terms of minimal detectable tilt $S_{d,\alpha}$ is dependent on the speckle shift extraction precision σ_{prec}. For the high-speed camera approach, σ_{prec} is either limited by the noise floor σ_{nf} or the shift extraction algorithm precision ($0.05d_{px}$). For the diode-based system, σ_{prec} is simply limited by σ_{nf}. The noise level σ_{nf} is computed by taking the standard deviation of a photoacoustic measurement data set before excitation. Figure 39 illustrates two exemplary photoacoustic measurements and the noise level derivation. For the high-speed camera data sets 20 and for the diode system data sets

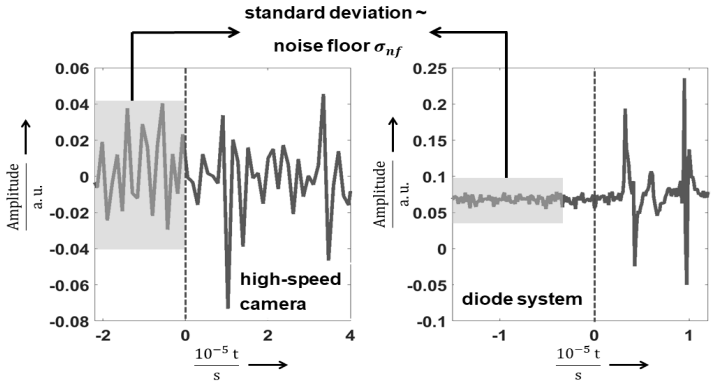

Figure 39: Exemplary data sets for the high-speed camera and diode system are shown. The standard deviation of data points before photoacoustic exciation define σ_{nf}. The dashed line marks the photoacoustic excitation time point.

150 data points before photoacoustic excitation are used for the standard deviation calculation.

By determining the noise floor σ_{nf} and taking into account the relevant imaging parameters (Z, pixel size d_{px}, magnification M, illumination diameter D_{ill}), $S_{d,\alpha}$ can be determined. The minimal detectable speckle shift $\delta_{s,min}$ is equals to the multiplication of d_{px} and σ_{nf} for the diode system. For the high-speed system, it is the same, if σ_{nf}>0.05. If 0.05>σ_{nf}, then $\delta_{s,min} = 0.05d_{px}$ is valid. By considering eq. (10), it is then possible to compute the minimal detectable tilt $S_{d,\alpha}$: $tan(S_{d,\alpha})=\frac{\delta_{s,min}}{ZM}$. With the assumption that the investigated speckle pattern or single speckle consists of reflections from the complete illuminated surface area with the diameter D_{ill}, the minimal detectable axial surface deformation is estimated by $S_{d,nm}=tan(S_{d,\alpha})D_{ill}$.

Following the computation of $S_{d,nm}$, the minimal detectable pressure S_d is determined according to eq. (19) [98].

$$S_d = \pi Z_{ac} S_{d,nm} f \tag{19}$$

The parameter f defines the frequency of the acoustic wave which should be detected. For the established system the maximum detectable frequency is half the acquisition frame rate. The determined sensitivity values are discussed and compared to values of other optical photoacoustic detection setups from literature.

4.6.2 Sensing range

The sensing range (i.e. the tilt interval which is covered by the remote speckle-analysis) is dependent on the sensitivity, sensor size and speckle shift extraction method. The sensitivity defines the minimal detectable tilt as treated in the previous section. The maximal detectable tilt α_{max} is defined by the sensor size of the sensing system and the speckle shift extraction method. Regarding the shift extraction method, it needs to be distinguished between the multiple speckle-analysis which is applied for the high-speed camera sensing system and the single speckle-analysis which is applied for the diode-based sensor. The sensing ranges for both speckle shift extraction methods are discussed.

4.6.3 Shift extraction linearity and robustness

In order to evaluate the linearity and robustness against neighbouring speckles, meaning speckles which are not located inside the original image but appear in the shifted speckle image, shift simulations are carried out. For the multiple speckle-analysis, a 128×16 image of a high-speed acquisition is considered. The used image is shown in fig. 40. This image is chosen since it

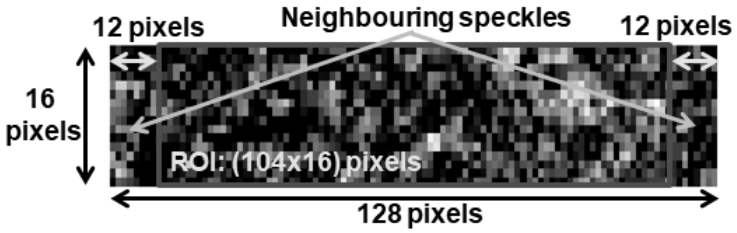

Figure 40: The unshifted speckle image is shown which is shifted in horizontal direction. For the shift extraction, an image border of 12 pixels is set which reduces the ROI to 104×16 pixels.

offers spatial speckle information over the whole image region and is thus

convenient for analyzing the shift extraction linearity and robustness against neighbouring speckles. In order to evaluate the shift extraction according to eqs. (11) and (12) this image is shifted in horizontal direction with -10 pixel to 10 pixel ($x_{s0,real}$) with a shift resolution of 0.01 pixels using MATLAB R2019b and a new image is generated. From this shifted image, the shift x_{s0} relatively to the original image is extracted by eqs. (11) and (12) and parabolic interpolation. For the shift extraction, a horizontal image boarder of 12 pixel is set. Due to this boarder, the outside pixels of the original image and shifted image are not considered for the shift extraction and the resolution for the ROI (region of interest) is limited to 104×16. However, neighbouring speckles which are outside the lower resolution image (104×16) for the original image will appear inside the ROI for the shifted image. Thus, the robustness of the shift extraction method against neighbouring speckles can be evaluated. Figure 41 shows the four selected speckle patterns with centralized single speckle for the evaluation of the single speckle-analysis. The images are moved in horizontal direction with a shift amplitude of -0.26 to 0.26 of the diode pixel size ($x_{sp,real}$). For each shifted image, the horizontal center of mass x_{sp} for the sensing diodes region which is indicated in fig. 41 is computed according to eq. (16).

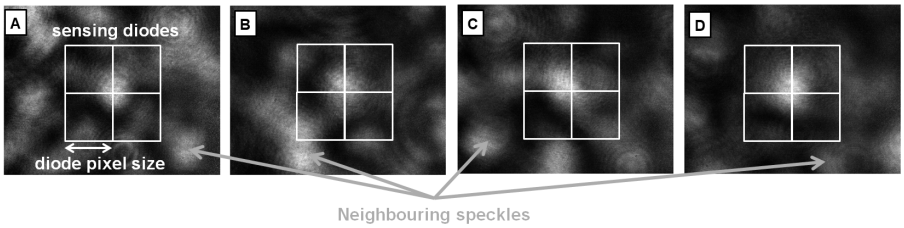

Figure 41: Speckle images (A,B,C,D) which are evaluated for its single speckle-sensing capability. The diode sensing regions are indicated by the rectangles.

4.6.4 Sensing depth

In order to evaluate the generated pressures, surface deformations and the sensing depth of the remote speckle-sensing technique for photoacoustic detection, the relevant optical and acoustical parameters of the materials used in this thesis are compared to tissue . Skin is selected as tissue matrix and blood as tissue absorber since blood vessel imaging inside skin is a common photoacoustic application. The properties are compared for the wavelengths 532 nm and 1064 nm. These wavelengths are selected due to their broad availability and common usage for PAT. Based on the material properties, eqs. (3) and (15), it is possible to compare the photoacoustic surface

deformations for the realistic skin/blood-model parameters to the phantoms used in this thesis.

In order to precisely compute the sensing depth of speckle-analysis for photoacoustic detection on skin tissue, analytical calculations for the resulting surface pressure are performed with a skin/blood model which is illustrated in fig. 42. For this model, a blood vessel is situated inside skin tissue and the

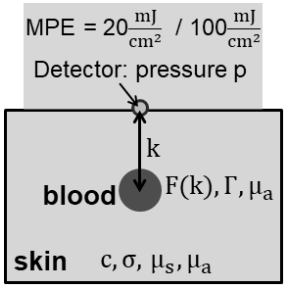

Figure 42: The skin/blood model for the computation of the photoacoustic surface pressures for the evaluation of the sensing depth is illustrated.

wavelengths 532 nm and 1064 nm are considered. First, $\mu_{eff}=\sqrt{3\mu_a(\mu_a+\mu_s')}$ is computed (see section 2.1.2) for the skin tissue with the optical parameters for skin: μ_a=1.3 $\frac{1}{cm}$ (532 nm), μ_a=0.37 $\frac{1}{cm}$ (1064 nm), μ_s'=32.3 $\frac{1}{cm}$ (532 nm), μ_s'=16.8 $\frac{1}{cm}$ (1064 nm) [27]. When taking the MPE for single pulse excitation (20 $\frac{mJ}{cm^2}$ for 532 nm and 100 $\frac{mJ}{cm^2}$ for 1064 nm) as the fluence on the skin tissue surface, it is possible to compute the depth dependent fluence F according to eq. (2). With this depth dependent fluence, the absorption coefficients (μ_a=280 $\frac{1}{cm}$ for 532 nm and μ_a=6 $\frac{1}{cm}$ for 1064 nm) and Γ=0.13 for blood, the initial generated pressure p_0 for a blood absorber at various depths k can be calculated according to eq. (3). With p_0 and by considering the acoustic attenuation σ of skin, the pressure at the surface can be estimated for a specific absorber radius r according to eq. (20) [53]. The abbreviation U stands for the Heaviside function.

$$p(t) = p_0 U(r - |k - ct|)\frac{k - ct}{2k} e^{-\sigma k} \tag{20}$$

For the computations, the absorber radius is set to 125 µm / 250 µm / 250 µm and σ=0.60 cm^{-1} (see table 1 for 5 MHz). The resulting surface pressures for different depths k and absorber radii r are compared to the determined detection sensitivities S_d of the detection systems in this thesis in order to estimate their sensing depths.

4.7 Investigation of wavelength influence

After the proof of concepts for photoacoustic sensing by multiple- and single speckle-analysis and their comparison, it is essential to investigate the wavelength influence on the speckle quality. This section describes the materials and methods for the investigation of the hypothesis H7 that focuses on this wavelength influence. Figure 43 illustrates the necessary steps. The

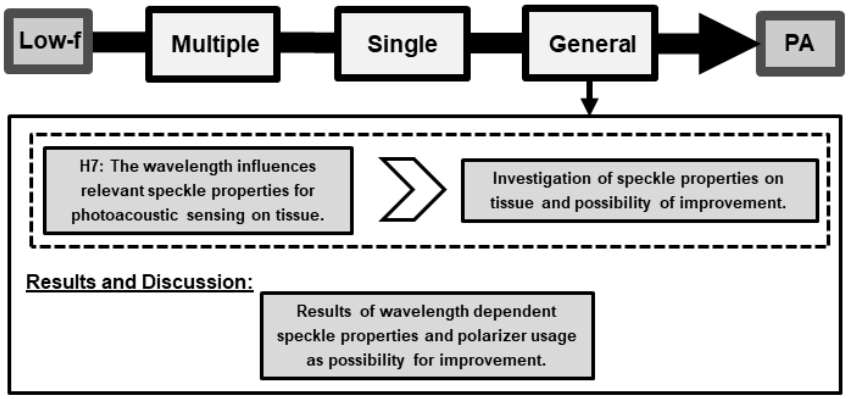

Figure 43: H7 and its subdivision are illustrated.

wavelength influence on the speckle size and contrast is analysed by using five illumination wavelengths in the range of 405 nm to 780 nm, ex-vivo skin tissue and a camera. In addition, the possibility to improve the speckle properties by using a polarizer is investigated. It was decided to conduct this general study after the previously described proof of concept measurements with a wavelength of 532 nm due to three reasons. First, it was known from literature that a speckle wavelength of 532 nm is feasible of reliable vibration detection on tissue [83]. Second a convenient CW-light source at the wavelength of 532 nm was available. Third, the financial means for acquiring light sources were limited in the beginning of the working period.

4.7.1 Investigation of speckle properties

Figure 44 illustrates the setup and a tissue sample for the investigation of the wavelength influence on the speckle size and speckle contrast. Five laser-diodes (Roithner Lasertechnik GmbH, Vienna, Austria) with similar beam properties and different wavelengths are selected: 405 nm, 450 nm, 520 nm, 635 nm, 780 nm. The diodes spectra can be found in the appendix. Three

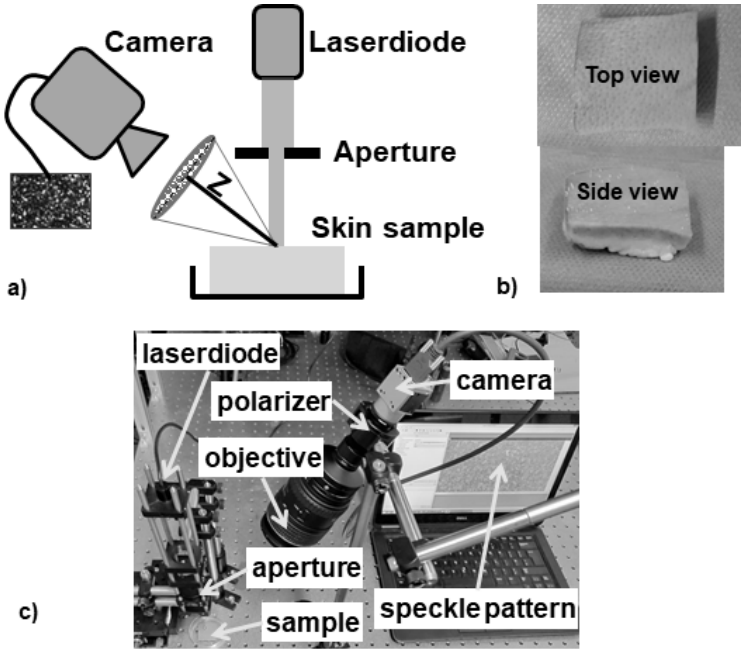

Figure 44: The experimental setup for the investigation of the wavelength influence on the speckle size and speckle contrast is illustrated (a). Pictures of an ex-vivo skin sample are shown (b). Picture of the experimental setup with polarizer usage is shown (c).

ex-vivo skin tissue samples are prepared from a pig head which is obtained form the local slaughterhouse (Contifleisch GmbH, Erlangen, Germany). An aperture (500 µm) is used to ensure a constant sample illumination diameter for the different diodes. The speckle pattern is imaged by a camera (Basler acA640-750) equipped with an objective (Tokina ATX 2.8/100 Pro D Macro AF) at Z=11 cm in order to ensure clear and detectable speckles for each wavelength. For each tissue sample, nine measurements are performed for each wavelength, resulting in a total number of 27 measurements for each wavelength. Overexposure of the sensor is avoided by adjusting the exposure time of the camera. The speckle images are processed using MATLAB. First, the image histograms are stretched to the same data limits for comparability. Then, the speckle parameters and their standard deviation are calculated: l_s is

calculated using the open-source code "SpeckleSize.m" with the full width at half maximum approach which is available via the MathWork File Exchange platform [99]. The parameter C is computed using eq. (9) for each speckle pattern image.

After this general investigation, the potential for speckle parameters improvement (l_s, C) by polarizer usage is investigated for 520 nm. Therefore, a polarizer is inserted between the camera and the objective (fig. 44). In total 27 measurements are done for the ex-vivo skin tissue. The imaging distance and the data analysis are unchanged compared to the previous described experimental study. Furthermore, the improvement by polarizer usage is discussed for illumination wavelengths between 400 nm and 532 nm. Smaller wavelengths are not considered as the MPE reduces below 400 nm and sensitive sensor materials below 400 nm are hard to find which complicates the speckle-sensing approach.

4.8 Photoacoustic imaging using speckle-sensing

The previously described photoacoustic measurements treat photoacoustic sensing at a single surface spot. However, for imaging it is required to detect the photoacoustic signal spatially resolved at the surface. Therefore, this section describes the materials and methods for the investigation of the hypothesis H8 which treats the possibility of photoacoustic imaging by speckle-analysis. Figure 45 illustrates the necessary steps. The described

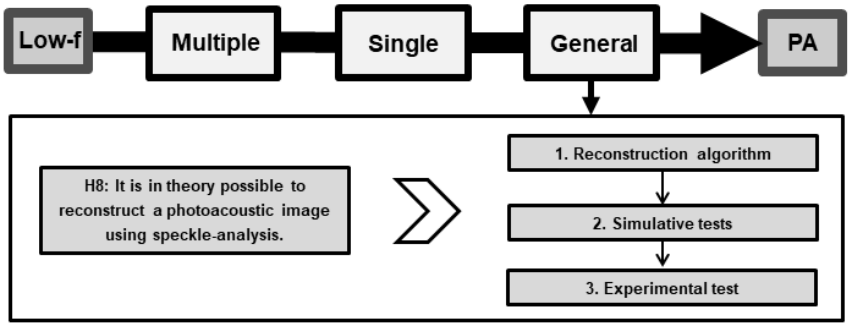

Figure 45: H8 and its subdivision are illustrated.

procedure has already been published in [P5]. First, the reconstruction algorithm using the speckle-analysis is explained. Second, this algorithm is tested on simulations for the photoacoustic surface deformation. Third, the experimental feasibility test is described. It needs to be mentioned that it is the first time to establish a photoacoustic image algorithm based on tilt measurements.

4.8.1 Reconstruction algorithm

The goal of each photoacoustic image reconstruction algorithm is the reconstruction of the initially generated pressure distribution $p_0(x_v, y_v, z_v, t = 0)$ by taking a spatially distributed surface parameter as an input. The single speckle-sensing technique which is introduced in this work measures the speckle centre of mass coordinates (x_{sp}, y_{sp}) according to eqs. (16) and (17). In the case of multiple speckle-sensing, the speckle pattern shifts x_{s0}, y_{s0} are extracted according to eq. (11). For both sensing modes, these measured parameters are representative for the surface tilt in horizontal direction α_x and vertical direction α_y of the detection area. Consequently, it is possible to reconstruct the temporal axial surface deformation inside the square detection area with length L_D according to eqs. (21) and (22).

$$\epsilon_x(x_d, y_d, t) = \frac{1}{L_D} \int_0^{L_D} \alpha_x(x_d, y_d, t) dx \tag{21}$$

$$\epsilon_y(x_d, y_d, t) = \frac{1}{L_D} \int_0^{L_D} \alpha_y(x_d, y_d, t) dy \tag{22}$$

The initials x and y for ϵ stand for the corresponding tilt reconstruction source. Median filtering for the temporal deformation is performed for outlier exclusion. After this reconstruction, eq. (23) considers the condition that the photoacoustic surface displacement is purely positive by setting negative values for $\epsilon_{x/y}$ to zero [71].

$$\text{if } \epsilon_{x/y}(x_d, y_d, t) < 0 \rightarrow \epsilon_{x/y}(x_d, y_d, t) = 0 \tag{23}$$

The lateral detector coupling is considered by an deconvolution of $\epsilon(x_d, y_d)$ for each time point using the maximum likelihood algorithm [100]. By rearranging eq. (15), $p(x_d, y_d, t)$ for each detector element can be computed with eq. (24).

$$p(x_d, y_d, t)_{x/y} = \frac{Z_{ac}}{2} \frac{\partial \epsilon_{x/y}(x_d, y_d, t)}{\partial t} \tag{24}$$

The variable $\mathrm{p}(x_d, y_d, t)$ describes the surface pressure at the detection area and eq. (7) can be used to compute $p_{0x/y}(x_v, y_v, z_v, t{=}0)$ inside the object volume.

4.8.2 Simulative test

The reconstruction algorithm is tested using the established model for photoacoustic surface deformation and tilt. Two silicone volumes (Vol1, Vol2) consisting of a mainly scattering matrix and spherical absorbers are tested. Figure 46 illustrates these two volumes. The simulative parameters are the following:

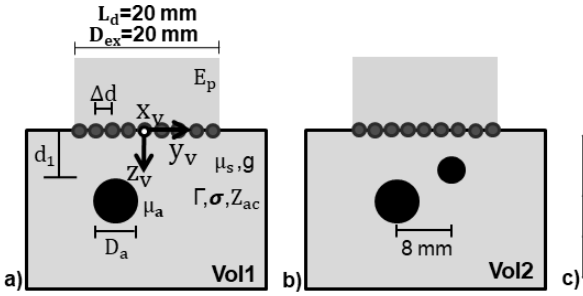

Volume	d_1 [mm]	D_a [mm]
Vol1	4	4
Vol2	4 / 2	4 / 2

Figure 46: The two silicone volumes (Vol1, Vol2) (a,b) and their spherical absorber sizes and positions (c) are shown.

D_{ex}=20 mm, E_p=300 mJ, $\mu_{s,Matrix}$=25 $\frac{1}{cm}$, $\mu_{a,Matrix}$=0.01 $\frac{1}{cm}$, $\mu_{a,Absorber}$=15 $\frac{1}{cm}$, $\mu_{s,Absorber}$=0.025 $\frac{1}{cm}$, g=0.6, c=970 $\frac{m}{s}$, Γ=0.6, σ=13 $\frac{db}{cm}$, L_d=2.0 cm, Δd=0.05 cm, Z_{ac}=1.3×10^6 $\frac{kg}{m^2 s}$. The pulse energy is chosen so that the energy exposure (95 $\frac{mJ}{cm^2}$) is below the MPE for single pulse excitation of soft tissue at 1064 nm. Two dimensional filtering of the displacement values of the detector field is performed with a 5 × 5 Gaussian filter with a standard deviation σ_{gauss}=3, and the Fresnel reflection at the excitation surface is approximated with the constant factor 0.05. The resulting temporal photoacoustic surface tilts (α_x, α_y) are used as the input for the previously described reconstruction algorithm. For verification, $\epsilon_{x/y}(x_d, y_d, t)$ is compared to the originally simulated values. Furthermore, cross-sections of $p_{0x/y}(x_v, y_v, z_v, t = 0)$ are compared against the corresponding sections of the energy density $H(x_v, y_v, z_v)$ from the MCS.

4.8.3 Experimental test

The established reconstruction method is tested by a first experimental feasibility test. Figure 47 illustrates the excitation, detection and object properties. A PCVP phantom with square absorber (side length 2 mm) is prepared. This

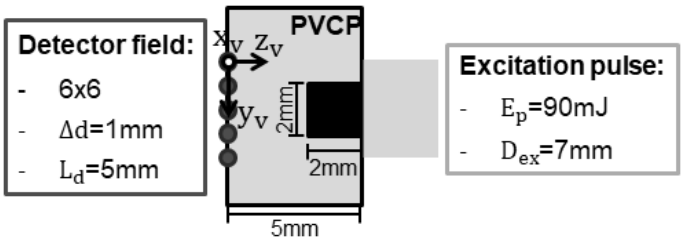

Figure 47: A PVCP-phantom with square absorber is photoacoustically excited in transmission-mode and the surface tilts are measured at several surface locations by single speckle-sensing. The excited volume is reconstructed with the established reconstruction method.

phantom (c=1340 $\frac{m}{s}$) is excited in transmission-mode with the following parameters: λ=1064 nm, D_{ex}=7 mm, E_p=90 mJ. The resulting exposure at the surface (233 $\frac{mJ}{cm^2}$) is above the MPE for single pulse excitation at 1064 nm (100 $\frac{mJ}{cm^2}$). However, this is desired, in order to achieve high signal amplitudes for the proof of concept experiment. The surface tilt is measured with the diode-based sensing system described in section 4.4 with the following parameters: L_D=5 mm, Δd=1 mm and a sampling rate of $8{\times}10^6$ Hz. The maximum intensity projections (MIP) of $p_0(x_v, y_v, z_v, t = 0)$ along the object axes are shown and compared to the phantom geometries.

5 Results and Discussion

5.1 Simulative feasibility investigation

The results for the simulative investigation of H1 are shown and discussed. Figure 48 illustrates H1, its subdivison and the structure of the results. First, the results of the two step verification procedure of the introduced model for photoacoustic surface deformations are shown and discussed. The simulated value of ϵ_{max} and the temporal surface shape are compared to interferometric measurements. Thereafter, the results for the feasibility test of photoacoustic detection using remote speckle-analysis with a commercial high-speed camera are presented and discussed.

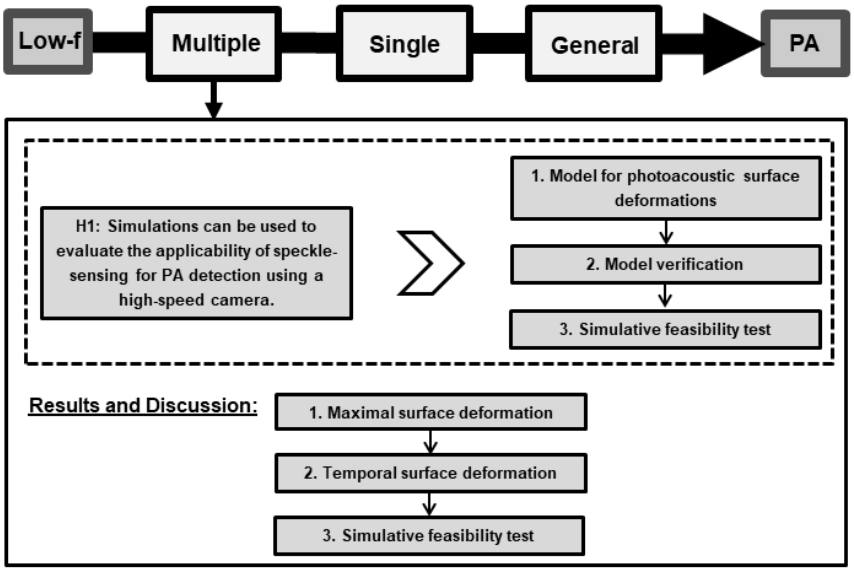

Figure 48: H1, its subdivision and the structure of the corresponding results section are illustrated.

5.1.1 Maximal surface deformation

Figure 49 shows the simulated maximal deformation values ($\epsilon_{max,simulation}$) related to the interferometric measurements ($\epsilon_{max,measure}$) for the twelve experiments shown in fig. 19. These results are obtained with a Gaussian filter at a standard deviation of σ_{gauss}=1 and a multiplication factor of 0.45 for the displacement values. With this post-processing, the simulated values match the measured values very well. Furthermore, there is a clear linear correlation for

a)

No.	ε max. simulation [nm]	ε max. measure [nm]	No.	ε max. simulation [nm]	ε max. measure [nm]
1	11.3	12.5	7	25.1	25.9
2	13.1	15.3	8	10.7	10.4
3	7.9	7.8	9	3.9	4.3
4	14.8	13.7	10	23.6	18
5	20.5	20.8	11	9.4	7.1
6	7.5	4	12	4.5	4.8

b)

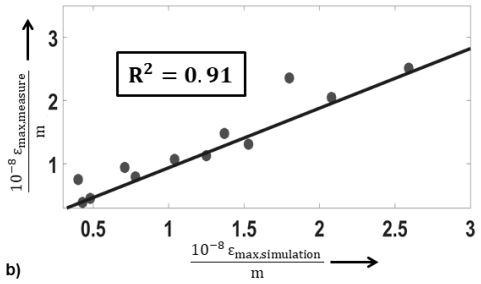

Figure 49: The simulated maximal deformation values are compared to the interferometric measurements in the table (a) and a linear correlation ($R^2 = 0.91$) is determined (b).

the two parameters (R^2=0.91, $\epsilon_{max,simulation}$=0.9435$\epsilon_{max,measure}$-7.6×$10^{-11}$). These two facts prove the usability of the model for photoacoustic surface deformations in regard to the maximal deformation value for silicone phantoms filled with $Ti0_2$ scatterers.

5.1.2 Temporal surface deformation

Figure 50 shows the simulative temporal surface deformation of the phantom centers from No. 2/5/7/8 in comparison to interferometric measurements from Horstmann et al. [34]. As shown in the previous paragraph, the max-

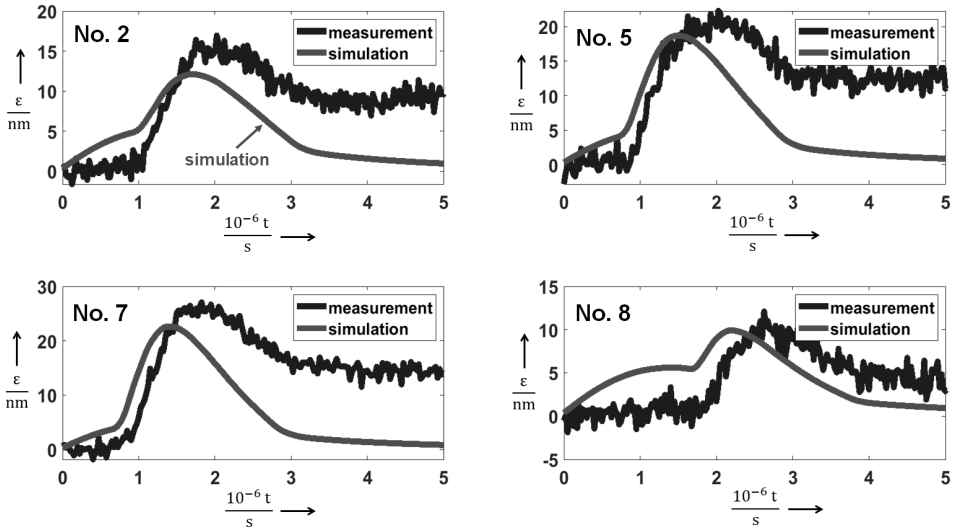

Figure 50: The temporal surface deformations of the phantom center obtained from simulations and interferometric measurements are compared to each other.

imal surface deformations are in good agreement for the simulations and

experimental measurements. In addition, the times when the deformation rise begins and reaches its maximum are the same for the simulations and measurements. The small differences can be explained by sound velocity inhomogeneities and measurement uncertainties for the phantom geometry and can be neglected. The slope of the simulated deformation corresponds to the measured deformation increase. Only for the initial phase before the actual photoacoustic deformation and the decrease of the deformation deviations can be observed. The simulations overestimate the photoacoustic deformation due to the optical absorption of the matrix material slightly. This is the reason for the slight deformation which happens before the photoacoustic deformation which has its origin at the absorber. This can be seen in fig. 50 for No.2/No.5/No.7 until approximately 1 µs and for No.8 until 2 µs. Furthermore, after some time, the simulative deformations reach the original value of zero, whereas the interferometric measurements show a drop to a plateau. This incomplete drop could be explained by viscoelastic effects of the silicone material, which are not considered by the simulation [34]. Summing up, the generated model for photoacoustic surface deformations is thus able to reproduce the purely thermoelastic surface deformations.

Figure 51 shows the simulative surface shape for the detection field and the corresponding interferometric measurements for four time point after photoacoustic excitation. Moreover, the simulative and interferometric data of a central line through the detection field are compared to each other. For each time point, the simulation data matches to the interferometric measurements. Since photoacoustic surface deformations are purely positive, the negative deformation values are a result of the noise for the interferometric setup. For the simulation, only positive deformation values are computed which matches to the assumption of purely positive photoacoustic surface displacement [75]. The comparison of the central line through the detection field manifest the observation that the simulation is capable of correctly reproducing the deformation values and shapes for the two detector field dimensions.

Considering the two step verification results, it can be concluded that the established model is capable of simulating the temporal surface deformations. Thus, the surface tilt from the deformation values can be computed by taking the spatial gradient. Since the speckle-sensing technique is sensitive to tilt changes, this calculated surface tilt can thus be used for the feasibility study of contact-free photoacoustic detection using speckle-analysis.

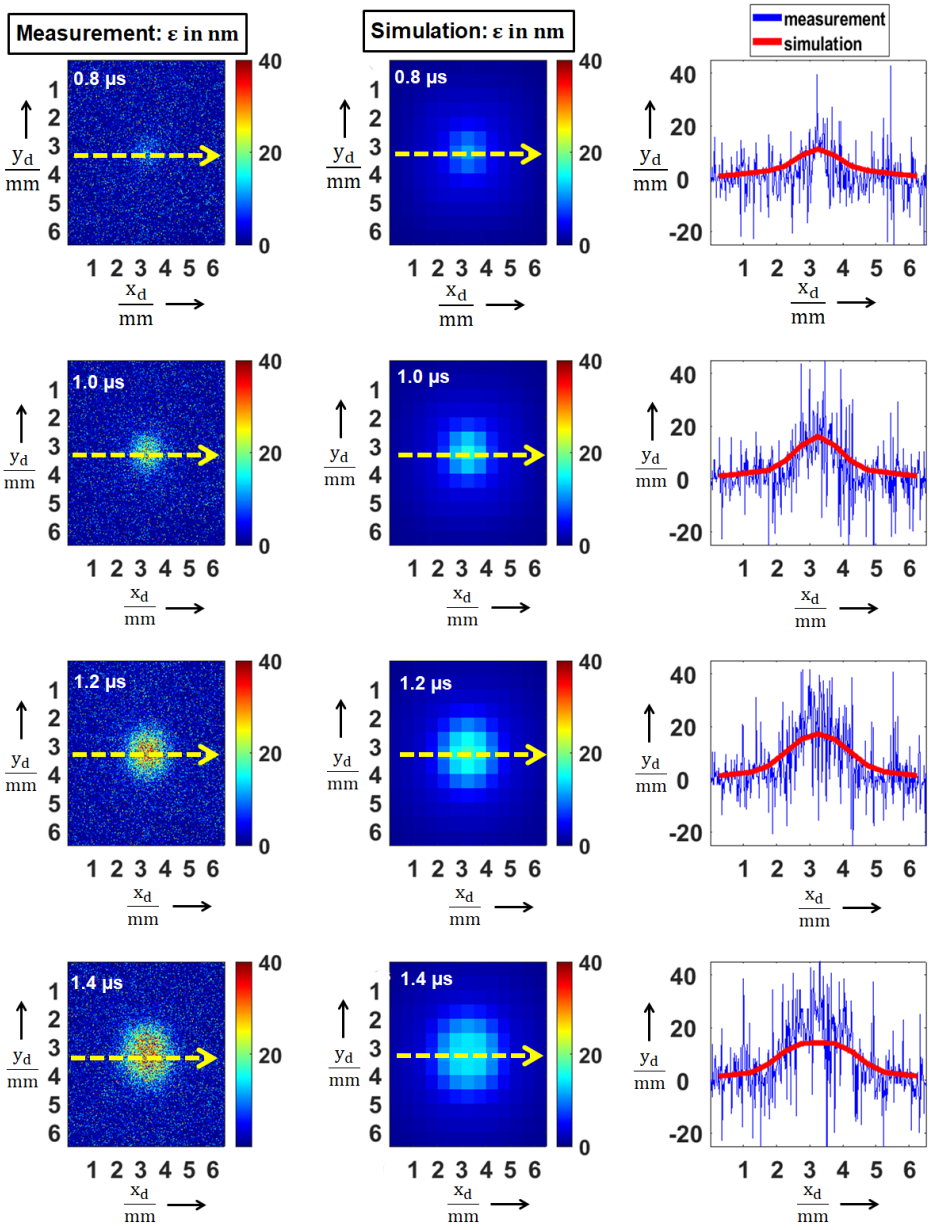

Figure 51: The simulative surface shape of the detector area is compared to interferometric measurements for four specific time points (0.8 µs, 1.0 µs, 1.2 µs, 1.4 µs) after photoacoustic excitation. The right column shows the line plot which is indicated in the simulative and interferometric data by an arrow. For each time point, the simulative deformation shape matches to the experimental measurements.

5.1.3 Simulative feasibility investigation

Figure 52 illustrates ϵ for three specific times after the excitation for the feasibility investigation. Furthermore, the corresponding surface tilts α_x and α_y are displayed. As expected for the spherical absorber, the temporal deformation behaviour is similar to the results shown in fig. 50.

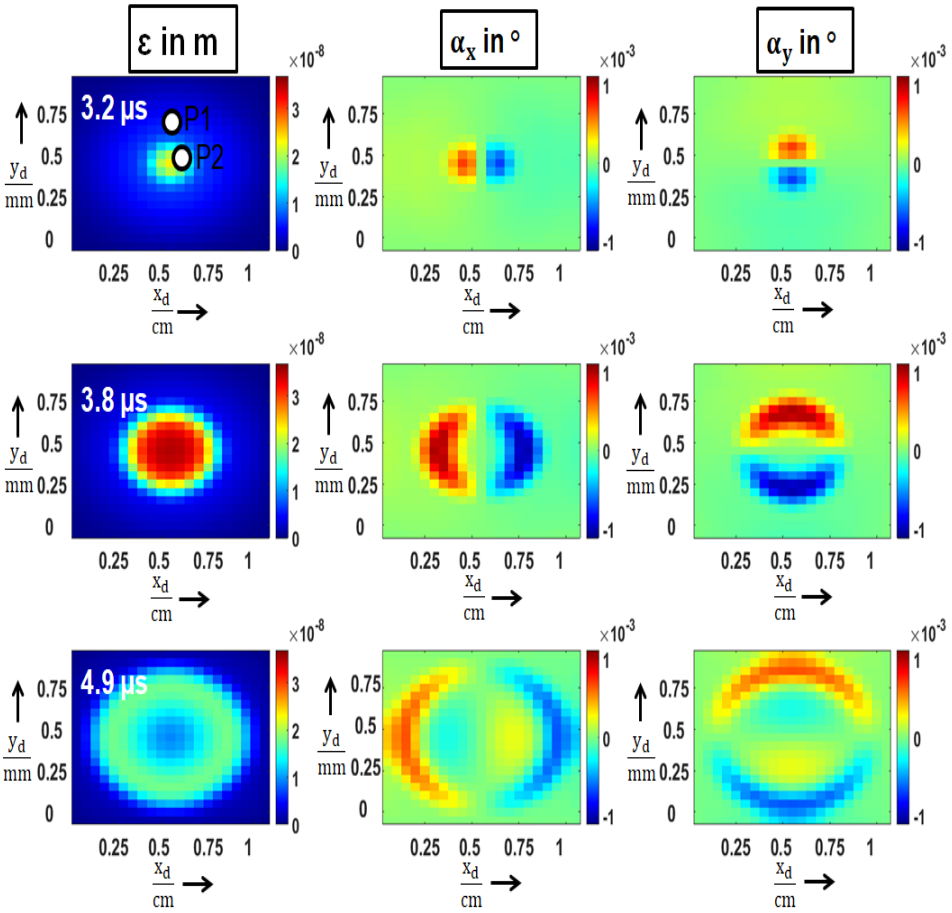

Figure 52: The axial surface deformation ϵ together with the corresponding tilts α_x and α_y are shown for three selected times after the photoacoustic excitation.

In order to investigate the detection capability of these surface tilts, which are smaller than 0.001°, it is necessary to analyse the temporal surface tilts $\alpha(t)$ for two specific points (P1, P2) inside the detection area. Figure 53 shows $\alpha(t)$ for P1 and P2 which are marked in fig. 52. For each point there is a surface tilt exactly when the photoacoustic signal deforms the surface. For P1 the maximal tilt values are: 0.00018° (α_x) and 0.0009° (α_y). For P2 the maximal tilt values

are: 0.0006° (α_x) and 0.0006° (α_y). The sampling rate of 820 kHz for the camera results in a time interval of 1.2 µs between the image frames. Since the speckle-sensing algorithm compares each speckle image with the speckle image before (eq. (11)), it is necessary to compute $\Delta\alpha$. As the tilt approximately equals zero 1.2 µs before each peak for P1 and P2 in fig. 53, the maximal tilt values for α_x and α_y correspond exactly to $\Delta\alpha_x$ and $\Delta\alpha_y$ in this case. According to eq. (10), the tilt values lead to a subjective speckle movement of 180 µm (0.00018°), 900 µm (0.0009°) and 600 µm (0.0006°) when assuming M=2 and Z=0.5 m. The shift detection accuracy of the speckle-sensing system is determined at 0.05×pixel size. Thus, each of these movements can be detected with a high-speed camera with a pixel size of 28 µm.

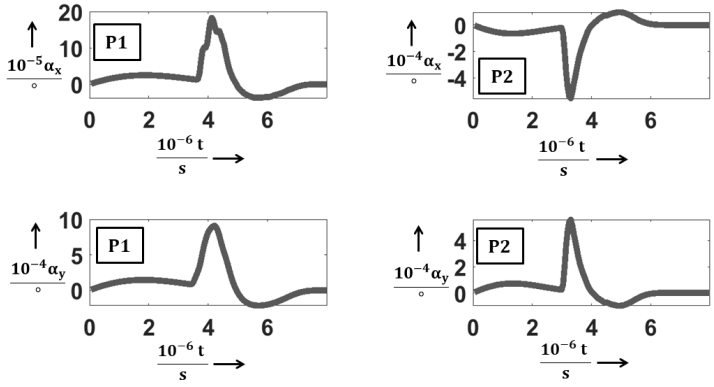

Figure 53: The temporal surface tilts in horizontal and vertical direction (α_x, α_y) of the locations P1 and P2 which are marked in fig. 52 are displayed.

5.2 Remote photoacoustic sensing using a high-speed camera

After the previous simulative results, this section shows and discusses the results of the experimental investigation of H2 and H3. These two hypotheses are treated in a single section since the same imaging unit is used for both. The evaluations are based on raw data that has already been used and published. In [P2] the free-space speckle-sensing results were published. In [P3] the fiber-based results were shown. Figure 54 illustrates H2/H3, their subdivison and the structure of the results. The results for the free-space speckle-sensing are treated before the results for the fiber-based speckle-sensing approach which prove the endoscopic usability of the speckle-sensing approach. For both cases, transmission-mode and reflection-mode measurements on PVCP phantoms and ex-vivo samples are shown and verified by contact transducer measurements.

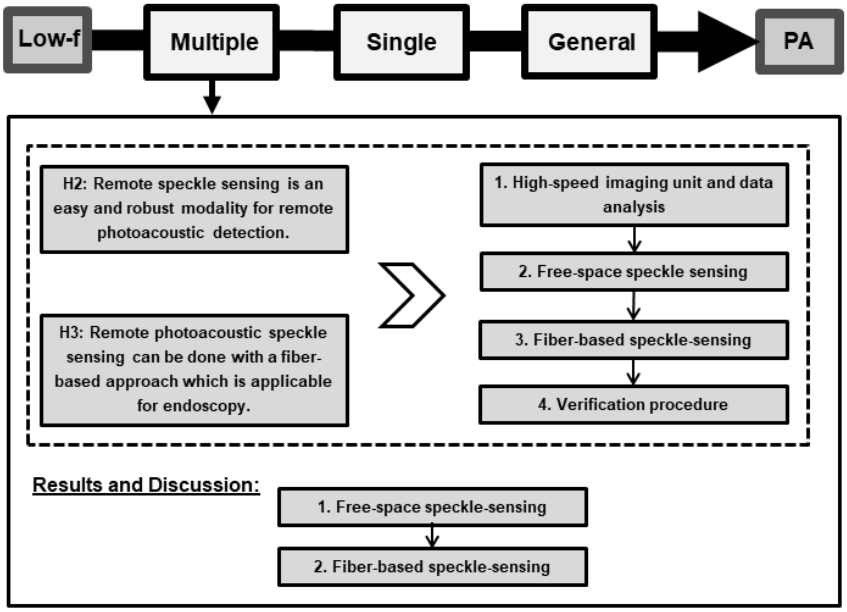

Figure 54: H2, H3, their subdivision and the structure of the corresponding result sections are illustrated.

5.2.1 Free-space speckle-sensing

5.2.1.1 Transmission-mode

Phantom Measurements The first experiments are performed on the optical phantoms made of PVCP. The photoacoustic measurements are done in transmission-mode: Photoacoustic excitation and remote detection take place on opposite phantom sides. Figure 55 shows measurement results of the three phantoms. The detection time of the first peak in the temporal vibration profile of the surface and in the verification measurements using the ultrasound transducer is marked with a black circle. The initial surface

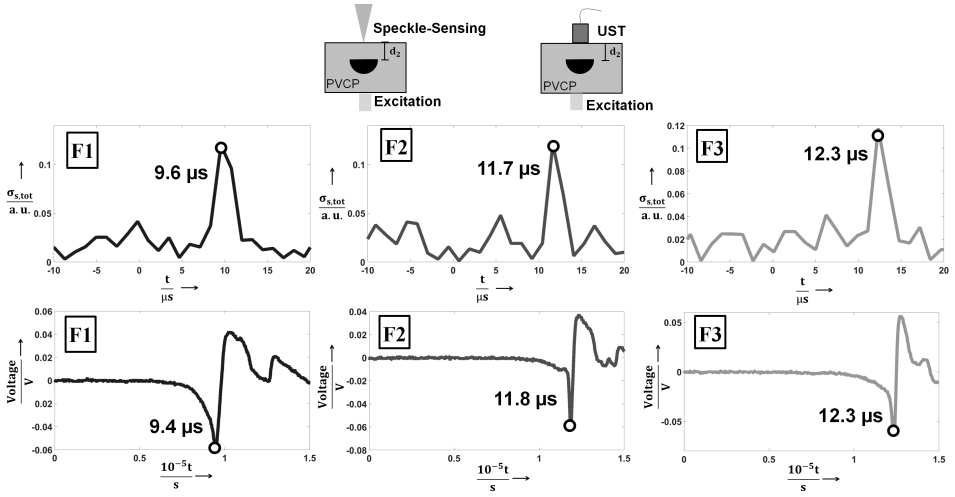

Figure 55: The temporal vibration profiles of the phantom surfaces measured in transmission-mode using speckle-sensing are shown in the upper row. The lower row displays the verification measurements using the ultrasound transducer (UST). Negative time points are related to measurements before the photoacoustic excitation. For the three samples, the detection times of the initial generated photoacoustic signal are noted and the corresponding signal peaks are marked.

expansion after the photoacoustic excitation results in a positive pressure on the piezo-element of the transducer which is related to a negative voltage signal as seen in fig. 55. The first minimum of the ultrasound transducer data is used for comparison since it corresponds to a positive surface deformation resulting in a detectable tilt α by the speckle-analysis.

For each phantom, the acquisition time of the photoacoustic signal by speckle-analysis corresponds to the verification measurements taking into account the measurement uncertainty. This uncertainty can be explained by the low sampling rate of 823500 frames per second for photoacoustic measurements. This sampling rate leads to a time resolution of 1.2 µs which is not sufficient

for precise photoacoustic sampling. As explained in the state of art, MHz sampling rates and thus sub-μs temporal sensing is required for high-resolution photoacoustic sensing. However, the sampling rate of the used high-speed camera is high enough for the feasibility study of the new photoacoustic detection modality and it needs to be mentioned that this thesis also investigates a faster sensing approach that provides better temporal resolution. It is therefore accepted that the temporal sensing resolution of 1.2 µs results in an approximate error of 0.6 µs for photoacoustic signal detection with the high-speed camera. For the phantoms F1-F3 the acquisition times increase as expected with increasing acoustic travel distance d_2 as follows: 9.6 µs, 11.7 µs and 12.3 µs. By using the speed of sound in PVCP (1330 $\frac{m}{s}$), an acoustic travel distance of 12.8 mm is calculated which matches d_2 for phantom F1 (see fig. 23). For phantom F2 and phantom F3 the acoustic distances 15.6 mm and 16.4 mm can be computed accordingly which is again in agreement to the phantom dimensions considering the uncertainty in the measurements. Figure 56 shows the mean value for all photoacoustic acquisition times using speckle analysis, its standard deviation, the times for the corresponding ultrasonic transducer detection and the theoretical acoustic transit time t_t. It is clearly visible that the detection times of the transducer (see fig. 55)

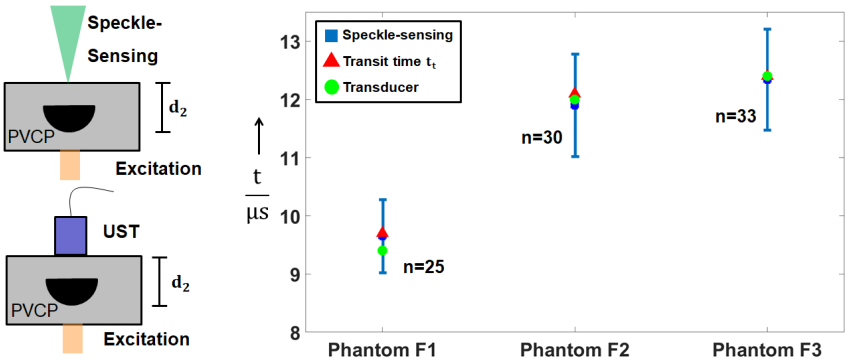

Figure 56: Statistical analysis for the transmission-mode measurements: Mean and standard deviation for the photoacoustic detection times using speckle-analysis. The state of the art measurements and theoretical transit times match the time interval for speckle-sensing.

match the time intervals defined by the speckle-sensing technique. For phantom F1 through F3, the values are as follows: 9.65 µs±0.63 µs, 11.9 µs±0.88 µs, 12.3 µs±0.87 µs, respectively. The small differences between the different acquisition times can be explained with a slight misalignment of the CW illumination spot or the transducer from the central phantom axis. This leads to different distances between the location of the initially generated acoustic signal and the illumination point or transducer on the surface. This in turn

results in slightly different detection times. The standard deviation for the speckle-analysis detection is as previously explained in the expected range of 0.6 µs.

Ex-vivo Measurements The ex-vivo sample is also analysed in transmission-mode. The average detection time for the photoacoustic signal is 5.73 µs. Since the acoustic signal passes fat tissue and also PVCP, an average speed of sound of 1400 $\frac{m}{s}$ can be assumed here. A value of 8.0 mm for d_2 can be reconstructed. This reconstruction does not match the geometrical distance for d_2 of 7.0 mm. The transducer measurement shows the corresponding pressure peak at 5.2 µs which matches the phantom geometrical dimensions. The transducer data shows a second signal peak at 7.4 µs which is related to a laser induced ultrasound (LIU) signal generated at the surface where the short laser pulse hits the tissue. This detection time matches the measured ex-vivo phantom height of 10.4 mm using c=1400 $\frac{m}{s}$. A further experiment is done in order to exclude that the measured signal using speckle-sensing is not the LIU generated at the phantom surface where the laser is coupled into the phantom. To do so, the surface opposite to the speckle-sensing surface is marked by using a black spray. This leads to a high absorption of the laser pulse directly at the surface and generates a strong acoustic signal here. In total three measurements are analysed and an average arrival time for the initial acoustic signal is measured at 8.2 µs using speckle-sensing. Figure 57 shows transducer signals for the unmarked and marked sample surfaces together with the mean detection times. It is

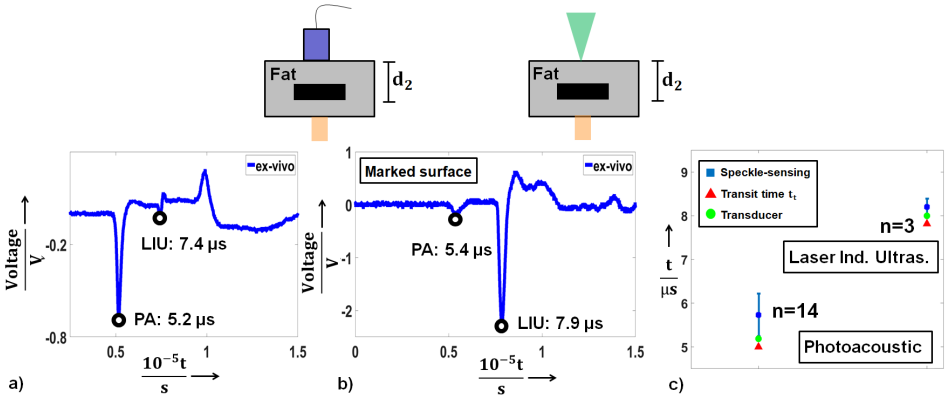

Figure 57: a,b) The ultrasound transducer measurements in transmission-mode are shown with the corresponding detection times of the photoacoustic and LIU signal. b) For the marked surface, the LIU signal is stronger than the photoacoustic signal. c) Mean detection times using speckle-sensing and its standard deviation for the photacoustic signal and for the LIU signal at the phantom surface.

visible in the transducer data that the laser induced signal at the surface increases at the costs of the photoacoustic signal for the marked surface due to the high absorption of the spray. For these ex-vivo experiments, the mean detection times for the speckle-analysis are not in complete agreement to the transducer data and the theoretical transit time. This effect can be explained by two reasons: tissue deformation and misalignment during the experiment. Deformation of the fat tissue can lead to different geometrical distances between absorber and detection surface and thus change the detection time. Slight misalignment of the CW illumination spot from the central phantom axis might furthermore increase the detection time for the speckle-sensing approach. In addition to these explanations, the verification measurements are very close to the remote measurements and there is the same behaviour for both experiments. Moreover, the influence of the LIU is excluded since it could be separated from the photoacoustic signal. These facts in total result in a successful verification for the ex-vivo measurements.

5.2.1.2 Reflection-mode

The optical phantoms and the ex-vivo sample are also measured in reflection-mode. Figure 58 shows the mean value and standard deviation for the photoacoustic signals using the speckle-analysis, the calculated detection time t_t using d_1 and the speed of sound. For the phantom F3 and the ex-vivo

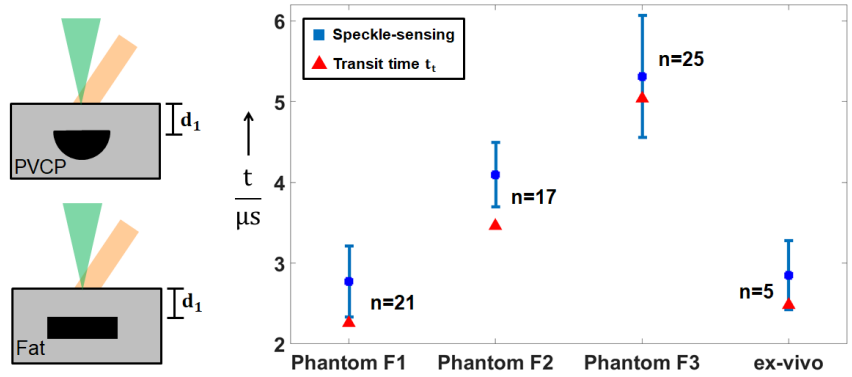

Figure 58: Mean detection times using speckle-sensing and its standard deviation for the photoacoustic measurements in reflection-mode. The theoretical acoustic transit time of the photoacoustic signal is used for verification.

sample, t_t matches the speckle-sensing results. For these samples, the mean times, standard deviations and t_t are the following: 5.31 µs±0.76 µs (5.04 µs), 2.85 µs±0.43 µs (2.48 µs). For the phantoms F1 and F2, t_t does not fall inside the speckle-sensing time interval: 2.77 µs±0.44 µs (2.26 µs), 4.1 µs±0.4 µs (3.46 µs). This mismatch together with the trend that the mean for the

speckle-sensing detection time is later than the estimated detection time for all samples can be explained with the parameter t_t. The estimated detection time t_t is calculated using d_1 which is the shortest distance between the sample surface and the absorber. In reality, light scattering leads to photoacoustic signal generation at locations at the absorber which have a larger distance to the detection spot of the sample surface than d_1. This leads to a later detection time using the speckle-sensing technique. Furthermore, manufacturing and measuring errors during the phantom manufacturing process might influence the phantom geometries and thus t_t. In addition, the ex-vivo tissue may have been deformed during experimental handling. The impact of these effects can be estimated geometrically for photoacoustic excitation of flat absorber surfaces. Figure 59 shows the maximal enlarged acoustic transit distance d_3 due to scattering of the excitation light for a central position of the CW-illumination. It gets obvious that this enlarged acoustic transit

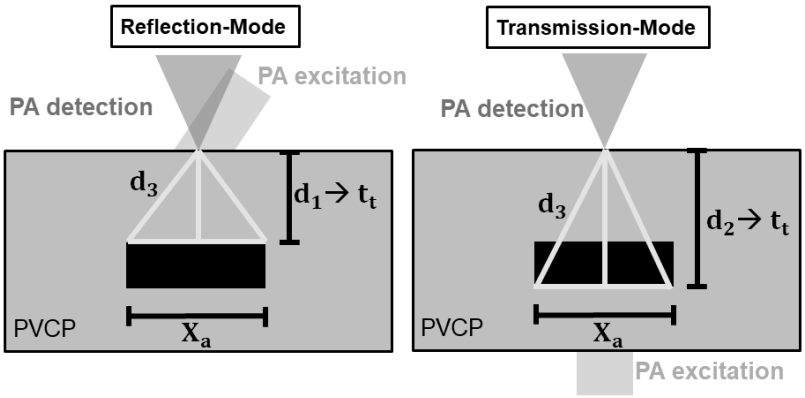

Figure 59: Geometrical explanation of the photoaocustic detection time increase compared to the assumed acoustic transit time t_t for reflection-mode and transmission-mode. Light scattering and alignment errors result in acoustic signal generation at the flat absorber surface which leads to an increased acoustic transit time d_3.

time has an impact on the detection time for flat absorber surfaces. With the geometrical relation shown in fig. 59 the ratio $X_{max}=\frac{d_3}{d_{1/2}}=\frac{1}{d_{1/2}}\sqrt{d_{1/2}^2+(\frac{X_a}{2})^2}$ is defined which describes the maximal increase of the acoustic transit time due to light scattering. The parameter X_a describes the absorber width. Since X_{max} describes the maximal increase some further effects need to be taken into account for determining the realistic ratio X_{real}. The parameter X_{max} neglects attenuation and does thus not consider the spatial dimensions of the CW-illumination for speckle generation and since the absorbers are big compared to the scattering width of the PA excitation light, the realistic ratio X_{real} is estimated with $X_a=\frac{X_a}{4}$. X_{real} can be compared to the ratio between the

mean speckle detection time and t_t (in brackets) for the three phantoms F1-F3: 1.24 (1.23), 1.11 (1.18), 1.05 (1.05). It gets obvious that the ratios are similar and thus the scattering has an significant effect on the detection time. In addition, the trend of decreasing mismatch between detection time and t_t for increasing absorber depth d_1 is correctly estimated. This can be explained with the geometrical relation in fig. 59. For a constant absorber size, the difference between d_3 and $d_{1/2}$ gets smaller for increasing $d_{1/2}$. The mentioned errors for measurement and the described geometrical error estimation hold for the following measurement results of the fiber-based phantom measurements with the high-speed camera.

Based on the repeatability, the successful separation from LIU and verification of the transmission-mode and reflection-mode measurements, it can be concluded that speckle-sensing is a reliable, easy and robust technique for the photoacoustic detection on phantoms which mimic optical and mechanical properties of tissue and ex-vivo samples. For the transmission-mode measurements it was even possible to compare the new detection technique to the state of the art detection modality by placing transducer on the sample surface. This, however, is not possible for the reflection-mode experiments since the transducer would make an optical excitation at the same surface side impossible. However, the detection times for the reflection-mode experiments match the theoretical transit times and allow therefore verification. Especially the proof of concept for the reflection-mode setup on biological tissue is an essential step towards a future application of the technique for example in wound imaging or as a laser surgery feedback system. For these possible applications, the excitation and remote sensing must also be performed on the same tissue side.

5.2.2 Fiber-based speckle-sensing

5.2.2.1 Transmission-mode

Figure 60 shows the measurement results for the three phantoms and the ex-vivo sample: The mean value for the photoacoustic detection time by speckle-sensing, the transducer detection time and the theoretical acoustic transit time. It is clearly visible that the ultrasound transducer times match the time intervals which are defined by the speckle approach. For phantom E3 and the ex-vivo sample, t_t falls also into this interval. The deviation for t_t and the mean detection time for the phantoms E1-E3 are as previously explained expected. For phantom 1 through 3, the speckle-sensing values and transducer times are as follows: 5.21 µs±0.47 µs (5.05 µs), 5.85 µs±0.36 µs (5.98 µs), 6.74 µs±0.46 µs (6.97 µs). For the ex-vivo tissue sample, the signal is detected at 7.1 µs±0.46 µs (7.02 µs).

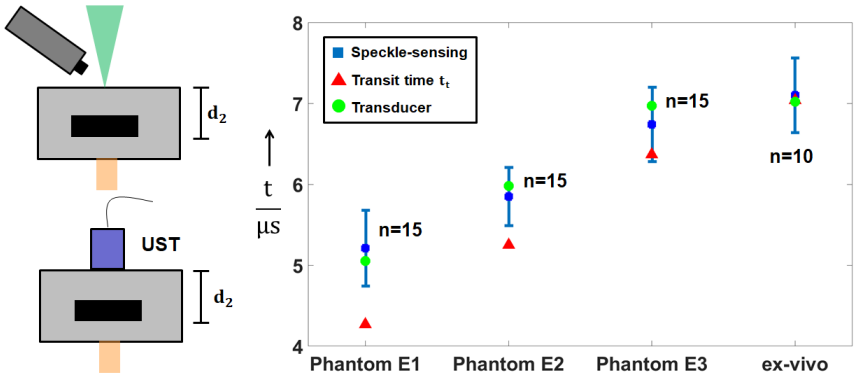

Figure 60: Mean detection times using speckle-sensing and its standard deviation for the transmission-mode photoacoustic measurements using an imaging fiber bundle. The theoretical transit time of the photoacoustic signal and transducer measurements are used for verification.

5.2.2.2 Reflection-mode

Figure 61 shows the mean acquisition times, their standard deviation and the theoretical transit time t_t of the acoustic signal at the sample surface. For phantom E1 to E3 the acquisition times are as follows: 1.94 µs±0.35 µs,

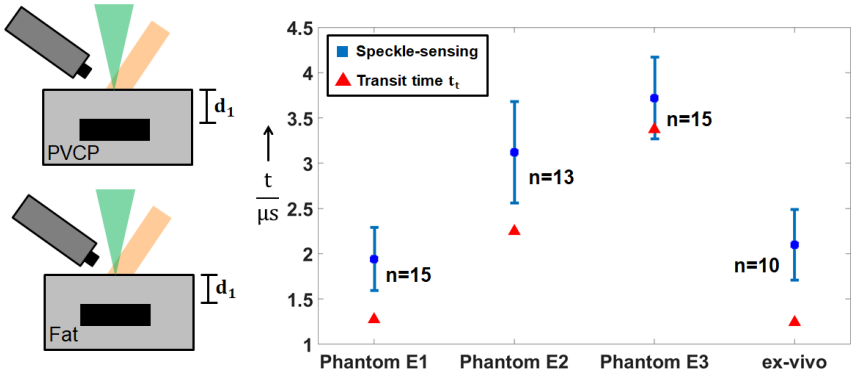

Figure 61: Mean detection times using speckle-sensing and its standard deviation for the reflection-mode photoacoustic measurements using an imaging fiber bundle. The theoretical transit time of the photoacoustic signal is used for verification.

3.12 µs±0.56 µs, 3.72 µs±0.45µs. For the ex-vivo sample the signal is detected at 2.1 µs±0.39 µs. The calculated recognition times t_t, for phantom 1 to 3 and the ex-vivo sample are as follows: 1.27 µs, 2.25 µs, 3.37 µs and 1.24 µs. For phantom E3, it can be clearly seen that the calculated detection time corresponds to the speckle-sensing time interval. For the other samples, t_t does not lie inside this interval. In general t_t is smaller than the mean detection time

for the phantoms which can be related to the previously explained measurement errors. Based on the repeatability and successful verification of the transmission-mode and reflection-mode measurements, it can be concluded that fiber-based speckle-sensing is a reliable technique for the photoacoustic detection on phantoms which mimic optical and mechanical properties of tissue and ex-vivo samples. Since the used imaging fiber fits into an endscopic working channel, the demonstrated measurements prove the applicability of the speckle-sensing technique for endoscopy. In particular, the proof of concept for the reflection-mode setup on biological tissue is an essential step towards the future application of the technique in an endoscopic imaging device or as a smart feedback system for minimally invasive laser procedures. For these possible applications, the excitation and remote sensing must also be performed on the same tissue side.

The main disadvantages of this feasibility study are the high exposure and low sampling rate. The combined exposure due to the CW-illumination and short pulse excitation is above the MPE for PA. However, the exposure could easily be reduced by pulsed speckle generation since it is sufficient to illuminate only during the photoacoustic measurement time. For the shown experiments, it would be enough to illuminate only during 15 µs after short pulse excitation and therefore a significant exposure reduction could be achieved. This pulsed speckle generation by a pulsed laser diode allowed a total exposure below the MPE for soft tissue for additional experiments of the author [P4]. In addition to this solvable issue, the used camera sampling rate is too low for precise sensing. In general, the sampling rate for photoacoustic signal detection is several megahertz (MHz). However, there is no camera available that can provide this high acquisition rate for remote photoacoustic detection using speckle-sensing. The camera used in this work (Vision Research, Phantom v1210) is one of the fastest high-speed cameras available at the moment and offers 823500 frames per second at a resolution of 128×16 pixels. This sampling rate is high enough to prove the concept of remote photoacoustic signal acquisition by speckle-analysis. However, a faster optical detection system is required for more precise signal acquisition.

5.3 Remote photoacoustic sensing using a low-resolution diode array

In this section, the results of the investigation of H4 which treats the usability of a faster sensing system and single speckle-sensing are shown and discussed. First, measurement data for Ph1-Ph3 are shown. Second, the mean photoacoustic detection times in transmission-mode and reflection-mode are analysed and compared to the theoretical detection times. The shown results have already been published by the author in [P4]. Figure 62 summarizes H4, its subdivison and the described results structure.

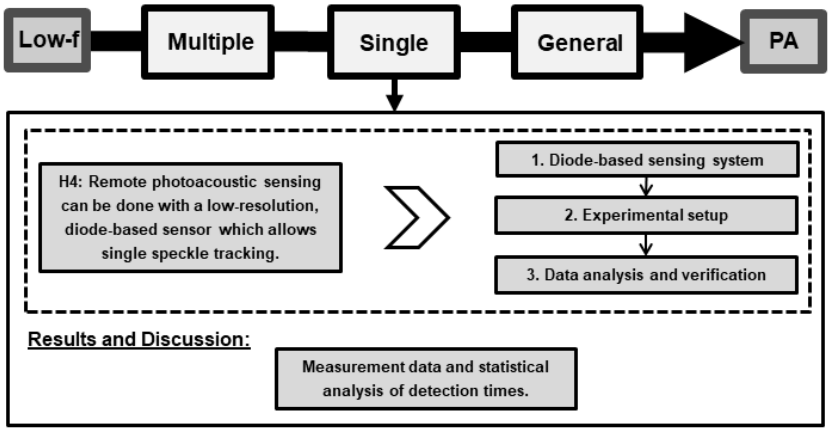

Figure 62: H4, its subdivision and the structure of the corresponding result sections are illustrated.

Figure 63 shows measurement results in transmission-mode of the three phantoms Ph1, Ph2 and Ph3. The speckle coordinates x_{sp}, y_{sp} and the vector length t_{sp} are illustrated which represent temporal vibration profiles of the surface under investigation. The detection time of the first peak in these profiles is marked with a black circle, because this time point corresponds to the photoacoustic signal. Compared to the shown results for the high-speed camera, these measurements provide an increased temporal resolution. For the phantoms Ph1-Ph3 the acquisition times increase as expected with increasing acoustic travel distance d_2. Considering t_{sp}, the acquisition time increases as follows: 3.13 µs, 3.63 µs and 4.38 µs. By using the speed of sound ($1330\,\frac{m}{s}$), the following acoustic travel distances are calculated: 4.163 mm, 4.828 mm and 5.825 mm. Thus, for each phantom, the acquisition time of the photoacoustic signal by speckle-analysis corresponds to the geometrical phantom dimensions (d_2: 4 mm, 5 mm, 6 mm) taking into account the measurement errors.

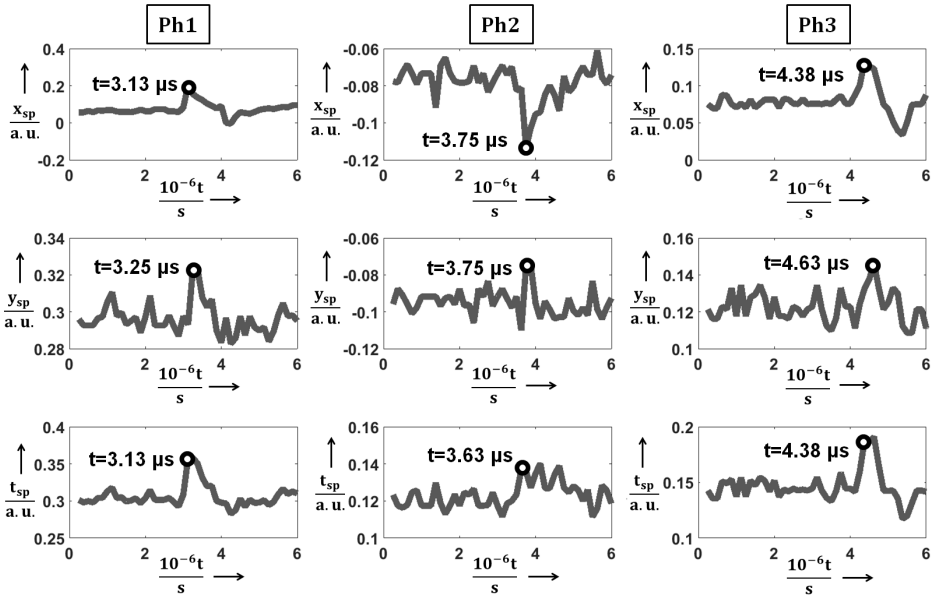

Figure 63: The speckle coordinates x_{sp}, y_{sp} and the vector length t_{sp} are illustrated for measurements of phantoms Ph1-Ph3. For the three samples, the detection times of the initial generated photoacoustic signal are noted and the corresponding signal peaks are marked.

Figure 64 shows the mean value for all photoacoustic acquisition times in transmission-mode considering t_{sp}, its standard deviation and the theoretical acoustic transit time t_t. For phantom Ph1 through Ph3, the values are as follows (t_t in brackets): 3.19 µs±0.06 µs (3.01 µs), 3.71 µs±0.09 µs (3.76 µs), 4.48 µs±0.17 µs (4.51 µs). It is clearly visible that the speckle-analysis mean detection times increase with bigger phantom dimensions and that they match to the acoustic transit times. The low standard deviations prove the repeatability and the fact that single speckle-sensing allows precise photoacoustic sensing compared to the high-speed camera experiments. The standard deviation is in the range of approximately 0.1 µs which results in a precision of 0.13 mm considering the speed of sound.

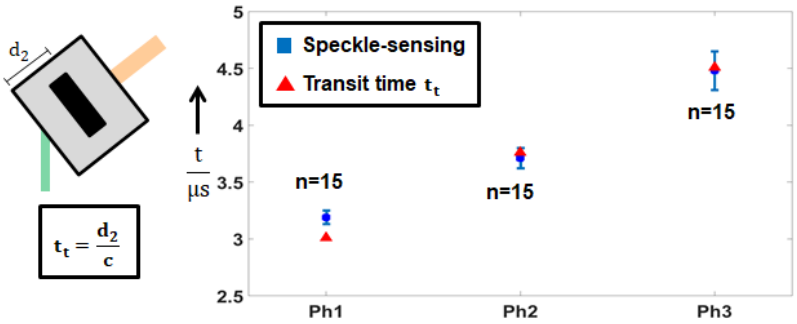

Figure 64: Mean detection times (t_{sp}) and its standard deviation for the transmission-mode photoacoustic measurements. The theoretical transit time of the photoacoustic signal is used for verification.

Figure 65 shows the mean value for all photoacoustic acquisition times considering t_{sp} in reflection-mode, its standard deviation and the theoretical acoustic transit time t_t. For the phantoms Ph4 and Ph5, the values are as follows (t_t in brackets): 2.15 µs±0.16 µs (2.26 µs), 2.99 µs±0.06 µs (3.01 µs). It is clearly visible that the speckle-analysis mean detection times increase with bigger phantom dimensions and that they match to the acoustic transit times.

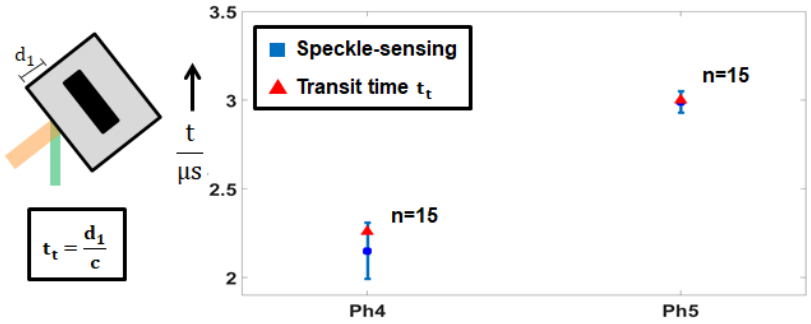

Figure 65: Mean detection times (t_{sp}) and its standard deviation for the reflection-mode photoacoustic measurements. The theoretical transit time of the photoacoustic signal is used for verification.

Figure 66 shows x_{sp}, y_{sp} and the vector length t_{sp} for a measurement of the skin tissue sample. As expected, the photoacoustic detection times match the sample dimensions. The detection time of 7.75 µs results in a transit distance of 10.075 mm which exactly matches the sample height of 10 mm. The mean photoacoustic detection time is consistent with the acoustic transit time: 7.72 µs±0.22 µs (7.69 µs). Based on the repeatability and successful

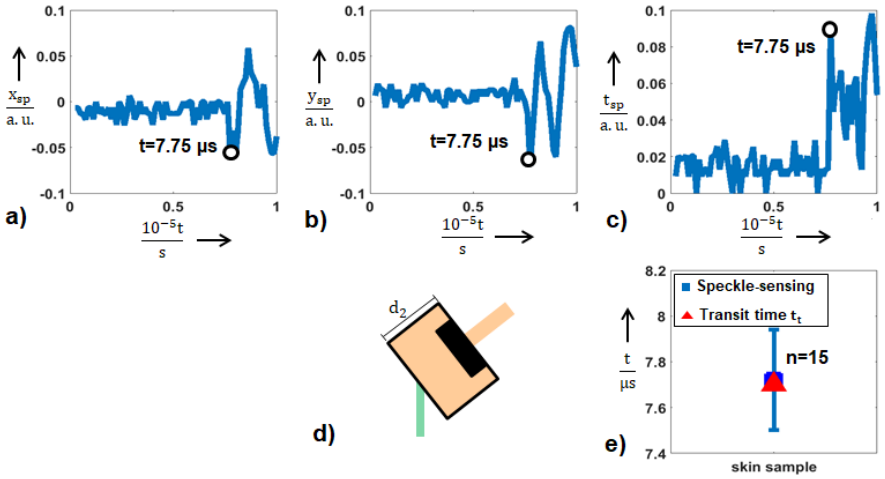

Figure 66: The speckle coordinates x_{sp}, y_{sp} and the vector length t_{sp} are illustrated for a measurement of the skin tissue sample. The detection times of the initial generated photoacoustic signal are noted and the corresponding signal peaks are marked (a,b,c). The measurement setup, mean detection time (t_{sp}), its standard deviation and the theoretical transit time of the photoacoustic signal are shown (d,e).

verification with the theoretical transit time t_t of the transmission-mode and reflection-mode measurements, it can be concluded that single speckle-sensing is a reliable technique for the photoacoustic detection on phantoms and on skin tissue samples. Furthermore, the cheaper low-resolution diode sensor, in contrast to the high-speed camera, reaches a high sampling rate of 8 MHz which allows precise photoacoustic sensing. These facts are essential steps towards the future application of the technique in a photoacoustic imaging systems or as a smart feedback system for laser procedures.

5.4 Automated single speckle tracking for remote photoacoustic sensing

The previous results were acquired by manual speckles identification. Therefore, this section shows and discusses the results of the automatization investigation of H5. Figure 67 illustrates H5, its subdivison and the structure of the results. First, the performance of the automated selection is evalu-

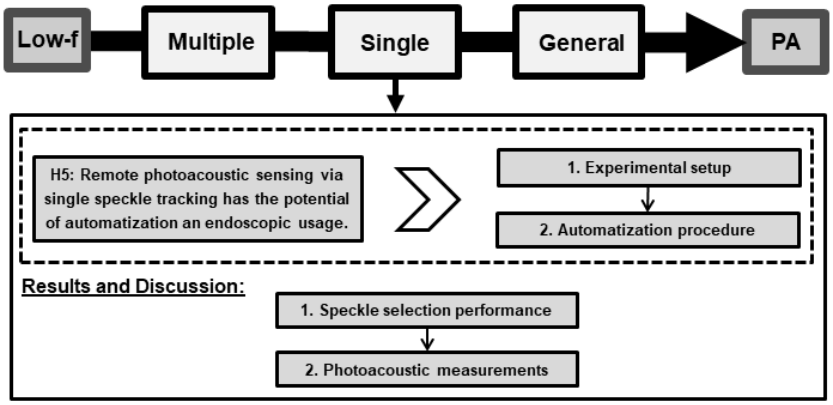

Figure 67: H5 and its subdivision are illustrated.

ated. Second, the results for the photoacoustic measurements are shown and discussed.

5.4.1 Speckle selection performance

In order to evaluate the speckle performance, 18 speckle images of a PVCP surface were analyzed by the algorithm and checked for successful speckle identification [S2]. Figure 68 shows four exemplary speckle images. A green speckle (fig. 68 a: (1)) fulfills all the required criteria (see table 3) whereas a red speckle does not fulfill at least one of the criteria. It gets obvious that the speckle identification algorithm correctly identifies and separates the speckles in the image. Furthermore, not appropriate speckles are excluded for photoacoustic measurement as expected. In 10 of the 18 cases, a suitable speckle for photoacoustic measurement is identified which results in a success probability of 55% for convenient speckle identification of a speckle pattern. This means that in 45% of the cases, a new speckle pattern region needs to be analyzed in order to find a suitable speckle for photoacoustic measurement. This could be achieved in future by moving the imaging fiber bundle in lateral directions in order to image and analyze a different speckle pattern area. This step was not implemented for the speckle identification

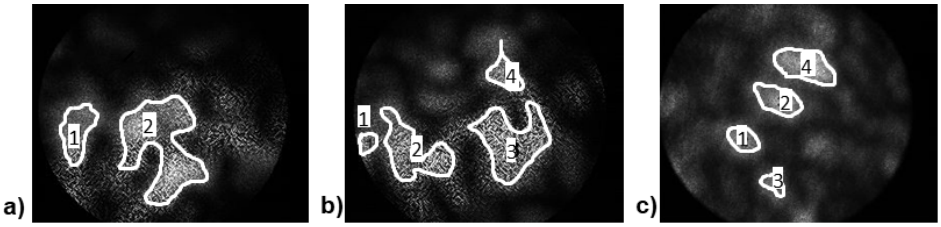

Figure 68: Three exemplary speckle images are shown (a,b,c). For one image (a), an appropriate speckle is marked green (1) since it fulfills the defined criteria (a). For the other two images, the identified speckles are not valued as suitable since they do not fulfill all defined criteria (b,c).

procedure in this thesis, however, it could easily be integrated in future to ensure fully automated and reliable speckle identification for photoacoustic measurement.

5.4.2 Photoacoustic measurements

Figure 69 shows the mean values for the photoacoustic acquisition times considering t_{sp}, their standard deviation and compares them to the theoretical transit time t_t. For the phantoms PhA1 and PhA2, the values are as follows (t_t

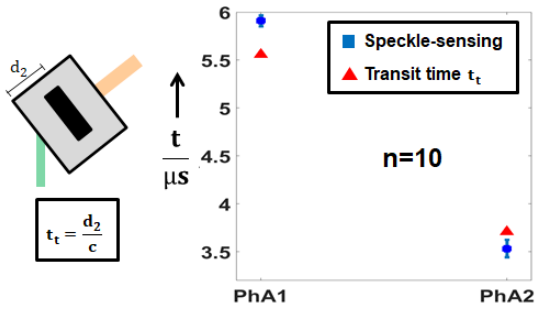

Figure 69: Mean detection times (t_{sp}) and its standard deviation for the measurements are shown. The theoretical transit time of the photoacoustic signal is used for verification.

in brackets): 5.91 µs±0.057 µs (5.56 µs), 3.53 µs±0.093 µs (3.71 µs) detection surface. Since the measurement results match to the acoustic transit times considering the measurement errors, it can be concluded that automated single speckle-sensing reliably detects the photoacoustic signal.

5.5 Evaluation of remote speckle-analysis for photoacoustic detection

In this section, the results of H6 which treats the general comparison of multiple- and single speckle-analysis are shown and discussed. Figure 70 illustrates H6 and the structure of the results section. First, the sensitivity

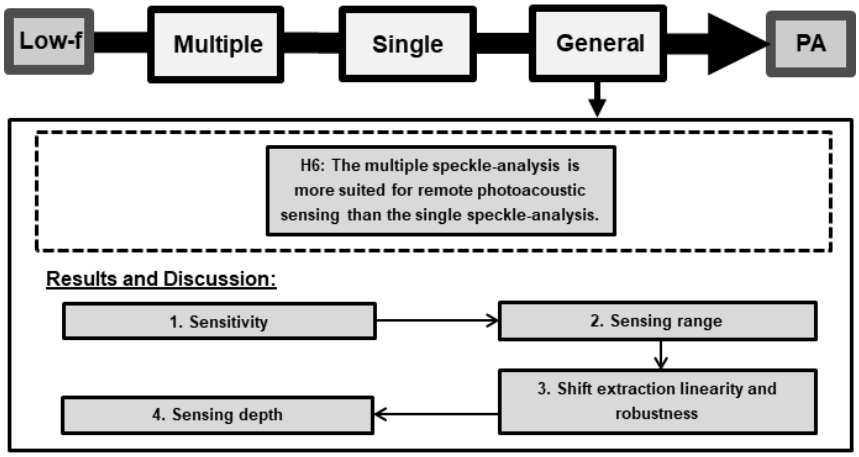

Figure 70: H6, and the structure of the corresponding result section are illustrated.

results for the established sensing systems in this work are shown and compared to literature. Second, the sensing ranges for multiple speckle-sensing and single speckle-sensing are discussed. Third, the results of the simulations regarding the shift extraction linearity are presented. Fourth, the phantom properties are compared to tissue and pressure computations with a realistic tissue model are carried out for the sensing depths determination.

5.5.1 Sensitivity

Table 4 summarizes the relevant parameters for the determination of $S_{d,nm}$ for the established sensing systems and sensing surfaces in this thesis. It gets obvious, that the speckle shift extraction precision is not noise-limited, but algorithm limited for the high-speed camera system: $0.05 > \sigma_{nf}$. Furthermore, the noise is lower for the diode sensing system as a result of the bigger pixels which allows the detection of more photons.

Table 4: Relevant parameters for $S_{d,nm}$ for the established sensing systems.

	high-speed camera			
	free-space		fiber-guided	
	PVCP	fat	PVCP	fat
σ_{prec}	$0.05 d_{px}$	$0.05 d_{px}$	$0.05 d_{px}$	$0.05 d_{px}$
σ_{nf}	0.017	0.015	0.008	0.012
d_{px} in μm	28	28	28	28
M	10	10	25	25
Z in cm	5	5	0.7	0.7
$S_{d,\alpha}$ in $10^{-5\circ}$	16.04	16.04	114.59	114.59
D_{ill} in mm	0.3	0.3	0.3	0.3
$S_{d,nm}$ in nm	0.84	0.84	2.4	2.4
	diode array			
	free-space		fiber-guided	
	PVCP	skin	PVCP	
σ_{prec}	-	-	-	
σ_{nf}	0.006	0.007	0.0057	
d_{px} in μm	1600	1600	1600	
M	5	5	50	
Z in cm	20	20	0.2	
$S_{d,\alpha}$ in $10^{-5\circ}$	55.0	64.2	522.54	
D_{ill} in mm	0.75	0.75	0.05	
$S_{d,nm}$ in nm	7.2	8.4	4.56	

Table 5 summarizes S_d and the relevant parameters for its calculation for the detection systems in this thesis according to eq. (19). To compare, f is selected at 410 kHz for all systems and in addition to 1 MHz for the diode system. It gets obvious that the high-speed camera measurements are more sensitive in comparison to the diode sensing system. This can be explained by the larger pixel size and illumination diameter which result in bigger values for $S_{d,\alpha}$ and $S_{d,nm}$ for the diode system. However, optimization of these parameters might improve the sensitivity in the case of the diode system.

Table 5: Relevant parameters for the determination of S_d for the established sensing systems. The values of $S_{d,1MHz}$ for the high-speed camera are in brackets since the system frame rate does not allow the detection of a 1 MHz acoustic wave.

	high-speed camera			
	free-space		fiber-guided	
	PVCP	fat	PVCP	fat
$S_{d,nm}$ in nm	0.84	0.84	2.4	2.4
Z_{ac} in $10^6 \frac{kg}{m^2 s}$	1.4	1.38	1.4	1.38
$S_{d,410kHz}$ in kPa	1.51	1.49	4.33	4.27
$S_{d,1MHz}$ in kPa	(3.69)	(3.64)	(10.56)	(10.41)
	diode array			
	free-space		fiber-guided	
	PVCP	skin	PVCP	
$S_{d,nm}$ in nm	7.2	8.4	4.56	
Z_{ac} in $10^6 \frac{kg}{m^2 s}$	1.4	1.99	1.4	
$S_{d,410kHz}$ in kPa	12.98	21.53	8.22	
$S_{d,1MHz}$ in kPa	31.67	52.52	20.06	

When comparing the technique to literature, S_d of the high-speed camera system is calculated at 1 MHz (see table 5). Horstmann et al. reached with a full-field speckle interferometry approach the following sensitivity parameters: $S_{d,nm}$=1 nm and S_d=1.5 kPa with a sensing bandwidth of 80 MHz [75]. These values however were achieved for measurements on silicone that has a lower impedance ($0.94 \times 10^6 \frac{kg}{m^2 s}$) than PVCP which results in low S_d. According to table 4 and table 5, the high-speed camera sensing system in this thesis achieves a similar performance. Nevertheless, it needs to be noted that in this thesis the maximal camera frame rate of 820 kHz is the limiting factor for the sensing bandwidth. Even so, the sensing bandwidth could be improved by repeated photoacoustic excitation and time gated speckle detection at costs of increased total acquisition time. This effect, however, is not expected to reduce $S_{d,\alpha}$ and therefore not S_d since the speckle shift extraction is limited to the algorithm precision at $\frac{1}{20} d_{px}$. Other groups even reached smaller sensitivities with other interferometric detection approaches:

- Laufer et al. (Fabry-Pérot cavity) [101]: $S_{d,nm}$=0.13 nm, $S_{d,1MHz}$=200 Pa

- Rousseau et al. (confocal Fabry-Pérot interferometry) [76]: $S_{d,nm}$=0.8 pm, $S_{d,1MHz}$=1 Pa
- Speirs and Bishop (Michelson Interferometer) [71]: $S_{d,nm}$=0.5 nm, $S_{d,1MHz}$=750 Pa
- Carp and Venugopaplan (Doppler Interferometer) [77]: $S_{d,nm}$=0.1 nm, $S_{d,1MHz}$=150 Pa

These lower sensitivities can be explained by the usage of spot detection by diodes for the interferometric approaches. These diodes are bigger than the high-speed camera pixel and detect thus more photons which results in a lower noise and thus better sensitivity. However, as explained in the state of the art, their setups are more complicated than the applied speckle-analysis in this thesis. In addition, the speckle-analysis sensitivity might even be improved by the usage of a high-speed camera with smaller, more sensitive pixels and tighter focusing of the CW illumination.

Piezo contact transducers, which are especially designed and optimized for broadband PA detection, achieve high sensitivities which are dependent on the size and detection bandwidth. For a detection of acoustic frequencies in the range of 10 MHz to 50 MHz with an element size of 30 mm², S_d can be estimated to lie between 1.5 Pa and 3.5 Pa [63]. Arrays have a smaller active area per detector element and thus lower sensitivity. An optimized ultrasonic line array can have a sensitivity of 110 Pa for a single element [64]. According to these numbers, the speckle-analysis sensitivity shown in this work is approximately a factor of 1000 worse than the state of the art technique.

5.5.2 Sensing range

In order to extract the speckle shift between the high-speed camera video frames, eq. (11) is applied for the multiple speckle-analysis. The speckle shift in horizontal (x_{s0}) and vertical sensor direction (y_{s0}) are computed by interpolation in regard to the sensor center. Thus the magnitude for the maximal speckle shift is equal to half the horizontal/vertical sensor size (w_{px}, h_{px}) in pixel. This maximal speckle shift therefore defines α_{max}. The single speckle-analysis tracks the centre of mass of a single speckle which is positioned in the center of the four measurement diodes (eqs. (16) and (17)). In general, the maximal detectable centre of mass coordinates ($x_{sp,max}$, $y_{sp,max}$) are defined by the single speckle diameter l_s and the diode size (d_{px}) by eq. (25).

$$x/y_{sp,max} = (1 - \frac{l_s}{2d_{px}})d_{px} \tag{25}$$

For a larger speckle shift in regard to the sensor center, the single speckle would not completely be on the sensor which leads to measurement errors. The maximum allowable speckle diameter is defined by twice the diode size. Larger speckles cannot be covered completely by the four diode sensor and therefore their movement could not be sensed properly. When assuming a speckle diameter of the pixel size, the maximum detectable centre of mass coordinates ($x_{sp,max}$, $y_{sp,max}$) are thus half the diode size.

Figure 71 illustrates the sensing ranges for the two data analysis methods.

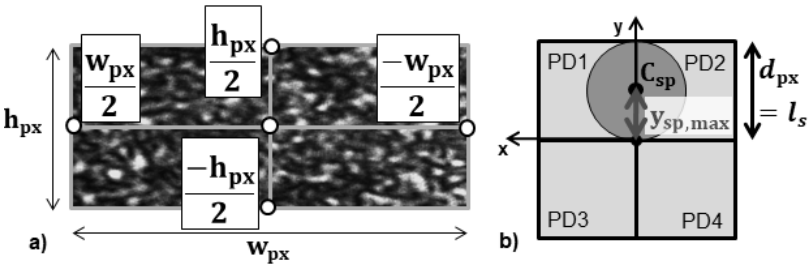

Figure 71: The sensing ranges for the two shift extraction methods are illustrated: multiple speckle-sensing (a) and single speckle-analysis (b). For the multiple speckle-analysis, the maximal detectable shifts are defined by the resolution of the video images. For the single speckle-analysis, the maximal detectable shift in vertical direction is shown for d_{px}=l_s.

Table 6 gives an overview on the maximal detectable tilts in horizontal and vertical direction ($\alpha_{max,x}$, $\alpha_{max,y}$) for the sensing methods in this thesis. Similar to the sensitivity calculations , $\alpha_{max,x}$ / $\alpha_{max,y}$ can be computed with x_{s0}=$\frac{w_{px}}{2}d_{px}$ / y_{s0}=$\frac{h_{px}}{2}d_{px}$. For the single speckle-analysis, $x/y_{sp,max}$ is determined according to eq. (25) with l_s=0.6d_{px}.

Table 6: Overview on sensor size, speckle shift extraction and surface tilt sensing ranges for multiple speckle-sensing and single speckle-sensing.

	multiple speckle	single speckle
$h_{px} \times w_{px}$	16x128	2x2
d_{px} in μm	28	1600
$x_{s0,max}$ | $y_{s0,max}$ in μm	224 | 1792	-
$x_{sp,max}$ | $y_{sp,max}$ in μm	-	1120 | 1120
$\alpha_{max,x}$ in °	0.0257	0.0642
$\alpha_{max,y}$ in °	0.2053	0.0642

Due to the rectangular sensor resolution for the high-speed camera system, $\alpha_{max,x}$ and $\alpha_{max,y}$ are different for multiple speckle-sensing. However, when using the higher values, the detectable tilt intervals can be defined at [16.04×10^{-5}°; 0.2053°] for the free-space high-speed camera system and at [55×10^{-5}°; 0.0642°] for the diode system. These intervals can be converted accordingly to the computations from tables 4 and 5 to pressure intervals for a PVCP surface and a 1 MHz acoustic wave: [3.69 kPA; 4730 kPA] for the multiple speckle-analysis and [20.06 kPA; 3690 kPa] for the single speckle-analysis. The multiple speckle analysis offers therefore a dynamic range of 1280 and the single speckle-analysis of 184. Both values are considered convenient for photoacoustic sensing.

5.5.3 Shift extraction linearity and robustness

Figure 72 compares the extracted shift x_{s0} to $x_{s0,real}$. The multiple speckle

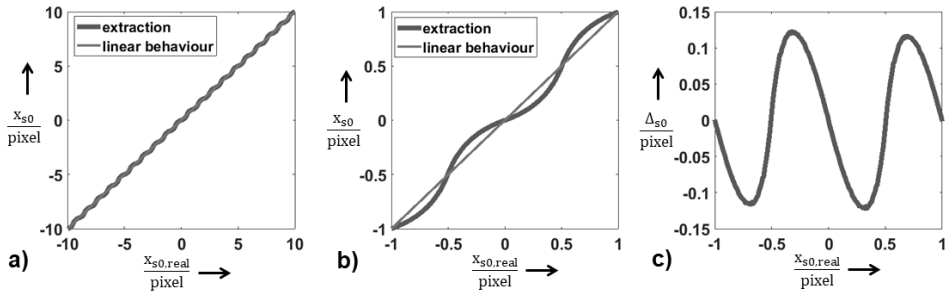

Figure 72: The extracted value for x_{s0} is compared to the given real shift $x_{s0,real}$ for the complete shift interval (a) and for a shift from -1 to 1 pixel (b). Figure (c) shows the difference Δ_{s0}=x_{s0}-$x_{s0,real}$ for $x_{s0,real}$ from -1 to 1 pixel.

shift extraction shows linear behaviour over the complete shift interval. Due to this observation, it can be stated that the method is robust against the influence of neighbouring speckles. However, there is a minor, pixel periodic error which is assumed to be related to the interpolation used for image shifting and shift extraction. The maximum of Δ_{s0}=x_{s0}-$x_{s0,real}$ is only 0.12 and therefore, this error is negligible (see fig. 72).

Figure 73 illustrates the computed values for x_{sp} for all shifts and speckle images in the case of single speckle-sensing and compares the results to linear behaviour. Though, it was tried to centralize the speckle, x_{sp} is not zero for a zero shift (see figure a). This can be explained with the speckle surrounding signal which also falls into the diode sensing regions. Due to this effect there is an offset for the computed x_{sp} compared to linear behaviour. This offset can be corrected, even so, there is still a clear difference between the computed

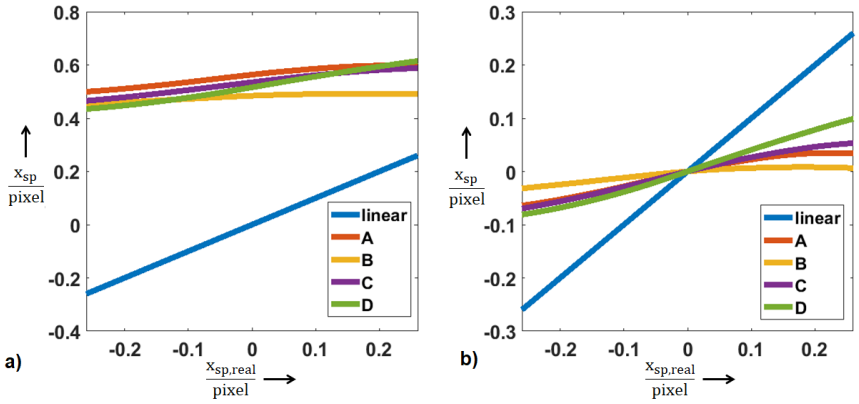

Figure 73: The computed values for x_{sp} are shown over $x_{sp,real}$ without (a), with zero offset correction (b) and compared to linear behaviour.

x_{sp} and linear behaviour (see figure b) which depends on central speckle size and intensity distribution. In addition, the connection between $x_{sp,real}$ and x_{sp} might be surjective. This means that there can be multiple values of x_{sp} for one $x_{sp,real}$. This effect occurs for speckle image B, as neighbouring speckles which are shifted into the diode sensing region lower the signal strongly for higher shift magnitudes.

5.5.4 Sensing depth

5.5.4.1 Comparability of phantoms and tissue

Table 7 summarizes the optical parameters for the PVCP phantoms and compares them to blood and skin for 532 nm and 1064 nm.

Table 7: Optical properties for PVCP, skin tissue and blood at 532 nm and 1064 nm. The data were collected from the following literature: Bashkatov et al. [27], Bosschaart at al. [102], Horstmann et al. [34], Fonseca at al. [55]. The scattering properties are calculated for g=0.9.

		PVCP		tissue	
		absorber	matrix	blood	skin
μ_a in $\frac{1}{cm}$	532 nm	-	-	280	1.3
	1064 nm	106	1	6	0.37
μ_s' in $\frac{1}{cm}$	532 nm	-	-	70	32.3
	1064 nm	0.1	21	60	16.8

For the experiments in the frame of this thesis, photoacoustic excitation was performed at 1064 nm. This wavelength is often used in research due to its lower scattering coefficient for phantoms and tissue. Furthermore, it offers an higher MPE for soft tissue than 532 nm. These effects together with the low skin absorption coefficient for 1064 nm result in a lower fluence decay with increasing depths. However, it needs to be noted that the blood absorption coefficient and absorption contrast to skin is lower at this wavelength compared to 532 nm. The absorption coefficient for the PVCP absorber was selected at 106 $\frac{1}{cm}$. This is significantly higher than the blood absorption at 1064 nm. Although, this high absorption coefficient helped to achieve a high signal amplitude which was desired for the proof of concept measurements and the setup development in the framework of this thesis. The scattering properties for the PVCP matrix material (μ_s'=21 $\frac{1}{cm}$) can be compared to skin tissue (μ_s'=16.8 $\frac{1}{cm}$). This fact in accordance with the similar absorption coefficient for skin and the PVCP matrix material result in a comparable fluence decay for the phantoms with tissue.

To evaluate the acoustic signal generation and detection, the local fluence, μ_a and acoustic parameters need to be considered. Table 8 summarizes the acoustic parameters for the PVCP phantoms and compares them to skin tissue. According to eq. (3), the initial photoacoustic pressure amplitude p_0

Table 8: Acoustic properties for silicone, PVCP, skin tissue and blood at 532 nm and 1064 nm. The optical properties are from Horstmann et al.[34]. The acoustic properties are from Fonseca et al. [55]. For the TiO_2-doped PVCP matrix the same increase for σ is assumed as for doped silicone compared to pure silicone [95]. The parameter Z for silicone is computed with ρ=0.97$\frac{g}{cm^3}$ [103].

acoustic parameter	PVCP	skin tissue
Γ	1.01	0.13 (blood)
σ in $\frac{db}{cm}$	2.48 (@ 1 MHz)	0.44 (@ 1 MHz)
Z_{ac} in $10^6 \frac{kg}{m^2 s}$	1.4	1.99
c in $\frac{m}{s}$	1340	1730

is linear proportional to μ_a, the local fluence F and Γ. Considering these parameters, the initially generated pressure amplitude for a PVCP phantom can be compared with the in-vivo application of blood imaging inside skin, when assuming a similar fluence at the absorber. The ratio between $p_{0,PVCP}$ and $p_{0,skin}$ is described by $\frac{\mu_{a,PVCP}\Gamma_{PVCP}}{\mu_{a,blood}\Gamma_{skin}}$ and is computed at 137 with the values

from table 7 for 1064 nm and table 8. This means that p_0 for a PVCP phantom at the absorber location is 137 times higher than for a blood vessel inside skin tissue at the same position as the PVCP absorber. When evaluating the resulting photoacoustic surface deformation, the acoustic damping coefficient σ and the impedance Z needs to be considered. First, σ is converted from $\frac{db}{cm}$ to cm^{-1}: 0.29 cm^{-1} (PVCP), 0.05 cm^{-1} (skin). The resulting surface deformation is proportional to $e^{-\sigma k}$ (k defines the absorber depth) and $\frac{1}{Z_{ac}}$ (eq. (15)). The relation for the resulting surface deformation between PVCP and skin is thus described by $137\times\frac{e^{-\sigma_{PVCP}k}}{e^{-\sigma_{skin}k}}\frac{Z_{ac,skin}}{Z_{ac,PVCP}}$ and is computed at $195\times e^{-0.04cm^{-1}k}$. For an absorber at a depth of 2 mm, the surface deformation amplitude for PVCP is thus a factor of 187 higher than for blood excitation inside skin tissue.

These computations prove the fact that the PVCP phantoms are highly beneficial for photoacoustic surface deformation compared to the in-vivo application. Thus, the absorber depths for the phantoms used in this thesis can not be related to the sensing depth for tissue applications. In order to estimate the achievable tissue sensing depth for the developed systems in the context of this thesis, however, analytical computations for a realistic tissue model for the resulting surface pressure are performed in the following section.

5.5.4.2 Tissue model

Figure 74 shows the fluence F over the depth k for an exposure with the MPE for 532 nm and 1064 nm. Due to the lower optical attenuation and higher

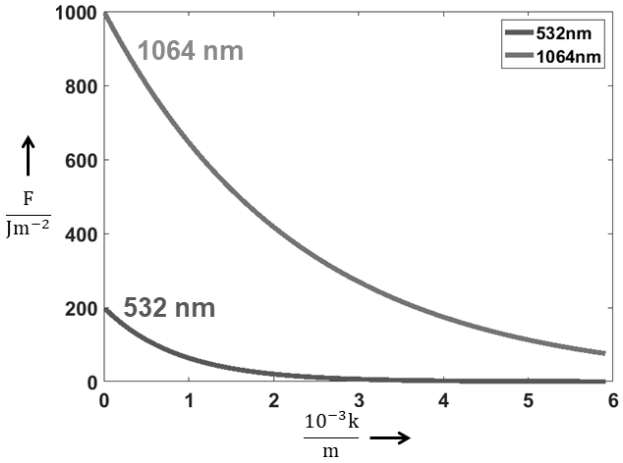

Figure 74: The fluence for excitation of skin tissue with the MPE is shown for 532 nm and 1064 nm.

MPE, the fluence for 1064 nm is significantly higher than for 532 nm. With this fluence, the maximal pressure amplitude at the surface is computed and plotted in fig. 75 over k. As expected, the pressure amplitudes are lower for

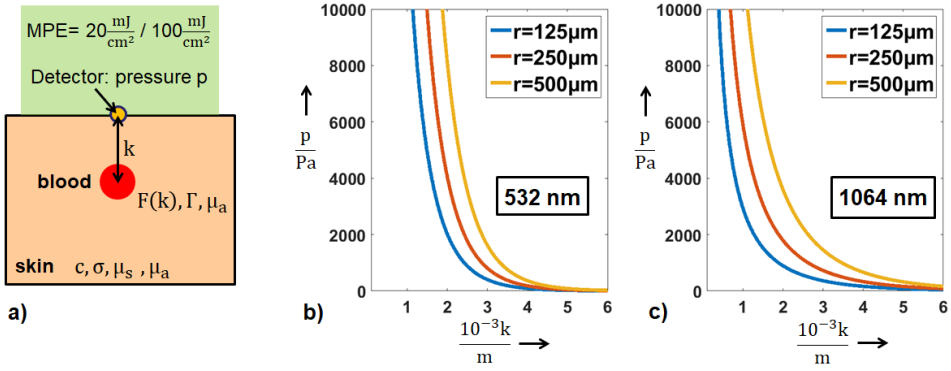

Figure 75: The model for the pressure computations is shown (a). Surface pressure p over the absorber depth for three absorber radii: Excitation with 532 nm (b) and excitation with 1064 nm (c).

smaller absorbers at specific tissue depths. For F, there is a clear difference regarding the two excitation wavelengths (fig. 74): F is higher for λ=1064 nm. However, the surface pressures are higher for 532 nm. This can be explained with the high absorption of blood at 532 nm which compensates the lower local fluence and results in higher surface pressures at a specific depth compared to 1064 nm. As explained in the state of the art section, the maximal pressures for surface near structures are in the kPa-range. For higher absorber depths, however, the pressures drop rapidly due to attenuation and spherical acoustic radiation.

In order to discuss the achievable sensing depth for blood sensing in skin tissue for the established speckle detection systems, the computed surface pressures are compared to the pressure sensitivities from section 5.5.1. Since, these pressure sensitivities are frequency dependent, it is important to note, that smaller absorber structures generate a higher frequency content (see section 2.2.1). Therefore, it is assumed that the required acoustic frequency for successful detection of the photoacoustic signal of a specific blood absorber with radius r is $\frac{c}{2r}$. Table 9 summarizes the absorber dimensions, relevant acoustic frequencies for a speed of sound of blood about 1575 $\frac{m}{s}$ and detection depths which are obtained from the data from fig. 75. The minimal detectable pressure S_d is computed according to eq. (19) for the high-speed camera system with $S_{d,nm}$=0.84 nm and for the diode array system with $S_{d,nm}$=4.56 nm. It needs to be noted, that the required acoustic frequencies can not be sampled by the high-speed camera system of this thesis. However, the sampling

rate could be improved in future for the same camera system and table 9 gives thus an overview for the high-speed camera system.

Table 9: Overview on the blood absorber radii r, resulting frequencies f, minimal detectable pressures S_d and achievable sensing depths k for the two speckle-sensing systems.

	high-speed camera			diode array		
r in μm	125	250	500	125	250	500
f in MHz	6.3	3.15	1.575	6.3	3.15	1.575
S_d in kPa	33.1	16.5	8.3	180	90	45
k in mm ($\lambda = 532$ nm)	0.63	1.24	1.99	0.2	0.54	1.1
k in mm ($\lambda = 1064$ nm)	-	0.47	1.26	-	-	-

As expected, the high-speed camera system achieves higher sensing depths compared to the diode array due to its better detection sensitivity. For the diode array system, it is even not possible to detect the photoacoustic signal of all absorbers for an excitation at 1064 nm. In addition, it is observed that higher sensing depths are reached for an excitation at 532 nm due to the high blood absorption which results in higher surface pressures. In general, it can be summarized that the high-speed camera system of this thesis would achieve sensing depths in the mm-range for absorber radii from 125 µm to 500 µm, assuming excitation at 532 nm and an increase of the frame rate. In contrast to these values, the diode system of this thesis is less suited for sensing blood in skin tissue. However, the sensitivity for both systems could be improved by a smaller pixel size or more precise shift extraction methods which could increase the sensing depths.

5.6 Speckle properties investigation

In this section, the results of the general speckle properties investigation of H7 are shown and discussed. Figure 76 illustrates H7, its subdivison and the structure of the results. First, the results for the wavelength dependent

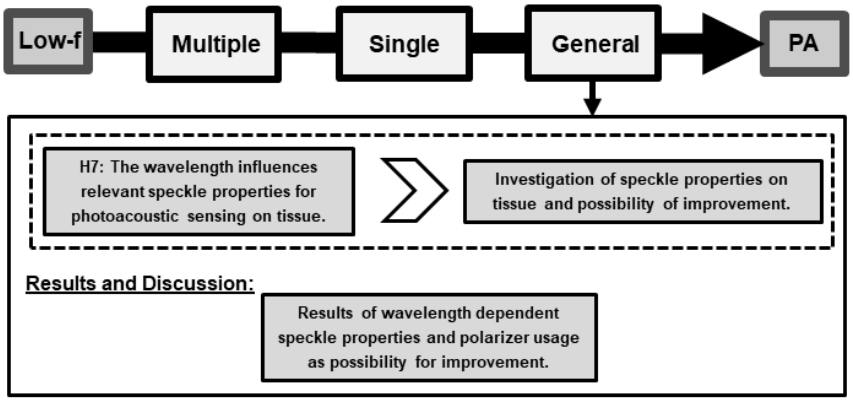

Figure 76: H7, its subdivision and the structure of the corresponding result section are illustrated.

speckle properties (speckle size and contrast) are presented. Second, the results for the polarizer usage are shown and its potential for speckle properties improvement is discussed.

Figure 77 shows acquired speckle patterns for the tissue samples. It is clearly

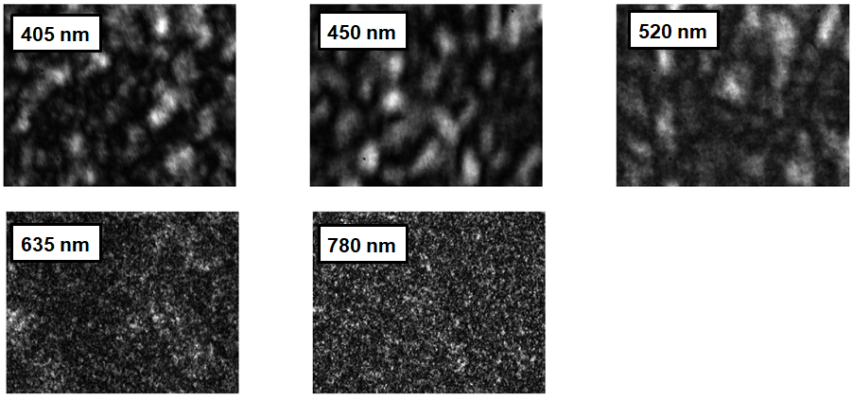

Figure 77: Speckle patterns for the different illumination wavelengths. There is a clear change for the speckle properties with the wavelength.

visible that the speckle size and contrast change for the investigated illumination wavelengths. There is a significant decrease of the speckle size

for 635 nm and 780 nm compared to 405 nm, 450 nm and 520 nm. Also, the speckle contrast decreases for 520 nm, 635 nm and 780 compared to the lower illumination wavelengths.

The results for the statistical analysis are shown in fig. 78. These results

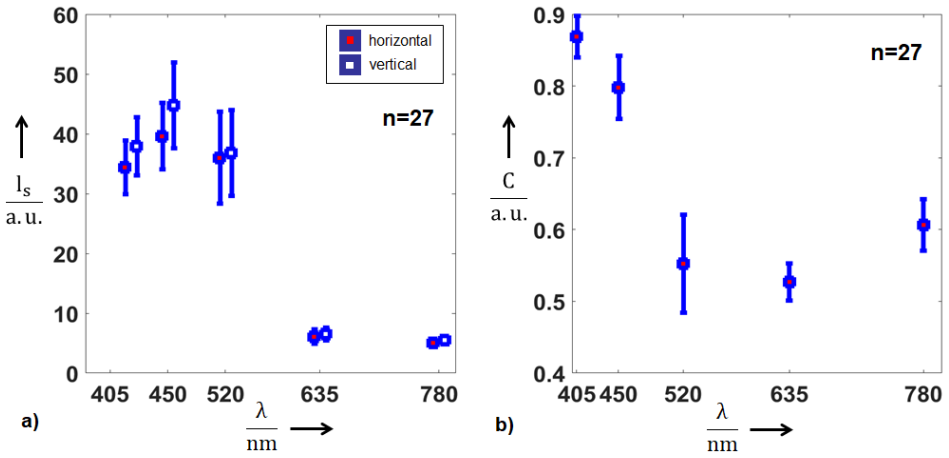

Figure 78: a: The mean horizontal and vertical speckle sizes and their standard deviation are shown. b: The mean speckle contrasts and their standard deviation are shown.

manifest the observations from fig. 77. The speckle size drops significantly for the high illumination wavelengths 635 nm and 780 nm. This can be explained with the illumination light penetration depth for the skin samples. For 635 nm and 780 nm light reaches high penetration depths up to 7 mm compared to the lower wavelengths due to reduced absorption and scattering for the sample [104]. The high penetration leads to volume scattering and the loss of polarization for the majority of reflected photons which prevents the formation of clear, large speckles. A similar behavior is evident for the speckle contrast. The small wavelengths 405 nm and 450 nm do not reach deep into the tissue: Due to increased absorption and scattering properties of the skin tissue, the light penetration depth drops to approximately 400 µm for 450 nm and only 250 µm for 405 nm [27]. This effect results in predominantly surface backscattering of the photons and allows the creation of clear big speckles. The slight rise of the speckle contrast which is visible at 780 nm might be due to reduced hemoglobin absorption in the tissue [105]. This reduced absorption leads to relatively more backscattered light than for 520 nm and 635 nm which could result in clearer speckle formation.

However, for the photoacoustic speckle-sensing approach, surface backscattering and clear speckles are desired in order to prevent disturbing influences from acoustic oscillations below the surface and allow precise sampling

of the photoacoustic surface deformations. Therefore, it can be concluded that illumination wavelengths in the red and near-infrared wavelength range are not suited for photoacoustic sensing by speckle-analysis due to their high light penetration depth in tissue, resulting in volume scattering of photons and small, unclear speckles. In contrast, the blue wavelength 405 nm and 450 nm offer predominantly surface back-scattering and clear speckle formation. Nevertheless, a low camera sensitivity might be a problem for these wavelengths in regard to the practical implementation. That is why, the influence of a polarizer usage on the speckle properties for 520 nm is experimentally investigated. Figure 79 illustrates the speckle properties for this wavelength with and without polarizer. It is evident that the polarizer usage improves the speckle contrast and size for 520 nm.

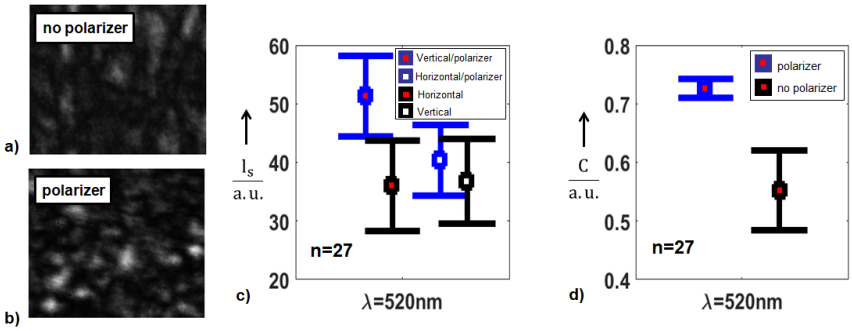

Figure 79: Speckle patterns with and without polarizer usage are shown (a,b). The mean speckle size (c) and speckle contrast (d) for polarizer usage are plotted.

This effect can be explained with the reduction of the penetration depth for the sensed photons that generate the speckle pattern. The penetration depth for 520 nm can be estimated at 1 mm [27]. Even so, when the polarizer is used, the depolarization length for light l_{depo} needs to be considered since only photons which maintain their polarization state are sensed. The depolarization length can be described by eq. (26) for Rayleigh-scattering ($l_{depo,R}$) and by eq. (27) for Mie-scattering ($l_{depo,M}$) [106].

$$l_{depo,R} = \frac{1}{\mu_s ln(\frac{10}{7})} \tag{26}$$

$$l_{depo,M} = \frac{1}{\mu_s' ln(\frac{10}{7})} \tag{27}$$

Considering the ratios for Rayleigh-scattering (R_r) and for Mie-scattering (R_m=1-R_r) of the total reduced scattering and assuming g=0.9, the depolarization length for given μ_s can be averaged according to eq. (28).

$$l_{depo} = (10R_m + R_r)l_{depo,R} = (10R_m + R_r)\frac{1}{\mu_s ln(\frac{10}{7})} \tag{28}$$

For 520 nm, l_{depo} is calculated at 598 µm (μ_s=$\frac{30}{mm}$, R_r=0.4 [27]). This value is significant less than the penetration depth for skin tissue at this wavelength (1 mm [27]). Therefore, the sensed polarized speckles originate from a smaller tissue volume which explains the increased speckle contrast and speckle size in fig. 79 for the polarizer usage.

Table 10 summarizes the penetration depths σ_{pen} and depolarization lengths for selected wavelengths between 400 nm and 532 nm considering skin tissue. The last line lists the half of the depolarization length since reflected photons are sensed for speckle-sensing. Due to this reason, the sensed photons travel the tissue twice and the penetration depth of polarized photons is equals to $\frac{l_{depo}}{2}$. Smaller wavelengths than 405 nm are not considered as the MPE reduces below 400 nm which complicates the speckle-sensing approach.

Table 10: Values for μ_s, R_r, σ_{pen} taken from [27].

λ [nm]	405	450	520	532
μ_s [$\frac{1}{mm}$]	69	53	30	28
R_r	0.7	0.6	0.4	0.38
σ_{pen} [μm]	300	550	1000	900
$\frac{l_{depo}}{2}$ [μm]	75	122	299	329

For each wavelength, l_{depo} is significantly smaller than σ_{pen}. Due to this reason and the same explanation as for the wavelength 520 nm, the results prove the potential for speckle properties improvement by polarizer usage for the selected wavelengths.

5.7 Photoacoustic imaging using speckle-sensing

Since only single spot sensing was shown before, this section shows and discusses the results of the investigation of H8 which treats imaging. The shown evaluations have already been published similarly in [P5]. Figure 80 illustrates H8, its subdivisons and the structure of the results. In the beginning,

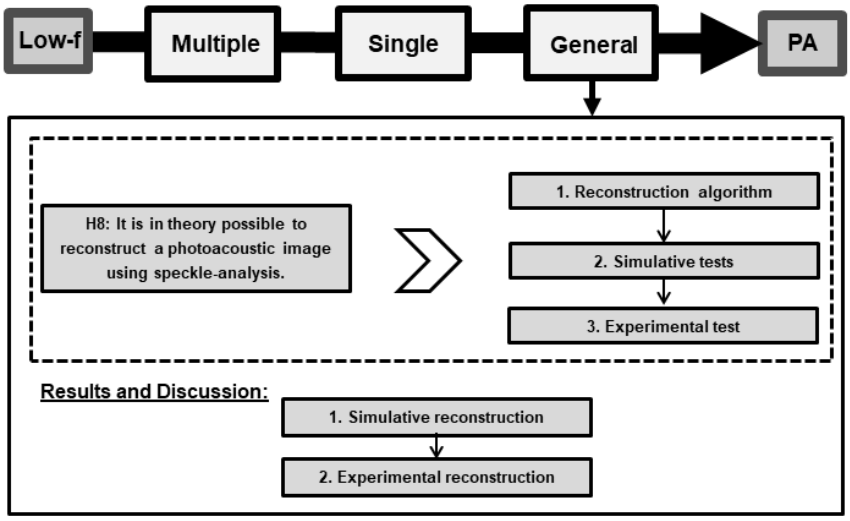

Figure 80: H8, its subdivision and the structure of the corresponding result section are illustrated.

the results for the reconstruction from the simulative data are presented and verified. For the first time, a reconstruction algorithm is established that requires tilt data. Afterwards, the reconstruction result for the experimental phantom feasibility test is shown and compared to the phantom geometry.

5.7.1 Simulative Reconstruction

Figure 81 shows the deformation shape of the detector field for Vol1 at 4.38 µs after photoacoustic excitation. Similar to the simulated deformation, there is a peak for the reconstructed ϵ_x due to the absorber inside the volume. The rectangular artefact at the image margins is a result of the deconvolution of the image for the consideration of detector point coupling. In general, the reconstructed deformation shape at the detection area matches the originally simulated deformation shape.

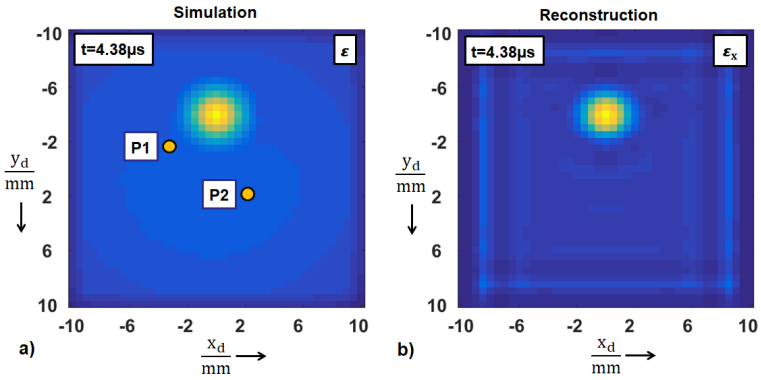

Figure 81: The simulated deformation (a) and reconstructed deformation (b) for Vol1 at 4.38 µs after photoacoustic excitation are shown.

Figure 82 illustrates the simulated and reconstructed temporal deformations and pressures at P1 and P2. For illustration purpose, the data is normalized to its maximum value. The simulated and reconstructed temporal deforma-

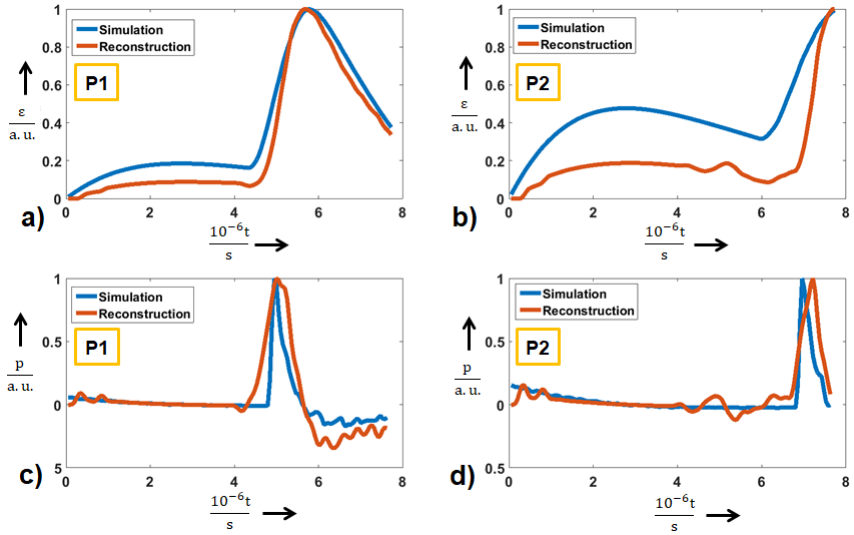

Figure 82: a,b) The simulated and reconstructed temporal deformations for the detector points P1 and P2 are plotted. c,d) The simulated and reconstructed temporal pressures for the detector points P1 and P2 are plotted.

tion courses match to each other. However, there is an offset between the reconstruction and simulation. This can be explained with the integration process introduced in eqs. (21) and (22). The integral computation starts at the detector margin at zero and not at the actual value which is unknown.

This results in an offset between the reconstructed deformation and the actual deformation. By differentiating the temporal deformation, the temporal pressure for each detector point is calculated according to eq. (24). Related to the simulated data, there is a slight time shift for the maximum peak for the reconstructed pressure for P2 which can be explained with the used smoothing average filter. Nevertheless, the courses for the simulation and reconstruction are in agreement for fig. 82. This comparison thus proves the temporal validity for the reconstruction approach.

With the reconstructed temporal pressure for each detector element, it is thus possible to compute $p_0(x_v, y_v, z_v, t = 0)$ with a back-projection algorithm. Figure 83 illustrates on the left side a cross-section through the obtained energy distribution from the MCS which is representative for the initially generated photoacoustic pressure. The right side of fig. 83 shows the reconstruction of the relevant cross-section. It is not possible to reconstruct

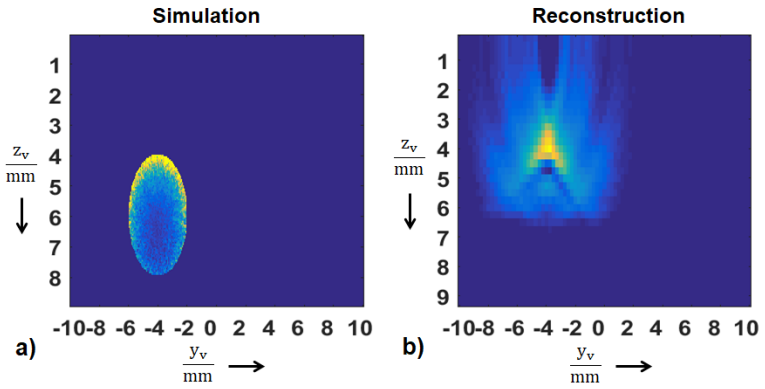

Figure 83: A cross-section of the energy distribution from the MCS (a) is compared to the reconstruction of the initially generated photoacoustic pressure (b).

the complete absorber since the excitation light only reaches the absorber surface. This surface region, however, is correctly reconstructed in position and size for Vol1. The ring-shaped image artefacts for the reconstructed cross-section are a result of the used back-projection algorithm. A simple delay and sum algorithm in time domain is implemented which produces ring shaped artefacts.

Figure 84 illustrates the deformations of the detection area at 4.38 µs after photoacoustic excitation, the initial energy distribution and pressure reconstruction for Vol2. In contrast to Vol1, there is an additional deformation

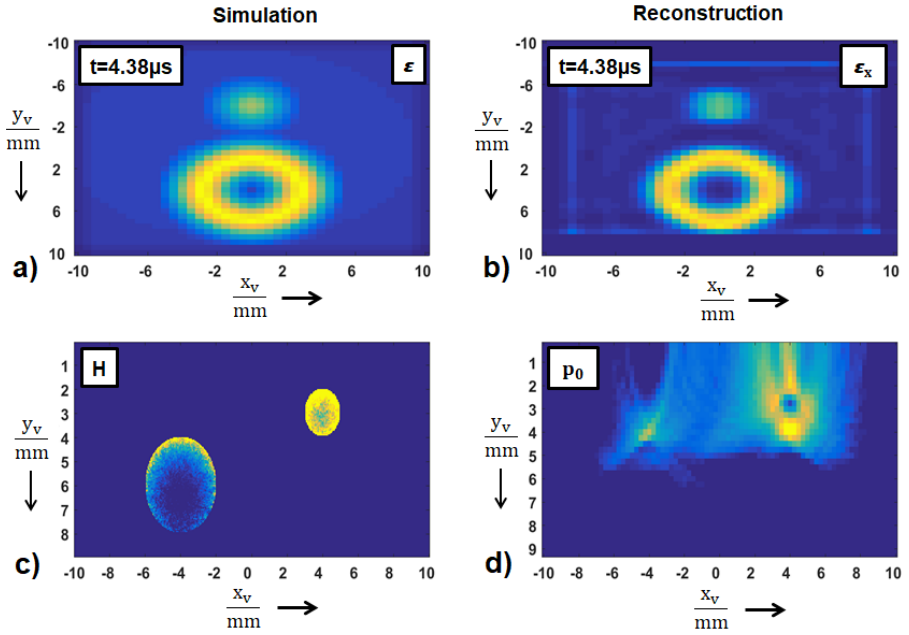

Figure 84: a,b) The simulated deformation (a) and reconstructed deformation (b) for Vol2 at 4.38 µs after photoacoustic excitation are shown. c,d: A cross-section of the energy distribution from the Monte Carlo Simulation (c) is compared to the reconstruction of the initially generated photoacoustic pressure (d).

ring visible which originates from the upper absorber inside Vol2. The spatial deformation shape is correctly reconstructed for Vol2 for this specific point in time. The right absorber is almost completely reconstructed in position and size. Although, as it is visible in the energy distribution from the MCS, the absorber center is not excited which is correctly reconstructed. The left absorber experiences a weaker photoacoustic excitation and only its upper surface is indicated in the reconstruction. In general, the reconstruction of p_0 is in agreement to the initial energy distribution for Vol2. The reconstruction results prove that it is in theory possible to reconstruct a photoacoustic image by remote speckle-sensing detection. However, there are slight inaccuracies visible in fig. 82 which are a result of errors for the spatial integral computation.

5.7.2 Experimental reconstruction

Figure 85 shows the maximum intensity projections of the reconstructed volume along x-, y- and z-direction (MIP_x, MIP_y, MIP_z). In MIP_z, there is an area visible which fits to the surface area of the absorber cube (2 mm×2 mm). In MIP_x and MIP_y, a thin rectangular shape with a side length of 2 mm is visible at a depth of 5 mm. The other side of this rectangle is very short since the laser pulse is directly absorbed at the phantom surface.

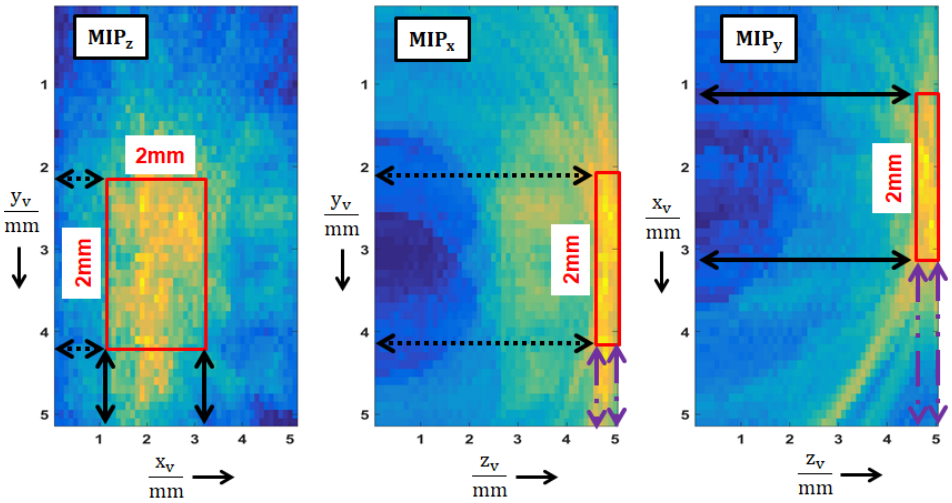

Figure 85: Maximum intensity projections (MIP) along the volume axes are shown. The rectangles indicate the absorber position. The arrows prove that the projections match to each other.

Furthermore, the positions of the detected areas are consistent for the MIPs. On the x-axis the highlighted area lies between 1.2 mm and 3.2 mm. For the y-axis, it is between 2.3 mm and 4.3 mm and for the z-axis it is situated between 4.7 mm and 5 mm. These observations result in the conclusion that the absorption volume is successfully reconstructed with the experimental measurements. In addition to the simulative data, it is thus shown by an easy feasibility experiment that image reconstruction for remote photoacoustic tomography by speckle-analysis is feasible.

6 Summary

In the course of this thesis, the remote speckle-analysis is investigated for its usability on remote photoacoustic signal detection and imaging. First, a model is established in order to evaluate the detectability of surface deformations by the speckle-analysis on phantoms in theory. Following this theoretical study, proof of concept experiments on phantoms and ex-vivo tissue are performed with a high-speed camera imaging system by analysing multiple speckles. In the context of these experiments, the transferability to endoscopy is tested by using an imaging fiber bundle. For verification, these experiments are compared to ultrasound transducer measurements which represent the current state of the art for photoacoustic detection. In order to speed up the speckle acquisition frame rate, the high-speed camera system is replaced by a low-resolution, diode-based sensor. With this system, the feasibility of remote photoacoustic detection by single speckle-analysis is tested with phantom and ex-vivo experiments. Furthermore, the automation and endoscopic potential of the single speckle-analysis with the low-resolution sensor is investigated by image processing algorithms and by the usage of an imaging fiber bundle. After this specific investigations about the multiple speckle and single speckle-analysis, general investigations about speckle-sensing are carried out. Due to this, the two speckle-analysis techniques are evaluated by discussing its sensing properties such as sensitivity, sensing range, linearity and sensing depth. In addition, the influence of the illumination wavelength on the speckle contrast and speckle size is examined for ex-vivo skin tissue. Finally, the imaging feasibility is examined by testing a reconstruction approach on simulative results and by a proof of concept experiment.

The main findings of this work can be summarized and grouped according to the defined hypotheses as follows:

- H1: The established model is capable of correctly simulating the magnitude, temporal course and spatial surface distribution of photoacoustic surface deformations and tilt for phantoms for deformations up to 30 nm. Based on computations with this model, it is possible to detect photoacoustic signals with the speckle-analysis.
- H2: The multiple speckle-analysis is an easy and robust modality for photoacoustic detection on phantoms and ex-vivo tissue. The photoacoustic detection can be performed in transmission and reflection-mode, whereby for the latter mode the influence of a laser-induced ultrasound signal is excluded. The high-speed camera system allows a frame rate of 823500 kHz which results in a measurement precision of approximately 0.8 mm.

- H3: Multiple speckle-sensing for photoacoustic detection can be done with a fiber-based approach which is applicable for endoscopy. The photoacoustic detection can be performed in transmission and reflection-mode by using an imaging fiber bundle which is applicable for endoscopy.
- H4: Photoacoustic sensing by single speckle-analysis can be done with a low-resolution, diode-based sensor which allows single speckle tracking. A sensing frame rate of 8 MHz is achieved which results in a sensing precision of approximately 0.13 mm.
- H5: Photoacoustic sensing by single speckle-analysis can be automated and is applicable for endoscopy. By the usage of a reference camera and image processing algorithms it is possible to automatically identify a suitable single speckle for sensing. This speckle can be positioned in the centre of the imaging system by mechanically moving the imaging fiber bundle which is applicable for endoscopy.
- H6: The multiple speckle-analysis is more suited for remote photoacoustic sensing than the single speckle-analysis. The multiple speckle-sensing system offers several advantages over the single speckle systems of this thesis: better sensitivity, higher dynamic range, shift extraction linearity, robustness against neighbouring speckles and no necessity for mechanical movements. Due to this findings, the multiple speckle-analysis is considered to be more suited for photoacoustic detection than the single speckle-analysis.
- H7: The illumination wavelength is a crucial parameter for speckle contrast and size. In general, the higher the scattering properties of the illuminated tissue, the better the speckle properties for remote sensing. When considering the rules for the MPE of tissue, an illumination at 400 nm is therefore recommended for speckle-analysis. In addition, the speckle properties for speckle-sensing on skin tissue can be improved by polarizer usage for illumination wavelengths ranging from 400 nm to 532 nm.
- H8: It is in theory possible to reconstruct a photoacoustic image using speckle-analysis. The initial pressure distribution inside an excited volume can be reconstructed by integrating the tilt measurement of the speckle-analysis and using a backprojection algorithm.

Based on these results for the defined hypotheses, the main hypothesis "speckle-sensing is a robust sensing technique which is suitable for PACT and PAE" can be confirmed.

7 Conclusion and future challenges

In this thesis, two speckle analysis techniques are used for remote photoacoustic sensing: the multiple speckle- and single speckle-analysis. The single speckle analysis offers a higher acquisition speed and thus measurement precision due to the lower pixel resolution compared to the multiple speckle-analysis. Nevertheless, the problem of the low acquisition frame rate for multiple speckle-sensing can be overcome in future by repeated photoacoustic excitation and time shifted speckle detection. In addition, there are several problems regarding the measurement properties, stability and precision for the single speckle approach. As shown in the previous sections, the multiple speckles approach offers better sensitivity and higher sensing range compared to the single speckle-analysis since. This is related to the facts that several speckles movements are analyzed and that the shift extraction method together with the small camera pixel size offers high precision for multiple speckles. However, more sensitive diodes and different algorithms for speckle shift extraction might for example improve the sensing sensitivity for single speckle-analysis. The sensing range could be easily improved by bigger diodes. However, there are general problems which affect the measurement performance of the single speckle approach. For the single speckle approach, the sensing system or an imaging fiber bundle needs to be moved mechanically in order to position a suitable speckle for the measurement. This procedure is time consuming and prone to error. In addition, the linearity for the speckle shift extraction is dependent on the speckle shape and size. Neighboring speckles may disturb the measurement resulting in speckle shift extraction errors. These factors could be compensated by an automatic speckle finding algorithm which analyzes the speckle and its surrounding for shift extraction linearity before the photoacoustic measurement. Even so, there is the possibility to overcome these problems by an algorithm, it would still reduce the number of speckles which are suitable for photoacoustic measurements. This reduction would increase the total measurement time since more time is needed for appropriate speckle identification. These mentioned problems limit the usability for precise and fast photoacoustic sensing or imaging by the single speckle approach. In addition, the multiple speckle-analysis offers a higher dynamic range and better detection sensitivity than the single speckle-analysis. Therefore, multiple speckle-analysis, which additionally is more robust and does not require mechanical movements, is considered to be the more suited approach for remote photoacoustic sensing.

The results of the thesis furthermore show that speckle analysis is usable for endoscopic applications and photoacoustic imaging. In addition, it can be automatized and it is found that an illumination in the blue wavelength range in combination with polarizer usage is advantageous for speckle properties and precise vibration detection. Therefore the defined main hypothesis "speckle-sensing is a robust sensing technique which is suitable for PACT and PAE" and can even be formulated more precise by "PA by multiple speckle-analysis is a robust sensing technique which is suitable for PACT and PAE".

When considering the future, in-vivo application of speckle-analysis for photoacoustic detection, several challenges arise to be considered and need to be solved. Since the limiting factor in this thesis for the measurement precision for the multiple speckle-analysis is the camera frame rate, a faster camera system or experimental setup needs to be established for more precise sensing. There are faster high-speed camera systems available than used in this thesis [107]. A faster high-speed camera system could replace the used camera of this thesis and enable more precise photoacoustic measurements by multiple speckle-analysis. A second option for the frame rate increase would be the sampling of the temporal speckle signal by repeated photoacoustic excitation and speckle-sensing. The temporal photoacoustic signal can be sampled by several photoacoustic excitations each following a laser pulse for speckle generation and detection. The time between the photoacoustic excitation pulse and speckle laser pulse can be shifted with a fixed time interval. The acoustic detection frequency is therefore defined by this time interval and not by a camera frame rate. With this approach, detection frequencies in the MHz range can easily be achieved, even so time precise triggering is needed and the complete measurement time for the temporal vibration is longer due to the repeated excitations [75].

The illumination exposure for the experiments shown in this work is far above the CW-MPE for soft tissue at 532 nm (200 $\frac{mW}{cm^2}$, see section 2.1.2) due to the CW illumination and focusing at 100 mW for speckle-generation. This high power, however, is needed for reaching the photon noise limited regime for the speckle acquisition. This problem could be tackled by two solution strategies. First, the speckle illumination light could be temporally gated. For a theoretical sensing depth of 4 mm, only a measurement time and thus an illumination time of approximately 5.6 µs is needed. Assuming repetitive excitation at 40 Hz, the illumination time per second would be reduced to 224 µs per second. When assuming circular illumination at a diameter of 400 µm the exposure is computed at F_0=0.45 $\frac{mJ}{cm^2}$. This exposure is far below the MPE for the illumination at this wavelength (MPE=3.4 $\frac{mJ}{cm^2}$, according to section 2.1.2) and therefeore still allows a sufficient high and safe short pulse

exposure for photoacoustic signal generation. Second, the speckle acquisition system could be replaced with a more sensitive detector which would reduce the needed exposure for a clear speckle detection.

It is expected to get a higher noise level in-vivo due to movements and influences from breathing, heart beat or blood flow. However, these effects occur at slower time scales than the photoacoustic measurements and their influences can be reduced by temporal filtering. A photoacoustic measurement takes approximately 5.6 µs which is very fast compared to the breathing and heart beat effects which have a frequency of approximately 0.15 Hz to 1.2 Hz. However, these influences result in a speckle decorrelation time of several ms and therefore it might happen that a speckle region changes its shape during the tracking process for a photoacoustic measurement. The speckle region could be tracked with a high-speed camera additionally to the photoacoustic sensing in order to ensure speckle correlation during the measurement.

A further limiting factor for in-vivo applications might be the disturbance due to a laser induced ultrasound signal at the tissue surface. For this thesis, predominantly low absorption surfaces were used to show the feasibility of remote photoacoustic detection. In reality, however, the excitation laser pulse will induce an ultrasound signal at the tissue surface due to absorption, for example of melanin. Due to this effect, the tissue surface changes initially its shape and the photoacoustic signal is mixed with acoustic reflections of the laser induced ultrasound from the tissue inside. This will make it more difficult to extract the purely photoacoustic signal from the surface tilt. Compensation methods for these mentioned disturbances are described in literature [108].

When aiming at image reconstruction, it needs to be mentioned that it is not possible to assign a single speckle of a speckle pattern to a location inside the illuminated surface area due to the required defocus and multiple scattering. The reconstructed vibration profile for multiple speckle-analysis and single speckle-analysis represents the temporal vibration profile for the CW-illuminated surface area. Therefore, in order to precisely sample the photoacoustic surface waves, a tight spot illumination is needed which has to be moved laterally between the measurements. The required illumination area thus defines the lateral sensing resolution. This resolution determines if the lateral surface wavelength λ_{lat} of an absorber can be resolved. The lateral surface wavelength is dependent on the spherical absorber radius r and the absorber surface opening angle α_{ac} which is defined by k and r when

assuming an acoustic wavelength of 2r [34]. This relation is described by eq. (29) and the formation of λ_{lat} is sketched in fig. 86 on the left side.

$$\lambda_{lat} = \frac{\lambda}{sin(2\alpha_{ac})} = \frac{2r}{sin2\alpha_{ac}} = \frac{2r}{sin(2(tan^{-1}(\frac{r}{k})))} \tag{29}$$

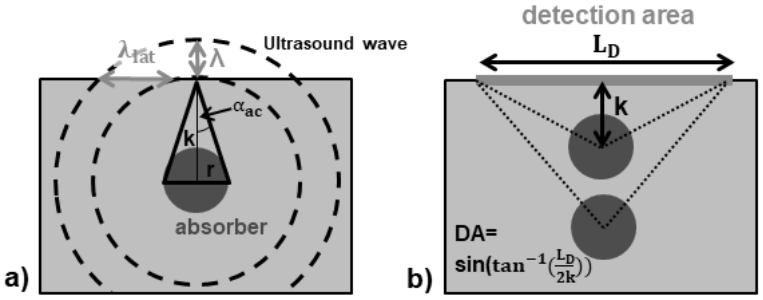

Figure 86: The lateral acosutic surface wavelength which is dependent on λ, r and k is sketched (a). Surface pressure p over the absorber depth for three absorber radii: Excitation with 532 nm (b) and excitation with 1064 nm (c). Figure after [34].

An absorber with r=100 µm and k=1 mm generates an lateral acoustic wavelength of λ_{lat}=1 mm. In order to resolve this wavelength a CW illumination with D_{ill}<0.5 mm is needed which can easily be achieved. Furthermore, when considering image reconstruction by lateral scanning of the illumination spot, the influence of the complete scanning field size L_D on the achievable imaging resolution needs to be mentioned. The achievable imaging resolution is dependent on the detection aperture DA=sin(tan^{-1}($\frac{L_D}{2k}$)) illustrated in fig. 86 since it defines the part of the spherical acoustic wavefront which is detected. It is assumed that a sampling frequency f allows the acquisition of an acoustic wavelength λ=2$\frac{c}{f}$. In general, the imaging resolution is dependent on the detection area size, sampling frequency f, speed of sound c and absorber depth. Equation (30) describes the achievable imaging resolution σ_x for an absorber at a depth k positioned centric below a detection field according to the Rayleigh-criterion [34].

$$\sigma_x = 0.61\frac{\lambda}{DA} = 0.61\frac{2\frac{c}{f}}{sin(tan^{-1}(\frac{L_D}{2k}))} \tag{30}$$

For a sampling rate of 8 MHz, k=1 mm and c=1400 $\frac{m}{s}$ and L_D=5 mm, an imaging resolution of 230 µm can be achieved in theory. In general, this imaging resolution decreases with lower absorber depth and larger detection area.

Large surface areas can be covered by the speckle-analysis with an appropriate scanning approach and therefore, the detection aperture is not considered as a limiting factor.

Appendix

Artificial phantom material preparation process

1. Shake the container of medium PVCP well to mix the PVCP with the softener until it is a homogenous white mixture.
2. Additive mixing.
   - Matrix: Measure an appropriate volume of the PVCP and an appropriate mass of the TiO_2 into a 50 mL centrifuge tube to create a mixture that is has a ratio of $\frac{4\,mg(TiO_2)}{ml(PVCP)}$.
   - Absorber: Measure appropriate volumes of the PVCP and black ink into a 50mL centrifuge tube to create a mixture that has a colour-concentration of 7 Vol.-%.
3. Twist the cap onto the centrifuge tube tightly and then shake the centrifuge tube to mix the liquids
4. Place the centrifuge tube in an ultrasound bath set to 60% power and 50 $^{\circ}C$ for 35 minutes. Ensure that the centrifuge tube is upright so that no water can enter the centrifuge tube.
5. Obtain a 250 mL pressure resistant glass bottle and place two small magnetic stirring bars into the bottom of the bottle.
6. Pour the mixture into the glass bottle, on top of the stirring bars.
7. Place the bottle onto a magnetic stirrer and heater and attach the cap which connects to a waking pump.
8. Set the magnetic stirrer and heater to 300 $^{\circ}C$ and 950 rpm. Turn on both the magnetic stirrer and heater and the waking pump.
9. Allow the mixture to mix for 22 mins. At the 10 minute point turn the rpm down to 400. For the last 2 minutes turn the rpm up to 950 again and keep the waking pump on the whole time.
10. Pour the mixture into the desired mould. Be careful to pour quickly so that the mixture does not solidify before the mould is filled to the appropriate height. Also, be careful not to pour the stirring bars into the mould.
11. Wait approximately 5 minutes, or until the mixture is solidified, then gently remove the phantom from the mould using a spoon, thin knife or other tool.
12. Use a knife to cut the solidified PVCP if desired.

Spectrum of laser diodes

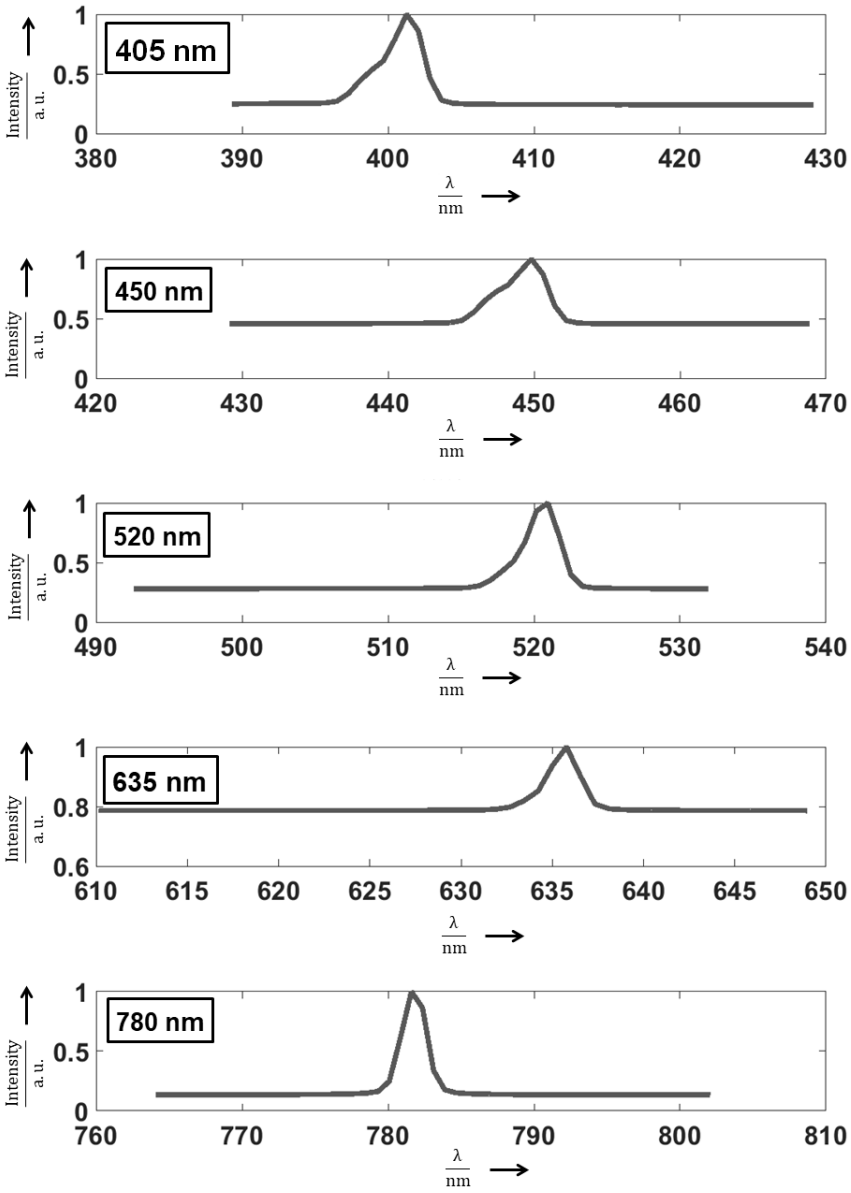

Bibliography

[1] Bean, William Bennett. "Sir William Osler: aphorisms from his bedside teachings and writings" (1954).

[2] Bercovich, Eyal and Javitt, Marcia C. "Medical Imaging: From Roentgen to the Digital Revolution, and Beyond". *Rambam Maimonides medical journal* 9.4 (2018).

[3] Pysz, Marybeth A; Gambhir, Sanjiv S, and Willmann, Jürgen K. "Molecular imaging: current status and emerging strategies". *Clinical radiology* 65.7 (2010), pp. 500–516.

[4] Kasban, H; El-Bendary, MAM, and Salama, DH. "A comparative study of medical imaging techniques". *International Journal of Information Science and Intelligent Systems* 4.2 (2015), pp. 37–58.

[5] Bushberg, Jerrold T and Boone, John M. *The essential physics of medical imaging*. Lippincott Williams & Wilkins, 2011, p. 352.

[6] Donath, Tilman; Pfeiffer, Franz; Bunk, Oliver; Grünzweig, Christian; Hempel, Eckhard; Popescu, Stefan; Vock, Peter, and David, Christian. "Toward clinical X-ray phase-contrast CT: demonstration of enhanced soft-tissue contrast in human specimen". *Investigative radiology* 45.7 (2010), pp. 445–452.

[7] Smith, Nadine Barrie and Webb, Andrew. *Introduction to medical imaging: physics, engineering and clinical applications*. Cambridge university press, 2010, 145ff, 204ff.

[8] Gułkowski, Sławomir and Olchowik, Jan M. "Hydrogen interactions in magnetic resonance imaging. Histogram-based segmentation of brain tissues". *Materials Science Poland* 24.4 (2006), pp. 1051–1056.

[9] Sun, Zhonghua; Ng, Kwan-hoong, and Vijayananthan, A. "Is utilisation of computed tomography justified in clinical practice? Part 1: application in the emergency department." *Singapore medical journal* (2010), TBA–TBA.

[10] Sistrom, Christopher Lee and McKay, Niccie L. "Costs, charges, and revenues for hospital diagnostic imaging procedures: differences by modality and hospital characteristics". *Journal of the American College of Radiology* 2.6 (2005), pp. 511–519.

[11] Cootney, Robert W. "Ultrasound imaging: principles and applications in rodent research". *Ilar Journal* 42.3 (2001), pp. 233–247.

[12] Dhawan, Atam P; D'Alessandro, Brian, and Fu, Xiaolei. "Optical imaging modalities for biomedical applications". *IEEE reviews in biomedical engineering* 3 (2010), pp. 69–92.

[13] Fujimoto, James G; Pitris, Costas; Boppart, Stephen A, and Brezinski, Mark E. "Optical coherence tomography: an emerging technology for biomedical imaging and optical biopsy". *Neoplasia (New York, NY)* 2.1-2 (2000), p. 9.

[14] Wilson, Katheryne E; Wang, Tzu Yin, and Willmann, Jürgen K. "Acoustic and photoacoustic molecular imaging of cancer". *Journal of Nuclear Medicine* 54.11 (2013), pp. 1851–1854.

[15] Haisch, Christoph. "Quantitative analysis in medicine using photoacoustic tomography". *Analytical and bioanalytical chemistry* 393.2 (2009), p. 473.

[16] Reza, Parsin Haji; Bell, Kevan; Shi, Wei; Shapiro, James, and Zemp, Roger J. "Deep non-contact photoacoustic initial pressure imaging". *Optica* 5.7 (2018), pp. 814–820.

[17] Wang, Lihong V and Hu, Song. "Photoacoustic tomography: in vivo imaging from organelles to organs". *science* 335.6075 (2012), pp. 1458–1462.

[18] Yao, Junjie and Wang, Lihong V. "Photoacoustic microscopy". *Laser & photonics reviews* 7.5 (2013), pp. 758–778.

[19] Park, Sungjo; Lee, Changho; Kim, Jeesu, and Kim, Chulhong. "Acoustic resolution photoacoustic microscopy". *Biomedical Engineering Letters* 4.3 (2014), pp. 213–222.

[20] Wang, Lihong V and Yao, Junjie. "A practical guide to photoacoustic tomography in the life sciences". *Nature methods* 13.8 (2016), p. 627.

[21] Zhang, Pengfei; Li, Lei; Lin, Li; Hu, Peng; Shi, Junhui; He, Yun; Zhu, Liren; Zhou, Yong, and Wang, Lihong V. "High-resolution deep functional imaging of the whole mouse brain by photoacoustic computed tomography in vivo". *Journal of biophotonics* 11.1 (2018), e201700024.

[22] Hu, Song and Wang, Lihong V. "Photoacoustic imaging and characterization of the microvasculature". *Journal of biomedical optics* 15.1 (2010), p. 011101.

[23] Yang, Joon-Mo; Maslov, Konstantin; Yang, Hao-Chung; Zhou, Qifa; Shung, K Kirk, and Wang, Lihong V. "Photoacoustic endoscopy". *Optics letters* 34.10 (2009), pp. 1591–1593.

[24] Qu, Yuan; Li, Chiye; Shi, Junhui; Chen, Ruimin; Xu, Song; Rafsanjani, Hasan; Maslov, Konstantin; Krigman, Hannah; Garvey, Laura; Hu, Peng, et al. "Transvaginal fast-scanning optical-resolution photoacoustic endoscopy". *Journal of biomedical optics* 23.12 (2018), p. 121617.

[25] Xi, Lei; Duan, Can; Xie, Huikai, and Jiang, Huabei. "Miniature probe combining optical-resolution photoacoustic microscopy and optical coherence tomography for in vivomicrocirculation study". *Applied optics* 52.9 (2013), pp. 1928–1931.

[26] Yao, Junjie and Wang, Lihong V. "Sensitivity of photoacoustic microscopy". *Photoacoustics* 2.2 (2014), pp. 87–101.

[27] Bashkatov, AN; Genina, EA; Kochubey, VI, and Tuchin, VV. "Optical properties of human skin, subcutaneous and mucous tissues in the wavelength range from 400 to 2000 nm". *Journal of Physics D: Applied Physics* 38.15 (2005), p. 2543.

[28] Ritz, Joerg-P; Roggan, Andre; Isbert, Christoph; Müller, Gerhard; Buhr, Heinz J, and Germer, Christoph-T. "Optical properties of native and coagulated porcine liver tissue between 400 and 2400 nm". *Lasers in Surgery and Medicine: The Official Journal of the American Society for Laser Medicine and Surgery* 29.3 (2001), pp. 205–212.

[29] Beard, Paul. "Biomedical photoacoustic imaging". *Interface focus* 1.4 (2011), pp. 602–631.

[30] Bigio, Irving J and Fantini, Sergio. *Quantitative biomedical optics: theory, methods, and applications*. Cambridge University Press, 2016.

[31] Xu, Minghua and Wang, Lihong V. "Photoacoustic imaging in biomedicine". *Review of scientific instruments* 77.4 (2006), p. 041101.

[32] Manohar, Srirang and Razansky, Daniel. "Photoacoustics: a historical review". *Advances in optics and photonics* 8.4 (2016), pp. 586–617.

[33] Maini, Anil K. *Lasers and optoelectronics: fundamentals, devices and applications*. John Wiley & Sons, 2013.

[34] Horstmann, Jens. "Kontaktlose photoakustische Tomographie". PhD thesis. 2016.

[35] Mallidi, Srivalleesha; Luke, Geoffrey P, and Emelianov, Stanislav. "Photoacoustic imaging in cancer detection, diagnosis, and treatment guidance". *Trends in biotechnology* 29.5 (2011), pp. 213–221.

[36] Jacques, Steven L. "Optical properties of biological tissues: a review". *Physics in Medicine & Biology* 58.11 (2013), R37.

[37] Anderson, R Rox and Parrish, John A. "The optics of human skin". *Journal of investigative dermatology* 77.1 (1981), pp. 13–19.

[38] Li, Mucong; Tang, Yuqi, and Yao, Junjie. "Photoacoustic tomography of blood oxygenation: a mini review". *Photoacoustics* 10 (2018), pp. 65–73.

[39] Lao, Yeqi; Xing, Da; Yang, Sihua, and Xiang, Liangzhong. "Noninvasive photoacoustic imaging of the developing vasculature during early tumor growth". *Physics in Medicine & Biology* 53.15 (2008), p. 4203.

[40] Stein, Erich W; Maslov, Konstantin I, and Wang, Lihong V. "Noninvasive, in vivo imaging of blood-oxygenation dynamics within the mouse brain using photoacoustic microscopy". *Journal of biomedical optics* 14.2 (2009), p. 020502.

[41] Bühler, Andreas. "Multi-spectral optoacoustic tomography: Methods and applications". PhD thesis. Technische Universität München, 2014.

[42] Ludwig, George D. "The velocity of sound through tissues and the acoustic impedance of tissues". *The journal of the acoustical society of America* 22.6 (1950), pp. 862–866.

[43] Szabo, Thomas L. *Diagnostic ultrasound imaging: inside out*. Elsevier, 2014.

[44] Sorge, Georg. *Faszination Ultraschall*. Springer, 2002.

[45] Sehgal, Chandra M and Greenleaf, James F. "Scattering of ultrasound by tissues". *Ultrasonic imaging* 6.1 (1984), pp. 60–80.

[46] Lyons, MARK E and Parker, Kevin J. "Absorption and attenuation in soft tissues. II. Experimental results". *IEEE transactions on ultrasonics, ferroelectrics, and frequency control* 35.4 (1988), pp. 511–521.

[47] Luo, Liaofu; Molnar, Joseph; Ding, Hui; Lv, Xiaogui, and Spengler, Gabriella. "Ultrasound absorption and entropy production in biological tissue: a novel approach to anticancer therapy". *Diagnostic Pathology* 1.1 (2006), p. 35.

[48] Azhari, Haim. *Basics of biomedical ultrasound for engineers*. John Wiley & Sons, 2010.

[49] Moran, CM; Bush, NL, and Bamber, JC. "Ultrasonic propagation properties of excised human skin". *Ultrasound in Medicine and Biology* 21.9 (1995), pp. 1177–1190.

[50] Nassiri, DK; Nicholas, D, and Hill, CR. "Attenuation of ultrasound in skeletal muscle". *Ultrasonics* 17.5 (1979), pp. 230–232.

[51] Wissmeyer, Georg; Pleitez, Miguel A; Rosenthal, Amir, and Ntziachristos, Vasilis. "Looking at sound: optoacoustics with all-optical ultrasound detection". *Light: Science & Applications* 7.1 (2018), p. 53.

[52] Li, Changhui and Wang, Lihong V. "Photoacoustic tomography and sensing in biomedicine". *Physics in Medicine & Biology* 54.19 (2009), R59.

[53] Wang, Lihong V and Wu, Hsin-i. *Biomedical optics: principles and imaging*. John Wiley & Sons, 2012.

[54] Andreev, Valeriy G; Karabutov, Alexander A, and Oraevsky, Alexander A. "Detection of ultrawide-band ultrasound pulses in optoacoustic tomography". *IEEE transactions on ultrasonics, ferroelectrics, and frequency control* 50.10 (2003), pp. 1383–1390.

[55] Fonseca, Martina; Zeqiri, Bajram; Beard, Paul, and Cox, Ben. "Characterisation of a PVCP based tissue-mimicking phantom for quantitative photoacoustic imaging". *European Conference on Biomedical Optics*. Optical Society of America. 2015, p. 953911.

[56] Cheong, Wai-Fung; Prahl, Scott A, and Welch, Ashley J. "A review of the optical properties of biological tissues". *IEEE journal of quantum electronics* 26.12 (1990), pp. 2166–2185.

[57] Chivers, RC and Hill, CR. "Ultrasonic attenuation in human tissue". *Ultrasound in medicine & biology* 2.1 (1975), pp. 25–29.

[58] Vijaya, MS. *Piezoelectric materials and devices: applications in engineering and medical sciences*. CRC Press, 2016.

[59] Caballero, Araque and Angel, Miguel. "Incorporating Sensor Properties in Optoacoustic Imaging". PhD thesis. Technische Universität München, 2013.

[60] Shung, K Kirk and Zippuro, Michael. "Ultrasonic transducers and arrays". *IEEE Engineering in Medicine and Biology Magazine* 15.6 (1996), pp. 20–30.

[61] Venkatragavaraj, E; Satish, B; Vinod, PR, and Vijaya, MS. "Piezoelectric properties of ferroelectric PZT-polymer composites". *Journal of Physics D: Applied Physics* 34.4 (2001), p. 487.

[62] Aldrich, John E. "Basic physics of ultrasound imaging". *Critical care medicine* 35.5 (2007), S131–S137.

[63] Winkler, Amy M; Maslov, Konstantin I, and Wang, Lihong V. "Noise-equivalent sensitivity of photoacoustics". *Journal of biomedical optics* 18.9 (2013), p. 097003.

[64] Wang, Xueding; Fowlkes, J Brian; Cannata, Jonathan M; Hu, Changhong, and Carson, Paul L. "Photoacoustic imaging with a commercial ultrasound system and a custom probe". *Ultrasound in medicine & biology* 37.3 (2011), pp. 484–492.

[65] Beard, Paul C; Zhang, Edward ZY, and Cox, Benjamin T. "Transparent Fabry-Perot polymer film ultrasound array for backward-mode photoacoustic imaging". *Photons Plus Ultrasound: Imaging and Sensing*. Vol. 5320. International Society for Optics and Photonics. 2004, pp. 230–237.

[66] Zhang, EZ; Laufer, JG; Pedley, RB, and Beard, PC. "In vivo high-resolution 3D photoacoustic imaging of superficial vascular anatomy". *Physics in Medicine & Biology* 54.4 (2009), p. 1035.

[67] Ansari, Rehman; Zhang, Edward Z; Desjardins, Adrien E, and Beard, Paul C. "All-optical forward-viewing photoacoustic probe for high-resolution 3D endoscopy". *Light: Science & Applications* 7.1 (2018), p. 75.

[68] Li, Hao; Dong, Biqin; Zhang, Zhen; Zhang, Hao F, and Sun, Cheng. "A transparent broadband ultrasonic detector based on an optical micro-ring resonator for photoacoustic microscopy". *Scientific reports* 4 (2014), p. 4496.

[69] Dong, Biqin; Chen, Siyu; Zhang, Zhen; Sun, Cheng, and Zhang, Hao F. "Photoacoustic probe using a microring resonator ultrasonic sensor for endoscopic applications". *Optics letters* 39.15 (2014), pp. 4372–4375.

[70] Johnson, Jami L; Wijk, Kasper van; Caron, James N, and Timmerman, Miriam. "Gas-coupled laser acoustic detection as a non-contact line detector for photoacoustic and ultrasound imaging". *Journal of Optics* 18.2 (2016), p. 024005.

[71] Speirs, Rory W and Bishop, Alexis I. "Photoacoustic tomography using a Michelson interferometer with quadrature phase detection". *Applied Physics Letters* 103.5 (2013), p. 053501.

[72] Lu, Jiao; Gao, Yingzhe; Ma, Zhenhe; Wang, Bo, and Wang, Yi. "Noncontact photoacoustic imaging by using a modified optical-fiber Michelson interferometer". *Photons Plus Ultrasound: Imaging and Sensing 2016*. Vol. 9708. International Society for Optics and Photonics. 2016, 97084B.

[73] Liu, Jun; Tang, Zhilie; Wu, Yongbo, and Wang, Yi. "Rapid and noncontact photoacoustic tomography imaging system using an interferometer with high-speed phase modulation technique". *Review of Scientific Instruments* 86.4 (2015), p. 044904.

[74] Hochreiner, Armin; Bauer-Marschallinger, Johannes; Burgholzer, Peter; Jakoby, Bernhard, and Berer, Thomas. "Non-contact photoacoustic imaging using a fiber based interferometer with optical amplification". *Biomedical optics express* 4.11 (2013), pp. 2322–2331.

[75] Horstmann, Jens; Spahr, Hendrik; Buj, Christian; Münter, Michael, and Brinkmann, Ralf. "Full-field speckle interferometry for non-contact photoacoustic tomography". *Physics in Medicine & Biology* 60.10 (2015), p. 4045.

[76] Rousseau, Guy; Blouin, Alain, and Monchalin, Jean-Pierre. "Non-contact photoacoustic tomography and ultrasonography for tissue imaging". *Biomedical optics express* 3.1 (2012), pp. 16–25.

[77] Carp, Stefan A and Venugopalan, Vasan. "Optoacoustic imaging based on the interferometric measurement of surface displacement". *Journal of biomedical optics* 12.6 (2007), p. 064001.

[78] Xu, Guan; Wang, Cheng; Feng, Ting; Oliver, David E, and Wang, Xueding. "Non-contact photoacoustic tomography with a laser Doppler vibrometer". *Photons Plus Ultrasound: Imaging and Sensing 2014*. Vol. 8943. International Society for Optics and Photonics. 2014, p. 894332.

[79] Dong, Biqin; Sun, Cheng, and Zhang, Hao F. "Optical detection of ultrasound in photoacoustic imaging". *IEEE Transactions on Biomedical Engineering* 64.1 (2016), pp. 4–15.

[80] Lamela, Horacio; Gallego, Daniel, and Oraevsky, Alexander. "Optoacoustic imaging using fiber-optic interferometric sensors". *Optics letters* 34.23 (2009), pp. 3695–3697.

[81] Hajireza, Parsin; Shi, Wei; Bell, Kevan; Paproski, Robert J, and Zemp, Roger J. "Non-interferometric photoacoustic remote sensing microscopy". *Light: Science & Applications* 6.6 (2017), e16278.

[82] Zalevsky, Zeev; Beiderman, Yevgeny; Margalit, Israel; Gingold, Shimshon; Teicher, Mina; Mico, Vicente, and Garcia, Javier. "Simultaneous remote extraction of multiple speech sources and heart beats from secondary speckles pattern". *Optics express* 17.24 (2009), pp. 21566–21580.

[83] Beiderman, Yevgeny; Horovitz, Israel; Burshtein, Natanel; Teicher, Mina; Garcia, Javier; Micó, Vicente, and Zalevsky, Zeev. "Remote estimation of blood pulse pressure via temporal tracking of reflected secondary speckles pattern". *Journal of biomedical optics* 15.6 (2010), p. 061707.

[84] Golberg, Mark; Ruiz-Rivas, Joaquin; Polani, Sagi; Beiderman, Yevgeny, and Zalevsky, Zeev. "Large-scale clinical validation of noncontact and continuous extraction of blood pressure via multipoint defocused photonic imaging". *Applied optics* 57.7 (2018), B45–B51.

[85] Bishitz, Yael; Ozana, Nisan; Schwarz, Ariel; Beiderman, Yevgeny; Garcia, Javier, and Zalevsky, Zeev. "Optical configuration of pigmented lesion detection by frequency analysis of skin speckle patterns". *Biomedical optics express* 7.3 (2016), pp. 1003–1014.

[86] Dainty, J Christopher. *Laser speckle and related phenomena*. Vol. 9. Springer science & business Media, 2013.

[87] Trivedi, V; Mahajan, S; Chhaniwal, V; Zalevsky, Z; Javidi, B, and Anand, A. "Optical temperature sensor using speckle field". *Sensors and Actuators A: Physical* 216 (2014), pp. 312–317.

[88] Briers, David; Duncan, Donald D; Hirst, Evan R; Kirkpatrick, Sean J; Larsson, Marcus; Steenbergen, Wiendelt; Stromberg, Tomas, and Thompson, Oliver B. "Laser speckle contrast imaging: theoretical and practical limitations". *Journal of biomedical optics* 18.6 (2013), p. 066018.

[89] Reddy, B Srinivasa and Chatterji, Biswanath N. "An FFT-based technique for translation, rotation, and scale-invariant image registration". *IEEE transactions on image processing* 5.8 (1996), pp. 1266–1271.

[90] Tian, Qi and Huhns, Michael N. "Algorithms for subpixel registration". *Computer Vision, Graphics, and Image Processing* 35.2 (1986), pp. 220–233.

[91] Culjat, Martin O; Goldenberg, David; Tewari, Priyamvada, and Singh, Rahul S. "A review of tissue substitutes for ultrasound imaging". *Ultrasound in medicine & biology* 36.6 (2010), pp. 861–873.

[92] Jacques, Steven L. "Coupling 3D Monte Carlo light transport in optically heterogeneous tissues to photoacoustic signal generation". *Photoacoustics* 2.4 (2014), pp. 137–142.

[93] Jacques, Steven L and Paltauf, Guenther. "Modeling pressure waves generated by pulsed laser irradiation of irregularly shaped absorbing objects within media". *Biomedical Optoacoustics II*. Vol. 4256. International Society for Optics and Photonics. 2001, pp. 90–100.

[94] Splinter, Robert and Hooper, Brett A. *An introduction to biomedical optics*. CRC press, 2006.

[95] Yamashita, Y; Hosono, Y, and Itsumi, K. "Low Sound Velocity and Acoustic Attenuation Silicone Rubber Lens Based on Nano-Powder-Composite for Medical Echo Ultrasound Array Probes". *2007 Sixteenth IEEE International Symposium on the Applications of Ferroelectrics*. IEEE. 2007, pp. 752–753.

[96] Wang, Yuehang; Lim, Rachel Su Ann; Zhang, Huijuan; Nyayapathi, Nikhila; Oh, Kwang W, and Xia, Jun. "Optimizing the light delivery of linear-array-based photoacoustic systems by double acoustic reflectors". *Scientific reports* 8.1 (2018), p. 13004.

[97] Wu, Jiabin; Chen, Yunshan; Gao, Shijie; Li, Yimang, and Wu, Zhiyong. "Improved measurement accuracy of spot position on an InGaAs quadrant detector". *Applied Optics* 54.27 (2015), pp. 8049–8054.

[98] Shabairou, Nadav; Lengenfelder, Benjamin; Hohmann, Martin; Klämpfl, Florian; Schmidt, Michael, and Zalevsky, Zeev. "All-optical, an ultra-thin endoscopic photoacoustic sensor using multi-mode fiber". *Scientific Reports* 10.1 (2020), pp. 1–8.

[99] The MathWorks, Inc. *Speckle Size via Autocorrelation*. 2020. https://de.mathworks.com/matlabcentral/fileexchange/25046-speckle-size-via-autocorrelation (visited on 04/01/2020).

[100] The MathWorks, Inc. *Deblur image using blind deconvolution*. 2020. https://www.mathworks.com/help/images/ref/deconvblind.html (visited on 01/23/2020).

[101] Laufer, Jan; Zhang, Edward; Raivich, Gennadij, and Beard, Paul. "Three-dimensional noninvasive imaging of the vasculature in the mouse brain using a high resolution photoacoustic scanner". *Applied optics* 48.10 (2009), pp. D299–D306.

[102] Bosschaart, Nienke; Edelman, Gerda J; Aalders, Maurice CG; Leeuwen, Ton G van, and Faber, Dirk J. "A literature review and novel theoretical approach on the optical properties of whole blood". *Lasers in medical science* 29.2 (2014), pp. 453–479.

[103] AG, Wacker Chemie. *ELASTOSIL RT 604 A/B*. 2020. https://www.wacker.com/h/de-de/siliconkautschuk/raumtemperaturvernetzender-siliconkautschuk-rtv-2/elastosil-rt-604-ab/p/000009552.

[104] Barun, Vladimir V; Ivanov, AP; Volotovskaya, AV, and Ulashchik, VS. "Absorption spectra and light penetration depth of normal and pathologically altered human skin". *Journal of applied spectroscopy* 74.3 (2007), pp. 430–439.

[105] Kim, Jae G; Xia, Mengna, and Liu, Hanli. "Extinction coefficients of hemoglobin for near-infrared spectroscopy of tissue". *IEEE Engineering in Medicine and Biology Magazine* 24.2 (2005), pp. 118–121.

[106] Vo-Dinh, Tuan. *Biomedical photonics handbook: biomedical diagnostics*. CRC press, 2014.

[107] Instruments, Shimadzu Scientific. *ELASTOSIL RT 604 A/B*. 2020. https://www.shimadzu.com/news/c-odogjnooooooimbt.html (visited on 08/03/2020).

[108] Jaeger, Michael; Bamber, Jeffrey C, and Frenz, Martin. "Clutter elimination for deep clinical optoacoustic imaging using localised vibration tagging (LOVIT)". *Photoacoustics* 1.2 (2013), pp. 19–29.

Own publications referring to this work

[P1] Lengenfelder, Benjamin; Hohmann, Martin; Klämpfl, Florian; Zam, Azhar; Weiß, Manuel; Rupitsch, Stefan J; Zalevsky, Zeev, and Schmidt, Michael. "Model for the description of remote photoacoustic sensing using speckle-analysis". *Opto-Acoustic Methods and Applications in Biophotonics IV*. Vol. 11077. International Society for Optics and Photonics. 2019, p. 110771I.

[P2] Lengenfelder, Benjamin; Mehari, Fanuel; Hohmann, Martin; Heinlein, Markus; Chelales, Erika; Waldner, Maximilian J; Klämpfl, Florian; Zalevsky, Zeev, and Schmidt, Michael. "Remote photoacoustic sensing using speckle-analysis". *Scientific reports* 9.1 (2019), pp. 1–11.

[P3] Lengenfelder, Benjamin; Mehari, Fanuel; Hohmann, Martin; Löhr, Cita; Waldner, Maximilian J; Schmidt, Michael; Zalevsky, Zeev, and Klämpfl, Florian. "Contact-free endoscopic photoacoustic sensing using speckle analysis". *Journal of biophotonics* 12.12 (2019), e201900130.

[P4] Lengenfelder, Benjamin; Hohmann, Martin; Späth, Moritz; Scherbaum, Daniel; Weiß, Manuel; Rupitsch, Stefan-J.; Schmidt, Michael; Zalevsky, Zeev, and Klämpfl, Florian. "Remote Photoacoustic Sensing Using Single Speckle Analysis by an Ultra-Fast Four Quadrant Photo-Detector". *Sensors* 21.6 (2021), p. 2109.

[P5] Lengenfelder, Benjamin; Hohmann, Martin; Röhm, Margarete; Schmidt, Michael; Zam, Azhar; Zalevsky, Zeev, and Klämpfl, Florian. "Image reconstruction for remote photoacoustic tomography using speckle-analysis". *Tissue Optics and Photonics*. Vol. 11363. International Society for Optics and Photonics. 2020, 113631F.

Students' theses referring to this work

[S1] Saffer, Judith. "Charakterisierung eines Phantommaterials für photoakustische Messungen zur Nachahmung von Gewebeeigenschaften". Projektarbeit. Friedrich Alexander-Universität Erlangen-Nürnberg, 2016.

[S2] Scherbaum, Daniel. "Remote endoscopic photoacoustic sensing using automated speckle finding". Master thesis. Friedrich Alexander-Universität Erlangen-Nürnberg, 2020.

Reihenübersicht

Koordination der Reihe (Stand 2022):
Geschäftsstelle Maschinenbau, Dr.-Ing. Oliver Kreis, www.mb.fau.de/diss/

Im Rahmen der Reihe sind bisher die nachfolgenden Bände erschienen.

Band 1 – 52
Fertigungstechnik – Erlangen
ISSN 1431-6226
Carl Hanser Verlag, München

Band 53 – 307
Fertigungstechnik – Erlangen
ISSN 1431-6226
Meisenbach Verlag, Bamberg

ab Band 308
FAU Studien aus dem Maschinenbau
ISSN 2625-9974
FAU University Press, Erlangen

Die Zugehörigkeit zu den jeweiligen Lehrstühlen ist wie folgt gekennzeichnet:

Lehrstühle:

FAPS	Lehrstuhl für Fertigungsautomatisierung und Produktionssystematik
FMT	Lehrstuhl für Fertigungsmesstechnik
KTmfk	Lehrstuhl für Konstruktionstechnik
LFT	Lehrstuhl für Fertigungstechnologie
LGT	Lehrstuhl für Gießereitechnik
LPT	Lehrstuhl für Photonische Technologien
REP	Lehrstuhl für Ressourcen- und Energieeffiziente Produktionsmaschinen

Band 1: Andreas Hemberger
Innovationspotentiale in der rechnerintegrierten Produktion durch wissensbasierte Systeme
FAPS, 208 Seiten, 107 Bilder. 1988.
ISBN 3-446-15234-2.

Band 2: Detlef Classe
Beitrag zur Steigerung der Flexibilität automatisierter Montagesysteme durch Sensorintegration und erweiterte Steuerungskonzepte
FAPS, 194 Seiten, 70 Bilder. 1988.
ISBN 3-446-15529-5.

Band 3: Friedrich-Wilhelm Nolting
Projektierung von Montagesystemen
FAPS, 201 Seiten, 107 Bilder, 1 Tab. 1989.ISBN 3-446-15541-4.

Band 4: Karsten Schlüter
Nutzungsgradsteigerung von Montagesystemen durch den Einsatz der Simulationstechnik
FAPS, 177 Seiten, 97 Bilder. 1989.
ISBN 3-446-15542-2.

Band 5: Shir-Kuan Lin
Aufbau von Modellen zur Lageregelung von Industrierobotern
FAPS, 168 Seiten, 46 Bilder. 1989.
ISBN 3-446-15546-5.

Band 6: Rudolf Nuss
Untersuchungen zur Bearbeitungsqualität im Fertigungssystem Laserstrahlschneiden
LFT, 206 Seiten, 115 Bilder, 6 Tab. 1989. ISBN 3-446-15783-2.

Band 7: Wolfgang Scholz
Modell zur datenbankgestützten Planung automatisierter Montageanlagen
FAPS, 194 Seiten, 89 Bilder. 1989.
ISBN 3-446-15825-1.

Band 8: Hans-Jürgen Wißmeier
Beitrag zur Beurteilung des Bruchverhaltens von Hartmetall-Fließpreßmatrizen
LFT, 179 Seiten, 99 Bilder, 9 Tab. 1989. ISBN 3-446-15921-5.

Band 9: Rainer Eisele
Konzeption und Wirtschaftlichkeit von Planungssystemen in der Produktion
FAPS, 183 Seiten, 86 Bilder. 1990.
ISBN 3-446-16107-4.

Band 10: Rolf Pfeiffer
Technologisch orientierte Montageplanung am Beispiel der Schraubtechnik
FAPS, 216 Seiten, 102 Bilder, 16 Tab. 1990. ISBN 3-446-16161-9.

Band 11: Herbert Fischer
Verteilte Planungssysteme zur Flexibilitätssteigerung der rechnerintegrierten Teilefertigung
FAPS, 201 Seiten, 82 Bilder. 1990.
ISBN 3-446-16105-8.

Band 12: Gerhard Kleineidam
CAD/CAP: Rechnergestützte Montagefeinplanung
FAPS, 203 Seiten, 107 Bilder. 1990.
ISBN 3-446-16112-0.

Band 13: Frank Vollertsen
Pulvermetallurgische Verarbeitung eines übereutektoiden verschleißfesten Stahls
LFT, XIII u. 217 Seiten, 67 Bilder, 34 Tab. 1990.
ISBN 3-446-16133-3.

Band 14: Stephan Biermann
Untersuchungen zur Anlagen- und Prozeßdiagnostik für das Schneiden mit CO_2-Hochleistungslasern
LFT, VIII u. 170 Seiten, 93 Bilder, 4 Tab. 1991. ISBN 3-446-16269-0.

Band 15: Uwe Geißler
Material- und Datenfluß in einer flexiblen Blechbearbeitungszelle
LFT, 124 Seiten, 41 Bilder, 7 Tab. 1991. ISBN 3-446-16358-1.

Band 16: Frank Oswald Hake
Entwicklung eines rechnergestützten Diagnosesystems für automatisierte Montagezellen
FAPS, XIV u. 166 Seiten, 77 Bilder. 1991. ISBN 3-446-16428-6.

Band 17: Herbert Reichel
Optimierung der Werkzeugbereitstellung durch rechnergestützte Arbeitsfolgenbestimmung
FAPS, 198 Seiten, 73 Bilder, 2 Tab. 1991. ISBN 3-446-16453-7.

Band 18: Josef Scheller
Modellierung und Einsatz von Softwaresystemen für rechnergeführte Montagezellen
FAPS, 198 Seiten, 65 Bilder. 1991.
ISBN 3-446-16454-5.

Band 19: Arnold vom Ende
Untersuchungen zum Biegeumformen mit elastischer Matrize
LFT, 166 Seiten, 55 Bilder, 13 Tab. 1991. ISBN 3-446-16493-6.

Band 20: Joachim Schmid
Beitrag zum automatisierten Bearbeiten von Keramikguß mit Industrierobotern
FAPS, XIV u. 176 Seiten, 111 Bilder, 6 Tab. 1991.
ISBN 3-446-16560-6.

Band 21: Egon Sommer
Multiprozessorsteuerung für kooperierende Industrieroboter in Montagezellen
FAPS, 188 Seiten, 102 Bilder. 1991.
ISBN 3-446-17062-6.

Band 22: Georg Geyer
Entwicklung problemspezifischer Verfahrensketten in der Montage
FAPS, 192 Seiten, 112 Bilder. 1991.
ISBN 3-446-16552-5.

Band 23: Rainer Flohr
Beitrag zur optimalen Verbindungstechnik in der Oberflächenmontage (SMT)
FAPS, 186 Seiten, 79 Bilder. 1991.
ISBN 3-446-16568-1.

Band 24: Alfons Rief
Untersuchungen zur Verfahrensfolge Laserstrahlschneiden und -schweißen in der Rohkarosseriefertigung
LFT, VI u. 145 Seiten, 58 Bilder, 5 Tab. 1991. ISBN 3-446-16593-2.

Band 25: Christoph Thim
Rechnerunterstützte Optimierung von Materialflußstrukturen in der Elektronikmontage durch Simulation
FAPS, 188 Seiten, 74 Bilder. 1992.
ISBN 3-446-17118-5.

Band 26: Roland Müller
CO_2 -Laserstrahlschneiden von kurzglasverstärkten Verbundwerkstoffen
LFT, 141 Seiten, 107 Bilder, 4 Tab. 1992. ISBN 3-446-17104-5.

Band 27: Günther Schäfer
Integrierte Informationsverarbeitung bei der Montageplanung
FAPS, 195 Seiten, 76 Bilder. 1992.
ISBN 3-446-17117-7.

Band 28: Martin Hoffmann
Entwicklung einerCAD/CAM-Prozeßkette für die Herstellung von Blechbiegeteilen
LFT, 149 Seiten, 89 Bilder. 1992.
ISBN 3-446-17154-1.

Band 29: Peter Hoffmann
Verfahrensfolge Laserstrahlschneiden und –schweißen: Prozeßführung und Systemtechnik in der 3D-Laserstrahlbearbeitung von Blechformteilen
LFT, 186 Seiten, 92 Bilder, 10 Tab. 1992. ISBN 3-446-17153-3.

Band 30: Olaf Schrödel
Flexible Werkstattsteuerung mit objektorientierten Softwarestrukturen
FAPS, 180 Seiten, 84 Bilder. 1992.
ISBN 3-446-17242-4.

Band 31: Hubert Reinisch
Planungs- und Steuerungswerkzeuge zur impliziten Geräteprogrammierung in Roboterzellen
FAPS, XI u. 212 Seiten, 112 Bilder. 1992. ISBN 3-446-17380-3.

Band 32: Brigitte Bärnreuther
Ein Beitrag zur Bewertung des Kommunikationsverhaltens von Automatisierungsgeräten in flexiblen Produktionszellen
FAPS, XI u. 179 Seiten, 71 Bilder. 1992. ISBN 3-446-17451-6.

Band 33: Joachim Hutfless
Laserstrahlregelung und Optikdiagnostik in der Strahlführung einer CO_2-Hochleistungslaseranlage
LFT, 175 Seiten, 70 Bilder, 17 Tab. 1993. ISBN 3-446-17532-6.

Band 34: Uwe Günzel
Entwicklung und Einsatz eines Simula-tionsverfahrens für operative undstrategische Probleme der Produktionsplanung und -steuerung
FAPS, XIV u. 170 Seiten, 66 Bilder, 5 Tab. 1993. ISBN 3-446-17604-7.

Band 35: Bertram Ehmann
Operatives Fertigungscontrolling durch Optimierung auftragsbezogener Bearbeitungsabläufe in der Elektronikfertigung
FAPS, XV u. 167 Seiten, 114 Bilder. 1993. ISBN 3-446-17658-6.

Band 36: Harald Kolléra
Entwicklung eines benutzerorientierten Werkstattprogrammiersystems für das Laserstrahlschneiden
LFT, 129 Seiten, 66 Bilder, 1 Tab. 1993. ISBN 3-446-17719-1.

Band 37: Stephanie Abels
Modellierung und Optimierung von Montageanlagen in einem integrierten Simulationssystem
FAPS, 188 Seiten, 88 Bilder. 1993.
ISBN 3-446-17731-0.

Band 38: Robert Schmidt-Hebbel
Laserstrahlbohren durchflußbestimmender Durchgangslöcher
LFT, 145 Seiten, 63 Bilder, 11 Tab. 1993. ISBN 3-446-17778-7.

Band 39: Norbert Lutz
Oberflächenfeinbearbeitung keramischer Werkstoffe mit XeCl-Excimerlaserstrahlung
LFT, 187 Seiten, 98 Bilder, 29 Tab. 1994. ISBN 3-446-17970-4.

Band 40: Konrad Grampp
Rechnerunterstützung bei Test und Schulung an Steuerungssoftware von SMD-Bestücklinien
FAPS, 178 Seiten, 88 Bilder. 1995.
ISBN 3-446-18173-3.

Band 41: Martin Koch
Wissensbasierte Unterstützung derAngebotsbearbeitung in der Investitionsgüterindustrie
FAPS, 169 Seiten, 68 Bilder. 1995.
ISBN 3-446-18174-1.

Band 42: Armin Gropp
Anlagen- und Prozeßdiagnostik beim Schneiden mit einem gepulsten Nd:YAG-Laser
LFT, 160 Seiten, 88 Bilder, 7 Tab. 1995. ISBN 3-446-18241-1.

Band 43: Werner Heckel
Optische 3D-Konturerfassung und on-line Biegewinkelmessung mit dem Lichtschnittverfahren
LFT, 149 Seiten, 43 Bilder, 11 Tab. 1995. ISBN 3-446-18243-8.

Band 44: Armin Rothhaupt
Modulares Planungssystem zur Optimierung der Elektronikfertigung
FAPS, 180 Seiten, 101 Bilder. 1995.
ISBN 3-446-18307-8.

Band 45: Bernd Zöllner
Adaptive Diagnose in der Elektronikproduktion
FAPS, 195 Seiten, 74 Bilder, 3 Tab. 1995. ISBN 3-446-18308-6.

Band 46: Bodo Vormann
Beitrag zur automatisierten Handhabungsplanung komplexer Blechbiegeteile
LFT, 126 Seiten, 89 Bilder, 3 Tab. 1995. ISBN 3-446-18345-0.

Band 47: Peter Schnepf
Zielkostenorientierte Montageplanung
FAPS, 144 Seiten, 75 Bilder. 1995.
ISBN 3-446-18397-3.

Band 48: Rainer Klotzbücher
Konzept zur rechnerintegrierten Materialversorgung in flexiblen Fertigungssystemen
FAPS, 156 Seiten, 62 Bilder. 1995.
ISBN 3-446-18412-0.

Band 49: Wolfgang Greska
Wissensbasierte Analyse undKlassifizierung von Blechteilen
LFT, 144 Seiten, 96 Bilder. 1995.
ISBN 3-446-18462-7.

Band 50: Jörg Franke
Integrierte Entwicklung neuer Produkt- und Produktionstechnologien für räumliche spritzgegossene Schaltungsträger (3-D MID)
FAPS, 196 Seiten, 86 Bilder, 4 Tab. 1995. ISBN 3-446-18448-1.

Band 51: Franz-Josef Zeller
Sensorplanung und schnelle Sensorregelung für Industrieroboter
FAPS, 190 Seiten, 102 Bilder, 9 Tab. 1995. ISBN 3-446-18601-8.

Band 52: Michael Solvie
Zeitbehandlung und Multimedia-Unterstützung in Feldkommunikationssystemen
FAPS, 200 Seiten, 87 Bilder, 35 Tab. 1996. ISBN 3-446-18607-7.

Band 53: Robert Hopperdietzel
Reengineering in der Elektro- und Elektronikindustrie
FAPS, 180 Seiten, 109 Bilder, 1 Tab. 1996. ISBN 3-87525-070-2.

Band 54: Thomas Rebhahn
Beitrag zur Mikromaterialbearbeitung mit Excimerlasern - Systemkomponenten und Verfahrensoptimierungen
LFT, 148 Seiten, 61 Bilder, 10 Tab. 1996. ISBN 3-87525-075-3.

Band 55: Henning Hanebuth
Laserstrahlhartlöten mit Zweistrahltechnik
LFT, 157 Seiten, 58 Bilder, 11 Tab. 1996. ISBN 3-87525-074-5.

Band 56: Uwe Schönherr
Steuerung und Sensordatenintegration für flexible Fertigungszellen mitkooperierenden Robotern
FAPS, 188 Seiten, 116 Bilder, 3 Tab. 1996. ISBN 3-87525-076-1.

Band 57: Stefan Holzer
Berührungslose Formgebung mit-Laserstrahlung
LFT, 162 Seiten, 69 Bilder, 11 Tab. 1996. ISBN 3-87525-079-6.

Band 58: Markus Schultz
Fertigungsqualität beim 3D-Laserstrahlschweißen vonBlechformteilen
LFT, 165 Seiten, 88 Bilder, 9 Tab. 1997. ISBN 3-87525-080-X.

Band 59: Thomas Krebs
Integration elektromechanischer CA-Anwendungen über einem STEP-Produktmodell
FAPS, 198 Seiten, 58 Bilder, 8 Tab. 1997. ISBN 3-87525-081-8.

Band 60: Jürgen Sturm
Prozeßintegrierte Qualitätssicherung in der Elektronikproduktion
FAPS, 167 Seiten, 112 Bilder, 5 Tab. 1997. ISBN 3-87525-082-6.

Band 61: Andreas Brand
Prozesse und Systeme zur Bestückung räumlicher elektronischer Baugruppen (3D-MID)
FAPS, 182 Seiten, 100 Bilder. 1997. ISBN 3-87525-087-7.

Band 62: Michael Kauf
Regelung der Laserstrahlleistung und der Fokusparameter einer CO_2-Hochleistungslaseranlage
LFT, 140 Seiten, 70 Bilder, 5 Tab. 1997. ISBN 3-87525-083-4.

Band 63: Peter Steinwasser
Modulares Informationsmanagement in der integrierten Produkt- und Prozeßplanung
FAPS, 190 Seiten, 87 Bilder. 1997. ISBN 3-87525-084-2.

Band 64: Georg Liedl
Integriertes Automatisierungskonzept für den flexiblen Materialfluß in der Elektronikproduktion
FAPS, 196 Seiten, 96 Bilder, 3 Tab. 1997. ISBN 3-87525-086-9.

Band 65: Andreas Otto
Transiente Prozesse beim Laserstrahlschweißen
LFT, 132 Seiten, 62 Bilder, 1 Tab. 1997. ISBN 3-87525-089-3.

Band 66: Wolfgang Blöchl
Erweiterte Informationsbereitstellung an offenen CNC-Steuerungen zur Prozeß- und Programmoptimierung
FAPS, 168 Seiten, 96 Bilder. 1997. ISBN 3-87525-091-5.

Band 67: Klaus-Uwe Wolf
Verbesserte Prozeßführung und Prozeßplanung zur Leistungs- und Qualitätssteigerung beim Spulenwickeln
FAPS, 186 Seiten, 125 Bilder. 1997. ISBN 3-87525-092-3.

Band 68: Frank Backes
Technologieorientierte Bahnplanung für die 3D-Laserstrahlbearbeitung
LFT, 138 Seiten, 71 Bilder, 2 Tab. 1997. ISBN 3-87525-093-1.

Band 69: Jürgen Kraus
Laserstrahlumformen von Profilen
LFT, 137 Seiten, 72 Bilder, 8 Tab. 1997. ISBN 3-87525-094-X.

Band 70: Norbert Neubauer
Adaptive Strahlführungen für CO_2-Laseranlagen
LFT, 120 Seiten, 50 Bilder, 3 Tab. 1997. ISBN 3-87525-095-8.

Band 71: Michael Steber
Prozeßoptimierter Betrieb flexibler Schraubstationen in der automatisierten Montage
FAPS, 168 Seiten, 78 Bilder, 3 Tab. 1997. ISBN 3-87525-096-6.

Band 72: Markus Pfestorf
Funktionale 3D-Oberflächenkenngrößen in der Umformtechnik
LFT, 162 Seiten, 84 Bilder, 15 Tab. 1997. ISBN 3-87525-097-4.

Band 73: Volker Franke
Integrierte Planung und Konstruktion von Werkzeugen für die Biegebearbeitung
LFT, 143 Seiten, 81 Bilder. 1998. ISBN 3-87525-098-2.

Band 74: Herbert Scheller
Automatisierte Demontagesysteme und recyclinggerechte Produktgestaltung elektronischer Baugruppen
FAPS, 184 Seiten, 104 Bilder, 17 Tab. 1998. ISBN 3-87525-099-0.

Band 75: Arthur Meßner
Kaltmassivumformung metallischer Kleinstteile – Werkstoffverhalten, Wirkflächenreibung, Prozeßauslegung
LFT, 164 Seiten, 92 Bilder, 14 Tab. 1998. ISBN 3-87525-100-8.

Band 76: Mathias Glasmacher
Prozeß- und Systemtechnik zum Laserstrahl-Mikroschweißen
LFT, 184 Seiten, 104 Bilder, 12 Tab. 1998. ISBN 3-87525-101-6.

Band 77: Michael Schwind
Zerstörungsfreie Ermittlung mechanischer Eigenschaften von Feinblechen mit dem Wirbelstromverfahren
LFT, 124 Seiten, 68 Bilder, 8 Tab. 1998. ISBN 3-87525-102-4.

Band 78: Manfred Gerhard
Qualitätssteigerung in der Elektronikproduktion durch Optimierung der Prozeßführung beim Löten komplexer Baugruppen
FAPS, 179 Seiten, 113 Bilder, 7 Tab. 1998. ISBN 3-87525-103-2.

Band 79: Elke Rauh
Methodische Einbindung der Simulation in die betrieblichen Planungs- und Entscheidungsabläufe
FAPS, 192 Seiten, 114 Bilder, 4 Tab. 1998. ISBN 3-87525-104-0.

Band 80: Sorin Niederkorn
Meßeinrichtung zur Untersuchung der Wirkflächenreibung bei umformtechnischen Prozessen
LFT, 99 Seiten, 46 Bilder, 6 Tab. 1998. ISBN 3-87525-105-9.

Band 81: Stefan Schuberth
Regelung der Fokuslage beim Schweißen mit CO_2-Hochleistungslasern unter Einsatz von adaptiven Optiken
LFT, 140 Seiten, 64 Bilder, 3 Tab. 1998. ISBN 3-87525-106-7.

Band 82: Armando Walter Colombo
Development and Implementation of Hierarchical Control Structures of Flexible Production Systems Using High Level Petri Nets
FAPS, 216 Seiten, 86 Bilder. 1998. ISBN 3-87525-109-1.

Band 83: Otto Meedt
Effizienzsteigerung bei Demontage und Recycling durch flexible Demontagetechnologien und optimierte Produktgestaltung
FAPS, 186 Seiten, 103 Bilder. 1998. ISBN 3-87525-108-3.

Band 84: Knuth Götz
Modelle und effiziente Modellbildung zur Qualitätssicherung in der Elektronikproduktion
FAPS, 212 Seiten, 129 Bilder, 24 Tab. 1998. ISBN 3-87525-112-1.

Band 85: Ralf Luchs
Einsatzmöglichkeiten leitender Klebstoffe zur zuverlässigen Kontaktierung elektronischer Bauelemente in der SMT
FAPS, 176 Seiten, 126 Bilder, 30 Tab. 1998. ISBN 3-87525-113-7.

Band 86: Frank Pöhlau
Entscheidungsgrundlagen zur Einführung räumlicher spritzgegossener Schaltungsträger (3-D MID)
FAPS, 144 Seiten, 99 Bilder. 1999. ISBN 3-87525-114-8.

Band 87: Roland T. A. Kals
Fundamentals on the miniaturization of sheet metal working processes
LFT, 128 Seiten, 58 Bilder, 11 Tab. 1999. ISBN 3-87525-115-6.

Band 88: Gerhard Luhn
Implizites Wissen und technisches Handeln am Beispiel der Elektronikproduktion
FAPS, 252 Seiten, 61 Bilder, 1 Tab. 1999. ISBN 3-87525-116-4.

Band 89: Axel Sprenger
Adaptives Streckbiegen von Aluminium-Strangpreßprofilen
LFT, 114 Seiten, 63 Bilder, 4 Tab. 1999. ISBN 3-87525-117-2.

Band 90: Hans-Jörg Pucher
Untersuchungen zur Prozeßfolge Umformen, Bestücken und Laserstrahllöten von Mikrokontakten
LFT, 158 Seiten, 69 Bilder, 9 Tab. 1999. ISBN 3-87525-119-9.

Band 91: Horst Arnet
Profilbiegen mit kinematischer Gestalterzeugung
LFT, 128 Seiten, 67 Bilder, 7 Tab. 1999. ISBN 3-87525-120-2.

Band 92: Doris Schubart
Prozeßmodellierung und Technologieentwicklung beim Abtragen mit CO_2-Laserstrahlung
LFT, 133 Seiten, 57 Bilder, 13 Tab. 1999. ISBN 3-87525-122-9.

Band 93: Adrianus L. P. Coremans
Laserstrahlsintern von Metallpulver - Prozeßmodellierung, Systemtechnik, Eigenschaften laserstrahlgesinterter Metallkörper
LFT, 184 Seiten, 108 Bilder, 12 Tab. 1999. ISBN 3-87525-124-5.

Band 94: Hans-Martin Biehler
Optimierungskonzepte für Qualitätsdatenverarbeitung und Informationsbereitstellung in der Elektronikfertigung
FAPS, 194 Seiten, 105 Bilder. 1999. ISBN 3-87525-126-1.

Band 95: Wolfgang Becker
Oberflächenausbildung und tribologische Eigenschaften excimerlaserstrahlbearbeiteter Hochleistungskeramiken
LFT, 175 Seiten, 71 Bilder, 3 Tab. 1999. ISBN 3-87525-127-X.

Band 96: Philipp Hein
Innenhochdruck-Umformen von Blechpaaren: Modellierung, Prozeßauslegung und Prozeßführung
LFT, 129 Seiten, 57 Bilder, 7 Tab. 1999. ISBN 3-87525-128-8.

Band 97: Gunter Beitinger
Herstellungs- und Prüfverfahren für thermoplastische Schaltungsträger
FAPS, 169 Seiten, 92 Bilder, 20 Tab. 1999. ISBN 3-87525-129-6.

Band 98: Jürgen Knoblach
Beitrag zur rechnerunterstützten verursachungsgerechten Angebotskalkulation von Blechteilen mit Hilfe wissensbasierter Methoden
LFT, 155 Seiten, 53 Bilder, 26 Tab. 1999. ISBN 3-87525-130-X.

Band 99: Frank Breitenbach
Bildverarbeitungssystem zur Erfassung der Anschlußgeometrie elektronischer SMT-Bauelemente
LFT, 147 Seiten, 92 Bilder, 12 Tab. 2000. ISBN 3-87525-131-8.

Band 100: Bernd Falk
Simulationsbasierte Lebensdauervorhersage für Werkzeuge der Kaltmassivumformung
LFT, 134 Seiten, 44 Bilder, 15 Tab. 2000. ISBN 3-87525-136-9.

Band 101: Wolfgang Schlögl
Integriertes Simulationsdaten-Management für Maschinenentwicklung und Anlagenplanung
FAPS, 169 Seiten, 101 Bilder, 20 Tab. 2000. ISBN 3-87525-137-7.

Band 102: Christian Hinsel
Ermüdungsbruchversagen hartstoffbeschichteter Werkzeugstähle in der Kaltmassivumformung
LFT, 130 Seiten, 80 Bilder, 14 Tab. 2000. ISBN 3-87525-138-5.

Band 103: Stefan Bobbert
Simulationsgestützte Prozessauslegung für das Innenhochdruck-Umformen von Blechpaaren
LFT, 123 Seiten, 77 Bilder. 2000. ISBN 3-87525-145-8.

Band 104: Harald Rottbauer
Modulares Planungswerkzeug zum Produktionsmanagement in der Elektronikproduktion
FAPS, 166 Seiten, 106 Bilder. 2001.
ISBN 3-87525-139-3.

Band 105: Thomas Hennige
Flexible Formgebung von Blechen durch Laserstrahlumformen
LFT, 119 Seiten, 50 Bilder. 2001.
ISBN 3-87525-140-7.

Band 106: Thomas Menzel
Wissensbasierte Methoden für die rechnergestützte Charakterisierung und Bewertung innovativer Fertigungsprozesse
LFT, 152 Seiten, 71 Bilder. 2001.
ISBN 3-87525-142-3.

Band 107: Thomas Stöckel
Kommunikationstechnische Integration der Prozeßebene in Produktionssysteme durch Middleware-Frameworks
FAPS, 147 Seiten, 65 Bilder, 5 Tab.
2001. ISBN 3-87525-143-1.

Band 108: Frank Pitter
Verfügbarkeitssteigerung von Werkzeugmaschinen durch Einsatz mechatronischer Sensorlösungen
FAPS, 158 Seiten, 131 Bilder, 8 Tab.
2001. ISBN 3-87525-144-X.

Band 109: Markus Korneli
Integration lokaler CAP-Systeme in einen globalen Fertigungsdatenverbund
FAPS, 121 Seiten, 53 Bilder, 11 Tab.
2001. ISBN 3-87525-146-6.

Band 110: Burkhard Müller
Laserstrahljustieren mit Excimer-Lasern - Prozeßparameter und Modelle zur Aktorkonstruktion
LFT, 128 Seiten, 36 Bilder, 9 Tab.
2001. ISBN 3-87525-159-8.

Band 111: Jürgen Göhringer
Integrierte Telediagnose via Internet zum effizienten Service von Produktionssystemen
FAPS, 178 Seiten, 98 Bilder, 5 Tab.
2001. ISBN 3-87525-147-4.

Band 112: Robert Feuerstein
Qualitäts- und kosteneffiziente Integration neuer Bauelementetechnologien in die Flachbaugruppenfertigung
FAPS, 161 Seiten, 99 Bilder, 10 Tab.
2001. ISBN 3-87525-151-2.

Band 113: Marcus Reichenberger
Eigenschaften und Einsatzmöglichkeiten alternativer Elektroniklote in der Oberflächenmontage (SMT)
FAPS, 165 Seiten, 97 Bilder, 18 Tab.
2001. ISBN 3-87525-152-0.

Band 114: Alexander Huber
Justieren vormontierter Systeme mit dem Nd:YAG-Laser unter Einsatz von Aktoren
LFT, 122 Seiten, 58 Bilder, 5 Tab.
2001. ISBN 3-87525-153-9.

Band 115: Sami Krimi
Analyse und Optimierung von Montagesystemen in der Elektronikproduktion
FAPS, 155 Seiten, 88 Bilder, 3 Tab.
2001. ISBN 3-87525-157-1.

Band 116: Marion Merklein
Laserstrahlumformen von Aluminiumwerkstoffen - Beeinflussung der Mikrostruktur und der mechanischen Eigenschaften
LFT, 122 Seiten, 65 Bilder, 15 Tab.
2001. ISBN 3-87525-156-3.

Band 117: Thomas Collisi
Ein informationslogistisches Architekturkonzept zur Akquisition simulationsrelevanter Daten
FAPS, 181 Seiten, 105 Bilder, 7 Tab.
2002. ISBN 3-87525-164-4.

Band 118: Markus Koch
Rationalisierung und ergonomische Optimierung im Innenausbau durch den Einsatz moderner Automatisierungstechnik
FAPS, 176 Seiten, 98 Bilder, 9 Tab.
2002. ISBN 3-87525-165-2.

Band 119: Michael Schmidt
Prozeßregelung für das Laserstrahl-Punktschweißen in der Elektronikproduktion
LFT, 152 Seiten, 71 Bilder, 3 Tab.
2002. ISBN 3-87525-166-0.

Band 120: Nicolas Tiesler
Grundlegende Untersuchungen zum Fließpressen metallischer Kleinstteile
LFT, 126 Seiten, 78 Bilder, 12 Tab.
2002. ISBN 3-87525-175-X.

Band 121: Lars Pursche
Methoden zur technologieorientierten Programmierung für die 3D-Lasermikrobearbeitung
LFT, 111 Seiten, 39 Bilder, 0 Tab.
2002. ISBN 3-87525-183-0.

Band 122: Jan-Oliver Brassel
Prozeßkontrolle beim Laserstrahl-Mikroschweißen
LFT, 148 Seiten, 72 Bilder, 12 Tab.
2002. ISBN 3-87525-181-4.

Band 123: Mark Geisel
Prozeßkontrolle und -steuerung beim Laserstrahlschweißen mit den Methoden der nichtlinearen Dynamik
LFT, 135 Seiten, 46 Bilder, 2 Tab.
2002. ISBN 3-87525-180-6.

Band 124: Gerd Eßer
Laserstrahlunterstützte Erzeugung metallischer Leiterstrukturen auf Thermoplastsubstraten für die MID-Technik
LFT, 148 Seiten, 60 Bilder, 6 Tab.
2002. ISBN 3-87525-171-7.

Band 125: Marc Fleckenstein
Qualität laserstrahl-gefügter Mikroverbindungen elektronischer Kontakte
LFT, 159 Seiten, 77 Bilder, 7 Tab.
2002. ISBN 3-87525-170-9.

Band 126: Stefan Kaufmann
Grundlegende Untersuchungen zum Nd:YAG- Laserstrahlfügen von Silizium für Komponenten der Optoelektronik
LFT, 159 Seiten, 100 Bilder, 6 Tab.
2002. ISBN 3-87525-172-5.

Band 127: Thomas Fröhlich
Simultanes Löten von Anschlußkontakten elektronischer Bauelemente mit Diodenlaserstrahlung
LFT, 143 Seiten, 75 Bilder, 6 Tab.
2002. ISBN 3-87525-186-5.

Band 128: Achim Hofmann
Erweiterung der Formgebungsgrenzen beim Umformen von Aluminiumwerkstoffen durch den Einsatz prozessangepasster Platinen
LFT, 113 Seiten, 58 Bilder, 4 Tab. 2002. ISBN 3-87525-182-2.

Band 129: Ingo Kriebitzsch
3 - D MID Technologie in der Automobilelektronik
FAPS, 129 Seiten, 102 Bilder, 10 Tab. 2002. ISBN 3-87525-169-5.

Band 130: Thomas Pohl
Fertigungsqualität und Umformbarkeit laserstrahlgeschweißter Formplatinen aus Aluminiumlegierungen
LFT, 133 Seiten, 93 Bilder, 12 Tab. 2002. ISBN 3-87525-173-3.

Band 131: Matthias Wenk
Entwicklung eines konfigurierbaren Steuerungssystems für die flexible Sensorführung von Industrierobotern
FAPS, 167 Seiten, 85 Bilder, 1 Tab. 2002. ISBN 3-87525-174-1.

Band 132: Matthias Negendanck
Neue Sensorik und Aktorik für Bearbeitungsköpfe zum Laserstrahlschweißen
LFT, 116 Seiten, 60 Bilder, 14 Tab. 2002. ISBN 3-87525-184-9.

Band 133: Oliver Kreis
Integrierte Fertigung - Verfahrensintegration durch Innenhochdruck-Umformen, Trennen und Laserstrahlschweißen in einem Werkzeug sowie ihre tele- und multimediale Präsentation
LFT, 167 Seiten, 90 Bilder, 43 Tab. 2002. ISBN 3-87525-176-8.

Band 134: Stefan Trautner
Technische Umsetzung produktbezogener Instrumente der Umweltpolitik bei Elektro- und Elektronikgeräten
FAPS, 179 Seiten, 92 Bilder, 11 Tab. 2002. ISBN 3-87525-177-6.

Band 135: Roland Meier
Strategien für einen produktorientierten Einsatz räumlicher spritzgegossener Schaltungsträger (3-D MID)
FAPS, 155 Seiten, 88 Bilder, 14 Tab. 2002. ISBN 3-87525-178-4.

Band 136: Jürgen Wunderlich
Kostensimulation - Simulationsbasierte Wirtschaftlichkeitsregelung komplexer Produktionssysteme
FAPS, 202 Seiten, 119 Bilder, 17 Tab. 2002. ISBN 3-87525-179-2.

Band 137: Stefan Novotny
Innenhochdruck-Umformen von Blechen aus Aluminium- und Magnesiumlegierungen bei erhöhter Temperatur
LFT, 132 Seiten, 82 Bilder, 6 Tab. 2002. ISBN 3-87525-185-7.

Band 138: Andreas Licha
Flexible Montageautomatisierung zur Komplettmontage flächenhafter Produktstrukturen durch kooperierende Industrieroboter
FAPS, 158 Seiten, 87 Bilder, 8 Tab. 2003. ISBN 3-87525-189-X.

Band 139: Michael Eisenbarth
Beitrag zur Optimierung der Aufbau- und Verbindungstechnik für mechatronische Baugruppen
FAPS, 207 Seiten, 141 Bilder, 9 Tab. 2003. ISBN 3-87525-190-3.

Band 140: Frank Christoph
Durchgängige simulationsgestützte Planung von Fertigungseinrichtungen der Elektronikproduktion
FAPS, 187 Seiten, 107 Bilder, 9 Tab. 2003. ISBN 3-87525-191-1.

Band 141: Hinnerk Hagenah
Simulationsbasierte Bestimmung der zu erwartenden Maßhaltigkeit für das Blechbiegen
LFT, 131 Seiten, 36 Bilder, 26 Tab. 2003. ISBN 3-87525-192-X.

Band 142: Ralf Eckstein
Scherschneiden und Biegen metallischer Kleinstteile - Materialeinfluss und Materialverhalten
LFT, 148 Seiten, 71 Bilder, 19 Tab. 2003. ISBN 3-87525-193-8.

Band 143: Frank H. Meyer-Pittroff
Excimerlaserstrahlbiegen dünner metallischer Folien mit homogener Lichtlinie
LFT, 138 Seiten, 60 Bilder, 16 Tab. 2003. ISBN 3-87525-196-2.

Band 144: Andreas Kach
Rechnergestützte Anpassung von Laserstrahlschneidbahnen an Bauteilabweichungen
LFT, 139 Seiten, 69 Bilder, 11 Tab. 2004. ISBN 3-87525-197-0.

Band 145: Stefan Hierl
System- und Prozeßtechnik für das simultane Löten mit Diodenlaserstrahlung von elektronischen Bauelementen
LFT, 124 Seiten, 66 Bilder, 4 Tab. 2004. ISBN 3-87525-198-9.

Band 146: Thomas Neudecker
Tribologische Eigenschaften keramischer Blechumformwerkzeuge-Einfluss einer Oberflächenendbearbeitung mittels Excimerlaserstrahlung
LFT, 166 Seiten, 75 Bilder, 26 Tab. 2004. ISBN 3-87525-200-4.

Band 147: Ulrich Wenger
Prozessoptimierung in der Wickeltechnik durch innovative maschinenbauliche und regelungstechnische Ansätze
FAPS, 132 Seiten, 88 Bilder, 0 Tab. 2004. ISBN 3-87525-203-9.

Band 148: Stefan Slama
Effizienzsteigerung in der Montage durch marktorientierte Montagestrukturen und erweiterte Mitarbeiterkompetenz
FAPS, 188 Seiten, 125 Bilder, 0 Tab. 2004. ISBN 3-87525-204-7.

Band 149: Thomas Wurm
Laserstrahljustieren mittels Aktoren-Entwicklung von Konzepten und Methoden für die rechnerunterstützte Modellierung und Optimierung von komplexen Aktorsystemen in der Mikrotechnik
LFT, 122 Seiten, 51 Bilder, 9 Tab. 2004. ISBN 3-87525-206-3.

Band 150: Martino Celeghini
Wirkmedienbasierte Blechumformung: Grundlagenuntersuchungen zum Einfluss von Werkstoff und Bauteilgeometrie
LFT, 146 Seiten, 77 Bilder, 6 Tab.
2004. ISBN 3-87525-207-1.

Band 151: Ralph Hohenstein
Entwurf hochdynamischer Sensor- und Regelsysteme für die adaptiveLaserbearbeitung
LFT, 282 Seiten, 63 Bilder, 16 Tab.
2004. ISBN 3-87525-210-1.

Band 152: Angelika Hutterer
Entwicklung prozessüberwachender Regelkreise für flexible Formgebungsprozesse
LFT, 149 Seiten, 57 Bilder, 2 Tab.
2005. ISBN 3-87525-212-8.

Band 153: Emil Egerer
Massivumformen metallischer Kleinstteile bei erhöhter Prozesstemperatur
LFT, 158 Seiten, 87 Bilder, 10 Tab.
2005. ISBN 3-87525-213-6.

Band 154: Rüdiger Holzmann
Strategien zur nachhaltigen Optimierung von Qualität und Zuverlässigkeit in der Fertigung hochintegrierter Flachbaugruppen
FAPS, 186 Seiten, 99 Bilder, 19 Tab.
2005. ISBN 3-87525-217-9.

Band 155: Marco Nock
Biegeumformen mit Elastomerwerkzeugen Modellierung, Prozessauslegung und Abgrenzung des Verfahrens am Beispiel des Rohrbiegens
LFT, 164 Seiten, 85 Bilder, 13 Tab.
2005. ISBN 3-87525-218-7.

Band 156: Frank Niebling
Qualifizierung einer Prozesskette zum Laserstrahlsintern metallischer Bauteile
LFT, 148 Seiten, 89 Bilder, 3 Tab.
2005. ISBN 3-87525-219-5.

Band 157: Markus Meiler
Großserientauglichkeit trockenschmierstoffbeschichteter Aluminiumbleche im Presswerk Grundlegende Untersuchungen zur Tribologie, zum Umformverhalten und Bauteilversuche
LFT, 104 Seiten, 57 Bilder, 21 Tab.
2005. ISBN 3-87525-221-7.

Band 158: Agus Sutanto
Solution Approaches for Planning of Assembly Systems in Three-Dimensional Virtual Environments
FAPS, 169 Seiten, 98 Bilder, 3 Tab.
2005. ISBN 3-87525-220-9.

Band 159: Matthias Boiger
Hochleistungssysteme für die Fertigung elektronischer Baugruppen auf der Basis flexibler Schaltungsträger
FAPS, 175 Seiten, 111 Bilder, 8 Tab.
2005. ISBN 3-87525-222-5.

Band 160: Matthias Pitz
Laserunterstütztes Biegen höchstfester Mehrphasenstähle
LFT, 120 Seiten, 73 Bilder, 11 Tab.
2005. ISBN 3-87525-223-3.

Band 161: Meik Vahl
Beitrag zur gezielten Beeinflussung des Werkstoffflusses beim Innenhochdruck-Umformen von Blechen
LFT, 165 Seiten, 94 Bilder, 15 Tab.
2005. ISBN 3-87525-224-1.

Band 162: Peter K. Kraus
Plattformstrategien - Realisierung einer varianz- und kostenoptimierten Wertschöpfung
FAPS, 181 Seiten, 95 Bilder, 0 Tab.
2005. ISBN 3-87525-226-8.

Band 163: Adrienn Cser
Laserstrahlschmelzabtrag - Prozessanalyse und -modellierung
LFT, 146 Seiten, 79 Bilder, 3 Tab.
2005. ISBN 3-87525-227-6.

Band 164: Markus C. Hahn
Grundlegende Untersuchungen zur Herstellung von Leichtbauverbundstrukturen mit Aluminiumschaumkern
LFT, 143 Seiten, 60 Bilder, 16 Tab.
2005. ISBN 3-87525-228-4.

Band 165: Gordana Michos
Mechatronische Ansätze zur Optimierung von Vorschubachsen
FAPS, 146 Seiten, 87 Bilder, 17 Tab.
2005. ISBN 3-87525-230-6.

Band 166: Markus Stark
Auslegung und Fertigung hochpräziser Faser-Kollimator-Arrays
LFT, 158 Seiten, 115 Bilder, 11 Tab.
2005. ISBN 3-87525-231-4.

Band 167: Yurong Zhou
Kollaboratives Engineering Management in der integrierten virtuellen Entwicklung der Anlagen für die Elektronikproduktion
FAPS, 156 Seiten, 84 Bilder, 6 Tab.
2005. ISBN 3-87525-232-2.

Band 168: Werner Enser
Neue Formen permanenter und lösbarer elektrischer Kontaktierungen für mechatronische Baugruppen
FAPS, 190 Seiten, 112 Bilder, 5 Tab.
2005. ISBN 3-87525-233-0.

Band 169: Katrin Melzer
Integrierte Produktpolitik bei elektrischen und elektronischen Geräten zur Optimierung des Product-Life-Cycle
FAPS, 155 Seiten, 91 Bilder, 17 Tab.
2005. ISBN 3-87525-234-9.

Band 170: Alexander Putz
Grundlegende Untersuchungen zur Erfassung der realen Vorspannung von armierten Kaltfließpresswerkzeugen mittels Ultraschall
LFT, 137 Seiten, 71 Bilder, 15 Tab.
2006. ISBN 3-87525-237-3.

Band 171: Martin Prechtl
Automatisiertes Schichtverfahren für metallische Folien - System- und Prozesstechnik
LFT, 154 Seiten, 45 Bilder, 7 Tab.
2006. ISBN 3-87525-238-1.

Band 172: Markus Meidert
Beitrag zur deterministischen Lebensdauerabschätzung von Werkzeugen der Kaltmassivumformung
LFT, 131 Seiten, 78 Bilder, 9 Tab.
2006. ISBN 3-87525-239-X.

Band 173: Bernd Müller
Robuste, automatisierte Montagesysteme durch adaptive Prozessführung und montageübergreifende Fehlerprävention am Beispiel flächiger Leichtbauteile
FAPS, 147 Seiten, 77 Bilder, 0 Tab.
2006. ISBN 3-87525-240-3.

Band 174: Alexander Hofmann
Hybrides Laserdurchstrahlschweißen von Kunststoffen
LFT, 136 Seiten, 72 Bilder, 4 Tab.
2006. ISBN 978-3-87525-243-9.

Band 175: Peter Wölflick
Innovative Substrate und Prozesse mit feinsten Strukturen für bleifreie Mechatronik-Anwendungen
FAPS, 177 Seiten, 148 Bilder, 24 Tab. 2006.
ISBN 978-3-87525-246-0.

Band 176: Attila Komlodi
Detection and Prevention of Hot Cracks during Laser Welding of Aluminium Alloys Using Advanced Simulation Methods
LFT, 155 Seiten, 89 Bilder, 14 Tab. 2006. ISBN 978-3-87525-248-4.

Band 177: Uwe Popp
Grundlegende Untersuchungen zum Laserstrahlstrukturieren von Kaltmassivumformwerkzeugen
LFT, 140 Seiten, 67 Bilder, 16 Tab. 2006. ISBN 978-3-87525-249-1.

Band 178: Veit Rückel
Rechnergestützte Ablaufplanung und Bahngenerierung Für kooperierende Industrieroboter
FAPS, 148 Seiten, 75 Bilder, 7 Tab. 2006. ISBN 978-3-87525-250-7.

Band 179: Manfred Dirscherl
Nicht-thermische Mikrojustiertechnik mittels ultrakurzer Laserpulse
LFT, 154 Seiten, 69 Bilder, 10 Tab. 2007. ISBN 978-3-87525-251-4.

Band 180: Yong Zhuo
Entwurf eines rechnergestützten integrierten Systems für Konstruktion und Fertigungsplanung räumlicher spritzgegossener Schaltungsträger (3D-MID)
FAPS, 181 Seiten, 95 Bilder, 5 Tab. 2007. ISBN 978-3-87525-253-8.

Band 181: Stefan Lang
Durchgängige Mitarbeiterinformation zur Steigerung von Effizienz und Prozesssicherheit in der Produktion
FAPS, 172 Seiten, 93 Bilder. 2007. ISBN 978-3-87525-257-6.

Band 182: Hans-Joachim Krauß
Laserstrahlinduzierte Pyrolyse präkeramischer Polymere
LFT, 171 Seiten, 100 Bilder. 2007. ISBN 978-3-87525-258-3.

Band 183: Stefan Junker
Technologien und Systemlösungen für die flexibel automatisierte Bestückung permanent erregter Läufer mit oberflächenmontierten Dauermagneten
FAPS, 173 Seiten, 75 Bilder. 2007. ISBN 978-3-87525-259-0.

Band 184: Rainer Kohlbauer
Wissensbasierte Methoden für die simulationsgestützte Auslegung wirkmedienbasierter Blechumformprozesse
LFT, 135 Seiten, 50 Bilder. 2007. ISBN 978-3-87525-260-6.

Band 185: Klaus Lamprecht
Wirkmedienbasierte Umformung tiefgezogener Vorformen unter besonderer Berücksichtigung maßgeschneiderter Halbzeuge
LFT, 137 Seiten, 81 Bilder. 2007. ISBN 978-3-87525-265-1.

Band 186: Bernd Zolleiß
Optimierte Prozesse und Systeme für die Bestückung mechatronischerBaugruppen
FAPS, 180 Seiten, 117 Bilder. 2007. ISBN 978-3-87525-266-8.

Band 187: Michael Kerausch
Simulationsgestützte Prozessauslegung für das Umformen lokal wärmebehandelter Aluminiumplatinen
LFT, 146 Seiten, 76 Bilder, 7 Tab. 2007. ISBN 978-3-87525-267-5.

Band 188: Matthias Weber
Unterstützung der Wandlungsfähigkeit von Produktionsanlagen durch innovative Softwaresysteme
FAPS, 183 Seiten, 122 Bilder, 3 Tab. 2007. ISBN 978-3-87525-269-9.

Band 189: Thomas Frick
Untersuchung der prozessbestimmenden Strahl-Stoff-Wechselwirkungen beim Laserstrahlschweißen von Kunststoffen
LFT, 104 Seiten, 62 Bilder, 8 Tab. 2007. ISBN 978-3-87525-268-2.

Band 190: Joachim Hecht
Werkstoffcharakterisierung und Prozessauslegung für die wirkmedienbasierte Doppelblech-Umformung von Magnesiumlegierungen
LFT, 107 Seiten, 91 Bilder, 2 Tab. 2007. ISBN 978-3-87525-270-5.

Band 191: Ralf Völkl
Stochastische Simulation zur Werkzeuglebensdaueroptimierung und Präzisionsfertigung in der Kaltmassivumformung
LFT, 178 Seiten, 75 Bilder, 12 Tab. 2008. ISBN 978-3-87525-272-9.

Band 192: Massimo Tolazzi
Innenhochdruck-Umformen verstärkter Blech-Rahmenstrukturen
LFT, 164 Seiten, 85 Bilder, 7 Tab. 2008. ISBN 978-3-87525-273-6.

Band 193: Cornelia Hoff
Untersuchung der Prozesseinflussgrößen beim Presshärten des höchstfesten Vergütungsstahls 22MnB5
LFT, 133 Seiten, 92 Bilder, 5 Tab. 2008. ISBN 978-3-87525-275-0.

Band 194: Christian Alvarez
Simulationsgestützte Methoden zur effizienten Gestaltung von Lötprozessen in der Elektronikproduktion
FAPS, 149 Seiten, 86 Bilder, 8 Tab. 2008. ISBN 978-3-87525-277-4.

Band 195: Andreas Kunze
Automatisierte Montage von makromechatronischen Modulen zur flexiblen Integration in hybride Pkw-Bordnetzsysteme
FAPS, 160 Seiten, 90 Bilder, 14 Tab. 2008.
ISBN 978-3-87525-278-1.

Band 196: Wolfgang Hußnätter
Grundlegende Untersuchungen zur experimentellen Ermittlung und zur Modellierung von Fließortkurven bei erhöhten Temperaturen
LFT, 152 Seiten, 73 Bilder, 21 Tab. 2008. ISBN 978-3-87525-279-8.

Band 197: Thomas Bigl
Entwicklung, angepasste Herstellungsverfahren und erweiterte Qualitätssicherung von einsatzgerechten elektronischen Baugruppen
FAPS, 175 Seiten, 107 Bilder, 14 Tab. 2008.
ISBN 978-3-87525-280-4.

Band 198: Stephan Roth
Grundlegende Untersuchungen zum Excimerlaserstrahl-Abtragen unter Flüssigkeitsfilmen
LFT, 113 Seiten, 47 Bilder, 14 Tab. 2008. ISBN 978-3-87525-281-1.

Band 199: Artur Giera
Prozesstechnische Untersuchungen zum Rührreibschweißen metallischer Werkstoffe
LFT, 179 Seiten, 104 Bilder, 36 Tab. 2008. ISBN 978-3-87525-282-8.

Band 200: Jürgen Lechler
Beschreibung und Modellierung des Werkstoffverhaltens von presshärtbaren Bor-Manganstählen
LFT, 154 Seiten, 75 Bilder, 12 Tab. 2009. ISBN 978-3-87525-286-6.

Band 201: Andreas Blankl
Untersuchungen zur Erhöhung der Prozessrobustheit bei der Innenhochdruck-Umformung von flächigen Halbzeugen mit vor- bzw. nachgeschalteten Laserstrahlfügeoperationen
LFT, 120 Seiten, 68 Bilder, 9 Tab. 2009. ISBN 978-3-87525-287-3.

Band 202: Andreas Schaller
Modellierung eines nachfrageorientierten Produktionskonzeptes für mobile Telekommunikationsgeräte
FAPS, 120 Seiten, 79 Bilder, 0 Tab. 2009. ISBN 978-3-87525-289-7.

Band 203: Claudius Schimpf
Optimierung von Zuverlässigkeitsuntersuchungen, Prüfabläufen und Nacharbeitsprozessen in der Elektronikproduktion
FAPS, 162 Seiten, 90 Bilder, 14 Tab. 2009.
ISBN 978-3-87525-290-3.

Band 204: Simon Dietrich
Sensoriken zur Schwerpunktslagebestimmung der optischen Prozessemissionen beim Laserstrahltiefschweißen
LFT, 138 Seiten, 70 Bilder, 5 Tab. 2009. ISBN 978-3-87525-292-7.

Band 205: Wolfgang Wolf
Entwicklung eines agentenbasierten Steuerungssystems zur Materialflussorganisation im wandelbaren Produktionsumfeld
FAPS, 167 Seiten, 98 Bilder. 2009. ISBN 978-3-87525-293-4.

Band 206: Steffen Polster
Laserdurchstrahlschweißen transparenter Polymerbauteile
LFT, 160 Seiten, 92 Bilder, 13 Tab. 2009. ISBN 978-3-87525-294-1.

Band 207: Stephan Manuel Dörfler
Rührreibschweißen von walzplattiertem Halbzeug und Aluminiumblech zur Herstellung flächiger Aluminiumschaum-Sandwich-Verbundstrukturen
LFT, 190 Seiten, 98 Bilder, 5 Tab. 2009. ISBN 978-3-87525-295-8.

Band 208: Uwe Vogt
Seriennahe Auslegung von Aluminium Tailored Heat Treated Blanks
LFT, 151 Seiten, 68 Bilder, 26 Tab. 2009. ISBN 978-3-87525-296-5.

Band 209: Till Laumann
Qualitative und quantitative Bewertung der Crashtauglichkeit von höchstfesten Stählen
LFT, 117 Seiten, 69 Bilder, 7 Tab. 2009. ISBN 978-3-87525-299-6.

Band 210: Alexander Diehl
Größeneffekte bei Biegeprozessen-Entwicklung einer Methodik zur Identifikation und Quantifizierung
LFT, 180 Seiten, 92 Bilder, 12 Tab. 2010. ISBN 978-3-87525-302-3.

Band 211: Detlev Staud
Effiziente Prozesskettenauslegung für das Umformen lokal wärmebehandelter und geschweißter Aluminiumbleche
LFT, 164 Seiten, 72 Bilder, 12 Tab. 2010. ISBN 978-3-87525-303-0.

Band 212: Jens Ackermann
Prozesssicherung beim Laserdurchstrahlschweißen thermoplastischer Kunststoffe
LPT, 129 Seiten, 74 Bilder, 13 Tab. 2010. ISBN 978-3-87525-305-4.

Band 213: Stephan Weidel
Grundlegende Untersuchungen zum Kontaktzustand zwischen Werkstück und Werkzeug bei umformtechnischen Prozessen unter tribologischen Gesichtspunkten
LFT, 144 Seiten, 67 Bilder, 11 Tab. 2010. ISBN 978-3-87525-307-8.

Band 214: Stefan Geißdörfer
Entwicklung eines mesoskopischen Modells zur Abbildung von Größeneffekten in der Kaltmassivumformung mit Methoden der FE-Simulation
LFT, 133 Seiten, 83 Bilder, 11 Tab. 2010. ISBN 978-3-87525-308-5.

Band 215: Christian Matzner
Konzeption produktspezifischer Lösungen zur Robustheitssteigerung elektronischer Systeme gegen die Einwirkung von Betauung im Automobil
FAPS, 165 Seiten, 93 Bilder, 14 Tab. 2010. ISBN 978-3-87525-309-2.

Band 216: Florian Schüßler
Verbindungs- und Systemtechnik für thermisch hochbeanspruchte und miniaturisierte elektronische Baugruppen
FAPS, 184 Seiten, 93 Bilder, 18 Tab. 2010.
ISBN 978-3-87525-310-8.

Band 217: Massimo Cojutti
Strategien zur Erweiterung der Prozessgrenzen bei der Innhochdruck-Umformung von Rohren und Blechpaaren
LFT, 125 Seiten, 56 Bilder, 9 Tab. 2010. ISBN 978-3-87525-312-2.

Band 218: Raoul Plettke
Mehrkriterielle Optimierung komplexer Aktorsysteme für das Laserstrahljustieren
LFT, 152 Seiten, 25 Bilder, 3 Tab. 2010. ISBN 978-3-87525-315-3.

Band 219: Andreas Dobroschke
Flexible Automatisierungslösungen für die Fertigung wickeltechnischer Produkte
FAPS, 184 Seiten, 109 Bilder, 18 Tab. 2011.
ISBN 978-3-87525-317-7.

Band 220: Azhar Zam
Optical Tissue Differentiation for Sensor-Controlled Tissue-Specific Laser Surgery
LPT, 99 Seiten, 45 Bilder, 8 Tab. 2011. ISBN 978-3-87525-318-4.

Band 221: Michael Rösch
Potenziale und Strategien zur Optimierung des Schablonendruckprozesses in der Elektronikproduktion
FAPS, 192 Seiten, 127 Bilder, 19 Tab. 2011.
ISBN 978-3-87525-319-1.

Band 222: Thomas Rechtenwald
Quasi-isothermes Laserstrahlsintern von Hochtemperatur-Thermoplasten - Eine Betrachtung werkstoff-prozessspezifischer Aspekte am Beispiel PEEK
LPT, 150 Seiten, 62 Bilder, 8 Tab. 2011. ISBN 978-3-87525-320-7.

Band 223: Daniel Craiovan
Prozesse und Systemlösungen für die SMT-Montage optischer Bauelemente auf Substrate mit integrierten Lichtwellenleitern
FAPS, 165 Seiten, 85 Bilder, 8 Tab. 2011. ISBN 978-3-87525-324-5.

Band 224: Kay Wagner
Beanspruchungsangepasste Kaltmassivumformwerkzeuge durch lokal optimierte Werkzeugoberflächen
LFT, 147 Seiten, 103 Bilder, 17 Tab. 2011. ISBN 978-3-87525-325-2.

Band 225: Martin Brandhuber
Verbesserung der Prognosegüte des Versagens von Punktschweißverbindungen bei höchstfesten Stahlgüten
LFT, 155 Seiten, 91 Bilder, 19 Tab. 2011. ISBN 978-3-87525-327-6.

Band 226: Peter Sebastian Feuser
Ein Ansatz zur Herstellung von pressgehärteten Karosseriekomponenten mit maßgeschneiderten mechanischen Eigenschaften: Temperierte Umformwerkzeuge. Prozessfenster, Prozesssimuation und funktionale Untersuchung
LFT, 195 Seiten, 97 Bilder, 60 Tab. 2012. ISBN 978-3-87525-328-3.

Band 227: Murat Arbak
Material Adapted Design of Cold Forging Tools Exemplified by Powder Metallurgical Tool Steels and Ceramics
LFT, 109 Seiten, 56 Bilder, 8 Tab. 2012. ISBN 978-3-87525-330-6.

Band 228: Indra Pitz
Beschleunigte Simulation des Laserstrahlumformens von Aluminiumblechen
LPT, 137 Seiten, 45 Bilder, 27 Tab. 2012. ISBN 978-3-87525-333-7.

Band 229: Alexander Grimm
Prozessanalyse und -überwachung des Laserstrahlhartlötens mittels optischer Sensorik
LPT, 125 Seiten, 61 Bilder, 5 Tab. 2012. ISBN 978-3-87525-334-4.

Band 230: Markus Kaupper
Biegen von höhenfesten Stahlblechwerkstoffen - Umformverhalten und Grenzen der Biegbarkeit
LFT, 160 Seiten, 57 Bilder, 10 Tab. 2012. ISBN 978-3-87525-339-9.

Band 231: Thomas Kroiß
Modellbasierte Prozessauslegung für die Kaltmassivumformung unter Brücksichtigung der Werkzeug- und Pressenauffederung
LFT, 169 Seiten, 50 Bilder, 19 Tab. 2012. ISBN 978-3-87525-341-2.

Band 232: Christian Goth
Analyse und Optimierung der Entwicklung und Zuverlässigkeit räumlicher Schaltungsträger (3D-MID)
FAPS, 176 Seiten, 102 Bilder, 22 Tab. 2012.
ISBN 978-3-87525-340-5.

Band 233: Christian Ziegler
Ganzheitliche Automatisierung mechatronischer Systeme in der Medizin am Beispiel Strahlentherapie
FAPS, 170 Seiten, 71 Bilder, 19 Tab. 2012. ISBN 978-3-87525-342-9.

Band 234: Florian Albert
Automatisiertes Laserstrahllöten und -reparaturlöten elektronischer Baugruppen
LPT, 127 Seiten, 78 Bilder, 11 Tab. 2012. ISBN 978-3-87525-344-3.

Band 235: Thomas Stöhr
Analyse und Beschreibung des mechanischen Werkstoffverhaltens von presshärtbaren Bor-Manganstählen
LFT, 118 Seiten, 74 Bilder, 18 Tab. 2013. ISBN 978-3-87525-346-7.

Band 236: Christian Kägeler
Prozessdynamik beim Laserstrahlschweißen verzinkter Stahlbleche im Überlappstoß
LPT, 145 Seiten, 80 Bilder, 3 Tab. 2013. ISBN 978-3-87525-347-4.

Band 237: Andreas Sulzberger
Seriennahe Auslegung der Prozesskette zur wärmeunterstützten Umformung von Aluminiumblechwerkstoffen
LFT, 153 Seiten, 87 Bilder, 17 Tab. 2013. ISBN 978-3-87525-349-8.

Band 238: Simon Opel
Herstellung prozessangepasster Halbzeuge mit variabler Blechdicke durch die Anwendung von Verfahren der Blechmassivumformung
LFT, 165 Seiten, 108 Bilder, 27 Tab. 2013. ISBN 978-3-87525-350-4.

Band 239: Rajesh Kanawade
In-vivo Monitoring of Epithelium Vessel and Capillary Density for the Application of Detection of Clinical Shock and Early Signs of Cancer Development
LPT, 124 Seiten, 58 Bilder, 15 Tab. 2013. ISBN 978-3-87525-351-1.

Band 240: Stephan Busse
Entwicklung und Qualifizierung eines Schneidclinchverfahrens
LFT, 119 Seiten, 86 Bilder, 20 Tab. 2013. ISBN 978-3-87525-352-8.

Band 241: Karl-Heinz Leitz
Mikro- und Nanostrukturierung mit kurz und ultrakurz gepulster Laserstrahlung
LPT, 154 Seiten, 71 Bilder, 9 Tab. 2013. ISBN 978-3-87525-355-9.

Band 242: Markus Michl
Webbasierte Ansätze zur ganzheitlichen technischen Diagnose
FAPS, 182 Seiten, 62 Bilder, 20 Tab. 2013.
ISBN 978-3-87525-356-6.

Band 243: Vera Sturm
Einfluss von Chargenschwankungen auf die Verarbeitungsgrenzen von Stahlwerkstoffen
LFT, 113 Seiten, 58 Bilder, 9 Tab. 2013. ISBN 978-3-87525-357-3.

Band 244: Christian Neudel
Mikrostrukturelle und mechanisch-technologische Eigenschaften widerstandspunktgeschweißter Aluminium-Stahl-Verbindungen für den Fahrzeugbau
LFT, 178 Seiten, 171 Bilder, 31 Tab. 2014. ISBN 978-3-87525-358-0.

Band 245: Anja Neumann
Konzept zur Beherrschung der Prozessschwankungen im Presswerk
LFT, 162 Seiten, 68 Bilder, 15 Tab. 2014. ISBN 978-3-87525-360-3.

Band 246: Ulf-Hermann Quentin
Laserbasierte Nanostrukturierung mit optisch positionierten Mikrolinsen
LPT, 137 Seiten, 89 Bilder, 6 Tab. 2014. ISBN 978-3-87525-361-0.

Band 247: Erik Lamprecht
Der Einfluss der Fertigungsverfahren auf die Wirbelstromverluste von Stator-Einzelzahnblechpaketen für den Einsatz in Hybrid- und Elektrofahrzeugen
FAPS, 148 Seiten, 138 Bilder, 4 Tab. 2014. ISBN 978-3-87525-362-7.

Band 248: Sebastian Rösel
Wirkmedienbasierte Umformung von Blechhalbzeugen unter Anwendung magnetorheologischer Flüssigkeiten als kombiniertes Wirk- und Dichtmedium
LFT, 148 Seiten, 61 Bilder, 12 Tab. 2014. ISBN 978-3-87525-363-4.

Band 249: Paul Hippchen
Simulative Prognose der Geometrie indirekt pressgehärteter Karosseriebauteile für die industrielle Anwendung
LFT, 163 Seiten, 89 Bilder, 12 Tab. 2014. ISBN 978-3-87525-364-1.

Band 250: Martin Zubeil
Versagensprognose bei der Prozesssimulation von Biegeumform- und Falzverfahren
LFT, 171 Seiten, 90 Bilder, 5 Tab. 2014. ISBN 978-3-87525-365-8.

Band 251: Alexander Kühl
Flexible Automatisierung der Statorenmontage mit Hilfe einer universellen ambidexteren Kinematik
FAPS, 142 Seiten, 60 Bilder, 26 Tab. 2014.
ISBN 978-3-87525-367-2.

Band 252: Thomas Albrecht
Optimierte Fertigungstechnologien für Rotoren getriebeintegrierter PM-Synchronmotoren von Hybridfahrzeugen
FAPS, 198 Seiten, 130 Bilder, 38 Tab. 2014.
ISBN 978-3-87525-368-9.

Band 253: Florian Risch
Planning and Production Concepts for Contactless Power Transfer Systems for Electric Vehicles
FAPS, 185 Seiten, 125 Bilder, 13 Tab. 2014.
ISBN 978-3-87525-369-6.

Band 254: Markus Weigl
Laserstrahlschweißen von Mischverbindungen aus austenitischen und ferritischen korrosionsbeständigen Stahlwerkstoffen
LPT, 184 Seiten, 110 Bilder, 6 Tab. 2014. ISBN 978-3-87525-370-2.

Band 255: Johannes Noneder
Beanspruchungserfassung für die Validierung von FE-Modellen zur Auslegung von Massivumformwerkzeugen
LFT, 161 Seiten, 65 Bilder, 14 Tab. 2014. ISBN 978-3-87525-371-9.

Band 256: Andreas Reinhardt
Ressourceneffiziente Prozess- und Produktionstechnologie für flexible Schaltungsträger
FAPS, 123 Seiten, 69 Bilder, 19 Tab. 2014. ISBN 978-3-87525-373-3.

Band 257: Tobias Schmuck
Ein Beitrag zur effizienten Gestaltung globaler Produktions- und Logistiknetzwerke mittels Simulation
FAPS, 151 Seiten, 74 Bilder. 2014.
ISBN 978-3-87525-374-0.

Band 258: Bernd Eichenhüller
Untersuchungen der Effekte und Wechselwirkungen charakteristischer Einflussgrößen auf das Umformverhalten bei Mikroumformprozessen
LFT, 127 Seiten, 29 Bilder, 9 Tab. 2014. ISBN 978-3-87525-375-7.

Band 259: Felix Lütteke
Vielseitiges autonomes Transportsystem basierend auf Weltmodellerstellung mittels Datenfusion von Deckenkameras und Fahrzeugsensoren
FAPS, 152 Seiten, 54 Bilder, 20 Tab. 2014.
ISBN 978-3-87525-376-4.

Band 260: Martin Grüner
Hochdruck-Blechumformung mit formlos festen Stoffen als Wirkmedium
LFT, 144 Seiten, 66 Bilder, 29 Tab. 2014. ISBN 978-3-87525-379-5.

Band 261: Christian Brock
Analyse und Regelung des Laserstrahltiefschweißprozesses durch Detektion der Metalldampffackelposition
LPT, 126 Seiten, 65 Bilder, 3 Tab. 2015. ISBN 978-3-87525-380-1.

Band 262: Peter Vatter
Sensitivitätsanalyse des 3-Rollen-Schubbiegens auf Basis der Finite Elemente Methode
LFT, 145 Seiten, 57 Bilder, 26 Tab. 2015. ISBN 978-3-87525-381-8.

Band 263: Florian Klämpfl
Planung von Laserbestrahlungen durch simulationsbasierte Optimierung
LPT, 169 Seiten, 78 Bilder, 32 Tab. 2015. ISBN 978-3-87525-384-9.

Band 264: Matthias Domke
Transiente physikalische Mechanismen bei der Laserablation von dünnen Metallschichten
LPT, 133 Seiten, 43 Bilder, 3 Tab.
2015. ISBN 978-3-87525-385-6.

Band 265: Johannes Götz
Community-basierte Optimierung des Anlagenengineerings
FAPS, 177 Seiten, 80 Bilder, 30 Tab.
2015.
ISBN 978-3-87525-386-3.

Band 266: Hung Nguyen
Qualifizierung des Potentials von Verfestigungseffekten zur Erweiterung des Umformvermögens aushärtbarer Aluminiumlegierungen
LFT, 137 Seiten, 57 Bilder, 16 Tab.
2015. ISBN 978-3-87525-387-0.

Band 267: Andreas Kuppert
Erweiterung und Verbesserung von Versuchs- und Auswertetechniken für die Bestimmung von Grenzformänderungskurven
LFT, 138 Seiten, 82 Bilder, 2 Tab.
2015. ISBN 978-3-87525-388-7.

Band 268: Kathleen Klaus
Erstellung eines Werkstofforientierten Fertigungsprozessfensters zur Steigerung des Formgebungsvermögens von Alumi-niumlegierungen unter Anwendung einer zwischengeschalteten Wärmebehandlung
LFT, 154 Seiten, 70 Bilder, 8 Tab.
2015. ISBN 978-3-87525-391-7.

Band 269: Thomas Svec
Untersuchungen zur Herstellung von funktionsoptimierten Bauteilen im partiellen Presshärtprozess mittels lokal unterschiedlich temperierter Werkzeuge
LFT, 166 Seiten, 87 Bilder, 15 Tab.
2015. ISBN 978-3-87525-392-4.

Band 270: Tobias Schrader
Grundlegende Untersuchungen zur Verschleißcharakterisierung beschichteter Kaltmassivumformwerkzeuge
LFT, 164 Seiten, 55 Bilder, 11 Tab.
2015. ISBN 978-3-87525-393-1.

Band 271: Matthäus Brela
Untersuchung von Magnetfeld-Messmethoden zur ganzheitlichen Wertschöpfungsoptimierung und Fehlerdetektion an magnetischen Aktoren
FAPS, 170 Seiten, 97 Bilder, 4 Tab.
2015. ISBN 978-3-87525-394-8.

Band 272: Michael Wieland
Entwicklung einer Methode zur Prognose adhäsiven Verschleißes an Werkzeugen für das direkte Presshärten
LFT, 156 Seiten, 84 Bilder, 9 Tab.
2015. ISBN 978-3-87525-395-5.

Band 273: René Schramm
Strukturierte additive Metallisierung durch kaltaktives Atmosphärendruckplasma
FAPS, 136 Seiten, 62 Bilder, 15 Tab.
2015. ISBN 978-3-87525-396-2.

Band 274: Michael Lechner
Herstellung beanspruchungsangepasster Aluminiumblechhalbzeuge durch eine maßgeschneiderte Variation der Abkühlgeschwindigkeit nach Lösungsglühen
LFT, 136 Seiten, 62 Bilder, 15 Tab.
2015. ISBN 978-3-87525-397-9.

Band 275: Kolja Andreas
Einfluss der Oberflächenbeschaffenheit auf das Werkzeugeinsatzverhalten beim Kaltfließpressen
LFT, 169 Seiten, 76 Bilder, 4 Tab.
2015. ISBN 978-3-87525-398-6.

Band 276: Marcus Baum
Laser Consolidation of ITO Nanoparticles for the Generation of Thin Conductive Layers on Transparent Substrates
LPT, 158 Seiten, 75 Bilder, 3 Tab.
2015. ISBN 978-3-87525-399-3.

Band 277: Thomas Schneider
Umformtechnische Herstellung dünnwandiger Funktionsbauteile aus Feinblech durch Verfahren der Blechmassivumformung
LFT, 188 Seiten, 95 Bilder, 7 Tab.
2015. ISBN 978-3-87525-401-3.

Band 278: Jochen Merhof
Sematische Modellierung automatisierter Produktionssysteme zur Verbesserung der IT-Integration zwischen Anlagen-Engineering und Steuerungsebene
FAPS, 157 Seiten, 88 Bilder, 8 Tab.
2015. ISBN 978-3-87525-402-0.

Band 279: Fabian Zöller
Erarbeitung von Grundlagen zur Abbildung des tribologischen Systems in der Umformsimulation
LFT, 126 Seiten, 51 Bilder, 3 Tab.
2016. ISBN 978-3-87525-403-7.

Band 280: Christian Hezler
Einsatz technologischer Versuche zur Erweiterung der Versagensvorhersage bei Karosseriebauteilen aus höchstfesten Stählen
LFT, 147 Seiten, 63 Bilder, 44 Tab.
2016. ISBN 978-3-87525-404-4.

Band 281: Jochen Bönig
Integration des Systemverhaltens von Automobil-Hochvoltleitungen in die virtuelle Absicherung durch strukturmechanische Simulation
FAPS, 177 Seiten, 107 Bilder, 17 Tab.
2016.
ISBN 978-3-87525-405-1.

Band 282: Johannes Kohl
Automatisierte Datenerfassung für diskret ereignisorientierte Simulationen in der energieflexibelen Fabrik
FAPS, 160 Seiten, 80 Bilder, 27 Tab.
2016.
ISBN 978-3-87525-406-8.

Band 283: Peter Bechtold
Mikroschockwellenumformung mittels ultrakurzer Laserpulse
LPT, 155 Seiten, 59 Bilder, 10 Tab.
2016. ISBN 978-3-87525-407-5.

Band 284: Stefan Berger
Laserstrahlschweißen thermoplastischer Kohlenstofffaserverbundwerkstoffe mit spezifischem Zusatzdraht
LPT, 118 Seiten, 68 Bilder, 9 Tab.
2016. ISBN 978-3-87525-408-2.

Band 285: Martin Bornschlegl
Methods-Energy Measurement - Eine Methode zur Energieplanung für Fügeverfahren im Karosseriebau
FAPS, 136 Seiten, 72 Bilder, 46 Tab. 2016.
ISBN 978-3-87525-409-9.

Band 286: Tobias Rackow
Erweiterung des Unternehmenscontrollings um die Dimension Energie
FAPS, 164 Seiten, 82 Bilder, 29 Tab. 2016.
ISBN 978-3-87525-410-5.

Band 287: Johannes Koch
Grundlegende Untersuchungen zur Herstellung zyklisch-symmetrischer Bauteile mit Nebenformelementen durch Blechmassivumformung
LFT, 125 Seiten, 49 Bilder, 17 Tab. 2016. ISBN 978-3-87525-411-2.

Band 288: Hans Ulrich Vierzigmann
Beitrag zur Untersuchung der tribologischen Bedingungen in der Blechmassivumformung - Bereitstellung von tribologischen Modellversuchen und Realisierung von Tailored Surfaces
LFT, 174 Seiten, 102 Bilder, 34 Tab. 2016. ISBN 978-3-87525-412-9.

Band 289: Thomas Senner
Methodik zur virtuellen Absicherung der formgebenden Operation des Nasspressprozesses von Gelege-Mehrschichtverbunden
LFT, 156 Seiten, 96 Bilder, 21 Tab. 2016. ISBN 978-3-87525-414-3.

Band 290: Sven Kreitlein
Der grundoperationsspezifische Mindestenergiebedarf als Referenzwert zur Bewertung der Energieeffizienz in der Produktion
FAPS, 185 Seiten, 64 Bilder, 30 Tab. 2016.
ISBN 978-3-87525-415-0.

Band 291: Christian Roos
Remote-Laserstrahlschweißen verzinkter Stahlbleche in Kehlnahtgeometrie
LPT, 123 Seiten, 52 Bilder, 0 Tab. 2016. ISBN 978-3-87525-416-7.

Band 292: Alexander Kahrimanidis
Thermisch unterstützte Umformung von Aluminiumblechen
LFT, 165 Seiten, 103 Bilder, 18 Tab. 2016. ISBN 978-3-87525-417-4.

Band 293: Jan Tremel
Flexible Systems for Permanent Magnet Assembly and Magnetic Rotor Measurement / Flexible Systeme zur Montage von Permanentmagneten und zur Messung magnetischer Rotoren
FAPS, 152 Seiten, 91 Bilder, 12 Tab. 2016. ISBN 978-3-87525-419-8.

Band 294: Ioannis Tsoupis
Schädigungs- und Versagensverhalten hochfester Leichtbauwerkstoffe unter Biegebeanspruchung
LFT, 176 Seiten, 51 Bilder, 6 Tab. 2017. ISBN 978-3-87525-420-4.

Band 295: Sven Hildering
Grundlegende Untersuchungen zum Prozessverhalten von Silizium als Werkzeugwerkstoff für das Mikroscherschneiden metallischer Folien
LFT, 177 Seiten, 74 Bilder, 17 Tab. 2017. ISBN 978-3-87525-422-8.

Band 296: Sasia Mareike Hertweck
Zeitliche Pulsformung in der Lasermikromaterialbearbeitung – Grundlegende Untersuchungen und Anwendungen
LPT, 146 Seiten, 67 Bilder, 5 Tab. 2017. ISBN 978-3-87525-423-5.

Band 297: Paryanto
Mechatronic Simulation Approach for the Process Planning of Energy-Efficient Handling Systems
FAPS, 162 Seiten, 86 Bilder, 13 Tab. 2017. ISBN 978-3-87525-424-2.

Band 298: Peer Stenzel
Großserientaugliche Nadelwickeltechnik für verteilte Wicklungen im Anwendungsfall der E-Traktionsantriebe
FAPS, 239 Seiten, 147 Bilder, 20 Tab. 2017.
ISBN 978-3-87525-425-9.

Band 299: Mario Lušić
Ein Vorgehensmodell zur Erstellung montageführender Werkerinformationssysteme simultan zum Produktentstehungsprozess
FAPS, 174 Seiten, 79 Bilder, 22 Tab. 2017.
ISBN 978-3-87525-426-6.

Band 300: Arnd Buschhaus
Hochpräzise adaptive Steuerung und Regelung robotergeführter Prozesse
FAPS, 202 Seiten, 96 Bilder, 4 Tab. 2017. ISBN 978-3-87525-427-3.

Band 301: Tobias Laumer
Erzeugung von thermoplastischen Werkstoffverbunden mittels simultanem, intensitätsselektivem Laserstrahlschmelzen
LPT, 140 Seiten, 82 Bilder, 0 Tab. 2017. ISBN 978-3-87525-428-0.

Band 302: Nora Unger
Untersuchung einer thermisch unterstützten Fertigungskette zur Herstellung umgeformter Bauteile aus der höherfesten Aluminiumlegierung EN AW-7020
LFT, 142 Seiten, 53 Bilder, 8 Tab. 2017. ISBN 978-3-87525-429-7.

Band 303: Tommaso Stellin
Design of Manufacturing Processes for the Cold Bulk Forming of Small Metal Components from Metal Strip
LFT, 146 Seiten, 67 Bilder, 7 Tab. 2017. ISBN 978-3-87525-430-3.

Band 304: Bassim Bachy
Experimental Investigation, Modeling, Simulation and Optimization of Molded Interconnect Devices (MID) Based on Laser Direct Structuring (LDS) / Experimentelle Untersuchung, Modellierung, Simulation und Optimierung von Molded Interconnect Devices (MID) basierend auf Laser Direktstrukturierung (LDS)
FAPS, 168 Seiten, 120 Bilder, 26 Tab. 2017.
ISBN 978-3-87525-431-0.

Band 305: Michael Spahr
Automatisierte Kontaktierungsverfahren für flachleiterbasierte Pkw-Bordnetzsysteme
FAPS, 197 Seiten, 98 Bilder, 17 Tab. 2017. ISBN 978-3-87525-432-7.

Band 306: Sebastian Suttner
Charakterisierung und Modellierung des spannungszustandsabhängigen Werkstoffverhaltens der Magnesiumlegierung AZ31B für die numerische Prozessauslegung
LFT, 150 Seiten, 84 Bilder, 19 Tab. 2017. ISBN 978-3-87525-433-4.

Band 307: Bhargav Potdar
A reliable methodology to deduce thermo-mechanical flow behaviour of hot stamping steels
LFT, 203 Seiten, 98 Bilder, 27 Tab. 2017. ISBN 978-3-87525-436-5.

Band 308: Maria Löffler
Steuerung von Blechmassivumformprozessen durch maßgeschneiderte tribologische Systeme
LFT, viii u. 166 Seiten, 90 Bilder, 5 Tab. 2018. ISBN 978-3-96147-133-1.

Band 309: Martin Müller
Untersuchung des kombinierten Trenn- und Umformprozesses beim Fügen artungleicher Werkstoffe mittels Schneidclinchverfahren
LFT, xi u. 149 Seiten, 89 Bilder, 6 Tab. 2018.
ISBN: 978-3-96147-135-5.

Band 310: Christopher Kästle
Qualifizierung der Kupfer-Drahtbondtechnologie für integrierte Leistungsmodule in harschen Umgebungsbedingungen
FAPS, xii u. 167 Seiten, 70 Bilder, 18 Tab. 2018.
ISBN 978-3-96147-145-4.

Band 311: Daniel Vipavc
Eine Simulationsmethode für das 3-Rollen-Schubbiegen
LFT, xiii u. 121 Seiten, 56 Bilder, 17 Tab. 2018. ISBN 978-3-96147-147-8.

Band 312: Christina Ramer
Arbeitsraumüberwachung und autonome Bahnplanung für ein sicheres und flexibles Roboter-Assistenzsystem in der Fertigung
FAPS, xiv u. 188 Seiten, 57 Bilder, 9 Tab. 2018.
ISBN 978-3-96147-153-9.

Band 313: Miriam Rauer
Der Einfluss von Poren auf die Zuverlässigkeit der Lötverbindungen von Hochleistungs-Leuchtdioden
FAPS, xii u. 209 Seiten, 108 Bilder, 21 Tab. 2018.
ISBN 978-3-96147-157-7.

Band 314: Felix Tenner
Kamerabasierte Untersuchungen der Schmelze und Gasströmungen beim Laserstrahlschweißen verzinkter Stahlbleche
LPT, xxiii u. 184 Seiten, 94 Bilder, 7 Tab. 2018.
ISBN 978-3-96147-160-7.

Band 315: Aarief Syed-Khaja
Diffusion Soldering for High-temperature Packaging of Power Electronics
FAPS, x u. 202 Seiten, 144 Bilder, 32 Tab. 2018.
ISBN 978-3-87525-162-1.

Band 316: Adam Schaub
Grundlagenwissenschaftliche Untersuchung der kombinierten Prozesskette aus Umformen und Additive Fertigung
LFT, xi u. 192 Seiten, 72 Bilder, 27 Tab. 2019.
ISBN 978-3-96147-166-9.

Band 317: Daniel Gröbel
Herstellung von Nebenformelementen unterschiedlicher Geometrie an Blechen mittels Fließpressverfahren der Blechmassivumformung
LFT, x u. 165 Seiten, 96 Bilder, 13 Tab. 2019. ISBN 978-3-96147-168-3.

Band 318: Philipp Hildenbrand
Entwicklung einer Methodik zur Herstellung von Tailored Blanks mit definierten Halbzeugeigenschaften durch einen Taumelprozess
LFT, ix u. 153 Seiten, 77 Bilder, 4 Tab. 2019. ISBN 978-3-96147-174-4.

Band 319: Tobias Konrad
Simulative Auslegung der Spann- und Fixierkonzepte im Karosserierohbau: Bewertung der Baugruppenmaßhaltigkeit unter Berücksichtigung schwankender Einflussgrößen
LFT, x u. 203 Seiten, 134 Bilder, 32 Tab. 2019.
ISBN 978-3-96147-176-8.

Band 320: David Meinel
Architektur applikationsspezifischer Multi-Physics-Simulationskonfiguratoren am Beispiel modularer Triebzüge
FAPS, xii u. 166 Seiten, 82 Bilder, 25 Tab. 2019.
ISBN 978-3-96147-184-3.

Band 321: Andrea Zimmermann
Grundlegende Untersuchungen zum Einfluss fertigungsbedingter Eigenschaften auf die Ermüdungsfestigkeit kaltmassivumgeformter Bauteile
LFT, ix u. 160 Seiten, 66 Bilder, 5 Tab. 2019.
ISBN 978-3-96147-190-4.

Band 322: Christoph Amann
Simulative Prognose der Geometrie nassgepresster Karosseriebauteile aus Gelege-Mehrschichtverbunden
LFT, xvi u. 169 Seiten, 80 Bilder, 13 Tab. 2019.
ISBN 978-3-96147-194-2.

Band 323: Jennifer Tenner
Realisierung schmierstofffreier Tiefziehprozesse durch maßgeschneiderte Werkzeugoberflächen
LFT, x u. 187 Seiten, 68 Bilder, 13 Tab. 2019.
ISBN 978-3-96147-196-6.

Band 324: Susan Zöller
Mapping Individual Subjective Values to Product Design
KTmfk, xi u. 223 Seiten, 81 Bilder, 25 Tab. 2019.
ISBN 978-3-96147-202-4.

Band 325: Stefan Lutz
Erarbeitung einer Methodik zur semiempirischen Ermittlung der Umwandlungskinetik durchhärtender Wälzlagerstähle für die Wärmebehandlungssimulation
LFT, xiv u. 189 Seiten, 75 Bilder, 32 Tab. 2019.
ISBN 978-3-96147-209-3.

Band 326: Tobias Gnibl
Modellbasierte Prozesskettenabbildung rührreibgeschweißter Aluminiumhalbzeuge zur umformtechnischen Herstellung höchstfester Leichtbau-strukturteile
LFT, xii u. 167 Seiten, 68 Bilder, 17 Tab. 2019.
ISBN 978-3-96147-217-8.

Band 327: Johannes Bürner
Technisch-wirtschaftliche Optionen zur Lastflexibilisierung durch intelligente elektrische Wärmespeicher
FAPS, xiv u. 233 Seiten, 89 Bilder, 27 Tab. 2019.
ISBN 978-3-96147-219-2.

Band 328: Wolfgang Böhm
Verbesserung des Umformverhaltens von mehrlagigen Aluminiumblechwerkstoffen mit ultrafeinkörnigem Gefüge
LFT, ix u. 160 Seiten, 88 Bilder, 14 Tab. 2019.
ISBN 978-3-96147-227-7.

Band 329: Stefan Landkammer
Grundsatzuntersuchungen, mathematische Modellierung und Ableitung einer Auslegungsmethodik für Gelenkantriebe nach dem Spinnenbeinprinzip
LFT, xii u. 200 Seiten, 83 Bilder, 13 Tab. 2019.
ISBN 978-3-96147-229-1.

Band 330: Stephan Rapp
Pump-Probe-Ellipsometrie zur Messung transienter optischer Materialeigen-schaften bei der Ultrakurzpuls-Lasermaterialbearbeitung
LPT, xi u. 143 Seiten, 49 Bilder, 2 Tab. 2019.
ISBN 978-3-96147-235-2.

Band 331: Michael Scholz
Intralogistics Execution System mit integrierten autonomen, servicebasierten Transportentitäten
FAPS, xi u. 195 Seiten, 55 Bilder, 11 Tab. 2019.
ISBN 978-3-96147-237-6.

Band 332: Eva Bogner
Strategien der Produktindividualisierung in der produzierenden Industrie im Kontext der Digitalisierung
FAPS, ix u. 201 Seiten, 55 Bilder, 28 Tab. 2019.
ISBN 978-3-96147-246-8.

Band 333: Daniel Benjamin Krüger
Ein Ansatz zur CAD-integrierten muskuloskelettalen Analyse der Mensch-Maschine-Interaktion
KTmfk, x u. 217 Seiten, 102 Bilder, 7 Tab. 2019.
ISBN 978-3-96147-250-5.

Band 334: Thomas Kuhn
Qualität und Zuverlässigkeit laserdirektstrukturierter mechatronisch integrierter Baugruppen (LDS-MID)
FAPS, ix u. 152 Seiten, 69 Bilder, 12 Tab. 2019.
ISBN: 978-3-96147-252-9.

Band 335: Hans Fleischmann
Modellbasierte Zustands- und Prozessüberwachung auf Basis sozio-cyber-physischer Systeme
FAPS, xi u. 214 Seiten, 111 Bilder, 18 Tab. 2019.
ISBN: 978-3-96147-256-7.

Band 336: Markus Michalski
Grundlegende Untersuchungen zum Prozess- und Werkstoffverhalten bei schwingungsüberlagerter Umformung
LFT, xii u. 197 Seiten, 93 Bilder, 11 Tab. 2019.
ISBN: 978-3-96147-270-3.

Band 337: Markus Brandmeier
Ganzheitliches ontologiebasiertes Wissensmanagement im Umfeld der industriellen Produktion
FAPS, xi u. 255 Seiten, 77 Bilder, 33 Tab. 2020.
ISBN: 978-3-96147-275-8.

Band 338: Stephan Purr
Datenerfassung für die Anwendung lernender Algorithmen bei der Herstellung von Blechformteilen
LFT, ix u. 165 Seiten, 48 Bilder, 4 Tab. 2020.
ISBN: 978-3-96147-281-9.

Band 339: Christoph Kiener
Kaltfließpressen von gerad- und schrägverzahnten Zahnrädern
LFT, viii u. 151 Seiten, 81 Bilder, 3 Tab. 2020.
ISBN 978-3-96147-287-1.

Band 340: Simon Spreng
Numerische, analytische und empirische Modellierung des Heißcrimpprozesses
FAPS, xix u. 204 Seiten, 91 Bilder, 27 Tab. 2020.
ISBN 978-3-96147-293-2.

Band 341: Patrik Schwingenschlögl
Erarbeitung eines Prozessverständnisses zur Verbesserung der tribologischen Bedingungen beim Presshärten
LFT, x u. 177 Seiten, 81 Bilder, 8 Tab. 2020.
ISBN 978-3-96147-297-0.

Band 342: Emanuela Affronti
Evaluation of failure behaviour of sheet metals
LFT, ix u. 136 Seiten, 57 Bilder, 20 Tab. 2020.
ISBN 978-3-96147-303-8.

Band 343: Julia Degner
Grundlegende Untersuchungen zur Herstellung hochfester Aluminiumblechbauteile in einem kombinierten Umform- und Abschreckprozess
LFT, x u. 172 Seiten, 61 Bilder, 9 Tab. 2020.
ISBN 978-3-96147-307-6.

Band 344: Maximilian Wagner
Automatische Bahnplanung für die Aufteilung von Prozessbewegungen in synchrone Werkstück- und Werkzeugbewegungen mittels Multi-Roboter-Systemen
FAPS, xxi u. 181 Seiten, 111 Bilder, 15 Tab. 2020.
ISBN 978-3-96147-309-0.

Band 345: Stefan Härter
Qualifizierung des Montageprozesses hochminiaturisierter elektronischer Bauelemente
FAPS, ix u. 194 Seiten, 97 Bilder, 28 Tab. 2020.
ISBN 978-3-96147-314-4.

Band 346: Toni Donhauser
Ressourcenorientierte Auftragsregelung in einer hybriden Produktion mittels betriebsbegleitender Simulation
FAPS, xix u. 242 Seiten, 97 Bilder, 17 Tab. 2020.
ISBN 978-3-96147-316-8.

Band 347: Philipp Amend
Laserbasiertes Schmelzkleben von Thermoplasten mit Metallen
LPT, xv u. 154 Seiten, 67 Bilder. 2020. ISBN 978-3-96147-326-7.

Band 348: Matthias Ehlert
Simulationsunterstützte funktionale Grenzlagenabsicherung
KTmfk, xvi u. 300 Seiten, 101 Bilder, 73 Tab. 2020.
ISBN 978-3-96147-328-1.

Band 349: Thomas Sander
Ein Beitrag zur Charakterisierung und Auslegung des Verbundes von Kunststoffsubstraten mit harten Dünnschichten
KTmfk, xiv u. 178 Seiten, 88 Bilder, 21 Tab. 2020.
ISBN 978-3-96147-330-4.

Band 350: Florian Pilz
Fließpressen von Verzahnungselementen an Blechen
LFT, x u. 170 Seiten, 103Bilder, 4 Tab. 2020.
ISBN 978-3-96147-332-8.

Band 351: Sebastian Josef Katona
Evaluation und Aufbereitung von Produktsimulationen mittels abweichungsbehafteter Geometriemodelle
KTmfk, ix u. 147 Seiten, 73 Bilder, 11 Tab. 2020.
ISBN 978-3-96147-336-6.

Band 352: Jürgen Herrmann
Kumulatives Walzplattieren. Bewertung der Umformeigenschaften mehrlagiger Blechwerkstoffe der ausscheidungshärtbaren Legierung AA6014
LFT, x u. 157 Seiten, 64 Bilder, 5 Tab. 2020.
ISBN 978-3-96147-344-1.

Band 353: Christof Küstner
Assistenzsystem zur Unterstützung der datengetriebenen Produktentwicklung
KTmfk, xii u. 219 Seiten, 63 Bilder, 14 Tab. 2020.
ISBN 978-3-96147-348-9.

Band 354: Tobias Gläßel
Prozessketten zum Laserstrahlschweißen von flachleiterbasierten Formspulenwicklungen für automobile Traktionsantriebe
FAPS, xiv u. 206 Seiten, 89 Bilder, 11 Tab. 2020.
ISBN 978-3-96147-356-4.

Band 355: Andreas Meinel
Experimentelle Untersuchung der Auswirkungen von Axialschwingungen auf Reibung und Verschleiß in Zylinderrol-lenlagern
KTmfk, xii u. 162 Seiten, 56 Bilder, 7 Tab. 2020.
ISBN 978-3-96147-358-8.

Band 356: Hannah Riedle
Haptische, generische Modelle weicher anatomischer Strukturen für die chirurgische Simulation
FAPS, xxx u. 179 Seiten, 82 Bilder, 35 Tab. 2020.
ISBN 978-3-96147-367-0.

Band 357: Maximilian Landgraf
Leistungselektronik für den Einsatz dielektrischer Elastomere in aktorischen, sensorischen und integrierten sensomotorischen Systemen
FAPS, xxiii u. 166 Seiten, 71 Bilder, 10 Tab. 2020.
ISBN 978-3-96147-380-9.

Band 358: Alireza Esfandyari
Multi-Objective Process Optimization for Overpressure Reflow Soldering in Electronics Production
FAPS, xviii u. 175 Seiten, 57 Bilder, 23 Tab. 2020.
ISBN 978-3-96147-382-3.

Band 359: Christian Sand
Prozessübergreifende Analyse komplexer Montageprozessketten mittels Data Mining
FAPS, XV u. 168 Seiten, 61 Bilder, 12 Tab. 2021.
ISBN 978-3-96147-398-4.

Band 360: Ralf Merkl
Closed-Loop Control of a Storage-Supported Hybrid Compensation System for Improving the Power Quality in Medium Voltage Networks
FAPS, xxvii u. 200 Seiten, 102 Bilder, 2 Tab. 2021.
ISBN 978-3-96147-402-8.

Band 361: Thomas Reitberger
Additive Fertigung polymerer optischer Wellenleiter im Aerosol-Jet-Verfahren
FAPS, xix u. 141 Seiten, 65 Bilder, 11 Tab. 2021.
ISBN 978-3-96147-400-4.

Band 362: Marius Christian Fechter
Modellierung von Vorentwürfen in der virtuellen Realität mit natürlicher Fingerinteraktion
KTmfk, x u. 188 Seiten, 67 Bilder, 19 Tab. 2021.
ISBN 978-3-96147-404-2.

Band 363: Franziska Neubauer
Oberflächenmodifizierung und Entwicklung einer Auswertemethodik zur Verschleißcharakterisierung im Presshärteprozess
LFT, ix u. 177 Seiten, 42 Bilder, 6 Tab. 2021.
ISBN 978-3-96147-406-6.

Band 364: Eike Wolfram Schäffer
Web- und wissensbasierter Engineering-Konfigurator für roboterzentrierte Automatisierungslösungen
FAPS, xxiv u. 195 Seiten, 108 Bilder, 25 Tab. 2021.
ISBN 978-3-96147-410-3.

Band 365: Daniel Gross
Untersuchungen zur kohlenstoffdioxidbasierten kryogenen Minimalmengenschmierung
REP, xii u. 184 Seiten, 56 Bilder, 18 Tab. 2021.
ISBN 978-3-96147-412-7.

Band 366: Daniel Junker
Qualifizierung laser-additiv gefertigter Komponenten für den Einsatz im Werkzeugbau der Massivumformung
LFT, vii u. 142 Seiten, 62 Bilder, 5 Tab. 2021.
ISBN 978-3-96147-416-5.

Band 367: Tallal Javied
Totally Integrated Ecology Management for Resource Efficient and Eco-Friendly Production
FAPS, xv u. 160 Seiten, 60 Bilder, 13 Tab. 2021.
ISBN 978-3-96147-418-9.

Band 368: David Marco Hochrein
Wälzlager im Beschleunigungsfeld – Eine Analysestrategie zur Bestimmung des Reibungs-, Axialschub- und Temperaturverhaltens von Nadelkränzen –
KTmfk, xiii u. 279 Seiten, 108 Bilder, 39 Tab. 2021.
ISBN 978-3-96147-420-2.

Band 369: Daniel Gräf
Funktionalisierung technischer Oberflächen mittels prozessüberwachter aerosolbasierter Drucktechnologie
FAPS, xxii u. 175 Seiten, 97 Bilder, 6 Tab. 2021.
ISBN 978-3-96147-433-2.

Band 370: Andreas Gröschl
Hochfrequent fokusabstandsmodulierte Konfokalsensoren für die Nanokoordinatenmesstechnik
FMT, x u. 144 Seiten, 98 Bilder, 6 Tab. 2021.
ISBN 978-3-96147-435-6.

Band 371: Johann Tüchsen
Konzeption, Entwicklung und Einführung des Assistenzsystems D-DAS für die Produktentwicklung elektrischer Motoren
KTmfk, xii u. 178 Seiten, 92 Bilder, 12 Tab. 2021.
ISBN 978-3-96147-437-0.

Band 372: Max Marian
Numerische Auslegung von Oberflächenmikrotexturen für geschmierte tribologische Kontakte
KTmfk, xviii u. 276 Seiten, 85 Bilder, 45 Tab. 2021.
ISBN 978-3-96147-439-4.

Band 373: Johannes Strauß
Die akustooptische Strahlformung in der Lasermaterialbearbeitung
LPT, xvi u. 113 Seiten, 48 Bilder. 2021. ISBN 978-3-96147-441-7.

Band 374: Martin Hohmann
Machine learning and hyper spectral imaging: Multi Spectral Endoscopy in the Gastro Intestinal Tract towards Hyper Spectral Endoscopy
LPT, x u. 137 Seiten, 62 Bilder, 29 Tab. 2021.
ISBN 978-3-96147-445-5.

Band 375: Timo Kordaß
Lasergestütztes Verfahren zur selektiven Metallisierung von epoxidharzbasierten Duromeren zur Steigerung der Integrationsdichte für dreidimensionale mechatronische Package-Baugruppen
FAPS, xviii u. 198 Seiten, 92 Bilder, 24 Tab. 2021.
ISBN 978-3-96147-443-1.

Band 376: Philipp Kestel
Assistenzsystem für den wissensbasierten Aufbau konstruktionsbegleitender Finite-Elemente-Analysen
KTmfk, xviii u. 209 Seiten, 57 Bilder, 17 Tab. 2021.
ISBN 978-3-96147-457-8.

Band 377: Martin Lerchen
Messverfahren für die pulverbettbasierte additive Fertigung zur Sicherstellung der Konformität mit geometrischen Produktspezifikationen
FMT, x u. 150 Seiten, 60 Bilder, 9 Tab. 2021.
ISBN 978-3- 96147-463-9.

Band 378: Michael Schneider
Inline-Prüfung der Permeabilität in weichmagnetischen Komponenten
FAPS, xxii u. 189 Seiten, 79 Bilder, 14 Tab. 2021.
ISBN 978-3-96147-465-3.

Band 379: Tobias Sprügel
Sphärische Detektorflächen als Unterstützung der Produktentwicklung zur Datenanalyse im Rahmen des Digital Engineering
KTmfk, xiii u. 213 Seiten, 84 Bilder, 33 Tab. 2021.
ISBN 978-3-96147-475-2.

Band 380: Tom Häfner
Multipulseffekte beim Mikro-Materialabtrag von Stahllegierungen mit Pikosekunden-Laserpulsen
LPT, xxviii u. 159 Seiten, 57 Bilder, 13 Tab. 2021.
ISBN 978-3-96147-479-0.

Band 381: Björn Heling
Einsatz und Validierung virtueller Absicherungsmethoden für abweichungs-behaftete Mechanismen im Kontext des Robust Design
KTmfk, xi u. 169 Seiten, 63 Bilder, 27 Tab. 2021.
ISBN 978-3-96147-487-5.

Band 382: Tobias Kolb
Laserstrahl-Schmelzen von Metallen mit einer Serienanlage – Prozesscharakterisierung und Erweiterung eines Überwachungssystems
LPT, xv u. 170 Seiten, 128 Bilder, 16 Tab. 2021.
ISBN 978-3-96147-491-2.

Band 383: Mario Meinhardt
Widerstandselementschweißen mit gestauchten Hilfsfügeelementen - Umformtechnische Wirkzusammenhänge zur Beeinflussung der Verbindungsfestigkeit
LFT, xii u. 189 Seiten, 87 Bilder, 4 Tab. 2022.
ISBN 978-3-96147-473-8.

Band 384: Felix Bauer
Ein Beitrag zur digitalen Auslegung von Fügeprozessen im Karosseriebau mit Fokus auf das Remote-Laserstrahlschweißen unter Einsatz flexibler Spanntechnik
LFT, xi u. 185 Seiten, 74 Bilder, 12 Tab. 2022.
ISBN 978-3-96147-498-1.

Band 385: Jochen Zeitler
Konzeption eines rechnergestützten Konstruktionssystems für optomechatronische Baugruppen
FAPS, xix u. 172 Seiten, 88 Bilder, 11 Tab. 2022.
ISBN 978-3-96147-499-8.

Band 386: Vincent Mann
Einfluss von Strahloszillation auf das Laserstrahlschweißen hochfester Stähle
LPT, xiii u. 172 Seiten, 103 Bilder, 18 Tab. 2022.
ISBN 978-3-96147-503-2.

Band 387: Chen Chen
Skin-equivalent opto-/elastofluidic in-vitro microphysiological vascular models for translational studies of optical biopsies
LPT, xx u. 126 Seiten, 60 Bilder, 10 Tab. 2022.
ISBN 978-3-96147-505-6.

Band 388: Stefan Stein
Laser drop on demand joining as bonding method for electronics assembly and packaging with high thermal requirements
LPT, x u. 112 Seiten, 54 Bilder, 10 Tab. 2022.
ISBN 978-3-96147-507-0

Band 389: Nikolaus Urban
Untersuchung des Laserstrahlschmelzens von Neodym-Eisen-Bor zur additiven Herstellung von Permanentmagneten
FAPS, x u. 174 Seiten, 88 Bilder, 18 Tab. 2022.
ISBN: 978-3-96147-501-8.

Band 390: Yiting Wu
Großflächige Topographiemessungen mit einem Weißlichtinterferenzmikroskop und einem metrologischen Rasterkraftmikroskop
FMT, xii u. 142 Seiten, 68 Bilder, 11 Tab. 2022.
ISBN: 978-3-96147-513-1.

Band 391: Thomas Papke
Untersuchungen zur Umformbarkeit hybrider Bauteile aus Blechgrundkörper und additiv gefertigter Struktur
LFT, xii u. 194 Seiten, 71 Bilder, 16 Tab. 2022.
ISBN 978-3-96147-515-5.

Band 392: Bastian Zimmermann
Einfluss des Vormaterials auf die mehrstufige Kaltumformung vom Draht
LFT, xi u. 182 Seiten, 36 Bilder, 6 Tab. 2022.
ISBN 978-3-96147-519-3.

Band 393: Harald Völkl
Ein simulationsbasierter Ansatz zur Auslegung additiv gefertigter FLM-Faserverbundstrukturen
KTmfk, xx u. 204 Seiten, 95 Bilder, 22 Tab. 2022.
ISBN 978-3-96147-523-0.

Band 394: Robert Schulte
Auslegung und Anwendung prozessangepasster Halbzeuge für Verfahren der Blechmassivumformung
LFT, x u. 163 Seiten, 93 Bilder, 5 Tab. 2022.
ISBN 978-3-96147-525-4.

Band 395: Philipp Frey
Umformtechnische Strukturierung metallischer Einleger im Folgeverbund für mediendichte Kunststoff-Metall-Hybridbauteile
LFT, ix u. 180 Seiten, 83 Bilder, 7 Tab. 2022.
ISBN 978-3-96147-534-6.

Band 396: Thomas Johann Luft
Komplexitätsmanagement in der Produktentwicklung - Holistische Modellierung, Analyse, Visualisierung und Bewertung komplexer Systeme
KTmfk, xiii u. 510 Seiten, 166 Bilder, 16 Tab. 2022.
ISBN 978-3-96147-540-7.

Band 397: Li Wang
Evaluierung der Einsetzbarkeit des lasergestützten Verfahrens zur selektiven Metallisierung für die Verbesserung passiver Intermodulation in Hochfrequenzanwendungen
FAPS, xxii u.151 Seiten, 72 Bilder, 22 Tab. 2022.
ISBN 978-3-96147-542-1.

Band 398: Sebastian Reitelshöfer
Der Aerosol-Jet-Druck Dielektrischer Elastomere als additives Fertigungsverfahren für elastische mechatronische Komponenten
FAPS, xxv u. 206 Seiten, 87 Bilder, 13 Tab. 2022.
ISBN 978-3-96147-547-6.

Band 399: Alexander Meyer
Selektive Magnetmontage zur Verringerung des Rastmomentes permanenterregter Synchronmotoren
FAPS, xv u. 164 Seiten, 90 Bilder, 18 Tab. 2022.
ISBN 978-3-96147-555-1.

Band 400: Rong Zhao
Design verschleißreduzierender amorpher Kohlenstoffschichtsysteme für trockene tribologische Gleitkontakte
KTmfk, x u. 148 Seiten, 69 Bilder, 14 Tab. 2022.
ISBN 978-3-96147-557-5.

Band 401: Christian P. J. Schwarzer
Kupfersintern als Fügetechnologie für Leistungselektronik
FAPS, xxvii u. 234 Seiten, 125 Bilder, 24 Tab. 2022.
ISBN 978-3-96147-566-7.

Band 402: Alexander Horn
Grundlegende Untersuchungen zur Gradierung der mechanischen Eigenschaften pressgehärteter Bauteile durch eine örtlich begrenzte Aufkohlung
LFT, xii u. 204 Seiten, 58 Bilder, 6 Tab. 2022.
ISBN 978-3-96147-568-1.

Band 403: Artur Klos
Werkstoff- und umformtechnische Bewertung von hochfesten Aluminiumblechwerkstoffen für den Karosseriebau
LFT, x u. 192 Seiten, 73 Bilder, 12 Tab. 2022.
ISBN 978-3-96147-572-8.

Band 404: Harald Schmid
Ganzheitliche Erarbeitung eines Prozessverständnisses von Tiefziehprozessen mit Ziehsicken auf Basis mechanischer und tribologischer Analysen
LFT, xiii u. 211 Seiten, 78 Bilder, 5 Tab. 2022.
ISBN 978-3-96147-577-3.

Band 405: Johannes Henneberg
Blechmassivumformung von Funktionsbauteilen aus Bandmaterial
LFT, viii u. 176 Seiten, 101 Bilder, 2 Tab. 2022.
ISBN 978-3-96147-579-7.

Band 406: Anton Schmailzl
Festigkeits- und zeitoptimierte Prozessführung beim quasi-simultanen Laser-Durchstrahlschweißen
LPT, xiii u. 157 Seiten, 84 Bilder, 7 Tab. 2022.
ISBN 978-3-96147-583-4.

Band 407: Alexander Wolf
Modellierung und Vorhersage menschlichen Interaktionsverhaltens zur Analyse der Mensch-Produkt Interaktion
KTmfk, x u. 207 Seiten, 69 Bilder, 10 Tab. 2022.
ISBN 978-3-96147-585-8.

Band 408: Tim Weikert
Modifikationen amorpher Kohlenstoffschichten zur Anpassung der Reibungsbedingungen und zur Erhöhung des Verschleißschutzes
KTmfk, xvii u. 258 Seiten, 91 Bilder, 9 Tab. 2022.
ISBN 978-3-96147-589-6.

Band 409: Stefan Götz
Frühzeitiges konstruktionsbegleitendes Toleranzmanagement
KTmfk, ix u. 276 Seiten, 127 Bilder, 13 Tab. 2022.
ISBN 978-3-96147-593-3.

Band 410: Markus Hubert
Einsatzpotenziale der Rotationsschneidtechnologie in der Verarbeitung von metallischen Funktionsfolien für mechatronische Produkte
FAPS, xviii u. 139 Seiten, 86 Bilder, 7 Tab. 2022
ISBN 978-3-96147-603-9.

Band 411: Manfred Vogel
Grundlagenuntersuchungen und Erarbeitung einer Methodik zur Herstellung maßgeschneiderter Halbzeuge auf Basis eines neuartigen flexiblen Walzprozesses
LFT, ix u. 176 Seiten, 61 Bilder, 11 Tab. 2022.
ISBN 978-3-96147-605-3.

Band 412: Michael Weigelt
Multidimensionale Optionenanalyse alternativer Antriebskonzepte für die individuelle Langstreckenmobilität
FAPS, xv u. 222 Seiten, 89 Bilder, 38 Tab. 2022
ISBN 978-3-96147-607-7.

Band 413: Frank Bodendorf
Machine Learning im Cost Engineering des Supply Managements
FAPS, xiii u. 166 Seiten, 75 Bilder, 13 Tab. 2022
ISBN 978-3-96147-609-1.

Band 414: Maximilian Metzler
Planung und Simulation taktiler, intelligenter und kollaborativer Roboterfähigkeiten in der Montage
FAPS, xix u. 174 Seiten, 72 Bilder, 3 Tab. 2022.
ISBN 978-3-96147-611-4.

Band 415: Tina Buker
Ein Ansatz zur Reduktion produktinduzierter Nutzerstigmatisierung durch Förderung einer gleichermaßen gebrauchstauglichen wie emotionalen Produktgestalt
KTmfk, x u. 236 Seiten, 54 Bilder, 44 Tab. 2022.
ISBN: 978-3-96147-613-8.

Band 416: Marlene Kuhn
Model-based Traceability System Development for Complex Manufacturing Applying Blockchain and Graphs
FAPS, xv u. 167 Seiten, 63 Bilder, 10 Tab. 2022.
ISBN: 978-3-96147-615-2.

Band 417: Benjamin Lengenfelder
Remote photoacoustic sensing using speckle-analysis for biomedical imaging
LPT, xv u. 124 Seiten, 86 Bilder, 10 Tab. 2023.
ISBN: 978-3-96147-617-6.

Kurzzusammenfassung

In dieser Arbeit wird die kontaktfreie Speckleanalyse, für ihre Anwendung zur photoakustischen Detektion untersucht. Zuerst wird ein Simulationsmodell erstellt, das die Erfassbarkeit von photoakustischen Oberflächendeformationen durch die Speckleanalyse theoretisch bestätigt. Im Anschluss wird die Machbarkeit der kontaktfreien Detektion anhand von Experimenten an Phantomen und ex-vivo Gewebe mit einem Kamerasystem demonstriert. Für diese Messungen werden mehrere Speckles analysiert und im Rahmen dieser Experimente wird die endoskopische Anwendbarkeit der Technik anhand eines Faserbündels gezeigt. Um die Aufnahme der Speckles zu beschleunigen, wird das Kamerasystem durch einen diodenbasierten Sensor niedrigerer Auflösung ersetzt. Mit diesem schnelleren System wird die Machbarkeit der kontaktfreien photoakustischen Detektion und deren Automatisierbarkeit durch die Einzelspeckleanalyse experimentell nachgewiesen. Beide verwendeten Analysetechniken werden auf Basis ihrer Eigenschaften wie Empfindlichkeit, Messbereich, Linearität und Messtiefe verglichen. Weiterhin wird anhand von Untersuchungen an ex-vivo-Gewebe gezeigt, dass die Wellenlänge ein entscheidender Parameter für die Qualität eines Specklemusters und der Speckleanalyse ist. Schließlich wird die Möglichkeit der photoakustischen Bildgebung für die Speckleanalyse demonstriert, indem ein Rekonstruktionsansatz anhand von Simulationen und durch ein erstes Experiment getestet wird.

In this thesis the simple, contact-free speckle-analysis is investigated for its application in photoacoustic detection. First, a simulation model is created which theoretically confirms the detectability of photoacoustic surface deformations by speckle-analysis. Subsequently, the feasibility of contact-free detection is demonstrated by experiments on phantoms and ex-vivo tissue using a high-speed camera system. For these measurements multiple speckles are analyzed and within these experiments the endoscopic applicability of the technique by using an imaging fiber bundle is demonstrated. In order to speed up the acquisition of speckles, the high-speed camera system is replaced by a diode-based sensor of lower resolution. With this faster system the feasibility of contact-free photoacoustic detection and its automation by single speckle-analysis is experimentally demonstrated. Both used analysis techniques are compared based on their characteristics such as sensitivity, measuring range, linearity and measuring depth. Furthermore, investigations on ex-vivo tissue are used to show that the speckle wavelength is a crucial parameter for the quality of a speckle pattern and speckle-analysis. Finally, the possibility of photoacoustic imaging for speckle-analysis is demonstrated by testing a reconstruction approach by simulations and by a first experiment.

ISBN 978-3-96147-617-6

9 783961 476176

FAU UNIVERSITY PRESS 2023